Tris-heteroleptic Iridium Complexes for White Emission

By

Yanouk Cudré

UNIVERSITY OF BIRMINGHAM

A thesis submitted to

The University of Birmingham

For a degree of

DOCTOR OF PHILOSOPHY

School of Chemistry

College of Engineering and Physical Sciences

University of Birmingham

July 2017

I. Abstract

Within the past decades, extensive research has been focusing on developing electroluminescent technologies (OLED and LEC). Especially, a lot of effort has been dedicated to the search of efficient phosphorescent materials with highly tuneable emission maxima bearing late transition metal atoms. Emitters such as cyclometalated idirium complexes have been proven to be very successful in this regard, exhibiting colours from blue to red and being successfully applied in electroluminescent technologies. However, in order to decrease the manufacturing cost of these technologies, a single-centre white emitting material is highly desirable. In this context, this work investigates a new family of complexes bearing three different bidentate ligands known as tris-heteroleptic complexes to develop an emitter with a broad emission profile that would result in a white colour. Eighteen new tris-heteroleptic complexes with unprecedented ligand configurations have been synthesised by mixing different kind of ligands such as phenylpyridines (ppy), phenylpyrazoles (ppz) and phenylimidazoles (pim). This resulted in significant emission broadening with FWHM values up to nearly 6000 cm^{-1}.

II. Acknowledgements

At the moment of submitting my thesis, I am looking back over my shoulder and see all the people who supported me during these years by providing me with precious advices, support and friendship.

These people made these PhD years not only about work. They made these years represent a special chapter of my life that I will never forget.

I thank especially Etienne for giving the chance of doing this PhD. For all his precious advices and conversations (work related or not), for his help and support and unlimited availability.

Alongside him, I wish to address a special thank to the school of chemistry staff who make the everyday work possible. Especially, I received tremendous help and support from Neil, and later Cécile, with the NMR analyses; Louise, Chi and Alan for the X-Ray, Mass spec and HPLC analyses; Stuart, Ian and Steve for their availability and precious help.

To all the people I met from Chemistry or from elsewhere who became friends: Antoine, Tom and François but also Carlotta, Manu, Antoine, Chris, Antoine, Josh, Michel, Miguel, Alex, Ellie, Charlotte, Alexandros, Masoud, Ioana and Sanaz and all the others.

I did not forget my friends from Switzerland and they have not forgotten about me during these years: Maël, Lara, Marine, Simon, Mathieu, Nastasia, Julien, Amaël, Barbara, Laura, Valérie.

And my family: Géraldine, Martine, Yves, Mylane, Carine and Sarah.

And course I kept her for the end; the person who always supported me no matter what, who always gave me her trust and love and kept me going in the hard times; my love and best friend:

To Chloé.

III. TABLE OF CONTENTS

1 INTRODUCTION

1.1 General introduction

Since the industrial revolution, mankind never stopped increasing its consumption of artificial light and invented many technologies to answer this demand. The twentieth century saw the progressive marginalisation of gas for the production of artificial light to the profit of electricity.[1] Nowadays, electricity plays a very important role as an energy carrier and the technologies relying on it are uncountable. In 2010, the production of artificial light was estimated to represent 6.5 % of the world's primary energy.[2] It has been identified as one of the main energy consumption sources in buildings, both commercial and residential.[3] In Japan, the part of electricity used to produce artificial light represented nearly 14 % of the total electricity consumption in 2009[4] and the world energy council estimated this percentage to be 19 % for developed countries in its 2013 report.[5] As the world energy and electricity demand never stopped increasing, and is still projected to increase during the next decades,[6] tremendous efforts have been achieved in order to provide the world with more efficient electrical devices, use the available resources in the best possible way and meet with the challenges of the future energy consumption. In this regard, artificial lighting technologies are a perfect example. Incredible progress has been realised since first very unefficient incandescent light bulbs, with the development of technologies such as fluorescent tubes. In the last decades, devices such as LEDs have also become very efficient and popular, opening a new chapter in the artificial lighting history.[7] However, all light sources have drawbacks such as heat generation, incorporation of toxic gas or metals, bad extraction of produced light, short life spans or high costs. Therefore, the need for new, more efficient and cheaper light sources is always strong.

1.2 Electroluminescent technologies

As part of an answer to the world energy challenge, more efficient lighting sources are required. A solution could be to use electroluminescent devices along with, or instead of current lighting technologies. These electroluminescent devices are organic light emitting-diodes (OLED) and light-emitting electrochemical cells (LEC or LEEC).

As this work focuses on light-emitting molecules that can be applied to these technologies, the basics of their working principle and architectures are briefly discussed below. However, this work does not focus on OLED and LEC technologies per say, as almost every aspect of their architecture is a specific field of research.

These technologies both work on the same principle of electro-excitation. A thin layer of photoactive molecules is placed between two electrodes and an electrical current is applied. Electrons and holes are injected in the system and recombine at the emitter level, leaving the molecules in an electronic excited state. The emitting molecules then release the electrical energy under the form of photons when they go relax to their electronic ground state.

Both technologies are cold light sources that can be used for surface lighting and/or in flexible devices[8,9] and can be made by relatively easy printing methods. The main difference between the two is that LECs use charged electroluminescent materials when OLEDs use neutral ones.[10] Since OLED technology is also older and more developed, it occupies a larger market share with various applications.[11]

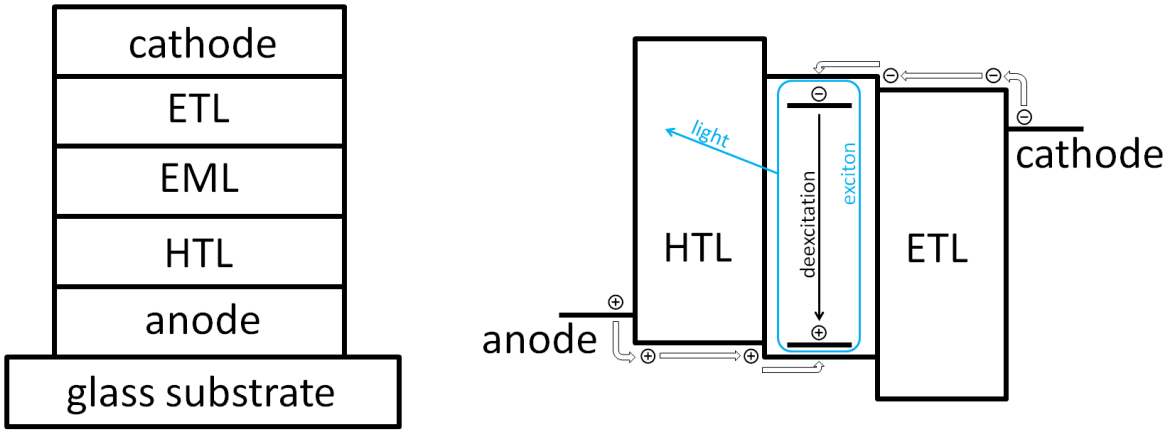

Figure 1.1: Schematic representation of an OLED device (left). Schematic representation of charge movement and light emission in an OLED device (right).

In an OLED, the emitting material is not only sandwiched between the electrodes but also between charge injection and transport layers in order to increase the device efficiency. The schematic OLED drawing (Figure 1.1, left) shows a situation where the emitting layer (EML) is surrounded by an electron transport layer (ETL) and a hole transport layer (HTL). These additional layers insure the efficient carrying of the charges from the electrodes to the emitting layer and prevent unwanted phenomena such as exciton quenching close to the electrodes.[12] The scheme presented above (Figure 1.1, right) shows the working principle of a simple OLED. Under the application of an electric potential, charges are injected from the electrodes to the adjacent layer (electrons at the cathode and holes at the anode). Electrons and holes then migrate through the ETL and HTL and are injected in the LUMO (electrons) and HOMO (holes) of the emitting material (inside the emitting layer), leaving it in an excited state (exciton). The high energy contained in this excited state is released under the form of light as the emitter relaxes into its ground state.

All the materials involved have to fulfil specific conditions. Cathodes and anodes are chosen respectively according to their low and high work functions respectively, usually from metals (such as Ca or Mg for the cathode) or metal oxides (indium tin oxide, ITO, mixture of SnO_2 and In_2O_3 for the anode). ETL and HTL materials have to be adapted to the emitter material and show adapted HOMO and LUMO energy levels as well as good holes and electrons conductivities (examples of such materials are shown in Figure 1.2). Additional layers such as electrons/hole blocking and injecting layers can be added to the device to facilitate the injection of charges from the electrodes to the transport layer and to prevent the charges to pass the EML. In addition, the emitting material has to be doped into a host material in order to avoid concentration quenching. Therefore, this material must also fulfil conditions such as high triplet energy (compared to the emitter).

By contrast, LEC architecture is simpler as the electron and hole transport layers are not required. Because of the ionic nature of the materials used, the charge repartition adapts itself in the emissive layer and produces efficient charge transport.[13] Therefore, these systems are less sensitive to the electrode used and can rely on air stable electrodes.[10,14,15]

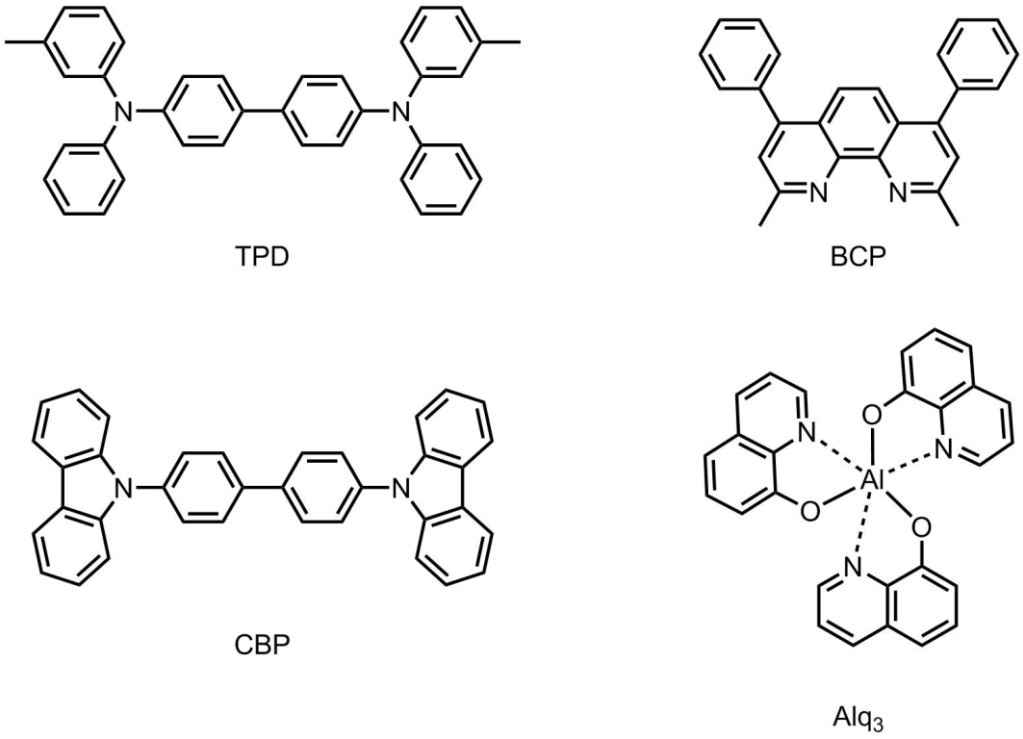

Figure 1.2: Examples of materials used in OLED technology: N,N′-Bis(3-methylphenyl)-N,N′-diphenylbenzidine (TPD) as a hole transporter, bathocuproine (BCP) and tris(8-hydroxyquinolinato)aluminium (Alq3) as electron transporter and 4,4′-bis(N-carbazolyl)biphenyl (CBP) as a host material for green emitters.

As for OLED, the emitting molecule is doped into a host that can be a polymer[16,17] or a small organic molecule.[15] They can also be used alone while relying on bulky groups to reduce self-quenching processes.[18,19] For charged complexes, the solubility in organic solvent is influenced by the counter-anion and can therefore be increased by changing this parameter making charged iridium complexes easy to use in liquid printing device fabrication.

Even though OLED technology is now more developed and shows good results in a wide range of applications such as screens and displays, its high manufacturing cost limits its use for wider low-cost applications. In this regard, LEC technology provides cheaper and easier to make devices to fill this gap. In the context of the present research, both neutral and charged complexes can be considered as the photophysical properties of the studied complexes are not influenced by the overall charge.

1.3 Photophysical principles of light emission

If a molecule absorbs a sufficient amount of energy, one of its electrons can be promoted from the HOMO to the LUMO. The molecule, previously lying in an energy state defined as the ground state (S_0), finds itself in an excited state of higher energy characterised by the new electronic configuration. The new electron distribution around the nuclei induces a geometry change in the molecule. A part of the energy absorbed then dissipates as heat with the molecule vibrating down to the minimal energy of the excited state. This process is known as internal conversion. If the LUMO electron has kept its spin and still opposes the spin of the HOMO electron, the excited state is a singlet (S_1, S_2, ... , S_n). If a spin flip occurs and the two electrons have the same spin, the excited state is a triplet (e.g. T_1). As the molecule finds itself in the most stable excited state conformation, it can release the remaining energy by "jumping" back to the ground state (S_0). The excited electron goes back to the HOMO and a photon is emitted which energy corresponds to the energy difference between the excited state and S_0.

However, excited states also can relax back to S_0 via non radiative pathways and the efficiency of the light emission process is modulated by its rate of occurrence in relation to the rate of all the non radiative processes possible. In order to obtain visible light emission, a molecule must satisfy two major criteria. 1) The energy difference between its emissive excited state and S_0 must be in the energy range of visible light. 2) The rate of its light emission must be higher than the rate of its non radiative relaxation pathways.

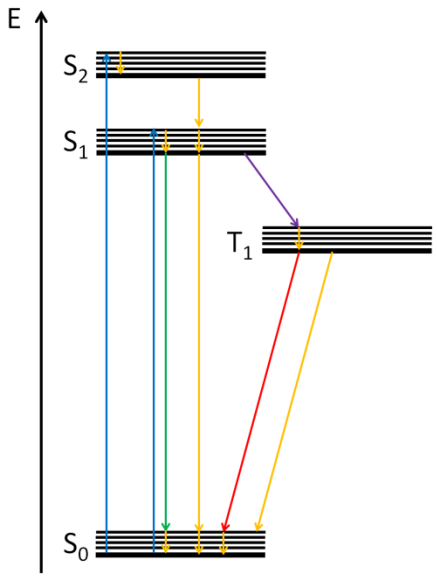

Figure 1.3: Simplified Jablonski diagram showing the possible energy pathway happening in a molecule. The thick black lines represent the lowest energy conformation of a state. The thin black lines represent the vibrational sub states. S_0 is the singlet ground state and S_1 and S_2 the two first singlet excited states. T_1 is the most stable triplet excited state. Blue arrows represent light absorption transitions. The green and red are fluorescence and phosphorescence respectively. The orange arrows show internal conversion and non radiative deactivation processes in general.

For a purely organic molecule, the spin flip of one electron to create a triplet state (T_1) known as intersystem crossing (ISC, purple arrow) is forbidden. The light emission therefore only happens from S_1. Light emission generated by a singlet to singlet ($S_1 \rightarrow S_0$) transition is designated as fluorescence (green arrow). The influence of a large atom is required to introduce spin-orbit coupling (SOC) that makes the ISC process efficient enough to allow a triplet to singlet relaxation ($T_1 \rightarrow S_0$), called phosphorescence.[20,21]

1.4 Why Iridium

The major reason for using transition metal complexes for electroluminescent devices is that electric generation of excited state gives rise to 75% of triplet states.[22–24] As purely organic fluorescent molecules do not benefit from the spin-orbit coupling provided by heavy transition metal atoms, light emission from these states is extremely slow and the molecules relax their energy via non radiative pathways.[25] These triplet excited states are then lost which means that the maximum electroluminescent quantum yield of a purely fluorescent molecule is 25% since only the singlet states are emissive.

Heavy atoms such as iridium are known to reduce the radiative lifetime of triplet excited states[26] allowing efficient light emission via phosphorescence pathways. Intersystem crossing (ISC, which describes the spin flip of the excited electron to create a triplet excited state $S_1 \rightarrow T_1$)[20] is also accelerated in presence of a heavy atom and increases the probability to observe phosphorescence. In other words, electro-excitation of a luminescent iridium complex can potentially result in a 100% efficient light emission mostly due to a phosphorescence process.[27]

Iridium being a third row transition metal, it provides a large splitting of d orbitals (Δ_0) further increased by the 3+ oxidation of the iridium ion in complexes. In addition the cyclometalation to high field ligands such as phenylpyridines further increase Δ_0.[21,28] A large Δ_0 reduces the chance of generating d-d* states leading to quenching of light emission and higher complex degradation rate under excitation. It also leaves a larger energy gap to tune the π and π^* energy levels, making highly colour-tuneable complexes.

1.5 Structure of iridium complexes

Iridium complexes for electroluminescence applications are generally formed of three bidentate cyclometalated ligands arranged around the metal centre in an octahedral geometry. These complexes are divided into three major families. One with three same ligands (L^L), giving a formula $Ir(L^L)_3$ referred to as tris-homoleptic complexes. One with two L^L ligands and a different ligand (X^X), referred to as bis-heteroleptic complexes of general formula $Ir(L^L)_2(X^X)$. For these complexes, the L^L ligands are called the main ligands while X^X is called the ancillary ligand. These two families of complexes represent the vast majority of luminescent iridium complexes present in the literature. However, there is a third family of complexes where the three ligands are different. These complexes are called tris-heteroleptic and have the general formula $Ir(L_1^L_1)(L_2^L_2)(X^X)$. In most cases L^L represents a cyclometalated species with a coordinated heterocycle and a carbon-metal bond (e.g. phenylpyridine (ppy),[29] phenypyrazole (ppz),[30] generally abbreviated C^N). The ancillary ligand X^X can represent for example acetylacetonate (acac),[31,32] 2,2'-bipyridines (bpy)[33] or picolinates (pic)[31,34] and are therefore abbreviated by their coordinating atoms (O^O, N^N or N^O).

1.5.1 Chirality and structural isomerism

If we consider tris-cyclometalated homoleptic complexes of general formula $Ir(C^N)_3$, the octahedral geometry generates a Λ/Δ chirality. Furthermore, since a C^N type ligand is asymmetric, facial (fac) and meridional (mer) diastereomers can be created for each Λ and Δ complex.[35,36] The Λ/Δ chirality does not play an important role in the physical properties of these complexes in solution as their symmetry, polarity and magnetism remain the same. Therefore, it does not impact the photophysical properties. This chirality is however useful when one considers using these complexes as catalysts.[37] In the present work drawings of

complexes only present one enantiomer for clarity, but racemic mixtures are assumed unless stated otherwise.

The mer/fac isomerism has much more influence on the properties of such complexes, as they drastically change local chemical environments and the overall symmetry. Mer and fac isomers are therefore easily differentiable by ^{1}H-NMR and separable by standard chromatography techniques (at least in theory). Moreover, they display different stabilities in solution and also differ in their photophysical properties.

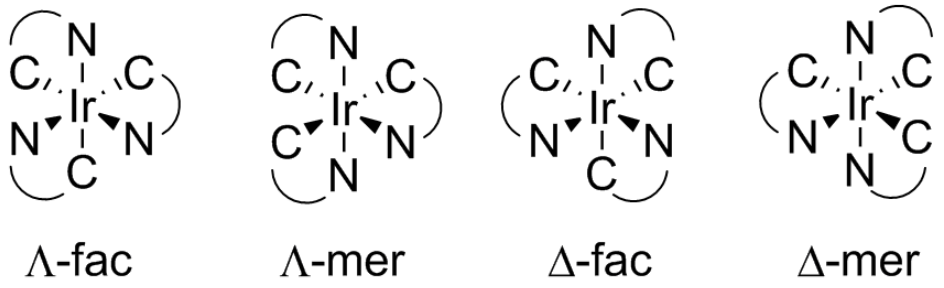

Figure 1.4: Meridional (mer) and facial (fac) representations of homoleptic tris-cyclometalated iridium complexes with C^N type ligands.

Bis-heteroleptic complexes are similar to homoleptic mer homoleptic complexes. If we consider that X^X is a non symmetrical ligand N^O (e.g. pic), the general formula becomes $Ir(C^N)_2(N^O)$ and the orientation of the N^O ligand allows to differentiate the two main ligands (Figure 1.5).

Keeping the C^N ligands in a pseudo facial position and changing the orientation of the N^O ligand allows to draw two pairs of enantiomers (Λ_1/Δ_1 and Λ_2/Δ_2). As for the homoleptic complexes, enantiomers of the same complex present almost identical properties and are impossible to differentiate by NMR or to separate by simple chromatography methods. Differences are observable when comparing the ones and the twos as the magnetic properties of the ligands are drastically affected by the orientation of the N^O ligand. Since $C_1^N_1$ is the

same as C_2^N_2, there is no distinction between the two rows of pseudo fac complexes shown below ($\Lambda_1/\Delta_2 = \Lambda_3/\Delta_3$ and $\Lambda_2/\Delta_2 = \Lambda_4/\Delta_4$).

Pseudo mer complexes display only two times two possibilities obtained by switching the orientation of one or both of the C^N ligands to obtain a trans N-Ir-N or trans C-Ir-C configuration. As the two C^N ligands are oriented the same way around the iridium, the orientation of the N^O ligand does not matter ($\Lambda_5/\Delta_5 = \Lambda_6/\Delta_6$ and $\Lambda_7/\Delta_7 = \Lambda_8/\Delta_8$). However, due to the asymmetry of N^O, the two C^N ligands are not magnetically equivalent (in a particular complex) and display separate NMR signals.

Tris-heteroleptic complexes display even more possible configurations with $\Lambda_1/\Delta_1 \neq \Lambda_3/\Delta_3$, $\Lambda_2/\Delta_2 \neq \Lambda_4/\Delta_4$, $\Lambda_5/\Delta_5 \neq \Lambda_6/\Delta_6$ and $\Lambda_7/\Delta_7 \neq \Lambda_8/\Delta_8$.

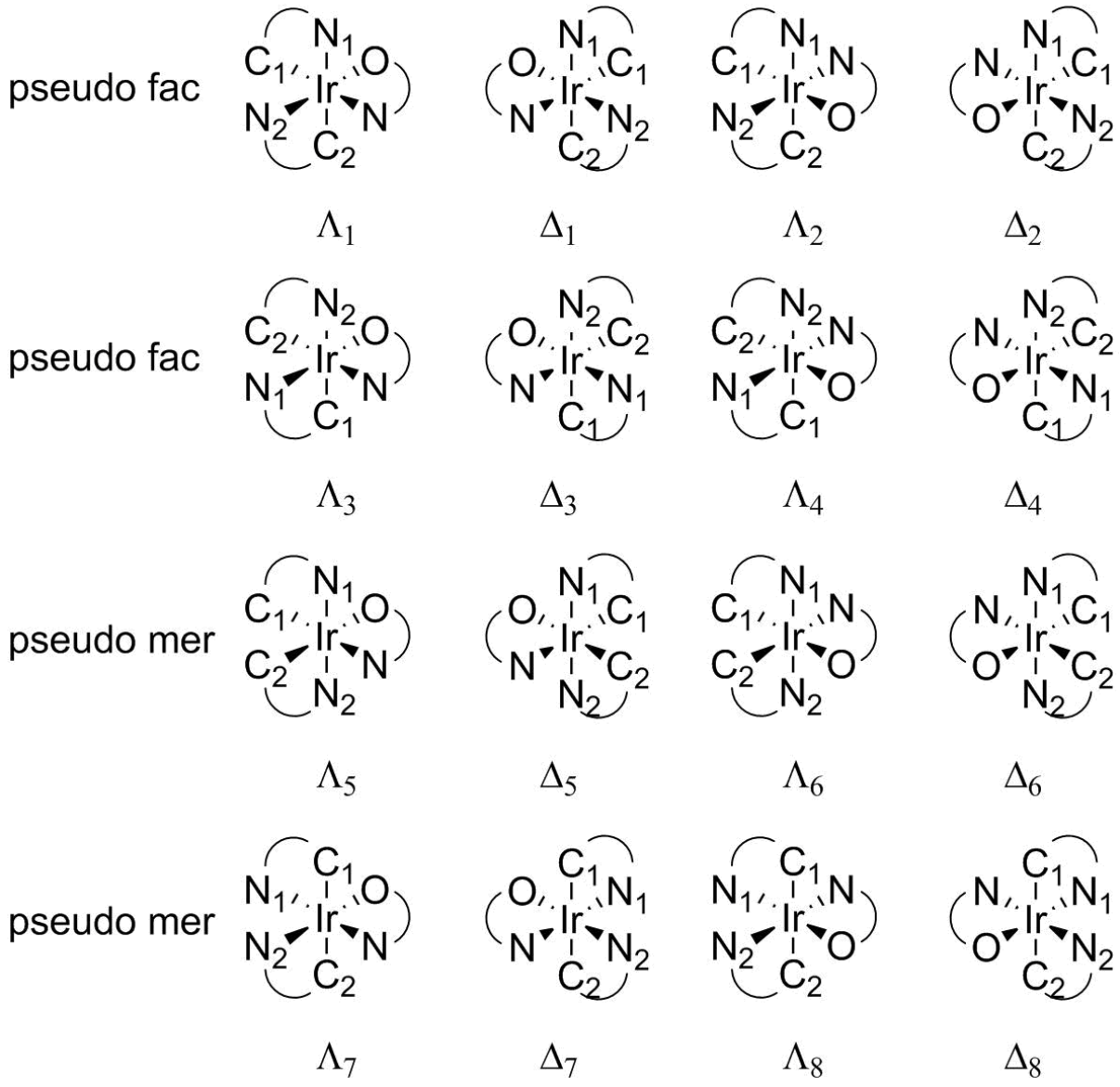

Figure 1.5: Representations of bis and tris-heteroleptic complexes with C^N type main ligands and asymmetric N^O type ancillary ligands. These ligands organisations are shown for the sake of the example do not all represent current products of iridium complexes syntheses. The pseudo mer and pseudo fac notation is based on the orientation of the C^N ligands only and refer to their orientation in a tris-homoleptic complex.

In practice, not all configurations presented above are formed during the synthesis of iridium complexes. With homoleptic complexes, the meridional configuration tends to be kinetically favoured while the facial configuration is the thermodynamically favoured product. Mer to fac isomerisation can often be achieved just by heating or prolonged light exposure of the mer product.[35]

Bis-heteroleptic and tris-heteroleptic complexes are synthesised in a way that strongly favours the N-Ir-N pseudo mer configuration (Λ_5/Δ_5 and Λ_6/Δ_6), but a complex with a flipped C^N ligand is a possible degradation product.[38] Pseudo mer configurations with trans-cyclometalated carbons (C-Ir-C) are never observed and are only depicted in Figure 1.5 for the sake of the argument. (However, in a situation where the ancillary ligand is also cyclometalated ($Ir(C_1\text{^}N_1)(C_2\text{^}N_2)(C_3\text{^}N_3)$), it is possible that facial and meridional configurations would coexist, allowing most of these configurations to be observed.)

This brings the number of different complexes actually encountered back to respectively one and two enantiomer couples for bis- and tris-heteroleptic complexes. Furthermore, replacing an asymmetric N^O ancillary ligand by a symmetric N^N or O^O ligand allows only one tris-heteroleptic enantiomer couple complexes as the difference between Λ_5/Δ_5 and Λ_6/Δ_6 is suppressed.

In this context, the syntheses of bis-heteroleptic complexes with symmetrical or asymmetrical ancillary ligands are equivalent while the introduction of a non-symmetrical ancillary ligand doubles the amount of isomers obtained when synthesising tris-heteroleptic complexes.

1.5.2 Bonding and electronic structure

Iridium(III) complexes of the type $Ir(C\hat{}N)_3$ can be described from a crystal field theory perspective.[28] They are formed of a triply charged $5d^6$ iridium cation counterbalanced by three ($^{-}C\hat{}N$) anions. Each ligand contributes to the filling of the valence shell with four electrons (two from the coordinating nitrogen and two from the cyclometalated carbon) which makes a total of 18 valence electrons.

The d orbital splitting is large, due to the combined influence of the third row metal and a strong ligand field provided by the cyclometalated ligands. The six remaining d electrons are therefore in a "low spin" configuration and the complex is diamagnetic.[21]

For bis-heteroleptic complexes, the third ligand often provides a third negative charge (e.g. O^{-}) but if it is not the case, the complex carries a positive charge counterbalanced by a surrounding counter anion (e.g. Cl^{-}, PF_6^{-}).

From a ligand field perspective, σ bonds are made from the interaction between the 5d, 6s and 6p metal orbitals with the sp^2 ligand orbitals from the aromatic nitrogens and cyclometalated carbons.[28,39,40] Therefore, they are not degenerate as depicted in Figure 1.6 and are only depicted as such to simplify the picture. The shared electrons are coming from the nitrogen lone pairs (3x2 electrons), d orbitals of the metal (3 electrons) and C-H bond broken during the cyclometalation process (3x1 electrons).

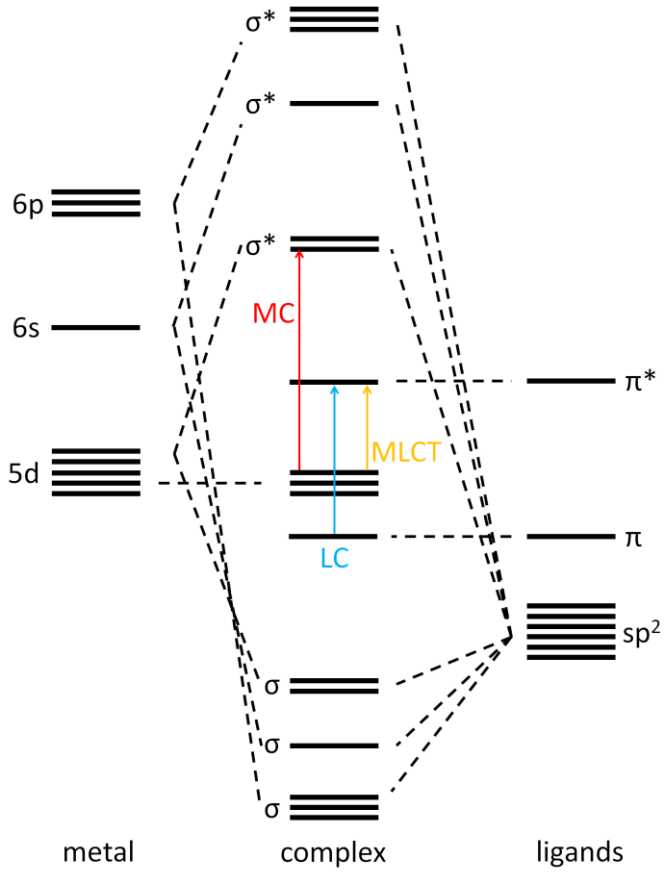

Figure 1.6: Simplified molecular orbital diagram for an octahedral iridium complex.

The creation of the six σ bonding orbitals is associated with six σ^* anti-bonding orbitals much higher in energy.

The six σ bonding orbitals being closer in energy to the ligand sp^2 orbitals than to the metal s, p, or d orbitals, they contain an increased "ligand character" while the corresponding anti-bonding σ^* are more metal based and contain an increased "metal character".

The energies of the σ and σ^* orbitals depend on their amount of s, p, d character (on the metal part) and of the nature the ligands used. The precise determination of these energies is not useful for electroluminescent applications as they lay way below the HOMO (bonding) and way above the LUMO (antibonding) energies. One notable exception is the two first σ^* orbital with strong metal-d character that correspond to the empty d orbital in the crystal field model.

Populating these orbitals via a MC transition would result in a metal-ligand bond destabilisation.[41]

In this model, three degenerate d orbitals of the metal core remain filled with six non-bonding d electrons, leaving the complex in a low spin configuration.

1.5.3 Excited states of iridium complexes

As photo excitation goes, an electron is promoted from the HOMOs located on the metal 5d non-bonding orbitals and on the π orbitals of the ligand (phenyl ring for a ppy ligand) to the LUMO, located on the π^*orbital of the ligand (on the pyridine part). The transition is said to be of mixed metal-to-ligand-charge-transfer (MLCT, $5d_{Ir}$ to $\pi^*_{pyridine}$) or ligand-centred (LC, π_{phenyl} to $\pi^*_{pyridine}$) character.[42,43]

To achieve a precise analysis of the possible molecular excited states, the simplistic HOMO-LUMO transition model must be extended as HOMO-1, -2 and LUMO+1, +2 (for example, but not only those) are also involved in electronic excitation. As these molecular orbitals are close in energy, there is a certain degree of quantum chemical mixing between them that influences the photophysical properties. As an example, the mixing of the metal 5d orbitals with the π orbitals of the ligands participates in the SOC necessary in generating efficient triplet emission.[25]

In depth analysis of all the states generated by the transitions allowed will not be attempted here. It can be achieved by DFT calculation methods, which can predict the absorption and emission spectra shapes and give insights on other photophysical properties such as quantum yields or radiative lifetimes.[25]

For the requirements of this work, a more simplistic model is sufficient.

Electronic excitation results in an excited state of mixed LC and MLCT character usually singlet (^{1}LC and ^{1}MLCT), the strong SOC induced by the large iridium atom allows an efficient ISC mechanism to happen, generating emissive ^{3}LC and ^{3}MLCT states.[20,25] The relative amounts of these states roughly determines the shape of the emission spectrum as LC emission is expected to be more defined with apparent vibrational peaks or shoulders. MLCT shaped emission is expected to be less defined and broader as well as shifted to a lower energy region of the emission spectrum.

In the process, metal centred states (MC) resulting from a d-σ^* transition can also be generated. Since the σ^* orbitals have a strong metal character, the transition is essentially metal based and can be referred to as a d-d* transition.[44]

In the case of the iridium complexes of interest, these states are generated mostly if they are thermally accessible from a close MLCT or LC state. In other words, if the π^* orbitals of the ligands and the d* orbitals of the metal are close in energy.

As these orbitals are antibonding, their population produces an elongation of one metal-ligand bond that can result in breaking a metal nitrogen bond.[45,46] This represents an efficient quenching of the excited state as well as degradation factor for electroluminescent materials. Therefore, a criterion for an efficient material is a large enough energy difference between π^* and d* orbitals.

1.5.4 Tris-homoleptic & Bis-heteroleptic Complexes

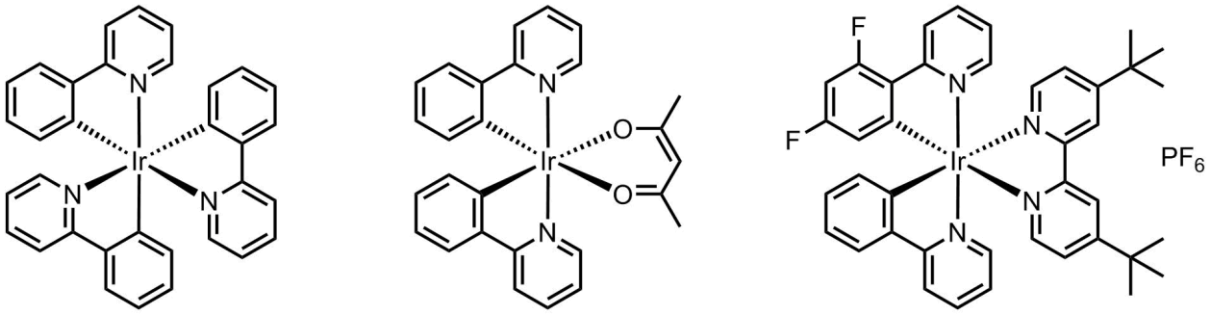

Figure 1.7: An example of tris-homoleptic complex, [Ir(ppy)$_3$] (left), of bis-heteroleptic complex [Ir(ppy)$_2$(acac)] (centre) and of tris-heteroleptic complex, [Ir(ppy)(diFppy)(dtb-bpy)][PF$_6$] (right).

Many transition metal complexes have been studied over the years for lighting applications in OLED and LEC, using different metal centres such as Ru[13,47,48] , Os[49–51] or Cu[15,52,53], but none of them provides the same tunability as iridium, with stable complexes emitting among the entire visible spectrum.

Iridium complexes can be divided into three major groups; the tris-homoleptic complexes[54] (like [Ir(ppy)$_3$], Figure 1.7 left, ppy: 2-phenylpyridine) having three identical ligands, the bis-heteroleptic complexes[55] (like [Ir(ppy)$_2$(acac)], Figure 1.7 centre, acac: acetylacetonate) having two identical main ligands, and a third ancillary ligand, and the tris-heteroleptic complexes where the three ligands are different[56] (like [Ir(ppy)(diFppy)(dtb-bpy)][PF$_6$], Figure 1.7 right, diFppy: 2-(2,4-difluorophenyl)pyridine, dtb-bpy: 4,4'-di-tert-butyl-2,2'-bipyridine). Homoleptic and bis-heteroleptic have been largely studied over the years, giving rise to a large number of compounds used for device application. Tris-heteroleptic complexes are very new and only a few of them have been studied until now (see below)

To offer a good approximation, the electronic transition involved in light emission can be considered as a HOMO-LUMO transition. Tuning the emission wavelength can then be understood as tuning the HOMO-LUMO energy gap by stabilizing or destabilizing these

orbitals.[54] This is made possible because these orbitals are located on distinct parts of the complex. Therefore, it is possible to alter the energy of one of them without drastically influencing the other.

From a practical point of view, donor or acceptor groups can be added on key locations of the complex to destabilise or stabilise either the HOMO or the LUMO. With a homoleptic complex like $[Ir(ppy)_3]$, the HOMO is delocalised between the metal core and the phenyl ring while the LUMO is located on the pyridine ring (as presented in Figure 1.8). A blue shift can then be obtained by adding an electron withdrawing group (or two) on the phenyl ring or by adding an electron donating group on the pyridine (or by doing both at the same time).

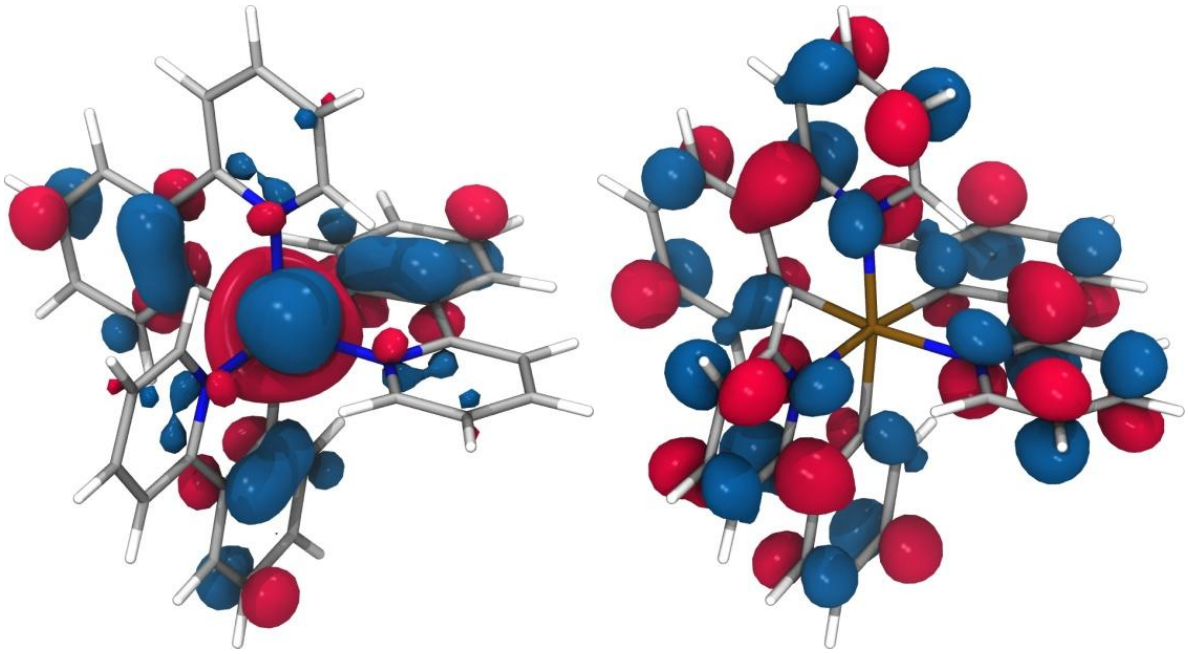

Figure 1.8: Kohn-Sham HOMO (left) and LUMO (right) of the fac tris-homoleptic compound [Ir(ppy)3]. A courtesy of Basile Curchod; as presented in literature.[57]

With a bis-heteroleptic complex such as $[Ir(ppy)_2(acac)]$ (Figure 1.9, centre), the same technique can be used and the emission is blue shifted by the addition of fluorine on the phenyl ring of the phenylpyridine ligand. The complex $[Ir(diFppy)_2(acac)]$ (Figure 1.9, right)

is the perfect example of this effect, with an emission maximum 36 nm blue shifted compared to the non-fluorinated complex due to the stabilization of the HOMO.

A chromophoric ancillary ligand can provide a more stable LUMO than the main ligands, resulting in a red shifted emission. This effect is obtained by replacing the acac ligand by a 2,2'-bipyridine (bpy) type ligand (Figure 1.9, left). In this last case, the emission is blue shifted by destabilizing the LUMO with a donor group added on the ancillary ligand.[20] However, different non-chromophoric ligands can also influence the HOMO-LUMO energy gap as it is the case for picolinic acid. Its different coordination properties to the metal centre have a stabilizing effect on the HOMO compared to acac, resulting in a blue shifted emission maximum.[59]

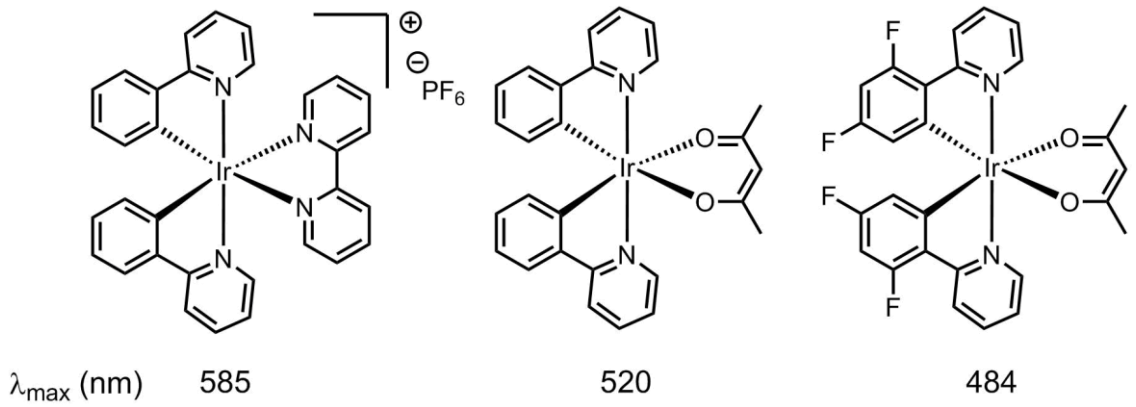

Figure 1.9: Emission maxima of complexes $[Ir(ppy)_2(bpy)][PF_6]$,recorded in MeCN (left)[60], $[Ir(ppy)_2(acac)]$, recorded in DCM (middle)[61] and $[Ir(diFppy)_2(acac)]$, recorded in DCM (right).[61]

1.5.5 Blue-emitting complexes

In the context of creating efficient electroluminescent devices using phosphorescent emitters, blue emitters represent a special challenge. Indeed, the large HOMO-LUMO gap needed to achieve high energy emission suffers some design limitations. As discussed above, the use of high LUMO ligands is limited by the thermal population of the ^{3}MC state resulting from the filling of antibonding metal orbitals.[43,46] To overcome this issue, the d orbital splitting is increased by introducing ancillary ligands with strong field effects that raise the energy difference without playing a direct role in the light emission process. However, the bonding d orbitals are also stabilised in the process. A strong stabilisation of these orbitals would reduce the MLCT character of the excited state, favouring the formation of pure LC excited states. This would induce a reduction of the SOC with a less efficient emission as a consequence.[25]

Research overview and limitations of blue phosphors are well summarised in the literature.[62–64] A brief overview of the different approaches and possibilities is presented here.

The first way of obtaining blue shifted emission is by substitution of the ligand. This effect (extensively discussed above) enables to obtain blue-shifted emission in tris-homoleptic iridium complexes by going from [Ir(ppy)$_3$] (em. max. In solution at RT: 510 nm) to [Ir(dFppy)$_3$] (em. max. 468 nm). It is also responsible for the room temperature emission obtained by substitution of the ppz ligand of [Ir(ppz)$_3$] with -CF_3 to form [Ir(tfmppz)$_3$] (em. max 428 nm).[35] Alternatively to tris-homoleptic complexes, bis-heteroleptic complexes can also be used, since the ancillary ligand properties can be used to tune the photophysical properties.

In this regard, the largely studied complex FIrpic is the perfect example (Figure 1.10, left).[34,65,66] Other ancillary ligands have been used with dFppy to obtain blue emission such as

a pyrazolyl-borate (Figure 1.10, FIr6, , centre)[67,68], (Figure 1.10, right) dFppz,[45] and also pyridyl-triazolate or pyridyl-tetrazolate.[69]

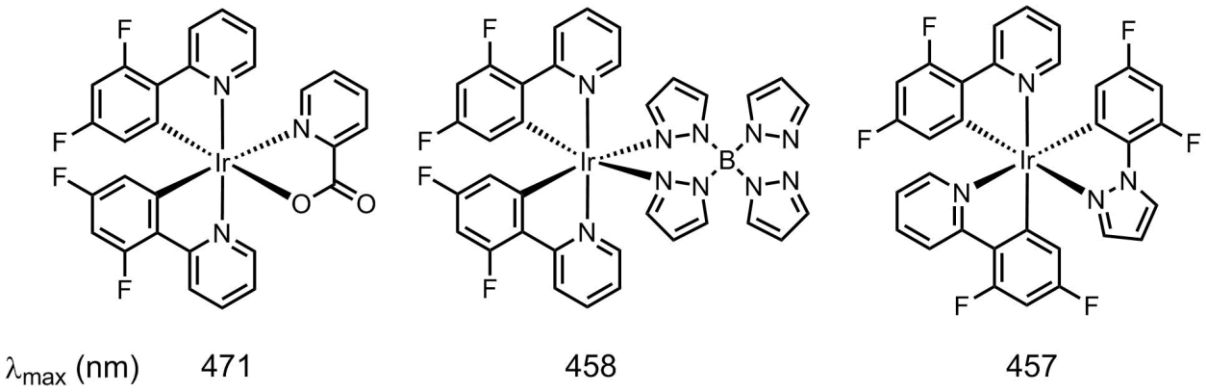

Figure 1.10: Blue emitters FIrpic (left), FIr6 (centre) and [Ir(dFppy)$_2$(dFppz)] (right).

Phosphine based ancillary ligands such as benzyldiphenylphosphine (P^C) or 5-(diphenylphosphinomethyl)-3-(trifluoromethyl)pyrazol (P^N) were shown to efficiently increase the d orbital splitting and reduce non radiative processes due to population of MC states.[70–72]

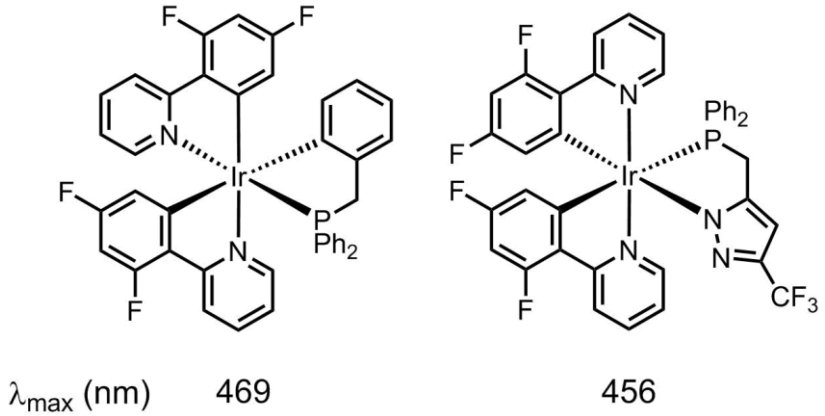

Figure 1.11: Bis-heteroleptic blue emitter complexes bearing dFppy main ligands and P^C or P^N type ancillary ligands.

Several alternatives to the dFppy main ligand have also been studied both in tris-homoleptic and bis-heteroleptic complexes. Many of these ligands have also been used as main or ancillary ligands, as for example phenyltriazole ligands.[71,73]

As an alternative to the use of dFppy, cyclometalated bipyridine ligands can be used as a way to obtain a more stabilised HOMO energy, by taking advantage of the withdrawing effect of the nitrogen atom and fluorine substituents.[74–76] Another common ligand architecture that has been extensively investigated over the last years because of its high ligand field strength is N heterocycle carbene (NHC, C^C) ligands. These ligands allow deep blue emission by providing high LUMO energies while the reinforced Ir-$C_{carbene}$ bond (compared to Ir-N bonds) strongly destabilises the metal based d^* orbitals. In addition to the blue emission, they also provide a great colour tunability when substituted with various groups[77] or mixed with various ancillary ligands.[78] They have been studied as tris-homoleptic complexes (Figure 1.12, left),[79–84] as well as main ligands (Figure 1.12, centre)[85,86] or ancillary ligands (Figure 1.12, right)[77,87–90] in bis-heteroleptic complexes They also have been used in tridentate bis-pincer ligands (not shown)[91] and cationic complexes (Figure 1.12, right).[84,87,91–93]

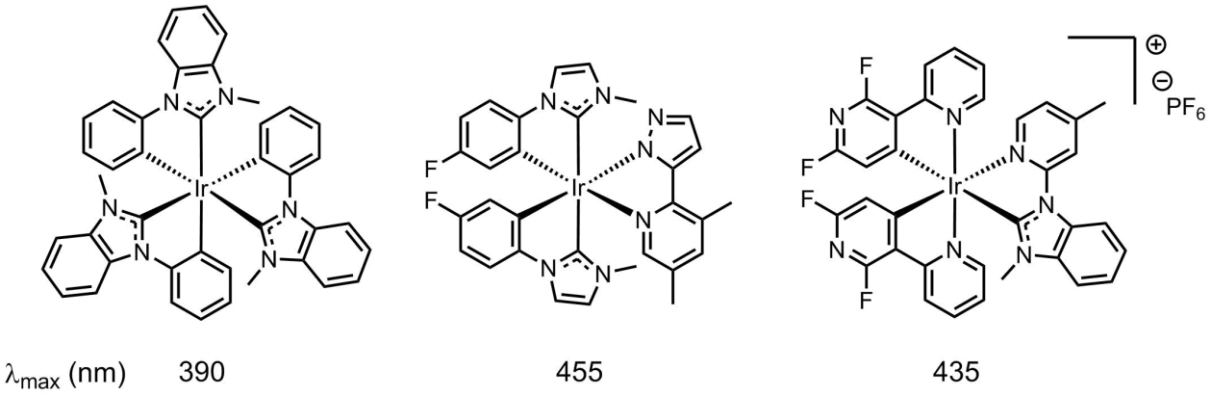

Figure 1.12: Complexes with carbene ligands; tris-homoleptic (left), with carbene main ligand (centre) and with carbene ancillary ligand (right).

1.5.6 Tris-heteroleptic complexes

The first tris-heteroleptic iridium complex was reported in 2001 by Stinner et al. as a metallointercalator for DNA probing purposes.[94] This tris-heteroleptic complex is different from all others as it is not cyclometalated but coordinated to six nitrogen atoms in three bidentate ligands; 2,2'-bipyridine (bpy), 1,10-phenanthroline (phen) and phenanthrene-9,10-diimine (phi). Therefore, the complex bears three positive charges; $[Ir(bpy)(phen)(phi)]^{3+}$. The synthesis pathway also differs from the standard methodology applied to the cyclometalated complexes, which consists in a simultaneous reaction of the two main ligands with an iridium starting material (Ir(III) salt or an (Ir(I) dimer) to form a chloro-bridged dimer as described below. Instead, the ligands are added stepwise to an $[Ir(phen)Cl_4]H$ starting material.[95] The bpy ligand is reacted first to obtain a cis-bischloro complex $[Ir(phen)(bpy)Cl_2]Cl$.[96] The bischloro complex is then converted in a cis-bisammine complex by exchange of the chloride with ammonia to obtain $[Ir(phen)(bpy)(NH_3)_2]OTf_3$ (using triflate, OTf, as counter anion). The last ligand is formed by a condensation reaction between 9,10-phenanthrene quinine and the NH_3 ligands.[97]

The first attempt to synthesise tris-heteroleptic complexes with cyclometalated ligands for electroluminescent application was published by Park et al.[98] The authors adapted a standard methodology for the synthesis of tris-homoleptic complexes[99] by making three different C^N ligands (dFppy, ppy and 1-(4-fluorophenyl)isoquinoline, piq-F) react simultaneously with $Ir(acac)_3$. By doing so, they hoped to obtain a tris-heteroleptic complex with complementary light emission centres for an overall white emission.

However, despites using different ligand ratio, the authors were confronted to a purification challenge arising from the high number of complexes formed (Eleven possibilities assuming

that only facial isomers are formed and ignoring the Λ/Δ enantiomerism.) and failed to obtain a pure compound.

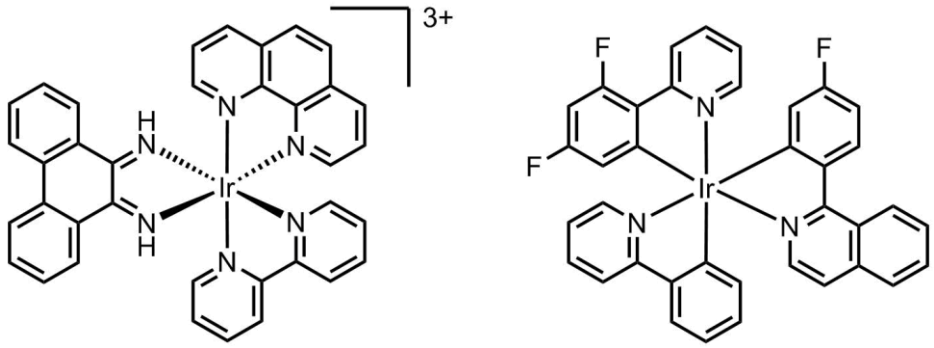

Figure 1.13: [Ir(phen)(bpy)(phi)]$^{3+}$ complex synthesised by Stinner et al. (left, showed without the OTf counter anions). [Ir(dFppy)(ppy)(piq-F)] as attempted by Park et al. (right).

Since 2001 and the study by Stinner et al. most tris-heteroleptic complexes published were synthesised following the standard two steps procedure (described in details below). First, the ligands are reacted with an iridium source to obtain a mixture of chloro-bridged dimers (of the type $\{Ir(C_1\text{^}N_1)(C_2\text{^}N_2)(\mu\text{-}Cl)\}_2$) followed by the insertion of an ancillary ligand and separation of the tris-heteroleptic complex from the side products.[56,61,100–103] These complexes always involve ppy-type ligands often modified in order to improve a device efficiency.[100–102] These studies have shown the applicability of tris-heteroleptic complexes as neutral or charged species for OLED or LEC applications.[56,100,103]

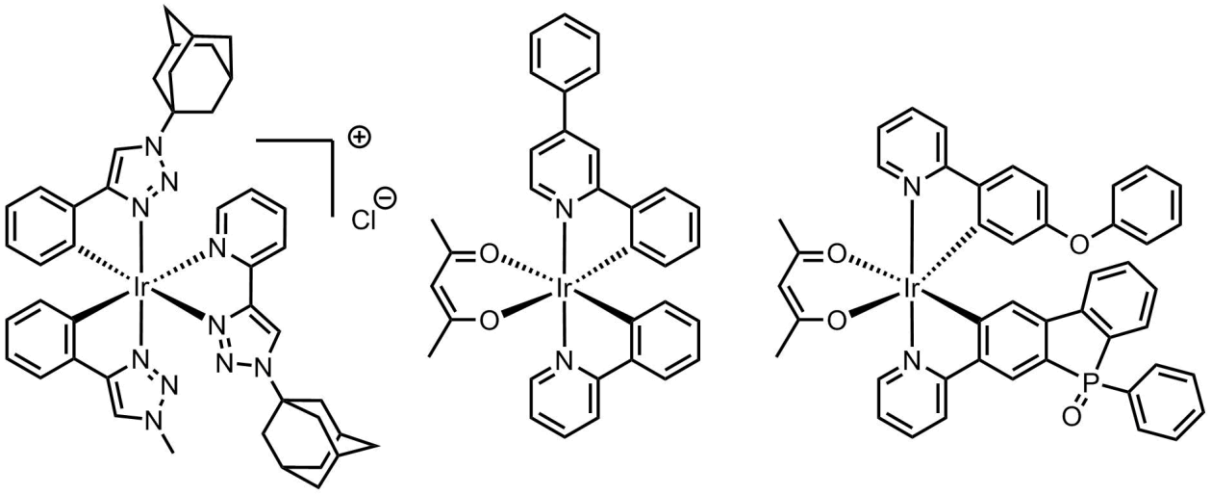

Figure 1.14: Cationic complex with adamantine substituted ligands (left) as published by Felici et al. Acac complex with substituted ppy ligands as published by Edkins et al. (centre) and Xu et al. (right).

Recently, Liao et al. explored a different approach for the synthesis of tris-heteroleptic complexes.[104] During the first step, they replaced the second C^N ligand by a neutral N^N one (4,4'-di-tert-butyl-2,2'-bipyridine, dtbbpy). Due to the different charge repartition of the ligand, the chloro-bridged dimer is not formed. Instead, they obtain a bis-chloro compound of the type $[Ir(C^N)(N^N)(Cl)_2]$ (in this case $[Ir(ppy)(dtbbpy)(Cl)_2]$). This product has the advantage of being different from side products and therefore easy to purify. Indeed, the side reaction implying only the C^N ligand forms chloro-bridged dimers while the one implying only the N^N ligand forms charged species of general formula $[Ir(N^N)_2(Cl)_2][Cl]$.[105–107]

The pure tris-heteroleptic precursor is then easily purified and can be reacted with dianionic ligands (in this example: 5,5′-di(trifluoromethyl)-3,3′-bipyrazol, bipz) to form the neutral product [Ir(ppy)(dtbbpy)(bipz)].

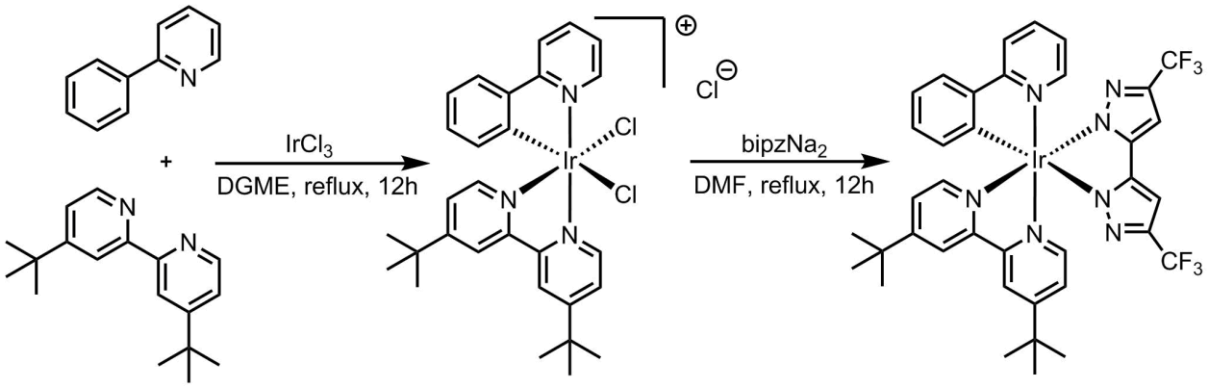

Figure 1.15: Synthesis of tris-heteroleptic complex as published by Liao et al.

Very recently, Aoki et al. successfully synthesised tris-heteroleptic complexes by two different methods. Firstly, they used a Zn^{2+}-promoted degradation method to remove one ligand from a $[Ir(C_1\text{^}N_1)_2(C_2\text{^}N_2)]$ type complex to obtain the corresponding chloro-bridged dimers $\{Ir(C_1\text{^}N_1)_2(\text{-}Cl)\}_2$ and $\{Ir(C_1\text{^}N_1)(C_2\text{^}N_2)(\text{-}Cl)\}_2$ which were reacted with acacNa in order to obtain the final product that had to be purified.[108] This represents an interesting approach as only two acac complexes are formed instead of three. However, the number of steps required for the entire process is increased due to the synthesis of the starting complex. The other approach is to use the properties of ancillary ligands to selectively modify one of the two main ligands.[109]

1.6 Project overviews and ambitions

1.6.1 White electroluminescent devices, the need of white emitting materials

White emitting electroluminescent devices are currently made by mixing two or more emitting materials of complementary colours. The way the emitters are organised in the device can follow different strategies[110] but all of them will result in the same drawbacks.

The first one is that it requires a quite complicated architecture (for OLEDs), as the different materials are distributed in different layers. The second drawback is the necessity to control precisely the amount of each material, in order to avoid unwanted energy transfers (e.g. red emitters absorbing blue light) and obtain a good quality of white light. Thirdly, all emitting materials have different stabilities and therefore, some degrade faster than others. This effect inevitably produces a colour change in the overall emission of the electroluminescent device. This problem is especially important for blue emitting iridium complexes. In order to increase the emitted energy, the HOMO-LUMO gap must be increased and the LUMO destabilised. By doing this, the energy gap between the LUMO and the anti-bonding d^* metal orbital decreases and MC states become thermally accessible. This results in a lower stability of blue emitters as the probability to break a metal-ligand bond is increased.

Therefore, the use of a white emitting material could provide means to overcome these issues and decrease the manufacturing cost of the devices.

1.6.2 White emitting materials and strategies

To create a white emitting material, one first approach could be to attach emitting centres together to get one molecule with an overall white emission resulting from the complementary wavelengths (Figure 1.16, A). This strategy does not present a particular improvement as it does not fix any of the issues presented above. It was exemplified by the work of De Cola et

al. where a triple centred Ir-Eu-Ir complex was used to emit white light, with the europium and iridium centres respectively emitting red and blue light.[111]

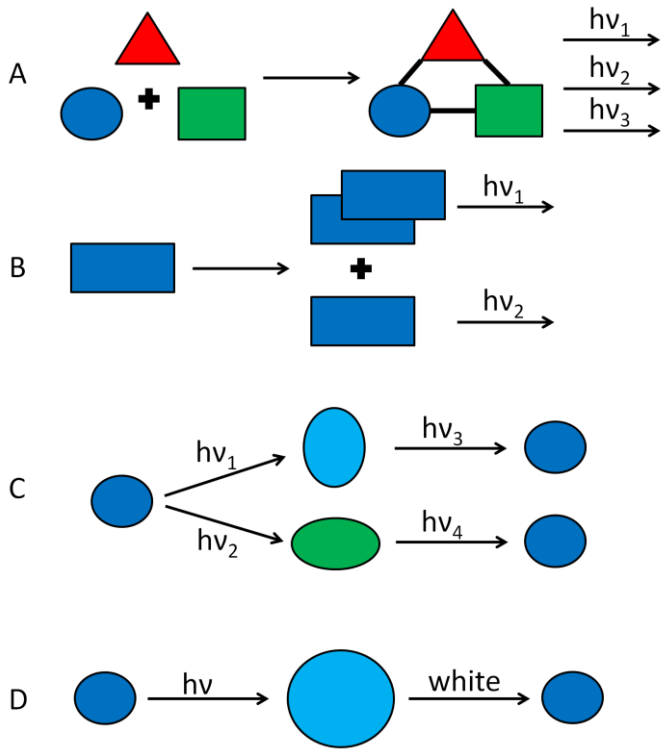

Figure 1.16: Schematic representation of different approaches for the generation of white-emitting single molecules.

This startegy is similar to the mixture approach used so far for electroluminescent devices. As it is likely that one centre would be less stable than the others, a device made with a multi-centred single emitter is also susceptible to encounter colour changes over time.

Another method consists in designing an emitter which interacts with itself (e.g. via π stacking interactions) to produce a modified emission (Figure 1.16, B). By controlling the ratio of free/interacting emitters in solid state, one can produce a dual emitting device with one kind of molecule. The difficulty of this approach would be to control the free/interacting ratio to obtain a good colour quality.

Some examples of white emitting systems following this approach exist with pure organic molecules, as is the case for the work of Mazzeo et al. where a large organic emitter was used (Figure 1.17).[112]

When in solution, the molecule shows a normal blue-green emission. In solid state, the blue-green signal is still present but a second signal appears in the red region, due to formation of cross-like dimers between the molecules, which change the overall emitted colour.

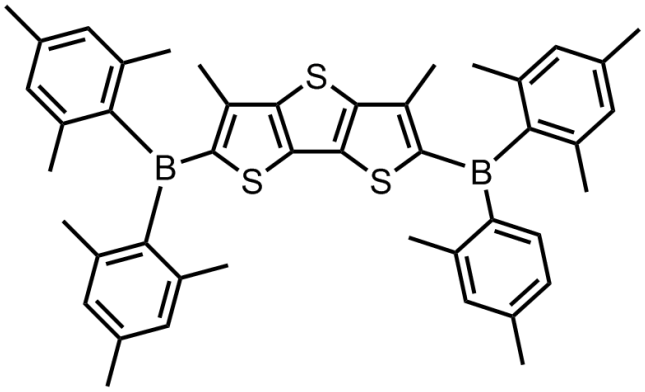

Figure 1.17: (3,5-dimethyl-2,6-bis(dimesitylboryl)dithieno[3,2-b:2',3'-d]thiophene.) used by Mazzeo et al.

The third approach consists in using a molecule that can produce two distinct excited states of different geometries and energies that would both be emissive. Such a molecule would be called a dual emitter (Figure 1.16, C).

Lastly, one could design a molecule whose emission spectrum is broad enough to cover the whole visible spectrum (Figure 1.16, D). Unlike a dual emitter, this molecule emission would not arise from two distinct excited states. Therefore, the emission spectrum would stay the same no matter what amount of energy is applied to excite the molecule.

A nice example of this method was highlighted by Hamada et al. back in 1996 with their work on bis(2-(2-(hydroxyphenyl)benzothiazolate)zinc ($Zn(BTZ)_2$, Figure 1.18, left)[113]. This

complex exhibited an especially broad emission profile, with full width at half maximum of 157 nm, resulting in a greenish-white colour when measured in thin film both by photo and electro excitation.

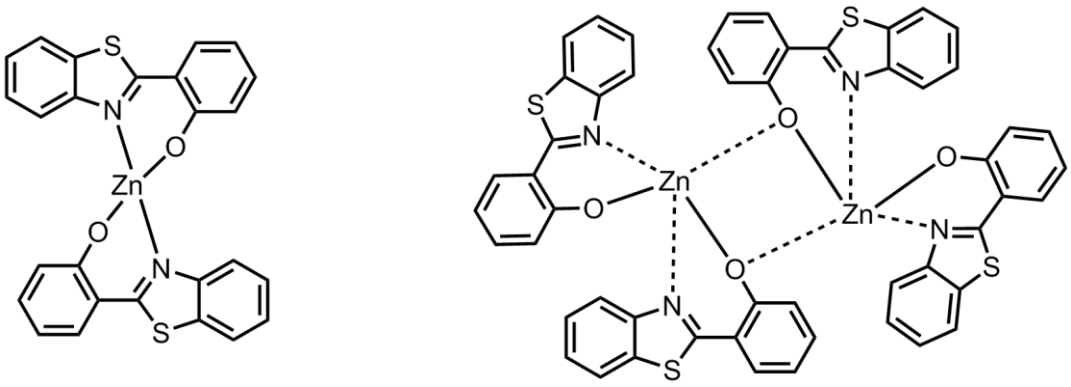

Figure 1.18: Representation of the emitter $Zn(BTZ)_2$ as a monomer (left) and as $[Zn(BTZ)_2]_2$.

This interesting result was only reported by Hamada et al. but not explained. Further investigations were conducted by Xu et al.[114] in an attempt to understand the mechanism of this broad emission. It appeared from this study that the emissive species was not a monomer, as was believed by Hamada et al. but a dimer where two of the BTZ ligands are shared between the Zn centres and the two others are linked to only one Zn atom (Figure 1.18, right). The emission spectra recorded at 77 K pointed out a significant difference between the fluorescence and the phosphorescence processes, both in solution and thin film. Therefore, the broad emission was the result of a mixture between the two emission processes.

1.6.3 Iridium complexes; towards tris–heteroleptic complexes

As far as iridium complexes are concerned, one example of broad emitter has also been published. This complex, (acetylacetonato)bis(1-methyl-2-phenylimidazole)iridium(III) (N966, Figure 1.19, left),[115] has shown an especially broad emission profile, both in solution and device (Figure 1.19, right), leading to an almost white emitted light (CIE coordinates: x = 0.281 ; y = 0.360).

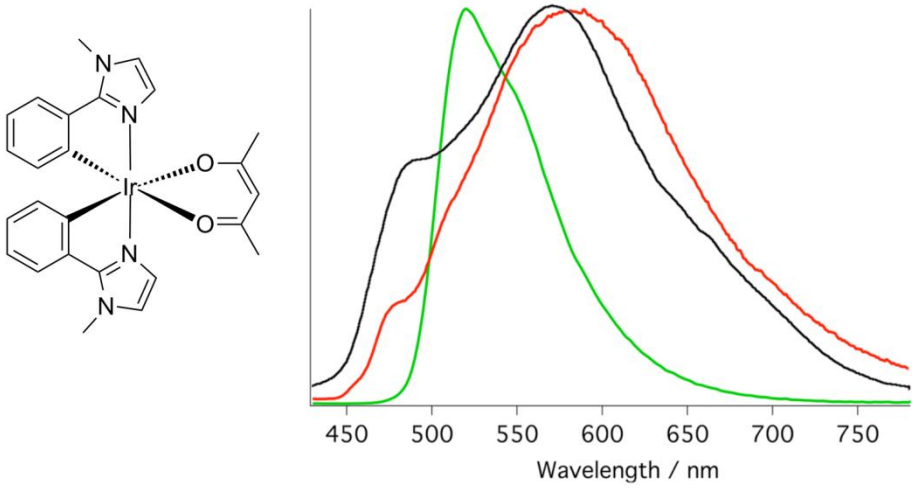

Figure 1.19: N966 (left) and its emission spectra (right) in solution (red line) and in a device (black line), compared with the emission spectrum of [Ir(ppy)$_3$] (green line).

In device, the efficiency was only 1 cd A^{-1} and the luminance more than 1000 cd m^{-2} but at a driving voltage of 9 V (10 times lower than $[Zn(BTZ)_2]_2$ at a similar voltage). Even if the performances were poor, this example shows that it is possible to develop a single centred white emitting complex using a broad emission profile.

The first explanation to this broad emission was based on theoretical calculations showing a degeneracy of the first three LUMOs (LUMO, LUMO+1 and LUMO+2). Calculations showed that the LUMO is made of π* orbitals delocalised over the bis(1-methyl-2-phenylimidazole) ligands (main ligand). Due to the donor properties of the main ligand, the LUMO+1 and LUMO+2 exhibit a mixing of π* orbitals from the main and acac ligands. As a result, the three orbitals are almost degenerate. In comparison, $[Ir(ppy)_2(acac)]$ LUMO and LUMO+1 orbitals are degenerate π* orbitals of the ppy ligands and are much more stabilised than the degenerate LUMO+2 and LUMO+3 localised on both ppy and acac ligands. The narrower emission profile of $[Ir(ppy)_2(acac)]$ is compared to that of N966 in Figure 1.19. The degeneracy of the first LUMOs localised over distinct parts of the complex where thought to be responsible for the broad emission profile of N966.

In order to obtain degenerate LUMO orbitals, one can use tris-heteroleptic complexes and take advantage of three ligands with different controllable properties to increase the broadness of the emission profile.

An attempt at doing this was published by Baranoff et al.[61] The tris-heteroleptic studied was an acac complex with two ppy ligands with and without 2',4'-difluorination.

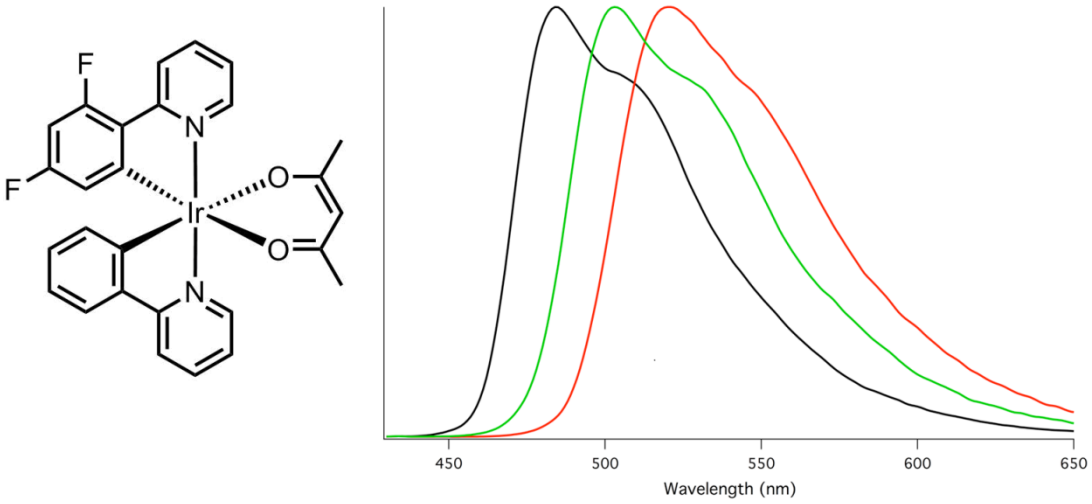

Figure 1.20: [Ir(diFppy)(ppy)(acac)](left) and its emission spectrum (green) together with the spectra of the two corresponding bis-heteroleptic complexes [Ir(ppy)$_2$(acac)] (red) and [Ir(diFppy)$_2$(acac)] (black).

Despite a degeneracy of the first two LUMOs of the complex, located on the two main ligands (diFppy and ppy), the emission is not broad, as shown in Figure 1.20 (green line). Instead, the emission profile is similar in shape to the profiles of the corresponding bis-heteroleptic complexes, with an emission maximum close to their average.

The calculations performed on this molecule show that despite a quasi degeneracy of the LUMOs and of the two most stable excited states, the geometry change induced by one or the other excited state is large enough to isolate the excited electron on one ligand. In other

words, the molecule is trapped in one or the other excited state geometry and the excited electron is not delocalised over the two ligands.

The hypothesis derived from this study as far as broad emission is concerned is that degeneracy of the LUMOs is not enough to predict the broadness of the emission spectrum. One has to take into account the excited state energies as well as their geometries.

Tris-heteroleptic complexes allow playing with three ligands at a time, each of which having their own properties. In order to achieve this, it is necessary to study how these ligands react with the iridium starting material and which properties each ligand brings to the overall complex. The tris-heteroleptic family has scarcely been studied and only a few of these molecules have been synthesised.

The reason for this poor representation of tris-heteroleptic complexes in literature comes from the difficulty to synthesise them following the usual method starting with $Ir(III)Cl_3$ and the difficulty to purify them, due to the mixture of complexes formed. A new method has been described recently[61], using an Ir(I) starting material which allows a reaction yield as high as 40%.

1.6.4 Synthesis of bis and tris-heteroleptic complexes

Bis-heteroleptic cyclometalated iridium complexes are usually synthesised in two steps[31], as presented in Figure 1.21. The main ligand is mixed with iridium trichloride ($IrCl_3$) and heated to reflux in an ethoxyethanol/water mixture. This results in the formation of a chloro-bridged dimer. This dimer is then reacted with the desired ancillary ligand by heating to reflux in DCM overnight. Details of the synthesis can differ in the case of some ancillary ligands. For example, a bpy type ligand will result in a positively charged complex. In this case, the

original chloride ion can be exchanged with hexafluorophosphate. If the ligand is an acid (e.g. picolinic acid) and needs to be activated by deprotonation, a base such as TBAOH is added.

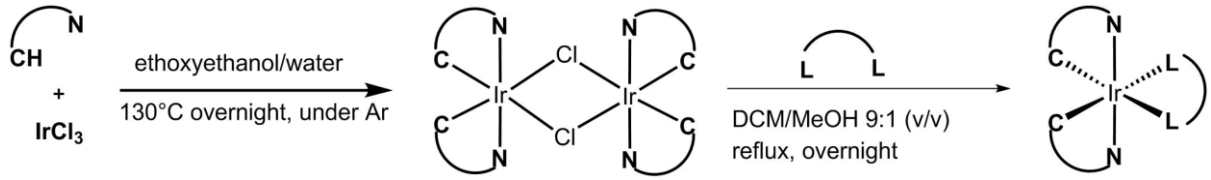

Figure 1.21: Standard procedure for the synthesis of cyclometalated bis-heteroleptic iridium complexes.

This methodology appeared to be inefficient when transposed to the synthesis of the tris-heteroleptic complex [Ir(dFppy)(ppy)(acac)].[61] As stated before, the method was adapted, using an iridium(I) starting material that allowed to improve the total yield while decreasing the reaction time of the first step from 12-24 hours to 3 hours. As there are now two different main ligands mixed together and reacting with the iridium starting material (Figure 1.23), it results in a mixture of 7 different dimers (Figure 1.22, without the Δ/Λ configurations of their iridium centres).

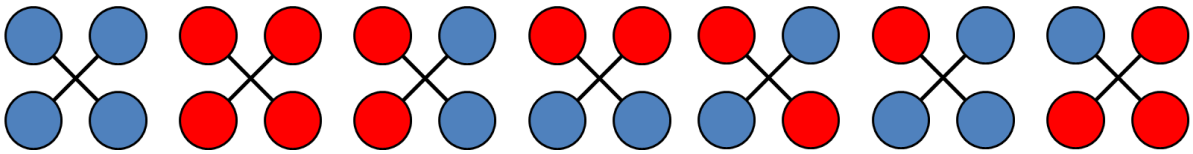

Figure 1.22: Schematic representation of the seven possible configurations of chloro-bridged iridium dimers with two different main ligands. The main ligands are symbolised by the blue and red discs. The black cross represent the Ir(μ-Cl)$_2$Ir architecture. The ligand configuration around the iridium atoms is supposed to be trans-nitrogen (N-Ir-N) only. The differentiation between Λ and Δ centres is ignored.

When reacted with a symmetrical ancillary ligand such as acac, these dimers will form 14 complexes. Eight will be bis-heteroleptics (4 of each type) and six tris-heteroleptics.

Therefore, assuming the ligands show the same reactivity with the iridium all the time, the maximum tris-heteroleptic yield would be 6/14 ≈ 0.43.

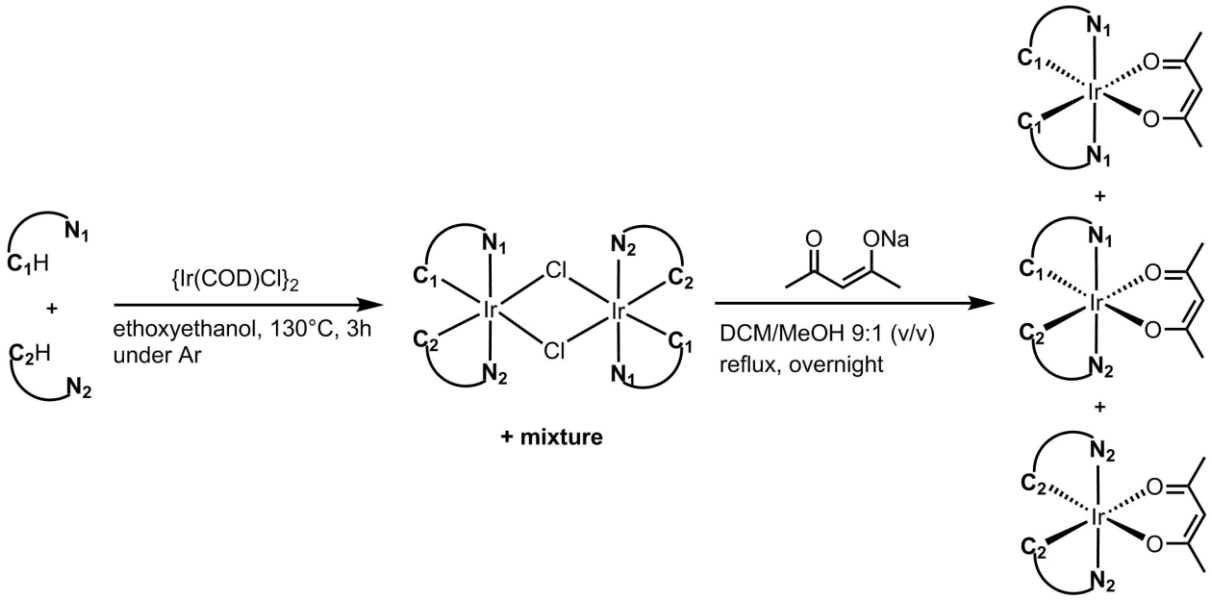

Figure 1.23: General methodology for the synthesis of cyclometalated tris-heteroleptic iridium complexes with an acetylacetonate ancillary ligand.

After reaction with acac complexes, the difficulty is to separate the tris-heteroleptic complex from the two bis-heteroleptic by-products. This task is more difficult if the ligands have similar properties such as same heterocycles or same substituents as the polarity differences of such complexes are small.

Once purified, the tris-heteroleptic acac complex can be turned back into a pure dimer by reacting with HCl. This pure dimer can finally be reacted with any ancillary ligand to potentially obtain any tris-heteroleptic complex desired (Figure 1.24). Alternatively, the acac ligand can be removed with BF_3 in acetonitrile to form a positively charged bis-acetonitrile cation. The anion is then exchanged with a PF_6 anion. The advantage of this approach is the increased solubility of the bis-acetonitrile complex over the dimer, making it easier to characterise and react with X^X ancillary ligands.

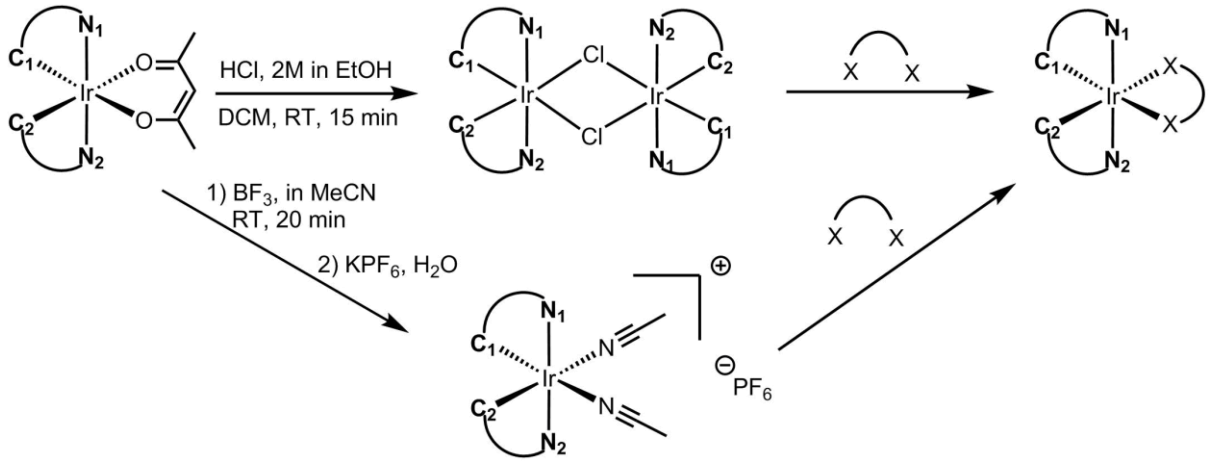

Figure 1.24: Methodologies for the ancillary ligand replacement from acac to a general L^L ligand. The conditions of the second step are ligand specific.

The tris-heteroleptic complex obtained after reacting with the X^X ligand does not require a complicated purification anymore. Depending on the X^X ligand used, it can easily be removed by dissolution into water (while the complex precipitates) or a recrystallisation process. In the worst case, a short chromatography column can be required.

The advantage of this synthesis is that it is easy to achieve with standard laboratory equipment. It also produces impurities that are easily removed (excluding the by-product complexes) allowing to obtain iridium complexes in very good purity. The major drawback is the formation of the bis-heteroleptic by-products and the tedious purification process that they imply. This process is made worse by the relative instability of acac complex on the acidic silica. Unfortunately, a more stable ancillary ligand than acac would also be more difficult to remove in order to obtain a pure tris-heteroleptic precursor (dimer or bis-MeCN), which represents a great advantage for ancillary ligand screening experiments.

In the present context, the acac ligand presents the double advantage of being easy to remove and symmetrical. The use of a non-symmetrical ancillary in the reaction of Figure 1.23 would

generate two tris-heteroleptic isomers which would only add more complexity to the separation task.

1.7 Conclusion

This chapter focused on the context of electroluminescent light emitting devices and their working principles. It presented the basics of light emission processes and introduced the iridium complexes studied in the present work. The development of single-centre white emitting molecule for electroluminescent device application was presented as a potential alternative to overcome the limitation of the current approach. It would allow the creation of devices with simplified architectures while suppressing the drawback inherent to the use of several emitters of complementary colours. The use of tris-heteroleptic complexes was proposed as well as the synthetic strategy to reach the goal of creating a broad emitting molecule with an overall white emission.

2 TRIS-HETEROLEPTIC IRIDIUM COMPLEXES; SYNTHESIS AND PURIFIFCATION

2.1 Introduction

This chapter focuses on the synthesis of the four series of complexes presented below (Figure 2.5, Figure 2.10 and Figure 2.13). The goals are to explain the methodology used for their synthesis and purification, to describe the challenges encountered and discuss the practical means of overcoming these challenges. The chapter also discusses the characterisation of these complexes, mainly by detailed NMR spectra analyses, but also by looking at the crystal structures. Electrochemical and photophysical studies of the complexes and their analyses are discussed in the next chapter.

The complexes are hereby divided in three main series, taking into account a chronological order of design and synthesis. This is why the tendency will be to discuss the results one series of complexes at a time, even though some links between them will be made if they appear to be relevant.

A fourth series, which involves the synthesis and purification of complexes with non symmetrical ancillary ligands, is also presented. Even though these products are an extension of the first series, their particular purification challenges justify the addition of a dedicated section.

As part of this chapter, the design and results of a preliminary ancillary ligand screening experiment is also discussed, as it represents a perfect example of the research possibilities resulting from the synthetic approach chosen in this work.

2.2 Synthesis of the ligands

The synthesis of each type of ligands used during this research is reported and briefly discussed. The aim is to present the main results (yields) and the difficulties encountered without providing too many details on the characterisations. An interested reader may consult the experimental details chapter.

2.2.1 Suzuki coupling reactions

Suzuki coupling reactions have been used to synthesise all phenylpyridine type ligands (except 2-phenylpyridine itself which is commercially available). The model method described for the synthesis of 2-(2,4-difluorophenyl)pyridine (dFppy)[116] was adapted for the syntheses of other ligands such as 2-(2,4-dimethoxyphenyl)pyridine (dMeOppy), 2-(2,4-dimethoxyphenyl)-4-methylpyridine (dMeOMeppy) and 2-(2,4-dimethoxyphenyl)-4-methoxypyridine (dMeOMeOppy). Commercially available 2-bromopyridines were chosen and reacted with commercially available phenylboronic acids.

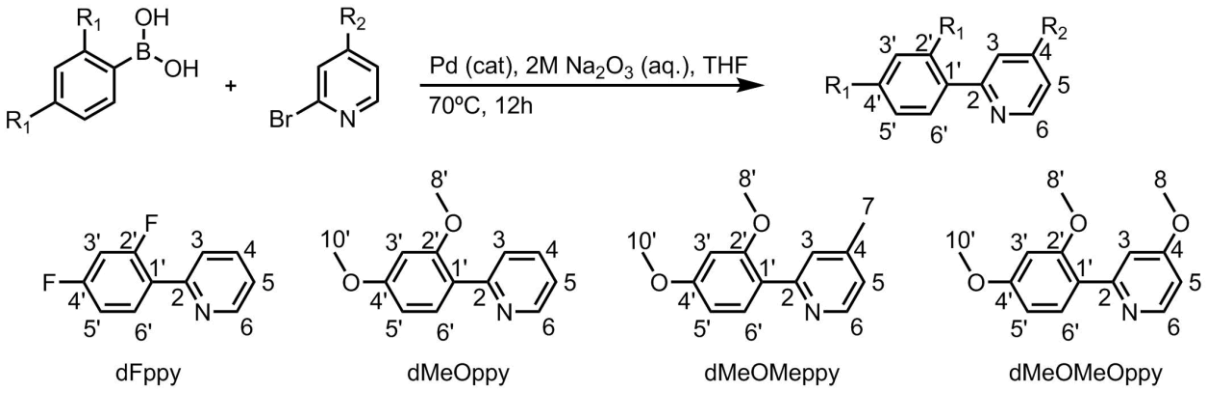

Figure 2.1: Suzuki coupling reaction equation and synthesised products (with the carbon atoms numbered for NMR assignment purposes). R_1 = -F, -OMe and R_2 = -H, -Me, -OMe.

The boronic acids were added in excess to maximise the reaction and to facilitate the purification process. This is especially necessary for dFppy where 2-bromopyridine has very similar R_f than the product and is therefore difficult to remove on silica gel columns.

For the synthesis of dimethoxylated ligands, the increased polarity of the product is lowering its R_f compared to the bromopyridines used.

Table 2.1: Substituents and reaction yields for the ligands synthesised by a Suzuki coupling reaction.

Ligand	R_1	R_2	Yield (%)
dFppy	-F	-H	98
dMeOppy	-OMe	-H	75
dMeOMeppy	-OMe	-Me	73
dMeOMeOppy	-OMe	-OMe	91

2.2.2 Synthesis of the phenylpyrazole ligands

1-(2,4-difluorophenyl)pyrazole (dFppz) was synthesised[117–119] by a condensation reaction of an hydrazine and 1,1,3,3-tetramethoxypropane. The reaction is achieved in good yield (62%) and a sligthly yellow oil is obtained after a few chromatography columns on silica gel. The presence of an impurity migrating close to the product can be problematic but this issue is resolved by evaporation of the solvent and drying of the crude under vacuum prior to base neutralisation.

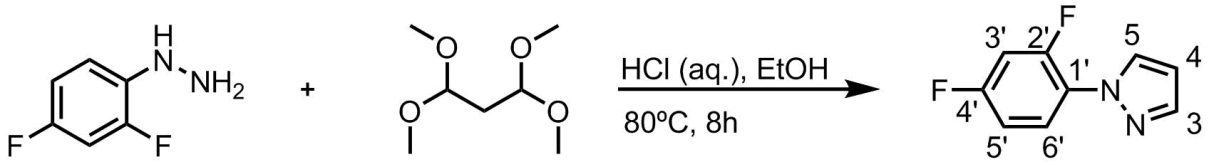

Figure 2.2: Reaction scheme for the synthesis of dFppz (with the carbon atoms numbered for NMR assignment purposes).

CF_3ppz was synthesised in two steps (Figure 2.3).[120,121]. First, a vinamidinium salt is made from trifluoroacetic acid and (*N*,*N*-dimethylformamide) DMF in the presence of phosphorus oxychloride ($POCl_3$). The product is harvested by precipitation in water under the form of a PF_6 salt that is more stable and easier to precipitate than the chloride salt.

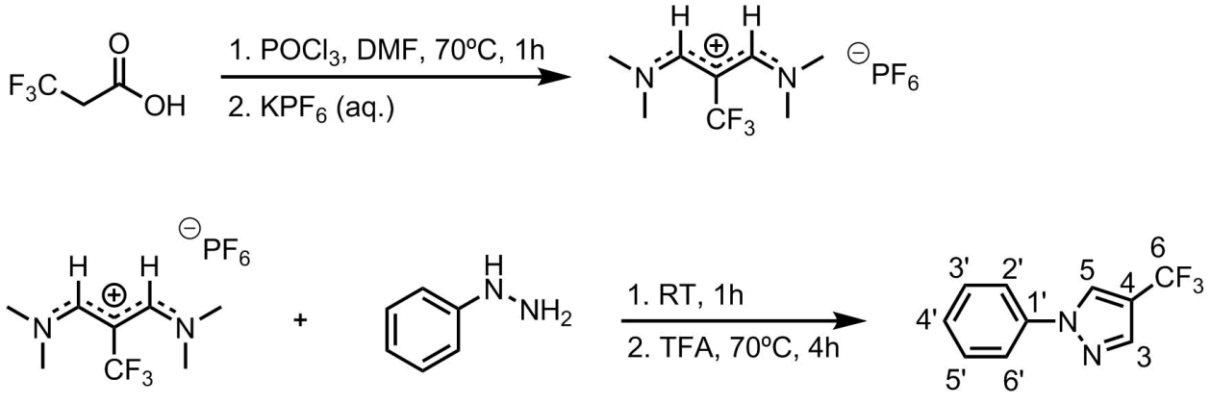

Figure 2.3: Reaction scheme for the synthesis of CF_3ppz (with the carbon atoms numbered for NMR assignment purposes).

The vinamidinium salt was not purified further and reacted with hydrazine to obtain the corresponding phenylpyrazole ligand. The product was purified by column chromatography.

This synthesis produces the ligand in average yield (51%). The major uncertainty affecting the yield is the purity of the vinamidinium salt as only one precipitation in water is performed. It is possible that some KPF_6 or other phosphorus salts from the synthesis remained. To ensure better quality of the vinamidinium salt, recrystallisation from water/2-propanol can be achieved. Nevertheless, the purity of the final ligand is more important and the efforts to purify such an intermediary product were judged unnecessary.

2.2.3 Synthesis of the phenyl imidazole ligand (mespim)

The synthesis of mespim is made via a one pot mixture of four reactants.[122] First, trimethylaniline is mixed with Glyoxal and stirred at RT. A yellow precipitate forms and ammonium chloride and benzaldehyde are added to the flask. After a short heating period, TFA is added and the reaction mixture is heated to reflux for an additional 8 hours.

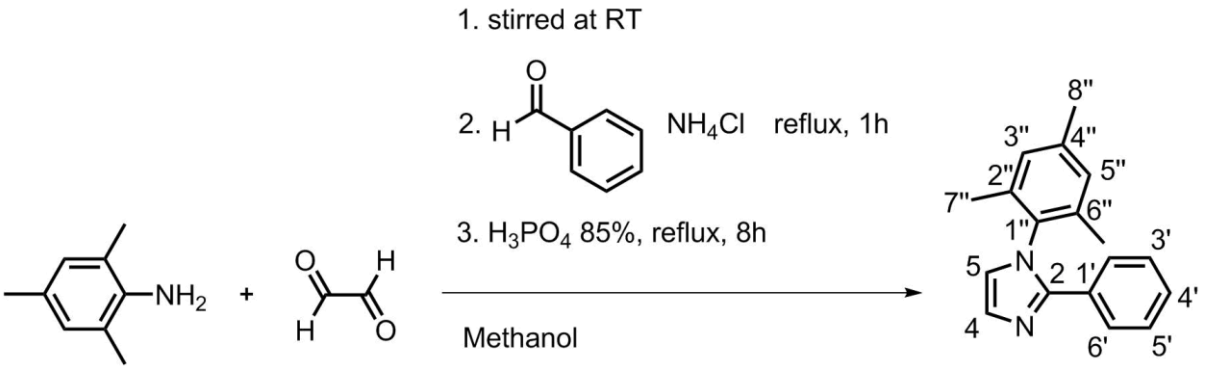

Figure 2.4: Reaction scheme for the synthesis of mespim (with the carbon atoms numbered for NMR assignment purposes, the 2' and 9'' carbons are not numbered for clarity).

The crude mixture is not clean and needs extensive chromatography purification before a sufficiently pure product can be obtained. The unclean crude mixture, and low yield (11%) obtained are consequences of the number of reactants involved where many by-products can be formed.

2.3 First series: complexes with ppy/ppz ligands

2.3.1 Choice of the ligands

In order to explore the new family of tris-heteroleptic complexes and study their photophysical properties, it is necessary control the changes induced by each ligand as much as possible.

The goal is to understand the influence of changing one ligand on the photophysical properties. Therefore, one needs to select ligands that differ sufficiently to induce a change, but not too drastically, to limit the chances of reaction failure.

The choice of acac brings a practical synthetic advantage, as the complexes generated are neutral and stable enough to be purified and characterised relatively easily. It also provides the opportunity to still replace the ancillary ligand later on if necessary.

Since it is a known non chromophoric ligand, acac does not interfere in the light emission process. Therefore, it allows to study the influence of two C^N chromophoric ligands and the photophysical properties without the effect of a chromophoric ancillary ligand coming in the way. Again, once an interesting combination of C^N ligand is discovered, one can easily remove the acac and start exploring the huge library of ancillary ligands available.

The drawback of this approach is that one has to carry a relatively unstable complex through all the purification process with a non negligible degradation due to acac decoordination.

Previous studies on a tris-heteroleptic complex suggested that two ppy based ligands provide LUMOs with similar energies, leading to the trapped excited state problem.[61] Therefore, it was decided to select a second C^N ligand that is bringing a higher LUMO to the system. The choice was made to use both 1-phenylpyrazole (ppz) and 1-(2,4-difluorophenyl)pyrazole (dFppz).

The hope was that a ligand with higher LUMO energy would provide an extended degree of excited state mixing and an increased delocalisation of the excited electron over the ligands that would result in a broad emission profile. Ppz ligands are known for their high LUMO energy (-2.24 eV for $[Ir(ppz)_2(acac)]$[123] evaluated with a similar method than used in this work where the LUMO of $[Ir(ppy)_2(acac)]$ is evaluated at -2.65 eV) and to form non emissive complexes at room temperature. In the present context they represent a convenient starting point, leaving a large margin to adapt the LUMO level of future ligands.

The atomic positions on the complexes (Figure 2.5) are assigned according to the normal ligand numbering positions followed by a letter to differentiate the three ligands (a, b and c). Prime marks are added to phenyl positions to distinguish them from the heteroaromatic ones. The acac ligand is always noted "c" even for a bis-heteroleptic complex (to facilitate comparisons between products). Numbers of heteroatoms and non protonated carbons are often omitted on drawings for clarity.

Complex **3** is the only already published tris-heteroleptic complex of the series. It represents a known model with which to compare the synthesis of the other products. **6** is the equivalent of **3** with only ppz ligands. **1**, **2**, **4** and **5** are their corresponding bis-heteroleptic complexes. They are by-products of the tris-heteroleptic complexes syntheses.

Complexes **7**, **8**, **9** and **10** are obtained by mixing ppy and ppz ligands, with and without any 2',4'-difluorination (**7** and **8**) and with the difluorination only on one ligand (**9** and **10**).

2.3.2 Synthetic details and purification

All acac complexes **1** to **10** were synthesised following the general procedure shown above (Figure 1.23). First, the ligands are heated up in the presence of an iridium source to obtain a mixture of chloro-bridged dimers. The obtained mixture is then reacted with sodium acetylacetonate (acacNa) in DCM/MeOH solvent mixture overnight. This approach results in the combination of the target tris-heteroleptic acac complex together with the two corresponding bis-heteroleptic complexes, $[Ir(ppy)_2acac]$ (**1**), $[Ir(dFppy)_2acac]$ (**2**), $[Ir(ppz)_2acac]$ (**4**) and $[Ir(dFppz)_2acac]$ (**5**).

As the relative amount of the target tris-heteroleptic complex compared to bis-heteroleptic complexes is embedded in the mixture of chloro-bridged iridium dimers, different reaction conditions were explored as a possible mean to improve the yield of tris-heteroleptic complexes. Three sets of conditions were tested, A, B and C, varying the iridium source, the temperature and the solvent.

Conditions:

A $IrCl_3\ xH_2O$, ethoxyethanol/water (7/3), 130°C, 12h.

B $\{Ir(COD)Cl\}_2$, ethoxyethanol, 130°C, 3h.

C $\{Ir(COD)Cl\}_2$, xylenes, 130°C, 3h.

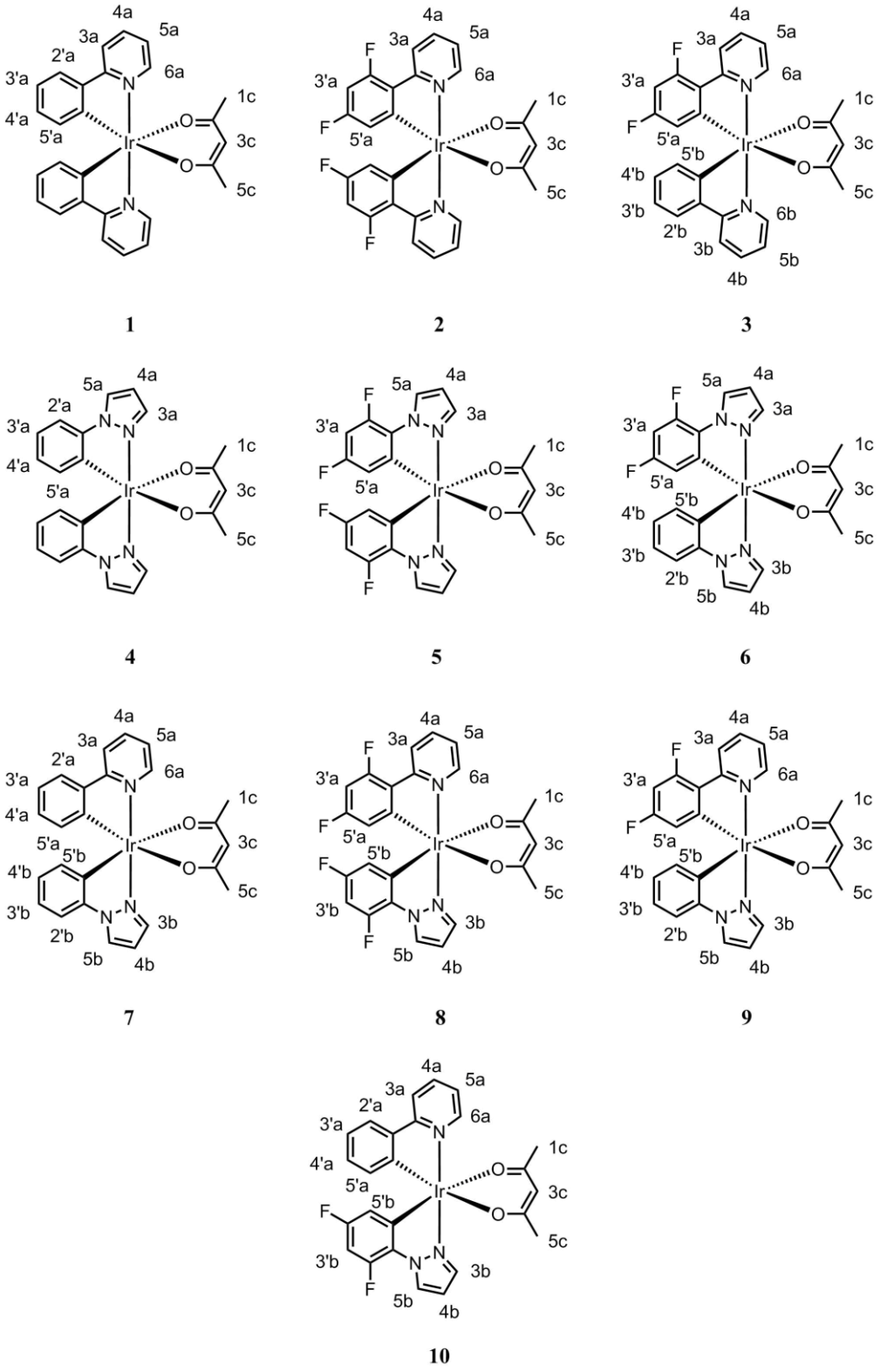

*Figure 2.5: Complexes of the first series: [Ir(ppy)$_2$(acac)] (**1**), [Ir(dFppy)$_2$(acac)] (**2**), [Ir(dFppy)(ppy)(acac)] (**3**), [Ir(ppz)$_2$(acac)] (**4**), [Ir(dFppz)$_2$(acac)] (**5**), [Ir(dFppz)(ppz)(acac)] (**6**), [Ir(ppy)(ppz)(acac)] (**7**), [Ir(dFppy)(dFppz)(acac)] (**8**), [Ir(dFppy)(ppz)(acac)] (**9**), [Ir(dFppz)(ppy)(acac)] (**10**).*

Conditions A are standard conditions for the synthesis of chloro-bridged iridium dimers. Conditions B were previously used for the synthesis of the tris-heteroleptic complex **3** where the use of an Ir(I) starting material tremendously decreased the reaction time from 12h to 3h. Conditions C were chosen to explore the effect of changing the solvent on the reaction yields.

As the reaction generates a mixture of seven possible dimers, all with a low solubility in most solvents, any purification attempt at this stage would have been unnecessarily tedious. The dimer mixtures were reacted directly with acacNa (which is a nearly quantitative reaction)[61] to obtain the three corresponding acac complexes (much more soluble than the dimers). At this stage, a ^{1}H-NMR spectrum of each crude mixture (A, B, C) was recorded to perform an NMR yield analysis.

The complexes can be purified by standard chromatography techniques with silica gel. In order to limit the degradation induced by the acidic silica,[61] a small amount of triethylamine is added. This limits the acidity of the silica but it also decreases the retention times and the separation effectiveness. A balance has to be found between, 1: limiting the degradation but making the separation less efficient. And 2: losing more of the product on the column but having a slightly better separation. It is not possible to get a perfect balance and the purification remains tedious (involving many columns) and costly in product.

The eluent of choice is pure DCM as it provides a good solubility as well as acceptable R_f values (Figure 2.6). Attempts to slow down fast migrating mixtures by adding hexane to the eluent only make the column more difficult to prepare as the solubility of the complexes are decreased. More eluent is then required to solubilise the crude and the deposition band on the silica will be broader, making the separation less efficient.

On the other hand, accelerating the migration of slow crudes by adding a small amount of MeOH or MeCN can be useful in some cases. But the risk is high that it also decreases the R_f differences between the complexes in the mixture.

In the end, ratios between the isolated yields of the three reaction products are not guaranteed to be representative of the real reaction yields. Firstly, the complex with the lowest R_f stays longer on the silica than the others. One can assume that a larger percentage of this complex is degraded by the silica, especially if the R_f differences between the complexes are large. Secondly, there is no guarantee that all the complexes have the same sensitivity to the silica. Some complexes might exhibit a higher degradation rate than others. This is especially plausible when the two main ligands have different hetero-aromatic rings.

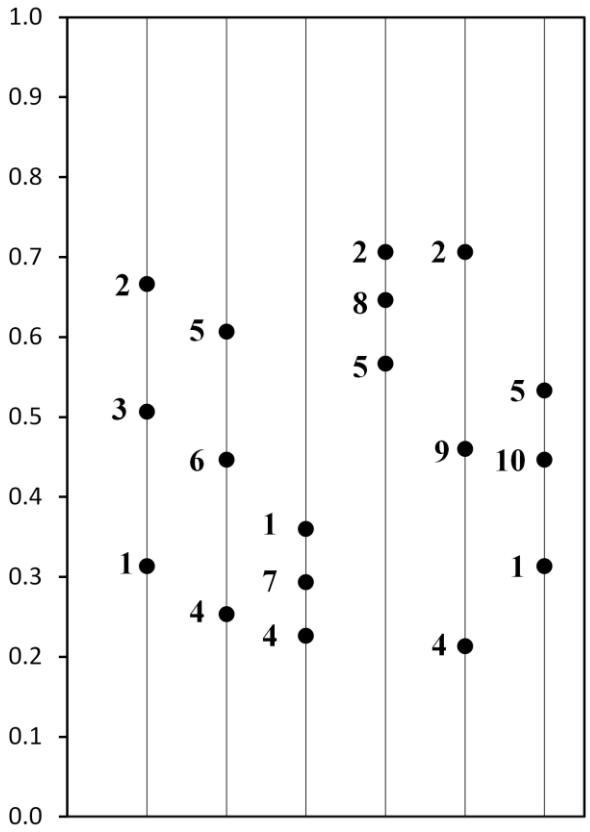

*Figure 2.6: Schematic view of measured TLC separation for the crudes of complexes **1** to **10**, with pure DCM as eluent and without triethylamine.*

All tris-heteroleptic complexes were not equally difficult to purify. Since they show an intermediate R_f compared to their corresponding bis-heteroleptic complexes, some tris-heteroleptic complexes are easier to separate than others. The R_f of the bis-heteroleptic complexes can be expressed in increasing order as follow: **4** < **1** < **5** < **2**. Therefore, the most difficult complex to purify is **7** because its R_f lies between the ones of **1** and **4** which are low. On the other hand, the easiest purification is for **9** because it lies between **2** and **4** which have the largest R_f difference among the series. This simple analysis also underlines how the purification difficulty can vary even between two complexes with similar structures and R_f, such as **9** and **10** (The position of the fluorinated phenyl ring placed on the ppy or on the ppz being the only structural difference). Because the bis-heteroleptic complexes involved have a much smaller R_f difference for **10**, it will be significantly more difficult to purify than **9**.

2.3.3 Proton NMR characterisation

The isolated complexes were characterized by ^{1}H NMR, ^{13}C NMR, ^{19}F NMR and 2D NMR techniques (COSY NOESY, HSQC).

In order to assign proton peaks, many complementary approaches are available. Firstly, it is relatively easy to determine which signal belongs to which ligand only by comparing the tris-heteroleptic spectrum with the two correspondingspectra of the bis-heteroleptic complexes. The spectrum of the tris-heteroleptic complex will look like a superimposition of the two others and chemical shift differences due to an environment change (such as fluorinated vs non fluorinated ligands) appear very clearly. This is true even if the two ligands are similar as it was shown in previous studies for **3**.[61] To demonstrate this effect, a comparison of the spectra of **4**, **5** and **6** is shown below (Figure 2.7). On these spectra, the shift induced by the fluorine atom on the 5 positions of the pyrazoles is manifest. It is also very easy to spot the 2' and 3' signals from the ppz ligand. The 4' signal is slightly hidden but it is still present.

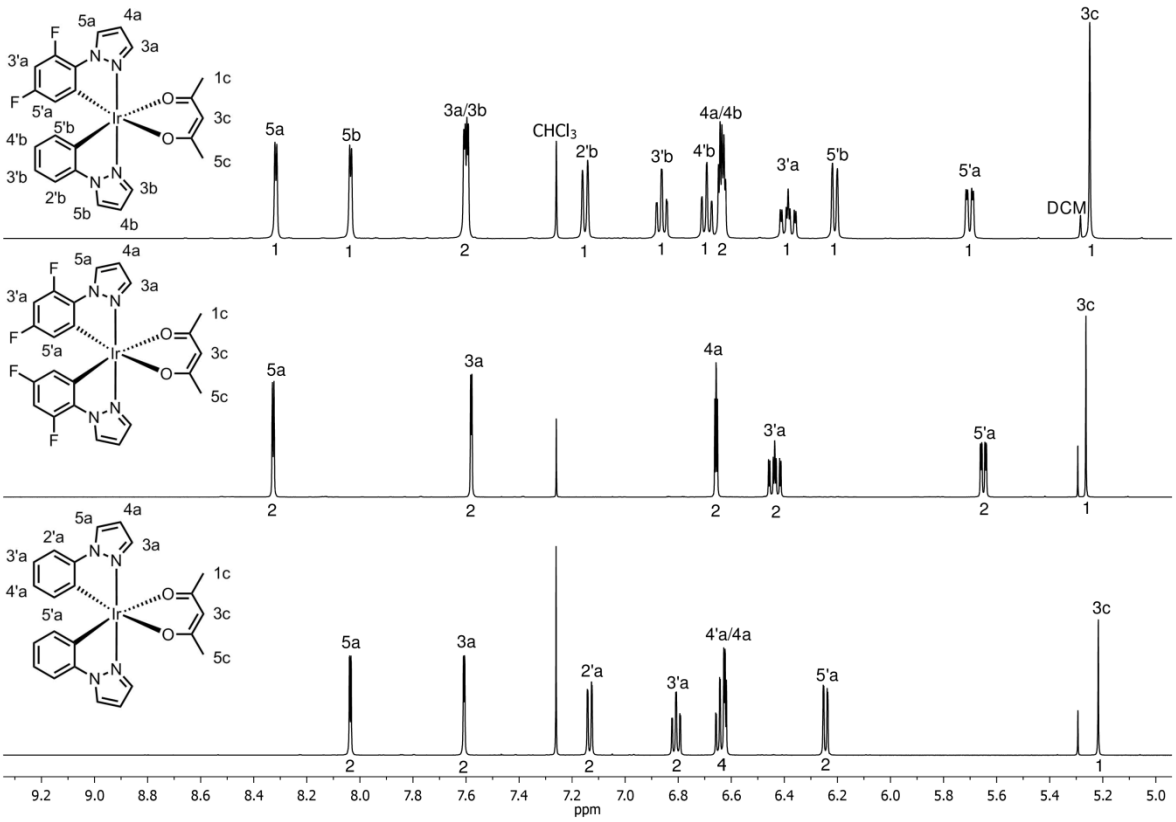

*Figure 2.7: Aromatic regions of the ^{1}H-NMR spectra of **6**, **5** and **4** measured in $CDCl_3$. The relative integral values are displayed below the signals.*

Other clues are given by the coupling constants and chemical shifts of the peaks. For example, the doublet signal around 6.2 ppm corresponds to the 5' proton of the phenyl ring. If the phenyl ring is 2',4'-difluorinated, the signal is shielded to 5.6 ppm and becomes a doublet of doublet (dd), due to its coupling with the ^{19}F nuclei. Similarly, the triplet on the 3' position also suffer shielding and becomes a very identifiable mixed ddd signal upon 2',4'-difluorination.

2D NMR techniques such as COSY and NOESY are useful to identify series of peaks when two ligands display very similar signals (e.g. the two phenyl rings of **7**). In this situation, COSY allows to distinguish the two series but not necessarily to assign them to one or the other ligand. A good quality NOESY spectrum can be helpful because it shows a coupling

between the 5 position of a pyrazole (3 position of a pyridine) with the 2' position of the phenyl ring. If the quality of the NOESY is good enough, it is even possible to see the coupling of the pyrazole position 3 (or of the pyridine position 6) with the 1 and 5 protons of the acac methyl groups. Because these methyl protons exhibit slightly separated signals on the ^{1}H-NMR spectrum (for tris-heteroleptic complexes) they can be differentiated that way.

2.3.4 Carbon NMR characterisation

Once the proton assignment is complete, it is easy to assign the protonated carbon signals by following the information displayed by the HSQC spectrum. Just like the ^{1}H spectrum, the ^{13}C spectrum of a tris-heteroleptic complex is also the sum of the spectra of its corresponding bis-heteroleptic complexes (Figure 2.8).

By combining analyses of coupling constants, HSQC measurements and spectra comparison, the ^{13}C signals of protonated carbons are relatively easy to assign. The characteristic doublet of doublet signals of the 3' and 5' positions of a 2',4'-difluorinated phenyl (observed at 97 and 117 ppm respectively) can be cited as examples, as well as the doublets of the dFppy-3 and dFppz-5 (showing up at 122 and 130 ppm).

The signals of the acac-1 and acac-5 carbons appear around 30 ppm. They are separated in two singlets in the case of tris-heteroleptic complexes with relatively small shifts (< 1 ppm). Just like for ^{1}H-NMR where it always shows up around 5.25 ppm, the acac-3 ^{13}C signal is also very stable and is always visible at almost 100 ppm. ^{13}C-NMR also allows observing the acac-2 and acac-4 signals appearing around 185 ppm. Just as for acac-1 and acac-5, two distinct singlets can be observed for tris-heteroleptic complexes with a chemical shift difference below 1 ppm.

Things become more complicated when considering the non protonated carbons: pyridine-2, phenyl-1', phenyl-6', 2',4'-difluorophenyl-1', 2',4'-difluorophenyl-2', 2',4'-difluorophenyl-4' and 2',4'-difluorophenyl-6'.

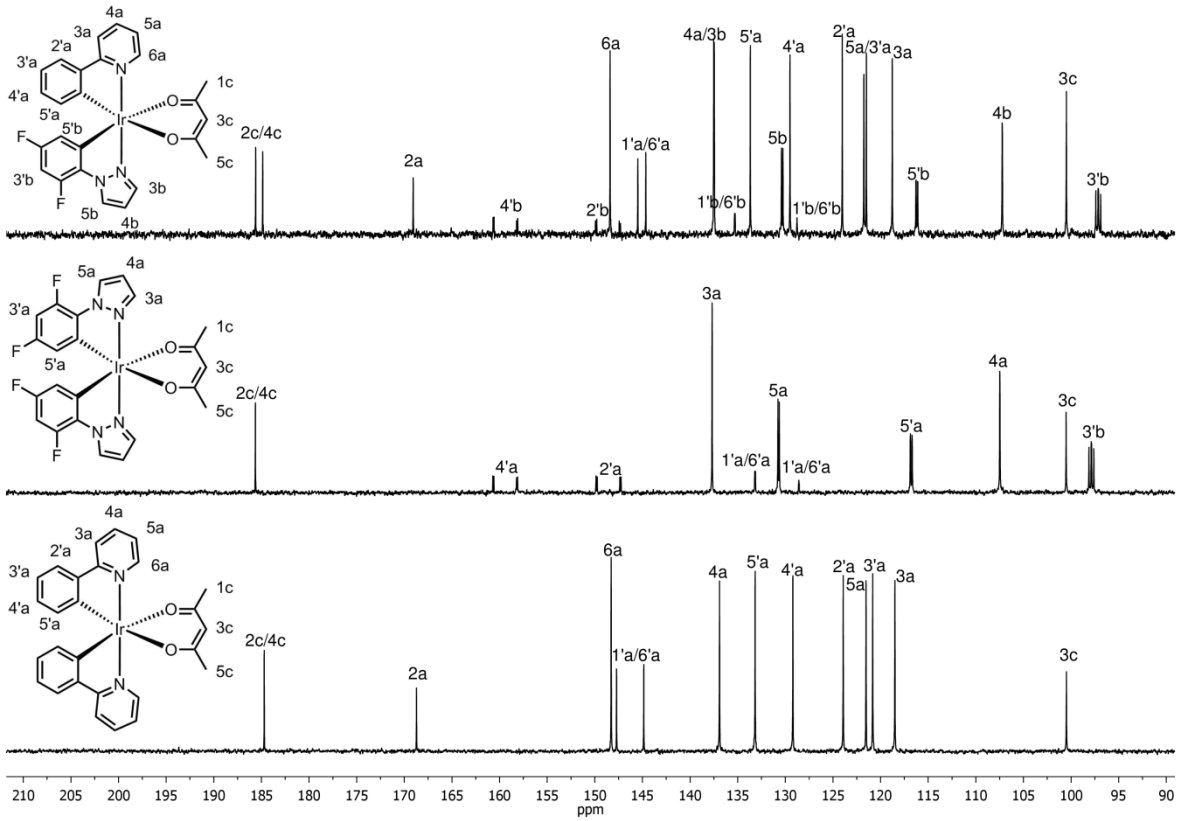

*Figure 2.8: Aromatic regions of the ^{13}C-NMR spectra of **10**, **5** and **1** measured in $CDCl_3$.*

These signals exhibit a very low intensity and require a very good measurement quality to be properly distinguishable from the baseline. Even then, their resolution is often poor and it can be difficult to observe their multiplicity. Among them, the signals with the better resolution are the singlets from the non fluorinated ligands (ppy-2, -1', -6' and ppz-1' and -6'). The ppy-2 signal is especially easy to assign as it remains around 168 ppm for all the complexes containing the ppy ligand (**1**: 168.72 ppm, **3**: 168.54 ppm, **7**: 169.31 ppm and **10**: 169.07 ppm). The dFppy-2 carbon is also easy to spot as it is a doublet located around 165 ppm (**2**:

165.49 ppm, **8**: 166.03 ppm, **9**: 166.25 ppm). The fluorinated carbons can also be assigned if the signal is strong enough as they are doublets of doublets with a large $^{1}J_{C\text{-}F}$ coupling constant (180 – 250 Hz) and a small $^{3}J_{C\text{-}F}$-coupling constant (10 -15 Hz).

The most problematic assignments reside in distinguishing 1' and 6' phenyl carbons. As they are often close to each other and could be interchanged quite easily. Furthermore, the dFppy and dFppz-1' and 6' carbons exhibit signals with very low intensities and badly defined splittings.

In an attempt to distinguish them, HMBC experiment was performed on compound **6**. The problem was that both 1' and 6' carbons were anticipated to couple with 3' and 5' protons for dFppz and potentially with 2', 3', 4' and 5' for ppz. The hope was to observe a $^{3}J_{C\text{-}H}$ coupling between the 1' carbon and the pyrazole proton 5 but it is not the case (Figure 9.42).

With the data and NMR experiments available, it is not possible to assign these signals with a hundred percent certainty. In order to do so, one can try other ^{13}C-^{1}H 2D NMR experiments than HSQC and HMBC, such as H2BC. This technique would allow observing only the coupling between ^{13}C and ^{1}H nuclei separated by two chemical bonds. For ppy and ppz, this would mean observing carbon 6' coupling only with proton 5' and carbon 1' coupling only with proton 2'. In dFppy and dFppz, the carbon 6' coupling with proton 5' would remain visible but the carbon 1'would show no coupling as the proton is replaced by a fluorine atom.

Nevertheless, the data provided by the experiments detailed above allow the assignment of all the other signals, providing a good characterization of these complexes.

2.3.5 NMR yield calculation

For the present series, isolated yields were judged less appropriate due to the acid induced degradation factor on chromatography columns. It is not guaranteed that the yield obtained would be representative of the reaction (since the more polar complexes stay longer on the column, they are subjected to more degradation). Therefore, the decision was made to study NMR yields (relying on the peak integral values) of the crude mixtures to still have an idea of which products are favoured. Furthermore, because of the purification challenge of some complexes and because of the high cost of the iridium starting materials, it is difficult to purify separately each batch from conditions A, B and C. The crudes were mixed and separated together.

As expected, the ^{1}H-NMR signals from the crude are a perfect combination of the signals from the three complexes as exemplified for complex (Figure 2.9). As the relative amount of each complex is accessible from integration of the signals, an average molar mass can be calculated from the ratio obtained, which rapidly gives access to an approximate yield for each complex without the need for purification.

In an attempt to explain the results obtained one must consider the reaction processes involved in the cyclometalation reaction. For a general representation of our case, one can consider the starting material of the type IrCl to react with a first ligand to obtain an intermediate of the type Ir(C^N)Cl.

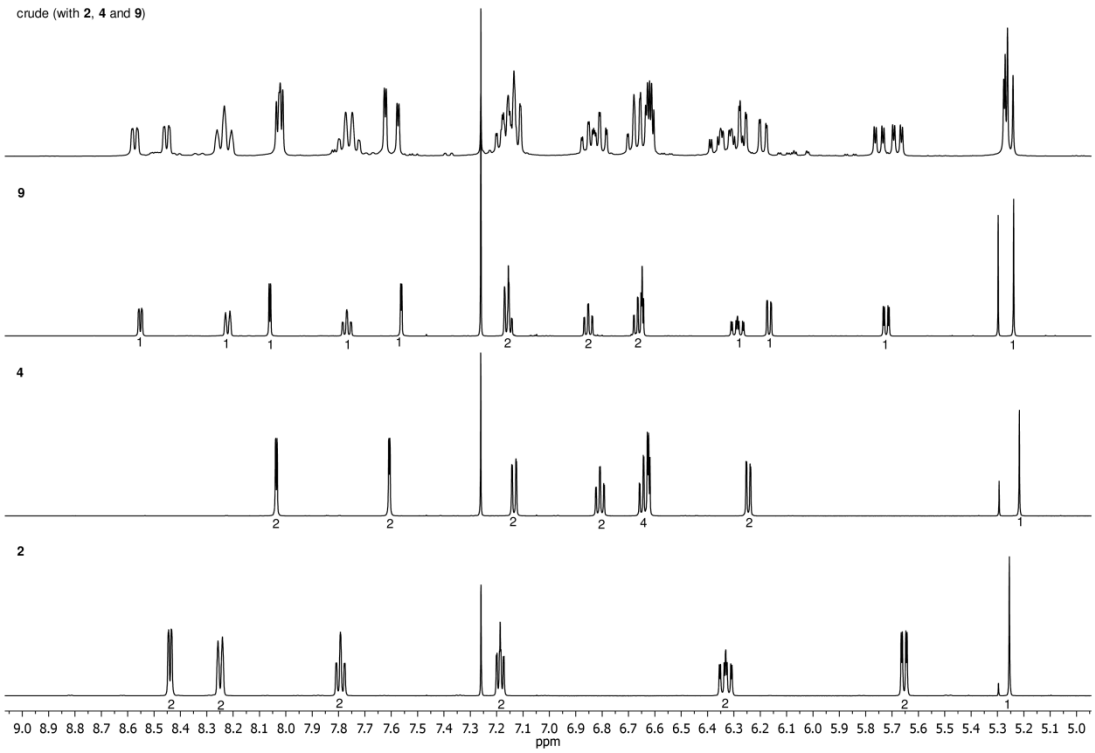

*Figure 2.9: Comparison of the aromatic region of the ^{1}H-NMR spectra (measured in $CDCl_3$) of the crude from **9** (obtained after using conditions C for the first step and containing **2**, **4** and **9**) and the spectra of the purified products **2**, **4** and **9**. The relative integral values are shown for the signals of the purified products.*

Then the intermediate reacts with a second ligand to form the chloro-bridged dimer. In the case of conditions A, the iridium(III) starting material reacts with the ligands through subsequent electrophilic substitution processes. With conditions B and C, the use of an iridium(I) starting material implies an oxidative addition process (to yield an Ir(III)(C^N)Cl intermediate) followed by an electrophilic substitution reaction leading to the formation of the dimer.[124–127]

*Table 2.2: Nmr yields of complexes **3**, **6** to **10** and of their corresponding bis-heteroleptic complexes for each condition set (A, B, and C). The yields are expressed in %.*

		condition set		
entry	Complex	A	B	C
1	**3**	30	37	42
2	**2**	19	12	15
3	**1**	18	12	16
4	overall	67	61	73
5	**6**	36	14	20
6	**5**	10	6	11
7	**4**	22	4	4
8	overall	68	24	35
9	**7**	14	43	32
10	**1**	13	23	11
11	**4**	30	4	1
12	overall	57	70	44
13	**8**	29	32	25
14	**2**	25	24	24
15	**5**	14	5	5
16	overall	68	61	54
17	**9**	30	18	36
18	**2**	22	33	17
19	**4**	19	4	2
20	overall	71	55	57
21	**10**	28	16	19
22	**1**	9	19	15
23	**5**	22	3	7
24	overall	59	38	41

Overall, the results show a little influence of the solvent as conditions B and C exhibit only small yield differences and a clear tendency to favour the same products.

Differences exist but they are most of the time contained within the margin of error of the measuring process. It is interesting to note that the tris-heteroleptic product is often favoured, the only exceptions being for the syntheses of **7**A, **9**B and **10**B (Table 2.2).

The reactions with only ppy-type ligands do not show a big reactivity difference between conditions A and B and C, as the overall yields are contained between 67 and 73 %, with bis-heteroleptic complexes showing similar yields both within and between conditions sets.

The same observation cannot be made for the all-ppz experiment (synthesis of **6**) as conditions A show higher yields than B and C. Low yields for bis-ppz complexes were consistently obtained with conditions B and C (Table 2.2 entries 6B, 6C, 7B, 7C, 11B, 11C, 15B, 15C, 19B, 19C, 23B and 23C). This underlines a decreased reactivity of the ppz and dFppz ligands towards oxidative addition. However, this does not affect the yield of tris-heteroleptic complexes with mixed ligands as conditions B and C reveal some very good values above 30 % (entries 9B, 9C, 13B and 17C). According to these cases, conditions B and C could represent a way of using the ligand reactivity difference to obtain good tris-heteroleptic yields while almost stopping the formation of one of the two by-products. However, the danger is to observe an increased yield of the second by-products that can reach or overcome the yield of the target molecule (entries 14C, 18B, 22B and 22C).

Considering conditions A, similar tris-heteroleptic yields and the same overall yields are obtained for the all-pyridine and all-pyrazole experiments (entries 1A and 5A, entries 4A and 8A). Furthermore, it is difficult to establish clear trends regarding the influence of the 2',4'-difluorination.

In the case of complex **7**, the major product of the reaction was the bis-ppz by-product (entry 11A), while the synthesis of **8** shows a high yield of the bis-dFppy product, almost reaching the yield of the tris-heteroleptic complex (entry 14A).

When the fluorination varies, the fluorinated ligand displays a small advantage as both bis-dFppy and bis-dFppz complexes were favoured compared to their corresponding non fluorinated bis-heteroleptic counterpart (entry 18A and 23A). However, for the synthesis of **9**, this difference is very small (only 3%).

Generally speaking, conditions A give good results and provide good reactivity with both ppy and ppz-type ligands. However, conditions B and C can reach better yields and produce less side products but they also present a higher risk of favouring a side product more than the target compound.

2.4 Second series: complexes with dMeOppy ligands

2.4.1 Choice of the ligands

It has been shown recently that by replacing fluorine substituents on the phenyl ring with methoxy, a similar HOMO-LUMO energy gap can be obtained.[57] Fluorine mostly exhibits a meta-directed inductive electron-withdrawing influence on a phenyl ring. Therefore, when placed at the meta position from a cyclometalated carbon, it has a stabilising effect on the metal centred HOMO. An ortho/para electron-withdrawing effect also exists but it is significantly smaller than the meta influence. A methoxy substituent, however, exhibits a small meta-directed inductive electron withdrawing effect but also a stronger ortho/para-directed mesomeric electron donating effect. Therefore, in the case of a 2',4'-dimethoxylated ppy (dMeOppy), the effect on the meta-positioned metal is electron-withdrawing and the effect on the ortho/para pyridine is electron donating. The result is a simultaneous HOMO stabilisation and LUMO destabilisation.

The second series of ligands studied here combine this 2',4'-dimethoxylation with an increasing electron donating effect inserted on the pyridine ring to incrementally destabilise the ligand LUMO. The standard proton on position 4 of the dMeOppy) is replaced by a slightly donating methyl group (2-(2,4-dimethoxyphenyl)-4-methylpyridine; dMeOMeppy) and by a more donating methoxy group (2-(2,4-dimethoxyphenyl)-4-methoxypyridine; dMeOMeOppy). This latter ligand can also be assumed to apply a further stabilising effect on the HOMO through stabilisation of the phenyl π orbitals via its meta-directed withdrawing effect.

These ligands are combined with the standard ligands dFppy and dFppz to provide a standard energy LUMO (dFppy) and a higher energy LUMO (dFppz). Doing so allows mixing ligands

with controlled LUMO energies in the same complex to see if they allow the formation of a degenerate excited state leading to a broader emission profile.

Furthermore, from a purely synthetic point of view, the insertion of methoxylated ligands with alongside fluorinated ligands should drastically improve the purification process of the tris-heteroleptic complexes formed. As the methoxy substituents are causing a polarity increase, R_f values are anticipated to decrease accordingly. The R_f difference between fluorinated and methoxylated complexes should be increased.

2.4.2 Synthesis details and purification

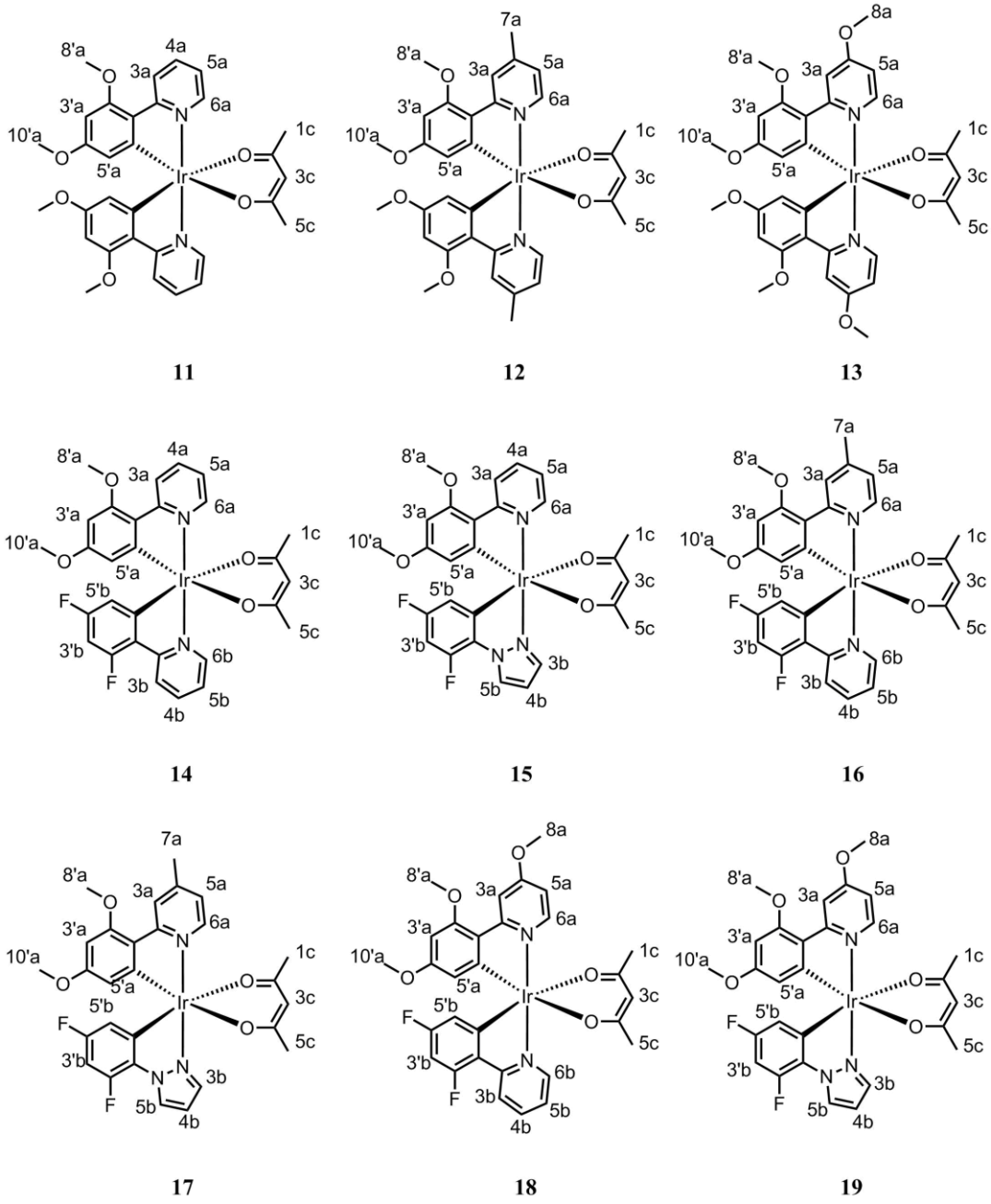

*Figure 2.10: Complexes of the second series: [Ir(dMeOppy)$_2$(acac)] (**11**), [Ir(dMeOMeppy)$_2$(acac)] (**12**), [Ir(dMeOMeOppy)$_2$(acac)] (**13**), [Ir(dMeOppy)(dFppy)(acac)] (**14**), [Ir(dMeOppy)(dFppz)(acac)] (**15**), [Ir(dMeOMeppy)(dFppy)(acac)] (**16**), [Ir(dMeOMeppy)(dFppz)(acac)] (**17**), [Ir(dMeOMeOppy)(dFppy)(acac)] (**18**), [Ir(dMeOMeOppy)(dFppz)(acac)] (**19**).*

Complexes synthesised are presented in Figure 1.23. Conditions B were always used and gave good results for the dFppy complexes (**14**, **16**, **18**) but very mediocre results with the dFppz complexes (**15**, **17**, **19**). Conditions A were tested on the latter complexes and much better yields were obtained (Table 2.3).

NMR spectra of crude products reveal that conditions A favour the formation of the bis-dFppz complex (**5**) and of the tris-heteroleptic complexes while the bis-dMeOXppy complexes (**11**, **12** and **13**) are only present in traces. Conditions B, present the opposite situation where the bis-dMeOXppy complexes are favoured, small amounts of tris-heteroleptic complexes are detected and **5** is virtually absent. For the crudes products of **14**, **16** and **18** synthesised with conditions B only, the tris-heteroleptic complex (**14**, **16** and **18**) is always the major product followed by the bis-dimethoxylated complexes (**11**, **12** and **13** respectively) and then **2**. No major reactivity difference was observed in the crudes proton NMRs as the ratios between the three complexes remained unaffected.

*Table 2.3: Isolated yields (%) of complexes **14-19** when synthesised with conditions A or B.*

	Conditions	
Complex	A	B
14	-	38
15	31	5
16	-	56
17	20	9
18	-	48
19	12	4

A few tests were performed on **19** to try improving the yield. First, by modification of conditions B, the dFppz ligand was added alone (1.1 equiv. to iridium atoms) and reacted at 80ºC for 2h before adding the dMeOMeOppy ligand. The reaction mixture was heated at 130ºC for an additional 3 hours.

After reaction with the acac ligand, the NMR crude revealed no change compared to the standard B procedure. The amount of **5** was undetectable and the major product was **13**. The signals from **19** were also almost undetectable.

The reaction of dFppz alone with the iridium(I) for 3 hours at 130ºC, followed by the addition of the dMeOMeOppy ligand and heating for an additional 3 hours only led to the formation of more **5** alongside **13** while only traces of **19** were observed.

Even though improving the yield of **19** with conditions B would have been a great advantage (due to the reduced reaction time), it is not possible to compete with conditions A when the dFppz ligand is involved.

Once synthesised, **14**-**19** are much easier to purify than the products from the first series. As anticipated, the retention time of a complex on silica gel increases accordingly to the number of methoxy groups it carries. Therefore, the R_f differences between the three species of each crudes are big (Figure 2.11). This difference is especially pronounced between the tris-heteroleptic complexes and the bis-dFppy and bis-dFppz by-products **2** and **5**. Consequently, **2** and **5** are easier to separate from the crude than the methoxylated species.

It is interesting to note that the addition of a methyl group does not change the R_f a lot, as only a small increase is measured (especially for **12** compared to **11**). Insertion of a third methoxy group on the ligand has a bigger impact, as denoted by the R_f decrease measured between **11** and **13**, and between **14** and **18**. The replacement of a dFppy by a dFppz appears equivalent in terms of R_f than the addition of a methoxy group, as **17** and **18** show a similar decrease compared to **16**.

Consequently to increased R_f differences inherent to the use of methoxy groups, only one or two columns are necessary to obtain any of these tris-heteroleptic complexes with a

satisfactory purity. Furthermore, as the R_f are low in pure DCM, it is possible to use shorter columns to achieve a good separation or to use a more polar eluent (such as DCM/MeCN mixtures). This, however, depends on how well the two methoxylated species of the crude are moving on the silica. It is possible than some of them leave tails or degrade more than others (especially when the amount of methoxy groups is high). Therefore, the complexes may be more difficult to separate than it looks on the TLC and longer columns may be needed in some cases.

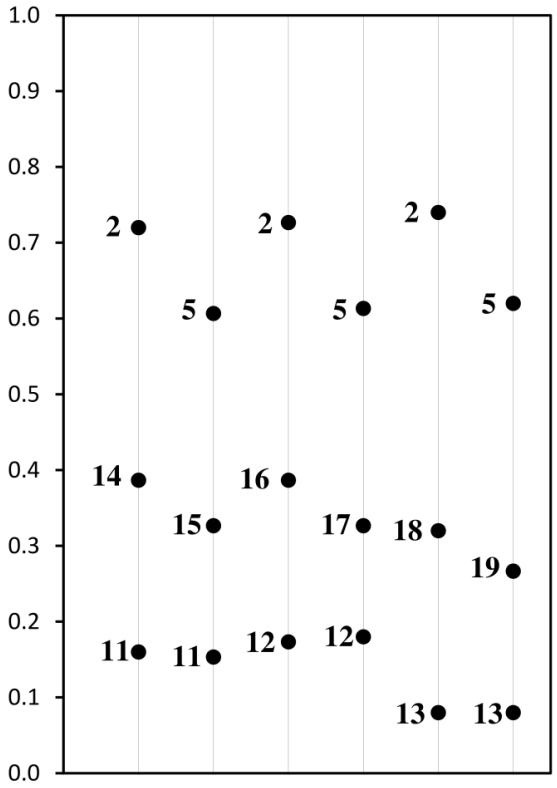

*Figure 2.11: Schematic view of measured TLC separation for the crudes of complexes **14** to **19**, with pure DCM as eluent and without triethylamine.*

However, with the addition of methoxy groups, a lower solubility in DCM was also observed, especially for the dFppz complexes **17** and **19**. This does not lead to major purification issues as the complexes are soluble enough to be purified by column chromatography with DCM as eluent.

2.4.3 NMR characterisations

NMR characterisation by ^{1}H, ^{13}C as well as 2D is essentially the same than for the 1st series, so the assignment process of these complexes is not described in details in this chapter but only focuses on some comparisons and new aspects.

Proton NMR of complexes **11-19** are characterised by the presence of the two perfectly distinguishable methoxy singlets 8'a and 10'a appearing with excellent reliability in the range of 3.86-3.88 ppm (8'a) and 3.47-3.56 ppm (10'a). The chemical shift difference is a consequence of the metalation process which is shielding the 10'a signal significantly but is almost not influencing the 8'a signal. Proton NMR spectra of the free ligands show the 8'a and 10'a peaks appearing very close to each other between 3.81 and 3.83 ppm. The carbon signals are also distinguishable but they are separated by less than one ppm (54.5-55.1 range) and the shift differences from the free ligands are also below 1 ppm.

The ^{1}H signals are assigned easily by COSY NMR as both 8'a and 10'a signals couple with the 3'a proton and while only the 10'a proton couples with the 5'a proton as well (even if these protons are far apart, a signal is often observed in COSY and always in NOESY). NOESY experiments also bring additional information, as a coupling between the protons 8'a and 3a is often observed (Figure 2.12).

The methyl singlet of complexes **12**, **16** and **17**, and the additional methoxy singlet of complexes **13**, **18** and **19** appear respectively between 2.52 and 2.56 ppm and between 2.96-3.98 ppm. The methyl singlet 7a is easily spotted, as it is the only signal in the 2.5 ppm area. Its ^{13}C signal is also easy to spot as it is the only one upfield from the acac methyl signals.

The singlet signal from proton 8a appears just downfield from 8'a and 10'a at 3.96-3.98 ppm and is also easily assigned by its COSY and NOESY couplings with the pyridine protons 3a, 5a and sometimes 6a.

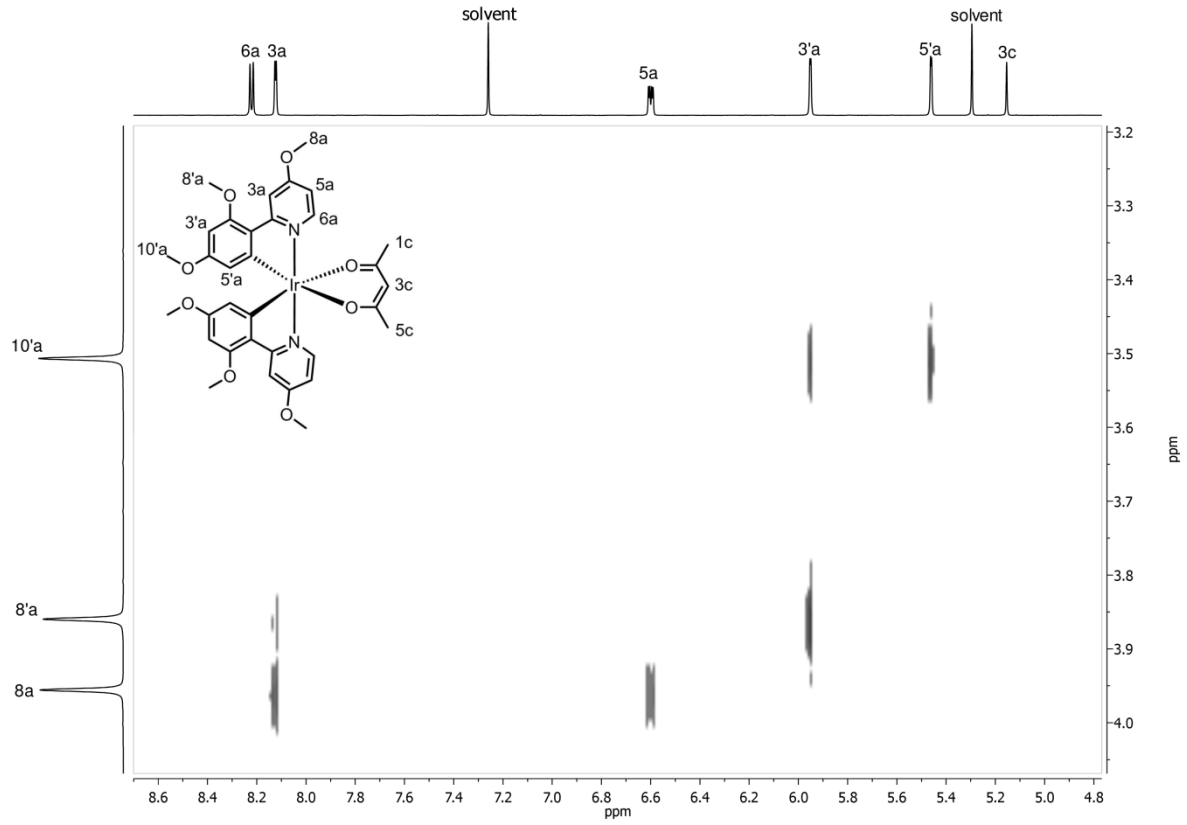

*Figure 2.12: Zoomed NOESY spectrum of [Ir(dMeOMeOppy)$_2$(acac)] (**13**) in $CDCl_3$, the solvent peak is assigned to residual $CHCl_3$.*

On ^{13}C spectra, non protonated carbons 4a appear around 148 ppm when the pyridine is methylated (**12**, **16** and **17**) and around 166 ppm for the 4-methoxypyridine (**13**, **18**, **19**). A HMBC experiment performed on **19** allowed to identify the 2'a and 4'a ^{13}C signals at 159.20-159.47 ppm and 160.21-160.81 ppm due to their respective couplings with protons 8'a and 10'a. This experiment did not bring more information to assign the signals from the 1'and 6' positions, still missing from the 1st series.

2.5 Third series: complexes with phenyl imidazole ligands

2.5.1 Choice of the ligands

The 1st series focussed on the synthesis of tris-heteroleptic complexes using ligands differing by their degree of fluorination, by the nature of their heterocycle, or both. It showed that by playing with the ligands properties, it is possible to create similar complexes with similar R_f and structural properties but that differ in their purification difficulty. The first series also mixed ligands with drastically different LUMO energies with the stable pyridine and the most destabilised pyrazole.

The second series proposed a way of improving the purification challenge by increasing the R_f difference of the bis-heteroleptic complexes present in the mixture. The 2',4'-dimethoxylated ppy ligands allow to do so, while keeping a HOMO-LUMO gap similar to those obtained with difluorinated ligands. Furthermore, the LUMO energy of the ligands was increased stepwise, adding more subtlety in the energy levels of the tris-heteroleptic products.

The third series studies a phenyl imidazole (pim) ligand, known for providing both broad emitting as well as fragile complexes.[115] These ligands have also been understudied in the past as only a few examples of complexes bearing 2-phenylimidazole ligands exist.[55] The most common family of imidazole based ligands are benzoimidazole which do not provide the same interesting properties.[128–133]

Pim has a LUMO energy that lies midway between ppy and ppz. The goal is to mix a pim with both dFppy and dFppz to compare what happens when mixed with ligands of higher and lower LUMO energies. The low stability of the pim ligand has been attributed to ligand degradation by reaction with molecular oxygen, leading to a ring opening oxidation process of the imidazole. In the pim ligand used here (which is 1-mesityl-2-phenylimidazole, mespim),

the original 1-methyl is replaced by a much more bulky 1-mesityl group, which sterically restrain the access of the imidazole ring to molecular oxygen.

Mespim is also mixed with a special ligand 1-phenyl-4-(trifluoromethyl)pyrazole (CF_3ppz) where the electron withdrawing trifluoromethyl group should stabilise the LUMO of the ppz ligand.

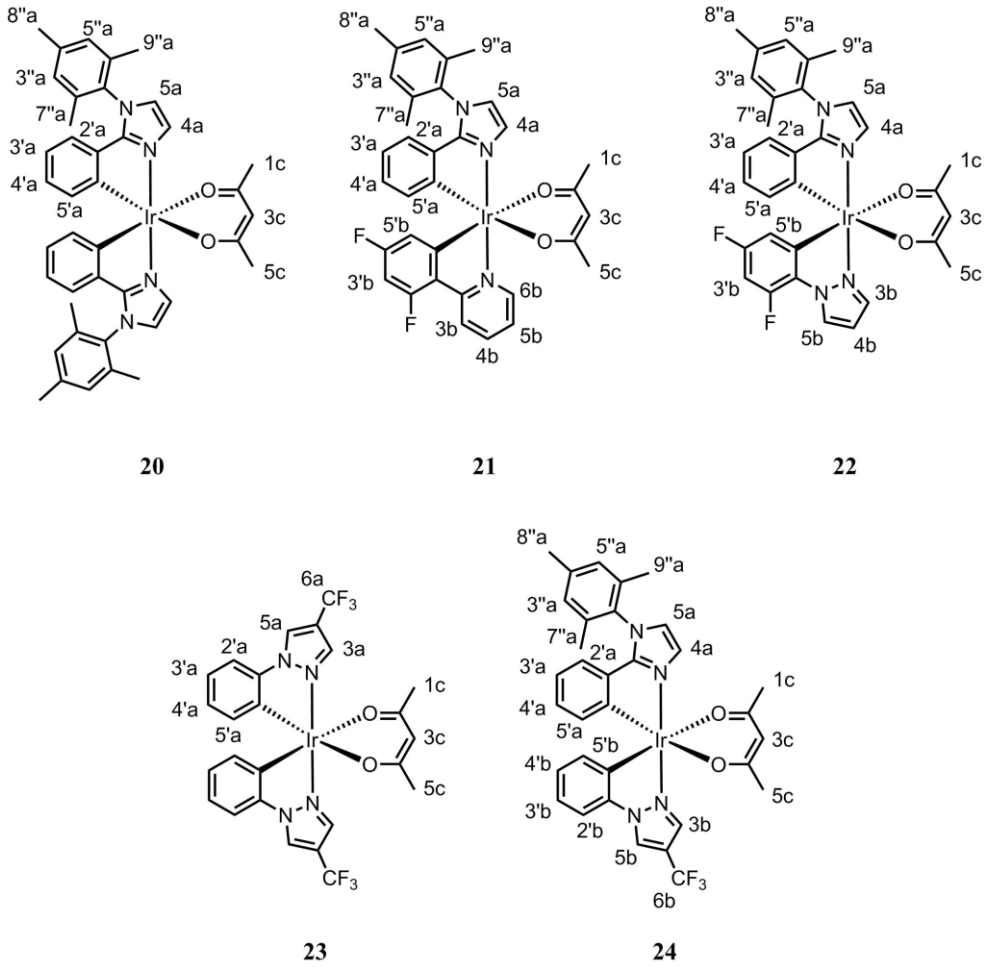

*Figure 2.13: Complexes of the third series: [Ir(mespim)$_2$(acac)] (**20**), [Ir(mespim)(dFppy)(acac)] (**21**), [Ir(mespim)(dFppz)(acac)] (**22**), [Ir(CF_3ppz)$_2$(acac)] (**23**), [Ir(mespim)(CF_3ppz)(acac)] (**24**).*

2.5.2 Synthesis & purification

This series started with the synthesis of the bis-heteroleptic complex **20**. Conditions A were used and the complex was obtained in good yield (75%, Table 2.4) after reaction with acac and a simple precipitation in MeOH/water. This complex appears very sensitive to silica and attempts at improving the purity by chromatography column or preparative TLC led to a certain amount of degradation by dimer formation, even when the silica was treated with triethylamine (this degradation can be seen on the TLC analysis as the complex leaves a spot on the base line and a tail on the migration path). Nevertheless, standard chromatography techniques can be used to remove impurities such as side products of the reaction or a hypothetical excess of ligand but it will always result in the formation of a small amount of dimer.

An alternative way of purifying this complex is to use recrystallisation. Complexes **1** to **19** were all recrystallysed easily by slow diffusion of the complex (dissolved in DCM) in hexane.

Unfortunately, the solubility of **20** in most organic solvents (including hexane and diethyl ether) is increased. Recrystallisation by diffusion does not work but slow evaporation of the solvent produces a good amount of crystal. A very pure product (Figure 9.69) was obtained with this method, even if they the crystals were most of the time not fitted for X-ray crystallography.

Products **21, 22, 23** and **24** were all synthesised from conditions A. The bis-heteroleptic complex **23** is obtained easily in good yield with no purification other than a simple precipitation in MeOH/water.

*Table 2.4: Isolated yields (%) of complexes **20-24** when synthesised with conditions A.*

Complex	yield (%)
20	75
21	13
22	27
23	84
24	20

Purification of **21** is fairly straightforward as only two Chromatography columns are required to obtain the product with a good purity. The low yield obtained for this complex is explained by the increased solubility of the dimer and acac complex in methanol, leading to a loss of product during filtrations. Alternatively, using conditions B could also improve the reaction yield. But as enough material was synthesised to perform all the experiments needed, alternative conditions were not tested.

Purifications of **22** and **24** are more difficult and respectively 5 and 7 columns are required to separate the entire product and a few more preparative TLC plates are necessary to obtain them perfectly clean.

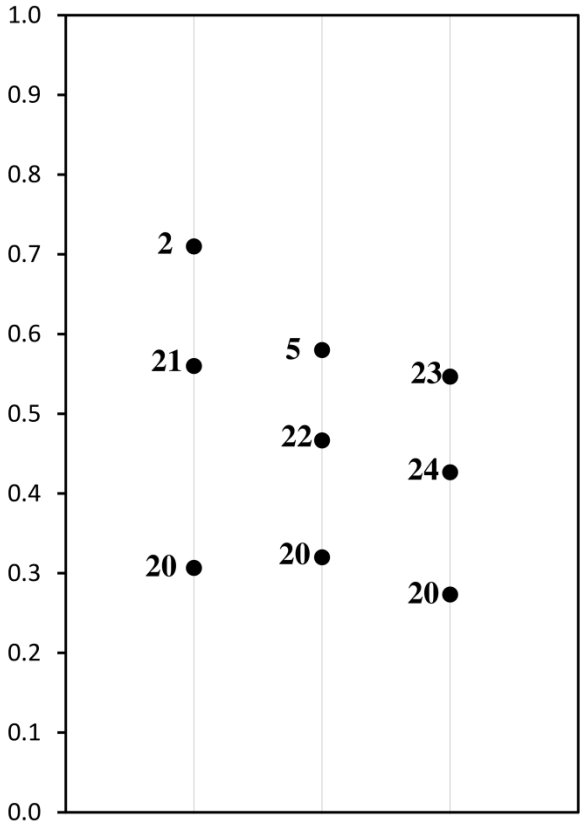

*Figure 2.14: Schematic view of measured TLC separation for the crudes of complexes **20** to **24**, with pure DCM as eluent and without triethylamine.*

Preparative TLC purification for both **22** and **24** revealed an impurity migrating slightly below the product that can be isolated.

Mass spectrometry analyses revealed three peaks for both impurities corresponding to the complex without acac ($[M - acac]^+$), and to the complex with the acac replaced by one or two acetonitrile molecule ($[M - acac + MeCN]^+$ and $[M - acac + 2MeCN]^+$. Even if no acetonitrile is used during the entire synthesis and purification process, it is not unusual to observe such peaks consequently to a formation in the mass spectrometer. The most probable hypothesis, confirmed by mass spectrometry, is that the impurities are complexes where the acac is replaced by something else that is easily removed during the ionisation process.

NMR analyses of the impurity from **22** (Figure 2.15) show a duplication of all signals as well as an important downfield shift of signals from the protons pointing towards the ancillary ligand (4a and 3b). The downfield shift tends to indicate the presence of a chloro-bridged dimer but the splitting of the peaks indicates the presence of two species. As the integration of the peaks from the two sets give similar values, the two species seem to be present in similar amounts.

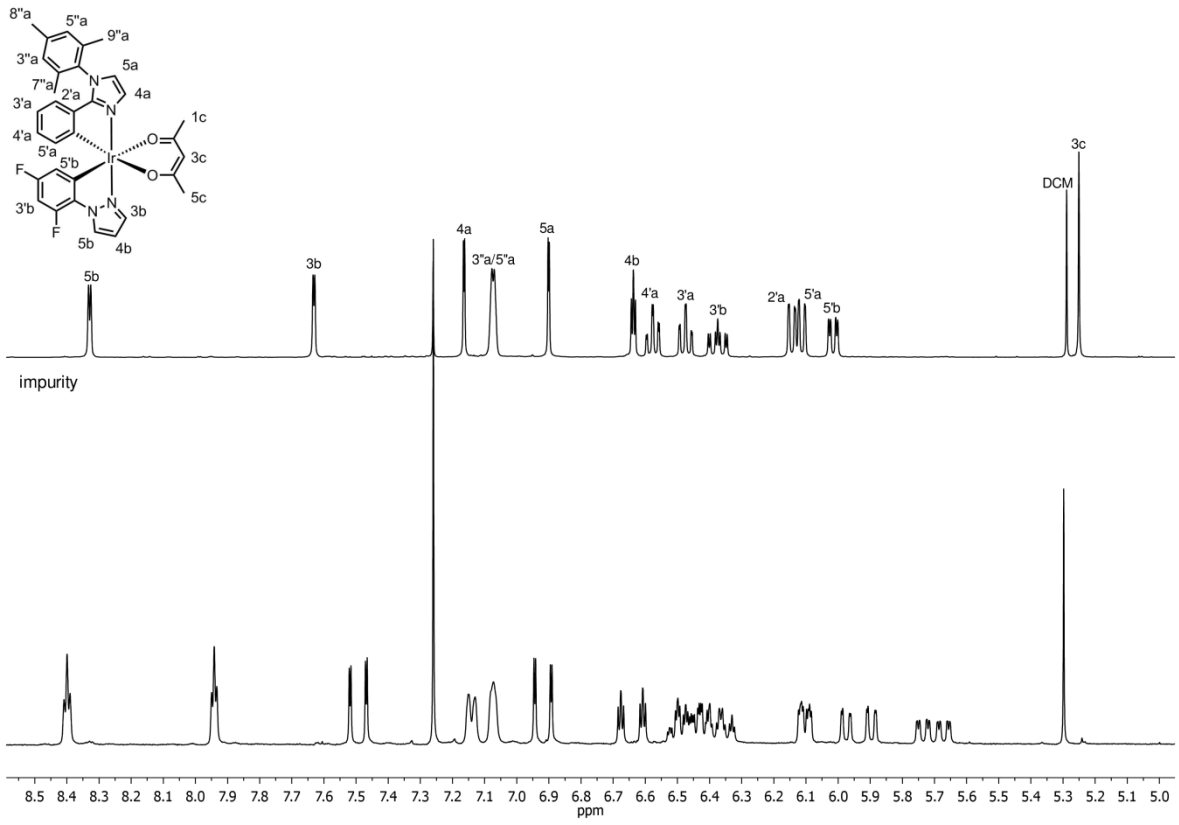

*Figure 2.15: ^{1}H-NMR spectra of **22** compared to the isolated impurity (measured in $CDCl_3$).*

This result is coherent with a dimer mixture where two different enantiomer couples can coexist (arrangements of Δ/Δ and Λ/Λ configurations. It is believed that Λ/Δ configurations are sterically disfavoured as the ligands of the two Ir centres are pointing toward each other) and generate the signals observed here.

Interestingly, the spectrum for the impurity from **24** does not show these two sets so clearly. An hypothesis is that the increased steric hindrance introduced by the CF_3 substituent is enough to restrain again the number of dimers formed.

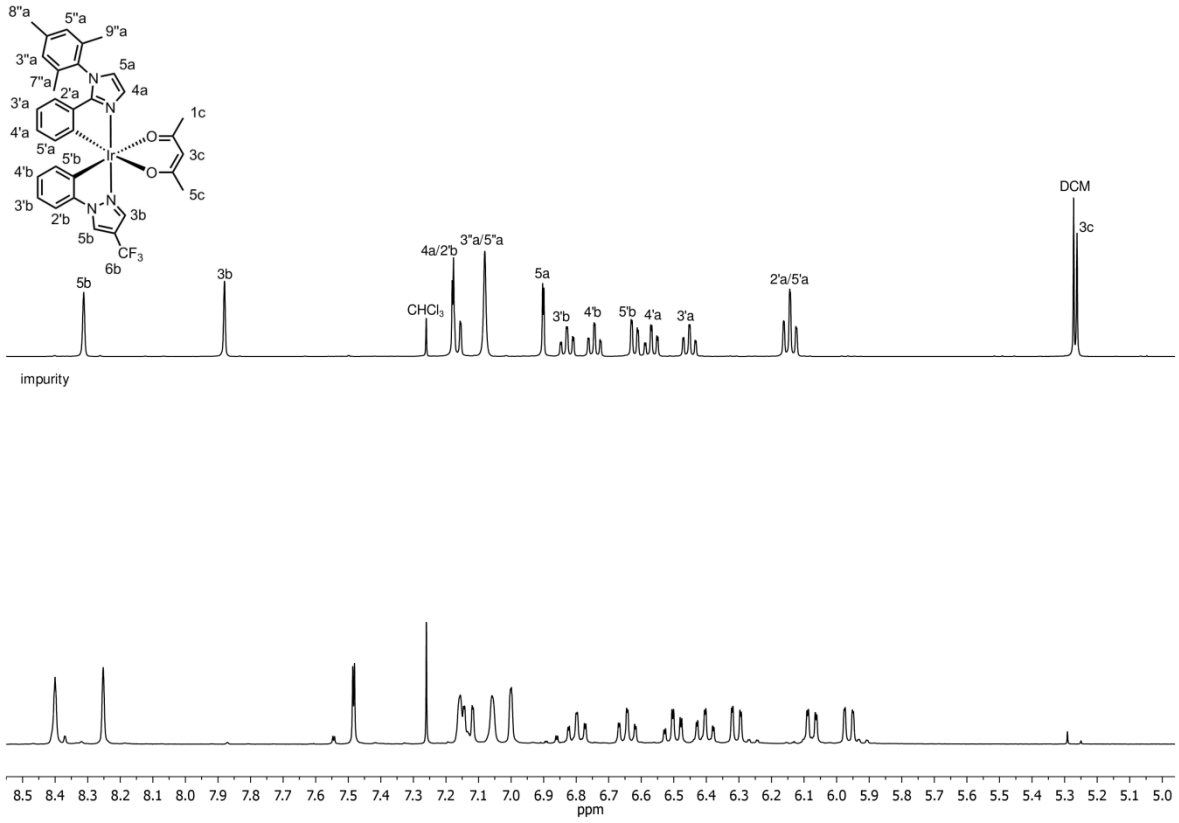

*Figure 2.16: ^{1}H-NMR spectra of **24** compared to the isolated impurity (measured in $CDCl_3$).*

2.5.3 NMR analyses

The NMR spectra of this series show new features introduced by the bigger mespim ligand. Four new non protonated carbons correspond to the mesityl positions 1'', 2'', 4'' and 6'' as well as the Imidazole-2 carbon. The ^{1}H spectra exhibit some interesting effects due to the particular spacial configuration of the complexes.

One effect is the ^{1}H magnetic anisotropy of 7''a and 9'' due to the mesityl group being almost perpendicular to the mespim core axis. As a result, one of the methyl group (defined here as 7''a) points towards the phenyl ring of the second cyclometalated ligand while the other methyl group (defined as 9''a) points towards the acac ligand.

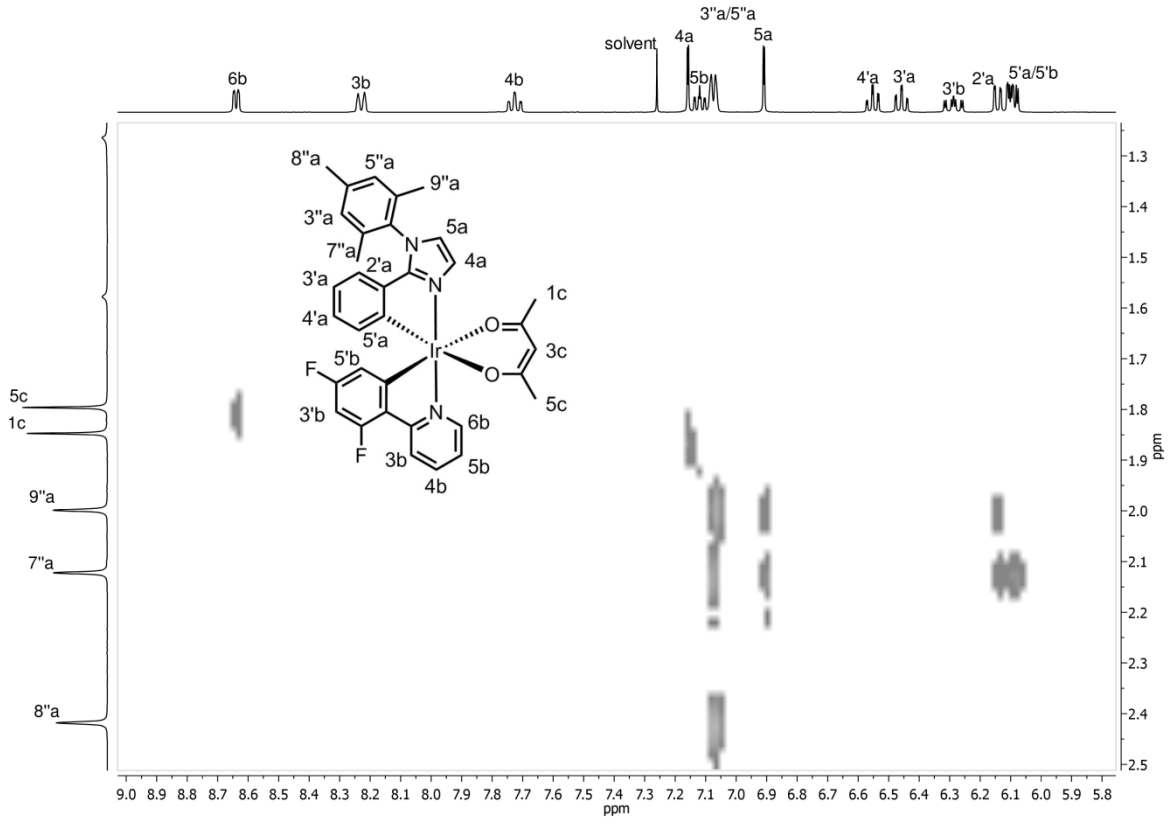

*Figure 2.17: Zoomed NOESY spectrum of [Ir(mespim)(dFppy)(acac)] (**21**, measured in $CDCl_3$).*

Both proton signals show a NOESY coupling with the 3’’a and 5’’a, as well as with the 5a and 2’a signals but only the 7’’a protons displayed a NOESY coupling with the 5’ proton of the other ligand. This effect, shown for complex **21** on Figure 2.17, was observed for all complexes involving a mespim ligand (**20**, **22**, **24**). Another manifestation of such anisotropy is the increased chemical shift difference between the 3’’a and 5’’a signals appearing when the second mespim is replaced by another ligand (Figure 2.18). This signal is mixed and appears as a singlet for **20**. It splits into two partly separated singlets (chemical shift difference of 0.04 ppm) for **22** with the replacement of one mespim by a dFppz ligand. The shift difference is slightly increased with **21**, as dFppy is slightly longer and than dFppz. Crystal structure comparisons of **20** and **21** show the whole Imidazole-mesityl structure being pushed away from the difluorinated phenyl ring. As a result, the local symmetry is disrupted, resulting in a bigger signal splitting.

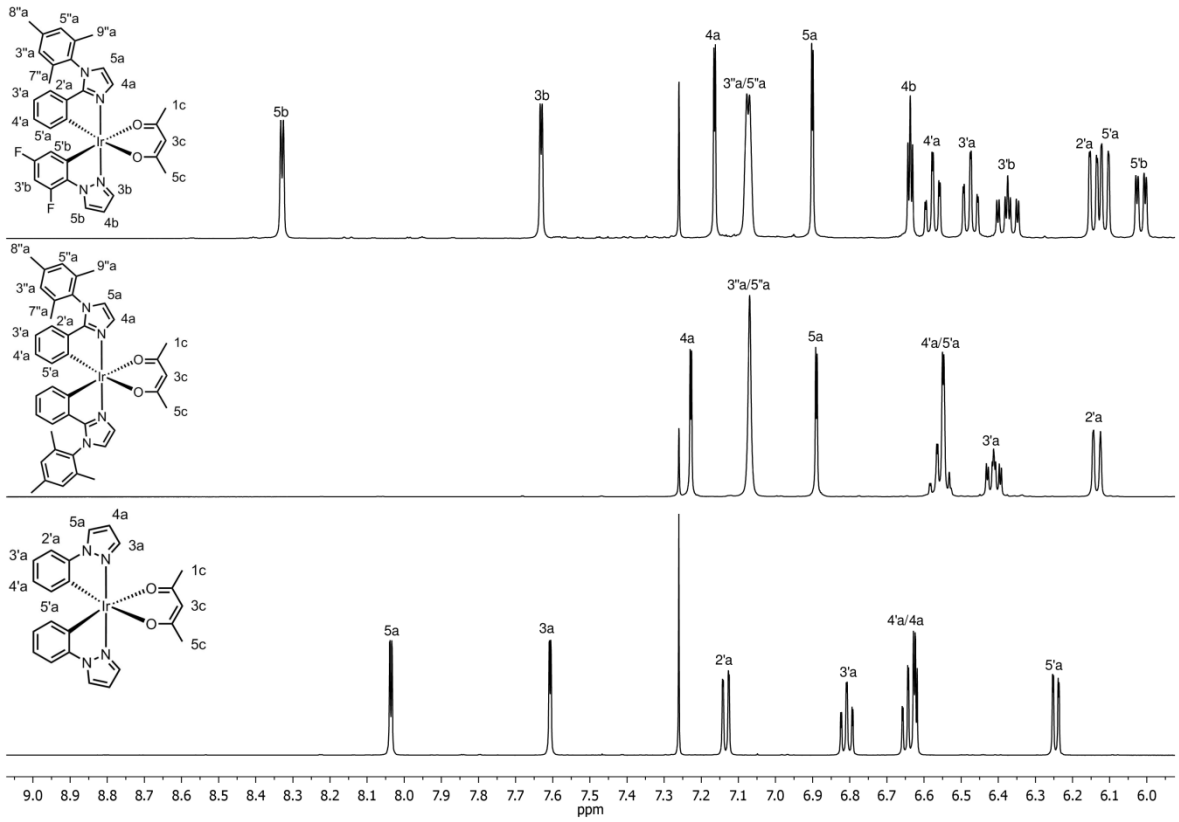

*Figure 2.18: Aromatic region of the ^{1}H-NMR spectra of complexes **22** (top), **20** (middle) and **4** (bottom) measured in $CDCl_3$.*

Another interesting magnetic effect is the shielding of the 2'a proton of **20**. On a standard non-fluorinated ligand such as ppz in **4**, the 2'a proton appears around 7.15 ppm. The same proton in **20** appears to be shielded by approximately 1 ppm and is observed around 6.15 ppm. This effect is a consequence of the spatial arrangement of the mespim ligand that results in the 2'a proton pointing towards the centre of the mesityl ring, undergoing the strong shielding effect of the local magnetic field. This effect decreases as protons get further away from the mesityl ring. The 3'a proton is then shifted by 0.35-0.4 ppm and 4'a only by around 0.1 ppm. The opposite effect is observed for the 5'a proton for which a downfield shift of around 0.3 ppm is observed compared to the same proton on **4**. This effect can be interpreted as resulting from the spatial positioning of 5'a in the plan extension of the second mesityl

ring. The local magnetic field generated by the mesityl ring is therefore deshielding the 5'a proton signal. This effect disappears when the second mespim is replaced by another ligand, such as dFppz for **22**, in which case the 5'a signal appears at the much more standard shift of 6.1 ppm. When the second mespim ligand is replaced (**21**, **22** and **24**), this deshielding influence of the mesityl group is reported on the 5'b protons (of dFppy, dFppz or CF_3ppz) which are shifted downfield by nearly 0.4 ppm (compared to the shift observed for the corresponding bis-heteroleptic complexes **2**, **5** and **23**).

The remaining positions are assigned by using the techniques described earlier. The non protonated carbon signal 2a from the imidazole is observed at 157-158 ppm and is confirmed by HMBC coupling with the ^{1}H signals from 4a, 5a and 2'a. The non protonated carbons of the mesityl ring are also assigned through HMBC couplings. For the 1''a carbon, a strong coupling is observed with the 7''a and 9''a methyl protons and a weaker coupling occurs with the 3''a/5''a protons. The 2''a and 6''a carbons distinctively couple with their corresponding methyl protons only (7''a or 9''a), and the 4''a carbon has the only signal coupling with the 8''a methyl protons. Unfortunately, the 1' and 6' carbon signals can still not be assigned for sure.

Other noticeable patterns are the carbon-4 and carbon-6 of the CF_3ppz that display two very distinguishable quartets with J_{C-F} coupling constants of respectively 39.8 and 266.7 Hz (Figure 9.76, Figure 9.78).

2.5.4 Failed attempts and syntheses

During the synthesis of the 3rd series, other phenyl imidazole ligands than mespim have been tested to synthesise tris-heteroleptic complexes either in combination with a ppz-type ligand or with a second pim ligand. These pim ligands are 4-methyl-1,2,5-triphenylimidazole and 1,4-dimethyl-2,5-diphenylimidazole. Both were selected for the presence of bulky phenyl substituents on the imidazole ring and both have been reported for their use in bis-heteroleptic complexes.[55]

Complex **F1** (failed 1, Figure 2.19) was synthesised by using conditions A, and the dimer mixture was reacted with acacNa by following the standard procedures. The crude mixture had to be filtered on silica gel but the ^{1}H-NMR spectrum obtained was promising as (Figure 2.20).

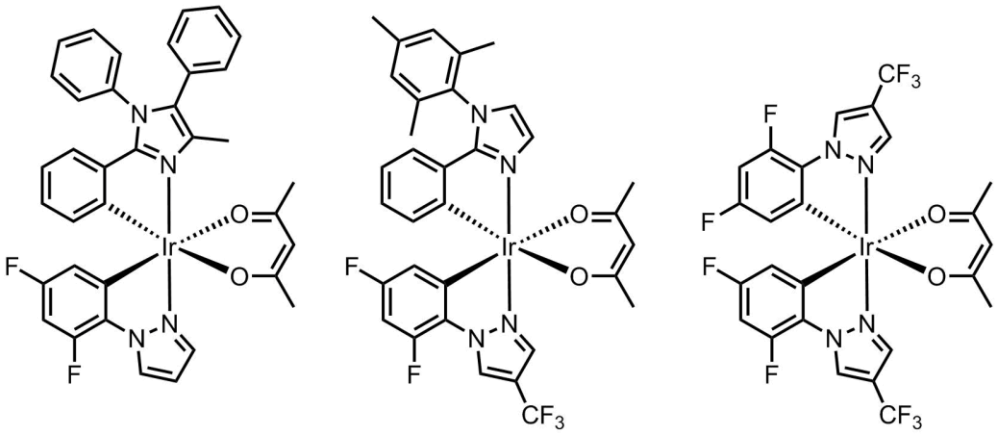

*Figure 2.19: Failed complexes **F1**, **F2** and **F3**.*

If it shows that the main product is the bis-heteroleptic complex **5**, the presence of a small amount of **F1** is also highlighted. This is shown by the small signals at 7.5 and 8.3 ppm, appearing just next to the 3a and 5a signals from **5**. As the product is purified by preparative TLC, one can see signals of **F1** increase and the ones from **5** decrease until only traces

remain. After 5 purifications, the product is almost pure but traces of **5** are still present. Furthermore, the product is degrading under normal atmospheric conditions (protected from light) and on silica and a brown baseline is observed on the baseline of every preparative TLC plate. Consequently, only a few milligrams were isolated after five purification rounds and the product was still not pure enough for photophysical analyses.

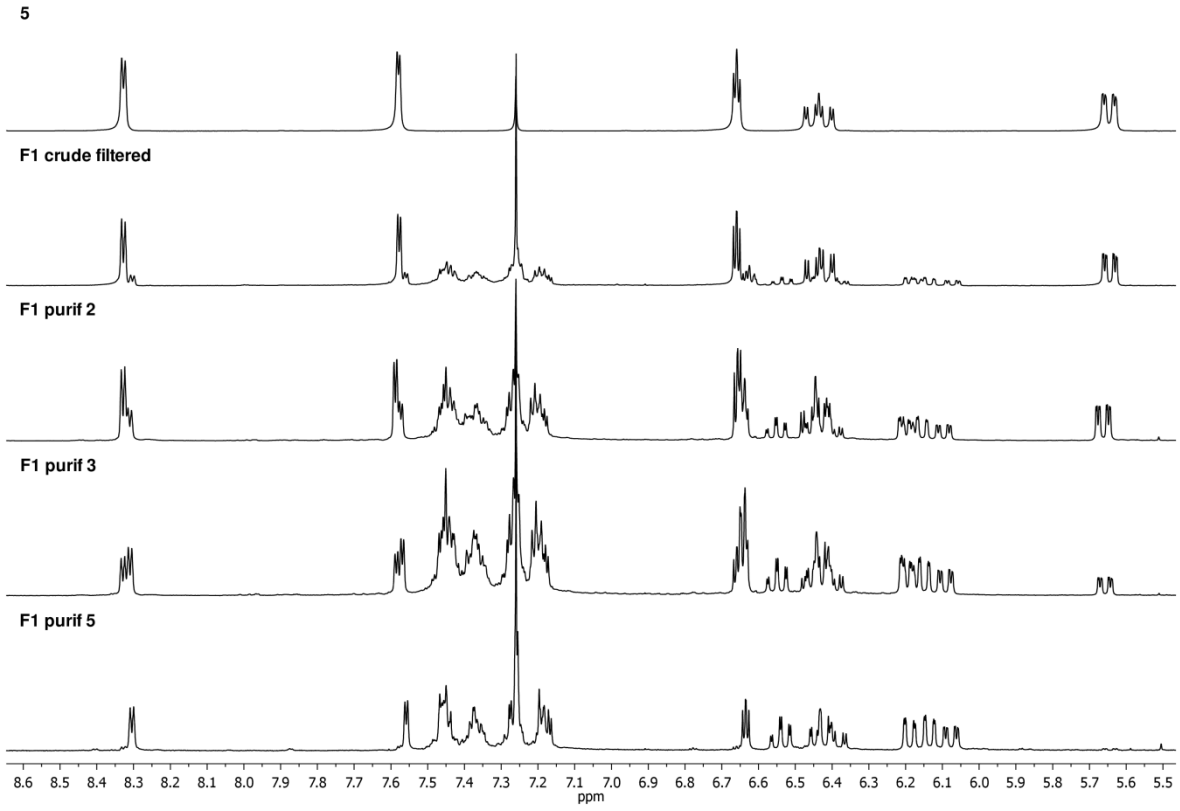

*Figure 2.20: ^{1}H-NMR spectra in $CDCl_3$ of **F1** at various purification stages, compared to the spectrum of pure [Ir(dFppz)$_2$(acac)] (**5**).*

Among the investigations of the imidazole series, a CF_3dFppz ligand was synthesised. The goal of such a ligand is to provide more stabilized LUMO on the pyrazole ring and while keeping the same dFppz core.

Using this ligand and mespim, the synthesis of complex **F2** was attempted with conditions A. The reaction mixture looked bad and only a black precipitate was obtained which did not lead to any product when reacted with acacNa. After careful repetition of the reaction with conditions A and repeated failure, the iridium source was changed and conditions B were used.

After reaction with the ligands, the precipitate obtained was better looking with a yellow colour. Unfortunately, attempted reactions with acac only led to a black precipitate without any traces of product. The synthesis of **F3** with conditions A was attempted to simplify the reaction and test the reactivity of the CF_3dFppz ligand.

The result showed no dimer formation as a black precipitate was obtained. When reacted with acacNa, no product was obtained. From these results, it is supposed that the reactivity loss is due to the complementary effect of the trifluoromethyl and fluorine substituents as both CF_3ppz and dFppz show good reactivity (at least with conditions A). Therefore, it can be assumed that the addition of too much electron-withdrawing character is killing reducing the reactivity of the ligand, no matter what conditions are used. As both oxidative addition (conditions B) and electrophilic substitution (conditions A) processes rely on heterocycle coordination via donation of the nitrogen lone pair to the metal prior to the metalation process. It is reasonable to assume that the increased electron-withdrawing influence is causing a basicity decrease of the nitrogen lone pair, making it unreactive (or not reactive enough) toward coordination to the metal centre.

2.6 Fourth series: pic complexes

On the side of the first series, tests were made to study the effect of different ancillary ligands in replacement of acac. Screening experiments were designed (see below) but they do not allow studying the properties of each complex individually. Furthermore, the introduction of asymmetrical ancillary ligands in the context of tris-heteroleptic complexes poses new purification challenges as well introducing interesting synthetic possibilities.

The attention has been especially focused on picolinate (pic) ancillary ligand as it produces complexes that are less sensitive to acidic degradation than acac, while being simple and commercially available. Furthermore, $[Ir(dFppy)_2(pic)]$ (FIrpic) is a well known sky-blue emitter that offers a valuable and well documented comparison point.

For the need of the study the acac ligands of complexes **3** and **9** were removed with BF_3 in acetonitrile to obtain the bis-acetonitrile complexes **3MeCN** and **9MeCN** (Figure 1.24). As these complexes carry an overall positive charge, they were stirred in an aqueous KPF_6 solution in order to obtain a $[complex][PF_6]$ salt that offers an increased solubility in organic solvents.

The picolinate ligand was added by refluxing the bis-MeCN complexes and picolinic acid in DCM overnight in the presence of Tetrabutylammonium hydroxide (TBAOH). The reaction achieves very good yield and the products are obtained after a simple precipitation in MeOH/water. The products are obtained as a mixture of the two pseudo-mer isomers differing by the orientation of their pic ligand. Each of these isomers is divided into two enantiomers Λ or Δ (Figure 2.21). By convention, the isomers where the pyridine of the fluorinated ligand (here dFppy) is pointing towards the pyridine ring of the pic complex are called “a” and the isomers where the other ligand (ppy or ppz) points towards the pyridine of the pic are called

"b". The eight complexes synthesised here are then Λ-**3a**, Δ-**3a**, Λ-**3b**, Δ-**3b** and Λ-**9a**, Δ-**9a**, Λ-**9b**, Δ-**9b**.

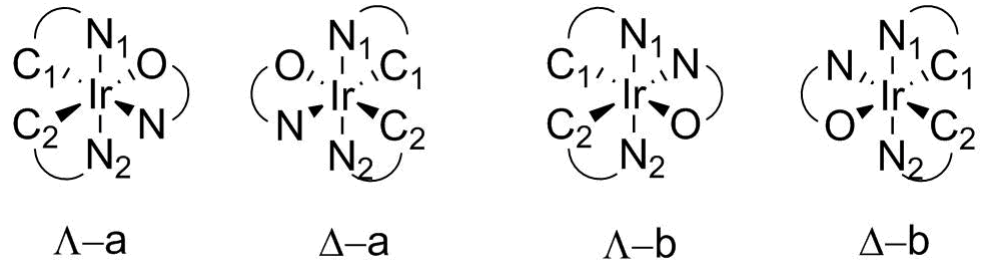

Figure 2.21: The two pairs of enantiomers generated by the synthesis of tris-heteroleptic pic complexes. In isomer-a, the C_1^N_1 ligand points towards the nitrogen of the N^O ligand. In the isomer-b, the C_2^N_2 ligand points towards the Nitrogen of the N^O ligand.

Since the Λ/Δ enantiomers are not separated, and do not present any distinction of interest here, their presence is omitted for clarity and the pic complexes are usually presented under their Λ form only (Figure 2.22).

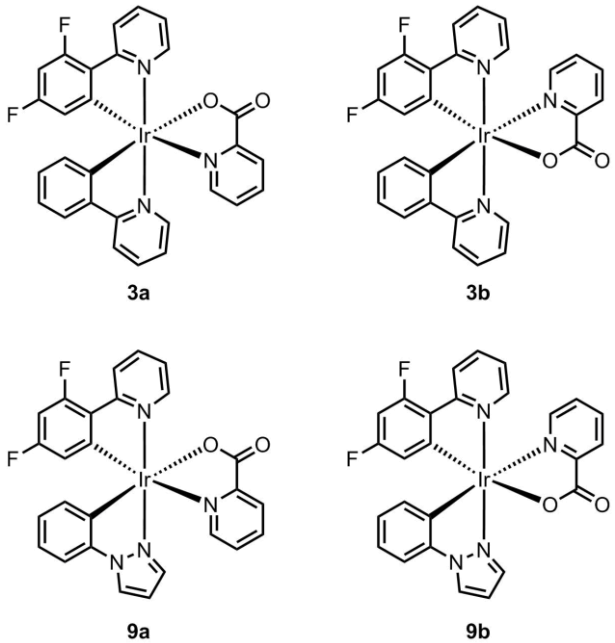

*Figure 2.22: Complexes of the fourth series: **3a**, **3b**, **9a** and **9b**.*

The challenge of the synthesis resides in the separation of isomers **a** and **b**, as they are expected to display very similar solubility and polarity, making them difficult to separate by standard chromatography techniques. The separation of the isomers on silica is likely to depend on how different the two cyclometalated ligands are, as polarity change induced by the orientation of the pic ligand will be more significant. This hypothesis is confirmed in the present situation with the isomers **9a** and **9b** being easier to separate than **3a** and **3b**, due to the replacement of the second pyridine by a pyrazole. The isomers **9a** and **9b** could be separated by preparative TLC plates, using multiple elutions and an eluent with reduced polarity. Even if multiple plates are necessary to obtain pure products, it is achievable whereas **3a** and **3b** remained completely mixed.

Preparative HPLC on reversed phase silica was used to separate the reaction mixtures. The method was developed for the **3a/3b** mixture directly on the preparative column, as attempts to transpose analytical HPLC methods to preparative HPLC failed. The first parameters investigated were the solvent polarity by using MeCN/water mixtures (60/40, 50/50, 45/55, 40/60, Figure 2.23). The samples were run by injecting 2 mL of a 10 mg/mL solution in MeCN. The polarity of the eluent was successively increased up to 60%. Tests with eluents containing more water were not performed by fear of the complex precipitating in the column. Furthermore, the 40/60 mixture does not provide a satisfactory separation as does none of the eluents presented so far.

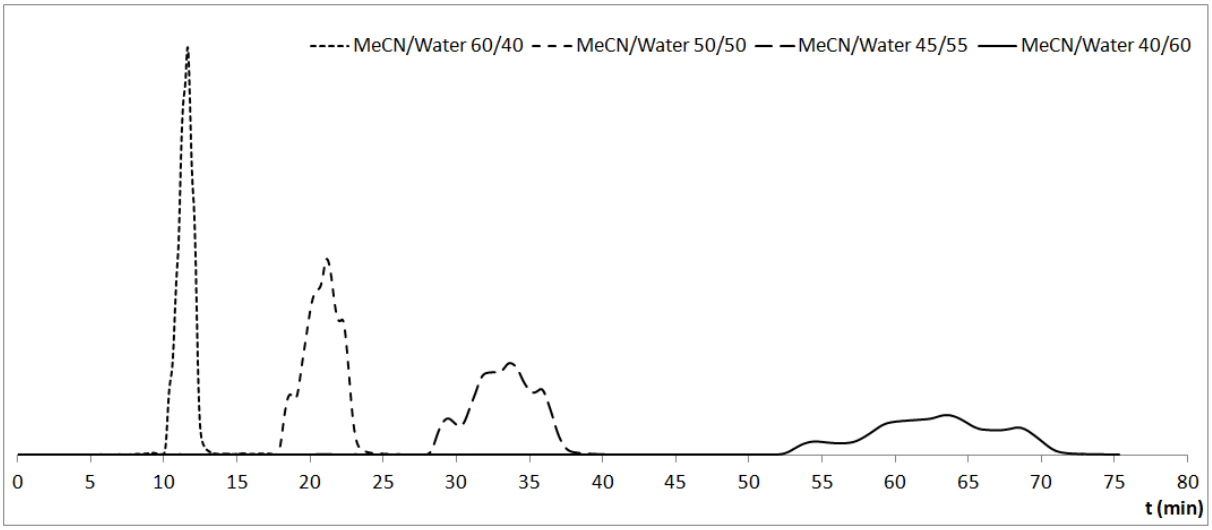

*Figure 2.23: Preparative HPLC chromatograms of **3a**/**3b** mixtures eluted with different mixtures of MeCN/water. All samples were run with 2mL injections of a 10mg/mL solution.*

Proton NMR analyses performed on fractions harvested around the four visible bumps of the broad peak from the 40/60 chromatogram reveal that the first and last bumps are composed of pure **3a** and **3b**. The two middle bumps (that contain the majority of the product) contain mixtures of both. Therefore, using this method to separate the isomers would be very time consuming and not very reliable, as a small variation in the harvesting method can lead to a bad separation.

Of all the organic solvents available and compatible with the preparative HPLC machine, acetonitrile is the only one providing sufficient complex solubility (especially as no temperature control was available with this machine). It is also the most polar one, but it is not polar enough to separate the complexes. Therefore, only MeCN/water mixtures are likely to provide the polarity needed to achieve an acceptable degree of separation. The problem is that complexes are not soluble in water. Therefore, increasing its percentage too much can induce the precipitation of the complex which would result in unpleasant consequences for the column.

Drastically reducing the complex concentration of the injected sample from 10 mg/mL to 1 mg/mL does not change the profile at all, but it was thought that maybe it could allow increasing the water proportion by delaying the precipitation process. Unfortunately, the amount of complex injected was too small and the profile too broad for the separation to be very efficient. The last parameter to change was the injected volume which was decreased from 2 mL to 1 and 0.5 mL (Figure 2.24)

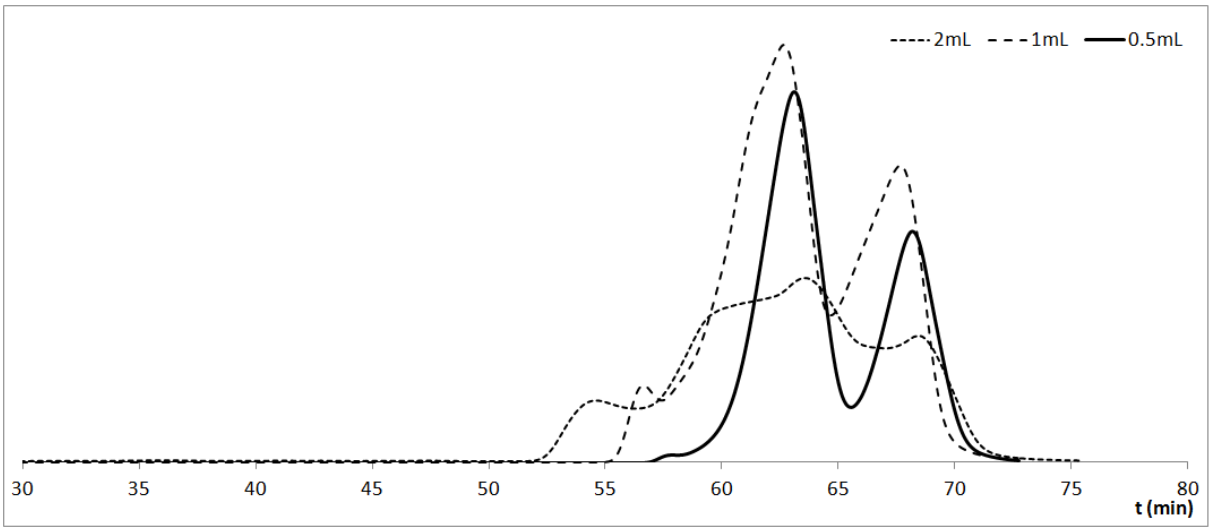

*Figure 2.24: Preparative HPLC chromatograms of **3a/3b** mixtures eluted with MeCN/water 40/60. All samples were injected with a 10mg/mL solution. The injected volume was changes from 2 mL to 1 mL and 0.5 mL.*

When injecting only 0.5 mL at a time, the chromatogram profile appears as two distinct peaks and even if the separation is still not perfect, it is good enough to obtain purified (or at least enriched) isomers and this method can also be used with multiple injections. The products obtained are not pure and a second round of HPLC is necessary to get the well separated isomers. Nevertheless, despites the time consuming aspect of the method, it allows to obtain pure isomers with no degradation. After HPLC, the acetonitrile is evaporated and the products can be harvested by filtration as they precipitate in water.

A similar method was used to separate **9a** and **9b**, keeping the same injection concentration and volume but with a less polar eluent (MeCN/water 50/50). The decreased retention time, the narrower peaks and the better separation obtained for these complexes allow separating the isomers in only one round of HPLC purification in a relatively short time using multiple injections (Figure 2.25).

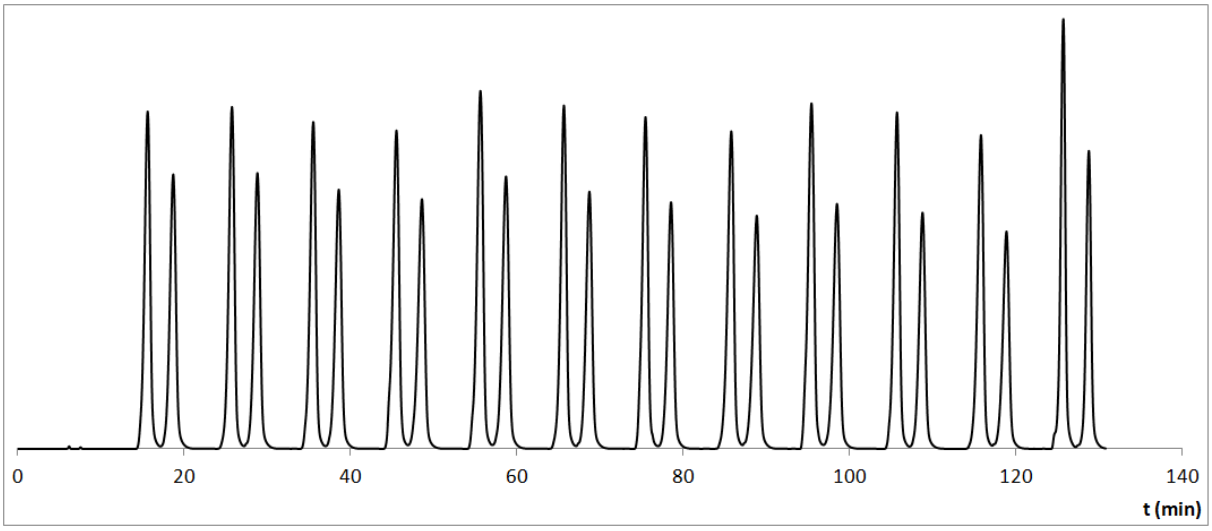

*Figure 2.25: Preparative HPLC chromatograms of **9a/9b** mixtures eluted with MeCN/water 50/50. All samples were injected with a 10mg/mL solution and 0.5 mL at a time.*

2.6.1 Applicability of preparative HPLC techniques for the separation of acac complexes.

Before discussing the NMR characteristic of pic complexes, it is useful to take a moment to discuss the HPLC methodology in the context of separating tris-heteroleptic acac complexes.

As explained above, one of the main challenges when synthesising tris-heteroleptic complexes is the separation of the target product from the two corresponding bis-heteroleptic complexes present as by-products of the reaction. Until now, only standard, normal pressure chromatography techniques such as silica gel columns or preparative TLC have been considered. These techniques have been shown to be successful at separating all the complexes synthesised so far but revealed themselves to be time consuming and quite

expensive in term of both solvent and silica usage. Preparative HPLC appears as a legitimate alternative as it provides a better separation, allows savings of solvent and silica and should not degrade the acac products, as the silica column used is packed with non acidic C_{18}-functionalised silica. In the past, H pressure chromatography techniques with chiral phases have been especially useful to separate Δ and Λ isomers.[134–137]

Tests were realised on a crude mixture of complex **7** which is the most challenging complex to purify from the first series. It quickly appeared that a good separation is possible within one round of purification, by using a 65/45 MeCN/water mixture, a 10 mg/mL solution and a 0.5 mL injection volume.

Unfortunately, ^{1}H-NMR analyses reveal the presence of a small amount of dimers in all the fractions (Figure 2.26), indicating that the complexes are being degraded. As the C_{18} silica is not supposed to be acidic, a potential explanation can be that remaining traces of trifluoroacetic acid (TFA, used during peptide purification and known to be particularly difficult to get rid of) in the HPLC tubes are sufficient to induce degradation.

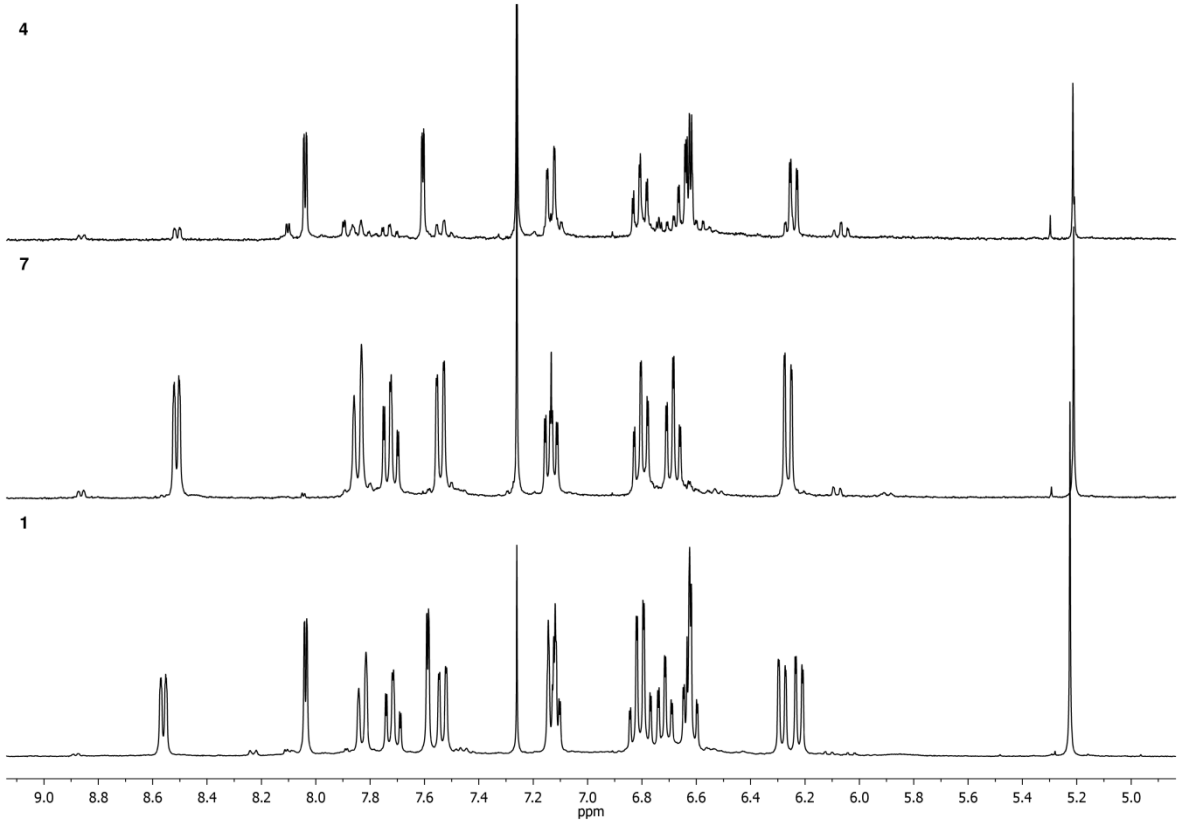

*Figure 2.26: ^{1}H-NMR spectra in $CDCl_3$ of **4**, **7** and **1** in their elution order, purified by preparative HPLC.*

Attempts to remove these remaining TFA traces (by washing the system with solvents) did not improve the purity of the separated products.

Nevertheless, the results are satisfactory and the HPLC separation of complex **7** is all in all faster and more efficient than using only standard chromatography columns and plates. The small amount of dimers generated can be removed quite easily with a short filtration on standard silica gel.

But the main concern that forbids the extensive use of HPLC during this work is the long term contamination of the column with dimer traces. As dimers are known for their low solubility in most solvents, the risk of contaminating the column with precipitated dimer is high. These traces of dimers could contaminate future samples in the long term, or in the worst case, block

the column. Because of the high cost of a preparative column, the risk was judged too high for the HPLC purifications to be continued.

A valid alternative to preparative HPLC would be to use automated chromatography systems with pre packed disposable columns. Quick tests on such a system performed on a crude mixture of **7** showed that one round of purification was enough to completely separate the bis-heteroleptic complexes from each other, leaving two fractions containing respectively **1**/**7**, and **4**/**7**. This result suggests a much better separation than with a first standard column, obtained within a significantly reduced time with a significantly reduced volume of eluent. With this technique, it can be anticipated that a tris-heteroleptic complex such as **7** could be purified in one day instead of one week without the risk of contaminating precious shared equipments with traces of precipitated dimers.

2.6.2 NMR analyses

Depending on the orientation of the pic ligand around the iridium centre, the local magnetic field experienced by protons can be significantly changed, leading to drastic NMR signal shifts from one isomer to the other.

The most significant shift is experienced by protons pointing towards the pic ligands (protons 6 of ppy/dFppy and 3 of ppz) as they find themselves trapped in the pyridine magnetic influence (Figure 2.27). These effects are believed to be mostly caused by spatial positioning around the pyridine ligand and not to the chemical bond rearrangement inherent to isomeric structural changes.

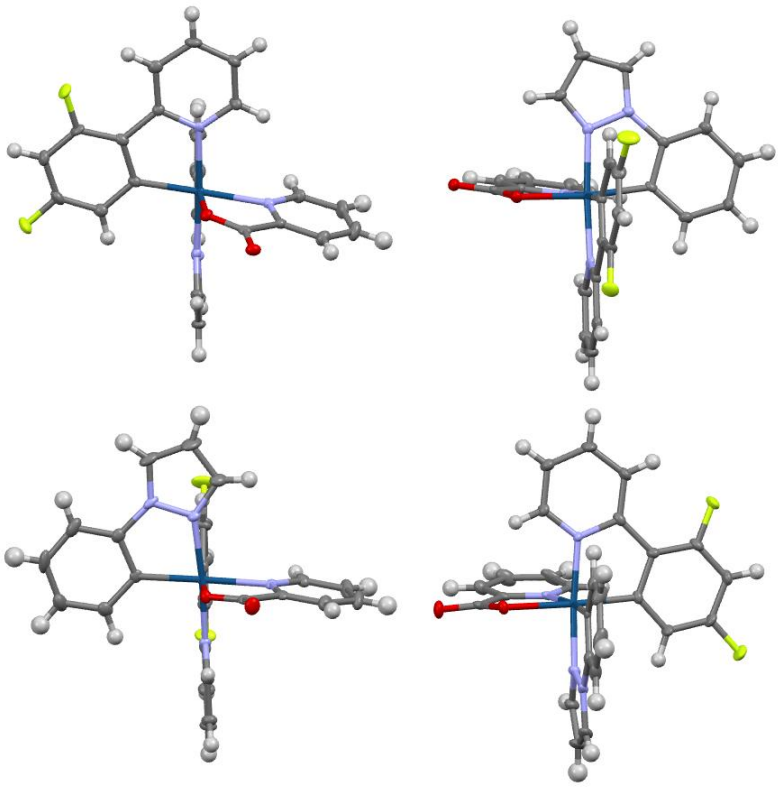

*Figure 2.27: ORTEP representations of **9a** (top) and **9b** (bottom). The left side shows the ligands pointing towards the pyridine ring of the pic ancillary ligand. The right side shows the ligands pointing towards the carboxilate part of pic.*

The changes are very similar between complexes **3a/3b** and **9a/9b** so the latter couple is mostly used as an example during the present discussion, as the increased ligand difference facilitates the exemplification.

Considering first complex **9a**, the signal submitted to the most significant changes belongs to proton 6a which is pointing directly towards the pyridine ring of the pic ligand. As it finds itself positioned above the pyridine shielding cone, its signal is shifted upfield by around 1 ppm compared to the standard signal from the acac complex **9**. The neighbouring proton 5a also experiences a significant (but smaller) influence with an upfield shift of around 0.2 ppm. The effect vanishes for protons 4a and 3a with shifts to the acac standard of respectively -0.04 and +0.03 ppm.

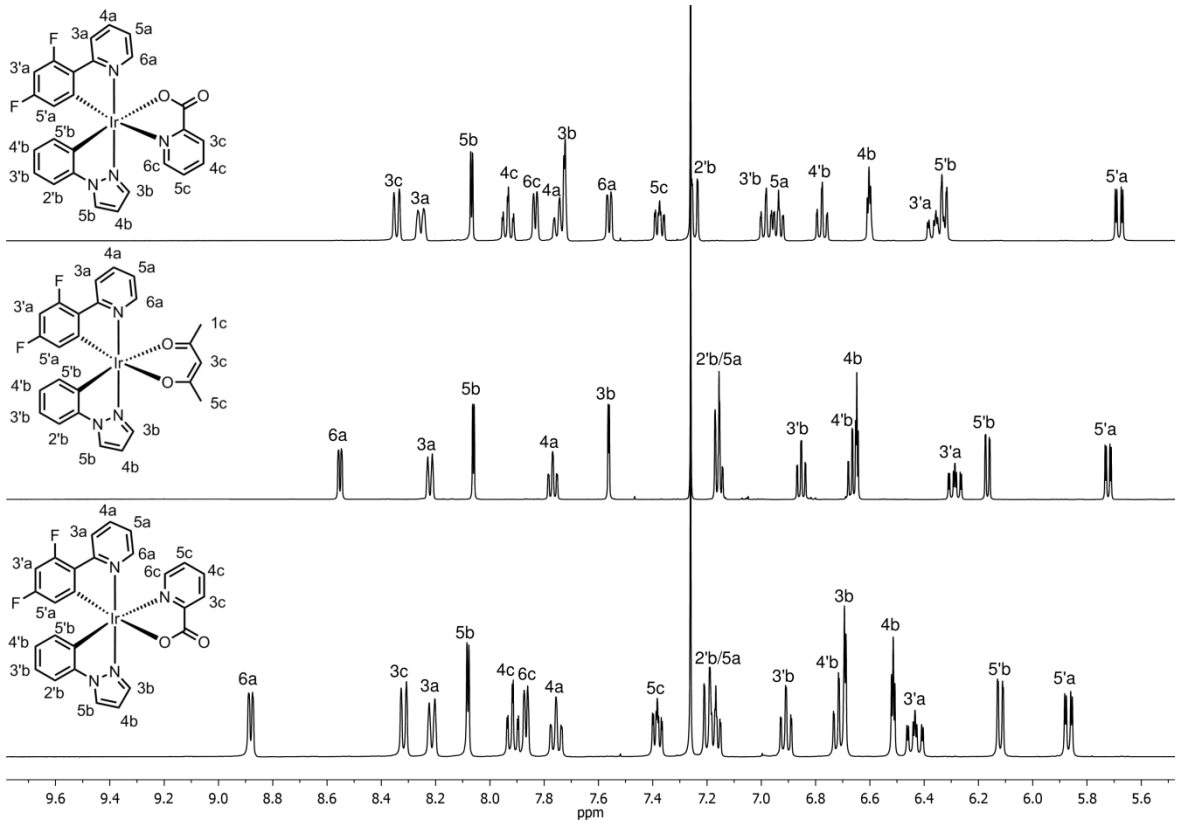

*Figure 2.28: ^{1}H-NMR spectra comparison of **9a** (top), **9** (middle) and **9b** (bottom), in $CDCl_3$.*

The same effect is observed on the other ligand for **9b** where the pyrazole proton 3b is shifted upfield by 0.85 ppm and 4b by 0.15 ppm.

The pic pyridine ring also exerts a deshielding influence on the phenyl protons of the second ligand as they are located in the prolongation of its plane. The effect is smaller than the previously described upfield shift but it is significant. Therefore, the ppz phenyl proton signals 2'b, 3'b, 4'b and 5'b in **9a** are shifted downfield by respectively 0.08, 0.13, 0.12 and 0.18 ppm compared to **9**. The influence on protons 3'a and 5'a of **9b** is of the same magnitude with 0.14 and 0.15 ppm shifts compared to **9**.

The last significant chemical shift difference with acac complexes is found for the protons pointing towards the carboxylate part of the pic ligand that undergo a downfield shift produced by a decreased shielding effect of the carboxylate group in comparison with acac. The 3b signal of **9a** and the 6a signal of **9b** are therefore shifted downfield by respectively 0.17 and 0.33 ppm compared to **9**. This latter increase in the chemical shift difference is coherent with the fact that pyridine is longer than pyrazole which brings its protons closer to the influential area. A difference is also observed when ppz is replaced with ppy, as proton 6b of **3a** is shifted by 0.22 ppm, while proton 6a of **3b** is shifted by 0.36 ppm compared to **3** (Figure 9.83). This effect is the manifestation of the molecule spatial geometry as X-ray crystallography measurements show that the dFppy proton 6 is further apart from the pic oxygen than the ppy proton 6 (by 0.055 Å).

One last observation to make regarding these chemical shift differences between spectra is that the signal from the pic pyridine protons 3c, 4c, 5c and 6c only undergo chemical shift differences of less than 0.10 ppm both between isomers a and b but also when comparing isomers of different cores (**3a/9a** and **3b/9b**).

The understanding of these chemical shift differences between isomers is very useful for the assignments of ^{1}H-NMR signals of these series. This is especially true when considering complexes such as **3a** and **3b** where many pyridine and phenyl signals can be mixed, making the COSY, NOESY, HSQC and HMBC spectra difficult to untangle. Nevertheless, certain specificities of the 2D spectra obtained are worth noting. The NOESY coupling between the phenyl-5' and the pyrazole-3 or pyridine-6 protons of the opposite ligand is always observed and is quite strong compared to most of the acac complexes (Figure 2.29, rectangles). Another NOESY specificity of the pic complexes is the coupling obtained between the pic 6c position and the protons from the heteroaromatic ring pointing towards it and from the phenyl-5' of the other ligand (Figure 2.29, circles).

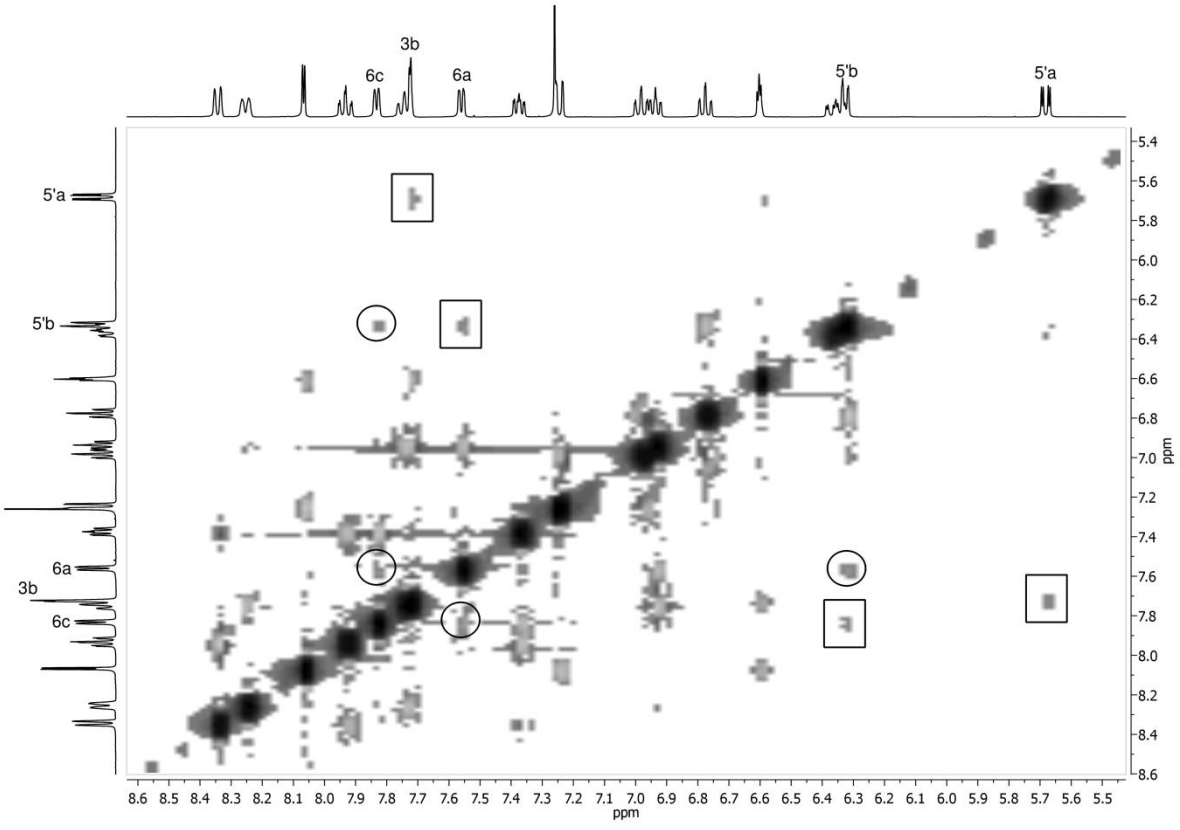

*Figure 2.29: NOESY spectrum of **9a**, in $CDCl_3$.*

The local magnetic field effects are not as important on ^{13}C-NMR spectra and only small variations (around 1 ppm) are observed between isomers **a** and **b,** and with acac complexes (Figure 2.30). Signals from protonated carbons are easily assigned through HSQC analyses and only two new non protonated signals are introduced, corresponding to the pic carbons 2c and 7c. The 2c position appears very close to the dFppy 1'a/6'a signal. It is characterised by a HMBC coupling with protons 4c and 6c. The 7c signal appears around 165 ppm and is only showing an HMBC coupling with 3c.

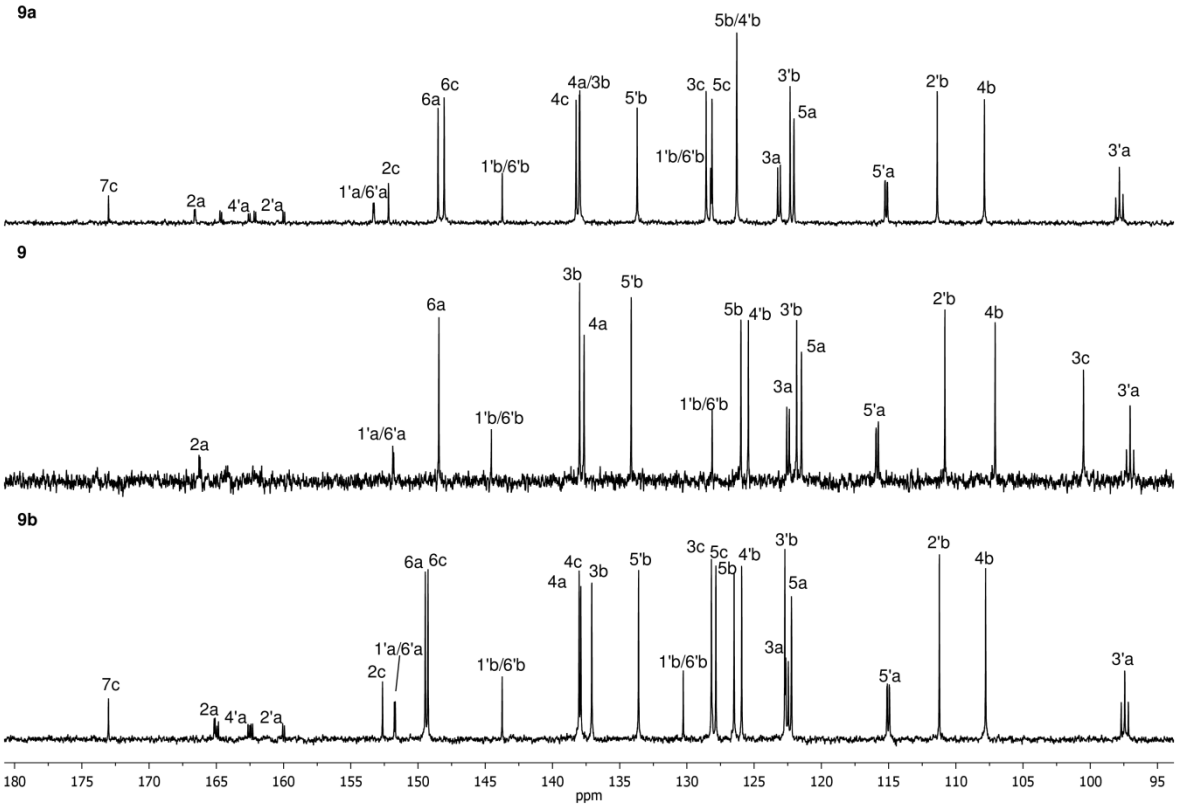

*Figure 2.30: ^{13}C-NMR spectra comparison of **9a** (top), **9** (middle) and **9b** (bottom), in $CDCl_3$.*

2.7 Luminescence profile search; applicability of the screening approach

In the search of interesting iridium complexes for electroluminescent applications, it is desirable to look for ways of speeding up the research process. With a two step synthesis involving chloro bridged dimer formation and ancillary ligand insertion, heteroleptic iridium complexes are good candidates for the design of a screening approach[58]. As most ancillary ligands can be inserted at room temperature, designing small scale test reaction for qualitative evaluation of the emission profiles is easy. This allows testing the effect on the emission spectrum of new ancillary ligand (to search for unexpected results) or to quickly study the effect of different substituents type or position in one family of ligand. This approach allows reacting small amount of iridium materials with small amounts of ligands and do not necessitate tedious purifications.

In the present context of tris-heteroleptic synthesis, the ideal goal is designing, synthesising and purifying acac complexes with interesting [Ir(C_1^N_1)(C_2^N_2)] cores. The pure acac complex can be turned in a pure dimer or in a bis-MeCN complex (Figure 1.24) to be used as a screening precursor.

The limitation of this approach lies in the use of standard emission profile measurement methods that require recording each emission spectrum individually on machines often designed for high precision measurements. This is fundamentally opposed to a screening approach which requires a fast, bulk, low quality measurements.

As an alternative to the standard measurement method, one can use a microplate reader with an integrated spectrofluorimeter. With a 96-hole plates and automated measuring of emission spectra, it is possible to tremendously decrease the sample preparation and the emission profile measurement time.

In the present work, we designed a quick screening experiment using such a microplate reader as a preliminary study. Due to the short availability of the machine (only available for test purposes), the results obtained are not optimised.

2.7.1 Experiment design and procedure

Stock solutions of precursors of complexes **1** to **10** (chloro-bridged dimers or bis-heteroleptics and bis-MeCN complexes), stock solutions of ligands and stock solution of TBAOH were created. In the present case, experiments were designed so that each plate would host one precursor, reacted with the whole ligand library for a total of 92 reactions. Some ligands were tested with and without TBAOH and the plate also contained a blank well filled with only DCM, a well filled with only the precursor solution, a well without ligand (with the precursor and TBAOH) and an empty well.

The problem here was that the test plates used were made of a plastic that was not very resistant to solvent. The covers were made of the same plastic so it was not possible to measure any spectrum while using a cover as they would turn opaque. Furthermore, the machine itself was not guaranteed to be resistant to excessive solvent vapours so using a plate filled with solvent without a cover was out of the question. Hopefully, the machine detctor is located above the plate so the solvent was left to evaporate and the spectra were measured on the solidified complexes while the plate was uncovered.

Of course these measurements could be made in solution, if adequate quartz plates and cover are available. But for this test experiment, it was not worth investing on such expensive glassware. As well, atmospheric control was not available so the spectra were measured under normal atmosphere.

2.7.2 Results

Ten plates were then prepared with the precursor solutions, left to dry, and spectra were measured using the microplate reader. The generated spectra were of various qualities, from only noise to profiles approaching those of pure complexes. A spectra comparison between the screening conditions and the standard method for acac complexes **1** and **2** (Figure 2.31) reveal changes in the emission profile. The emission maxima are slightly blue shifted and the intensities of the lower energy regions of the spectra are reduced, leading to narrower emission profiles.

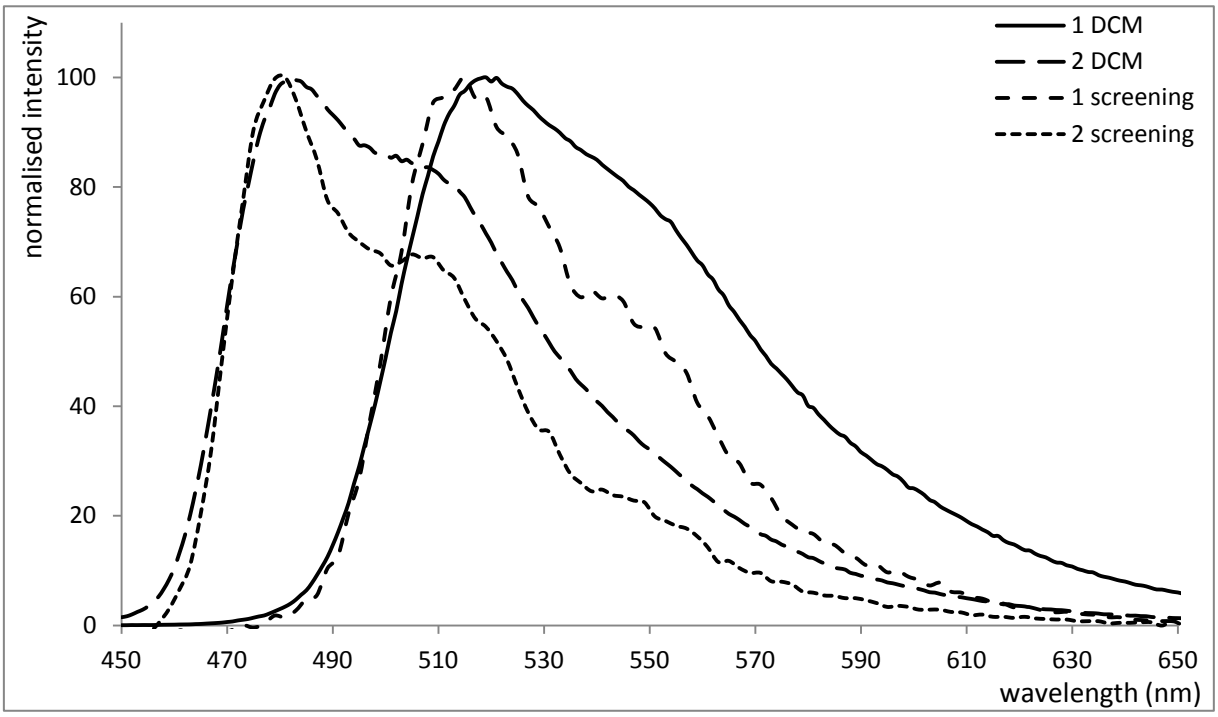

*Figure 2.31: Emission spectra of **1** and **2** measured pure in DCM under argon atmosphere and under screening conditions.*

This change is likely to be due to the interaction with the plastic of the plate which changes the complex environment. These changes are big enough to prevent the detection of potentially broad emitter. If a significant part of the emission profile is quenched for acac complexes, one can speculate that similar or worst quenching can happen with broader

emitting complexes. This effect, added to oxygen quenching that lowers the detection of less efficient complexes seriously reduces the chances of detecting broad emitting complexes with the present experimental setup.

Potentially interesting profile displaying blue emission profiles were also detected and a few reproducibility tests were performed with limited success.

As it is, the method shows two kinds of drawbacks that limit the production of good results. The major problem is the use of plastic plates instead of quartz plates with covers. This led to modified spectra and might potentially forbid the detection of interestingly broad profiles.

The second major problem is the lack of atmospheric control. As phosphorescent emitters are efficiently quenched by oxygen, measuring spectra under inert atmosphere would tremendously increase the detection limit of the method and some profiles appearing as very weak or as noise could become interesting. Furthermore, free ligand fluorescent emission would also become weaker in comparison with the complex phosphorescence. The profile measured would be closer to the one of the pure complex.

The great advantage of this method is to allow measuring more than 900 emission profiles in one week, the time consuming parts of the process being samples preparation and plate filling as it involves an important amount of pipetting. It is believed that if the problems inherent to this particular test are corrected, the use of a microplate reader would greatly improve the screening process for new interesting luminescent iridium complexes.

2.8 Conclusion

This chapter focused on the synthesis and purification of tris-heteroleptic complexes, using various combinations of ligand cores or substitutions. It examined different reaction condition sets, varying solvents and iridium starting materials. These syntheses revealed the influence of the iridium starting materials on the reactivity of some ligands and highlighted the possibility to improve the purification process of a complex by changing the location of the fluorine substituents.

This chapter also paid extensive attention to the examination of NMR spectra to characterise the products. The variety of methods available, their excellent precision and the rapid results they provide makes NMR the perfect tool for the characterisation of tris-heterolpetic iridium complexes. Simple ^{1}H spectra analyses already provide important structural information (like the orientation of a pic ligand) and 2D techniques such as NOESY allows differentiating signals separated by less than 0.05 ppm.

Finally, the successful separation of pic complexes isomers and the screening experiments opened new synthetic possibilities and investigation methods for the developments of interesting tris-heteroleptic iridium complexes.

3 PHOTOPHYSICAL PROPERTIES AND REDOX POTENTIALS

3.1 Introduction

The present chapter aims at presenting the photophysical results measured from the complexes presented in chapter 2. The discussion follows the same order and the series of complexes are discussed separately in their general order of synthesis except for the pic complexes that are joined to the first series. If they represented a special synthetic challenge and deserved a sub-chapter of their own in chapter 2, it makes more sense to discuss their photophysical properties alongside complexes from the first series.

More detailed procedure explanations and aims are provided as examples for the first complexes. Spectra or voltammograms that are not presented here can be consulted in the supporting information.

3.2 First series: ppy/ppz based complexes, and pic complexes

3.2.1 Cyclic voltammetry

Cyclic volammetry is used in the present context to measure oxidation and reduction potentials of the iridium complexes. The cyclic voltammograms are measured in a 0.1 M $TBAPF_6$ solution (in MeCN or DMF). The solvent is deaerated by bubbling argon directly from a cylinder until no more oxygen reduction peak is observed. The solvent choice is motivated by the complex solubility and by the availability of high purity solvents.

Platinum electrodes are used as working, counter and reference electrodes. This choice is dictated by the availability of these electrodes at the time of measurement. Such a system is not ideal due to the increased sensitivity of platinum in comparison with glassy carbon electrodes but it does not represent an important issue here. The measurement is performed without and with ferrocene. The values are all measured vs ferrocenium/ferrocene (Fc^+/Fc). On the voltammograms presented here, the reference peak is not shown and the data have been corrected accordingly, by placing the ferrocenium/ferrocene oxidation potential at zero (Figure 3.1).

Generally speaking, the oxidation potential is interesting in the present context as it gives access to an easy evaluation of the HOMO energy. When the experiment is performed, the potential at the electrode is increased until electrons from the complexes in solution are transferred to the electrode, creating an current peak (anodic). When the voltage is decreased again, the oxidised complex is reduced back as electrons are transferred from the electrode, and a second current peak appears (cathodic). This corresponds to the transfer of one electron from the electrode to the complex and from the complex to the electrode (usually assigned to an Ir(III)/Ir(IV) oxidation processes). It is assumed that the electron is transferred to and from

the HOMO. The oxidation potential (measured as the average of the potentials obtained at the anodic and cathodic peaks maxima) can then be related to the HOMO energy.

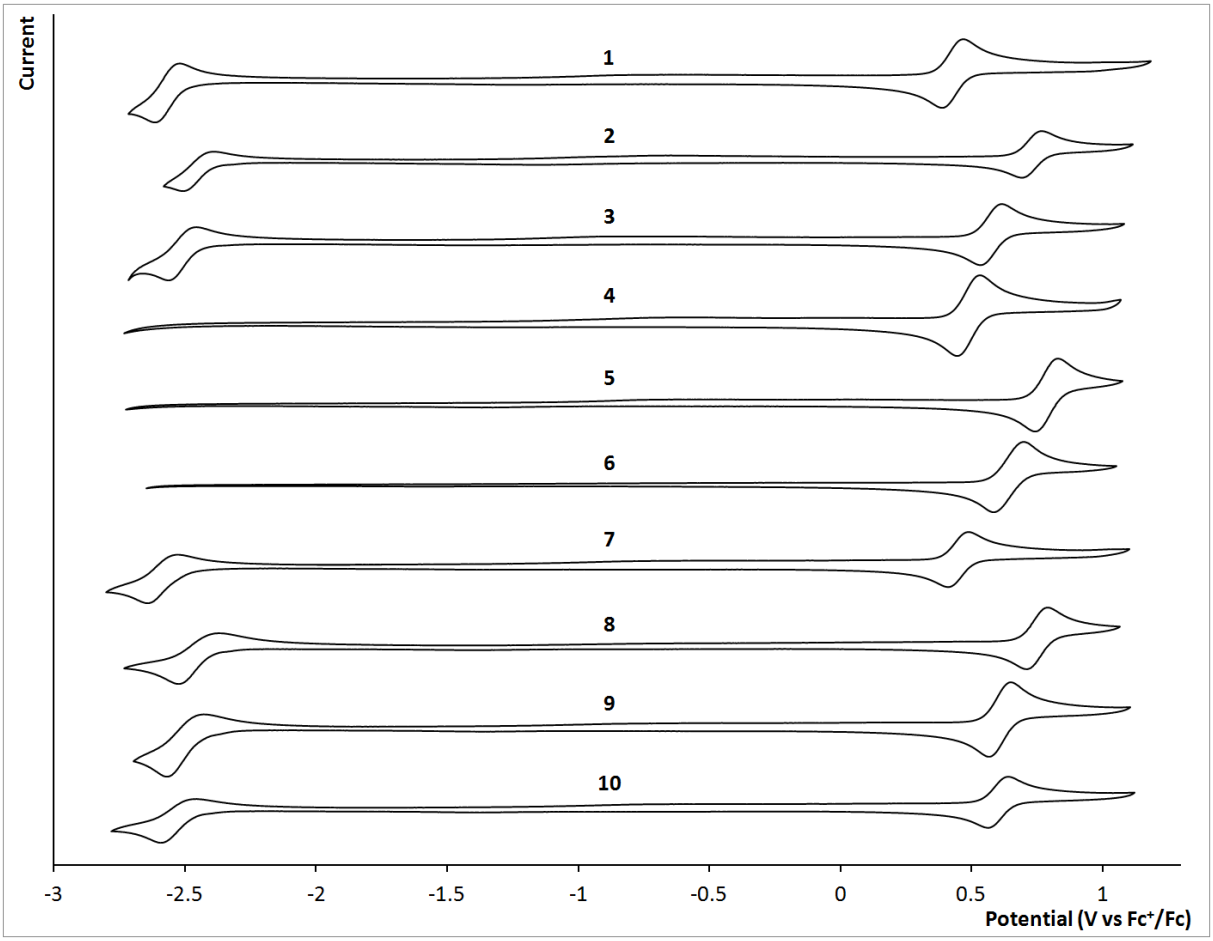

*Figure 3.1: Cyclic voltammograms of **1** to **10** (top to bottom), measured in MeCN (0.1 M $TBAPF_6$) vs Fc^+/Fc at 1 V/s scan rate.*

In the case of **1**, **2** and **3**, a higher potential is required for the oxidation of **2** to happen than for **1**, consequently to the HOMO stabilisation induced by the presence of fluorine substituents. In comparison with **1** and **2**, the oxidation potential of **3** appears as the average of the two others, as its HOMO is of intermediate energy.

The HOMO energy can be estimated, as the Fc^+/Fc oxidation potential lies 4.8 eV below the vacuum level.[138] Therefore, the HOMO energy is calculated as: $E_{HOMO} = -(E_{ox} + 4.8)$ (eV).

Even though this approach has limitations,[139] it provides an easy estimation method to compare complexes within a series and, to a certain extent, with complexes from other studies.

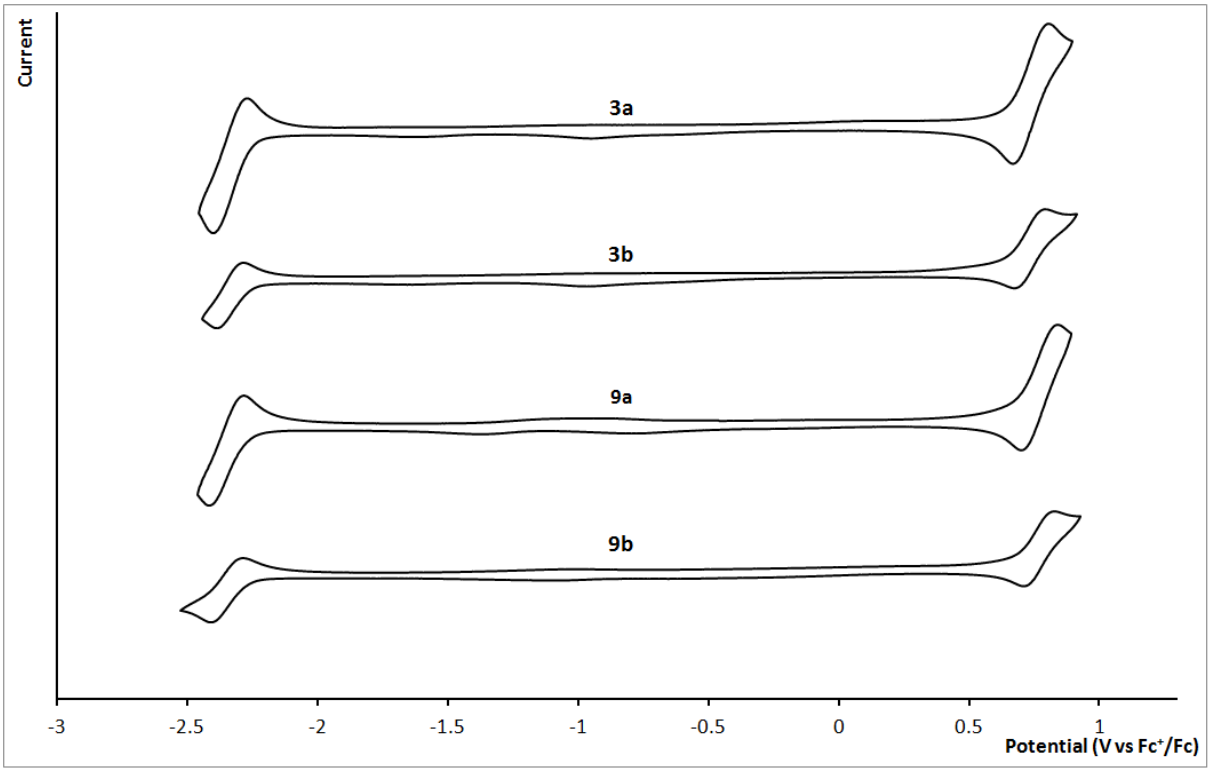

*Figure 3.2: Cyclic voltammograms of **3a**, **3b**, **9a** and **9b** (top to bottom), measured in MeCN (0.1 M $TBAPF_6$) vs Fc^+/Fc at 1 V/s scan rate.*

By the same logic, the reduction potential can be related to the LUMO energy and trends can be observed as complexes known for their higher LUMO energies also display lower reduction potentials. Ppz complexes which are known for their high LUMO energy exhibit low reduction potentials.[140] In the present work, the reduction potential of complexes **4**, **5** and **6**, were not measurable, as they lied outside of the observable window for the conditions used.

If the ligands of a tris-heteroleptic complex are different enough, the reduction potential can be assigned to one of the three ligands. This provides a strong and rapid clue about the LUMO

location. However, this assertion is valid only if the ligands exhibit sufficiently distinct reduction potentials.

*Table 3.1: Oxidation and reduction potentials for complexes **1** to **10** and **3a**, **3b**, **9a** and **9b**.*

	E_{ox} (V)	E_{red} (V)
1	0.43 (0.41)	-2.57 (-2.60)
2	0.73 (0.76)	-2.45 (-2.44)
3	0.58 (0.57)	-2.51 (-2.52)
4	0.49	-
5	0.79	-
6	0.64	-
7	0.45	-2.58
8	0.75	-2.44
9	0.61	-2.50
10	0.60	-2.52
3a	0.73	-2.33
3b	0.72	-2.34
9a	0.76	-2.35
9b	0.73	-2.33

Measurements performed with all Pt electrodes in deaerated MeCN (0.1 M $TBAPF_6$) vs Fc^+/Fc. The values displayed between brackets are from literature.[61]

In the context of the first series, the oxidation potential is strongly influenced by the degree of fluorination of the phenyl rings of the ligands but also (to a losser extent) by the nature of their heterocycles. For complexes with ligands that vary only by their fluorination degree (such as **1**, **2** and **3** or **4**, **5** and **6**), the oxidation potential of the tris-heteroleptic is the average value of the oxidation potentials measured for the corresponding bis-heteroleptics (Table 3.1). The complexes are separated by very consistent 0.15 V increments related to their number of fluorine substituents (0, 2 or 4). The replacement of pyridine by pyrazole when comparing **1**, **2**, **3** with **4**, **5**, **6** reveals a constant 0.06 V increase of the oxidation potential (0.03 per pyrazole). This effect is small in comparison to the changes induced by the difluorination of the phenyl ring but it appears significant, especially in the light of its consistency.

When the ligands are mixed, the oxidation potential remains the average of the two corresponding bis-heteroleptic complexes but, for **9** and **10**, but it also lies in-between the oxidation potentials of **3** and **6,** due to the addition of pyrazole rings. The increments measured for complexes **1** to **6** are still valid even though small variations occur.

Importantly, what seems to influence the oxidation potential is the number of fluorinated phenyl and pyrazole rings on the ligands and not how they are arranged around the iridium centre. This is highlighted by complexes **9** and **10** which have very similar oxidation potentials even though their fluorination/pyrazole ring are not on the same ligands. This is important, as it describes complexes with similar HOMO energies but with different ligand combinations. As explained in chapter 2, these ligand combinations can play a significant role in simplifying the purification process of the complexes so it represent an important parameter for the design of new tris-heteroleptic complexes.

Reduction potentials also follow the same trends and seem to be influenced mostly by the number of difluorinated phenyl rings. The variance, however, is smaller than for the oxidation potentials and adding a fluorinated phenyl only increases the potential by around 0.06 V.

As the pyrazole reduction is too low to be measured, the reduction potentials of the tris-heteroleptic complexes **7** to **10** can be attributed to the pyridine ligand, pointing at it as being the LUMO location.

For complexes **3a**, **3b**, **9a** and **9b**, both oxidation and reduction currents are observed and reversible. The oxidation and reduction potentials being shifted towards more positive values by approximately 0.15 V in comparison with the corresponding acac complexes. The differences between isomers **a** and **b** are very small and measured respectively for oxidation and reduction between 0.01 and 0.03 V.

3.2.2 UV-visible and luminescence spectroscopy

The UV-visible (absorption) and luminescence (emission) spectra were measured in DCM. The emission solutions have been deaerated by bubbling argon to minimise the emission quenching by oxygen. The absorption and emission profiles from complexes **1** to **10** are presented below (Figure 3.3, Figure 3.4 and Figure 3.5). Key properties calculated from the spectra are also presented (Table 3.2). All spectra presented here are plotted on a wavelength scale (nanometres, nm). Wavenumbers are only used in the present work to report the full-width-at-half-maximum values (FWHM, Table 3.2).

UV-visible spectra of complexes **1** to **10** are dominated by strong absorption bands with large molar extinction coefficients ($\varepsilon \approx 35 - 45 \times 10^3$ M^{-1} cm^{-1}) between 250 and 260 nm attributed to Ligand Centred (^{1}LC) $^1\pi$-π^* transitions.[31] The next region between 300 and 440 nm shows weaker transitions ($\varepsilon \approx 5 - 20 \times 10^3$ M^{-1} cm^{-1}) of charge transfer character (CT) attributed to electron transfer from the iridium centre to the ligand (metal to ligand charge transfer, ^{1}MLCT).[141] Weak transitions observed at longer wavelengths than 450 nm ($\varepsilon < 10^3$ M^{-1} cm^{-1}) are attributed to direct population of the ^{3}MLCT state.[59]

The absorption profiles of bis-ppz complexes **4**, **5** and **6** were found to be blue shifted compared to the ppy containing complexes. As they are not luminescent at room temperature, (and in addition to non-measurable reduction potentials) this is in agreement with high energy LUMOs. Consequently, the MLCT region of the absorption spectra for mixed ppy-ppz tris-heteroleptic complexes is dominated by ppy-like transitions with reduced molar extinction coefficients (approximately twice as low as for bis-ppy complexes, Figure 3.3, Figure 3.4 and Figure 3.5).

The higher energy part of the spectra (260 to 350 nm) seem to show a more ppz-like character as some bis-ppz transitions are also visible on the profiles of ppy-ppz complexes. This is

especially true for complexes **7** (Figure 3.3), **9** and **10** (Figure 3.5) where the transition around 300 nm from the corresponding bis-ppz complex is also observed.

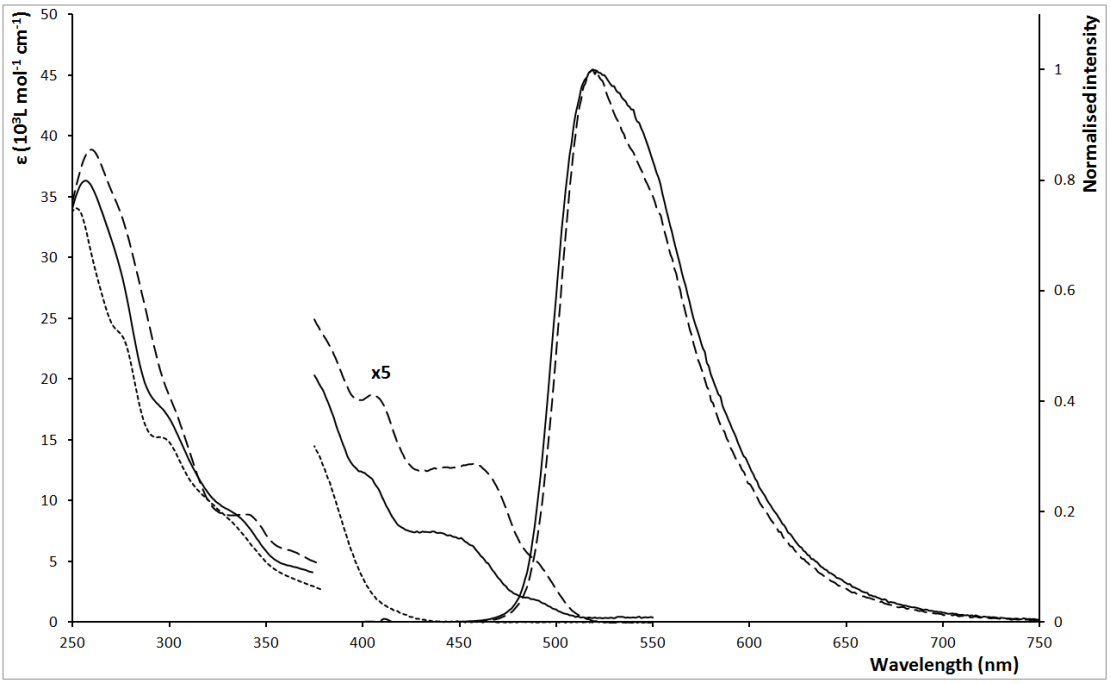

*Figure 3.3: Absorption (left) and emission (right) spectra of **1** (dashed line), **4** (dotted line) and **7** (solid line) measured in aerated DCM (abs.) and deaerated DCM (em.) solutions.*

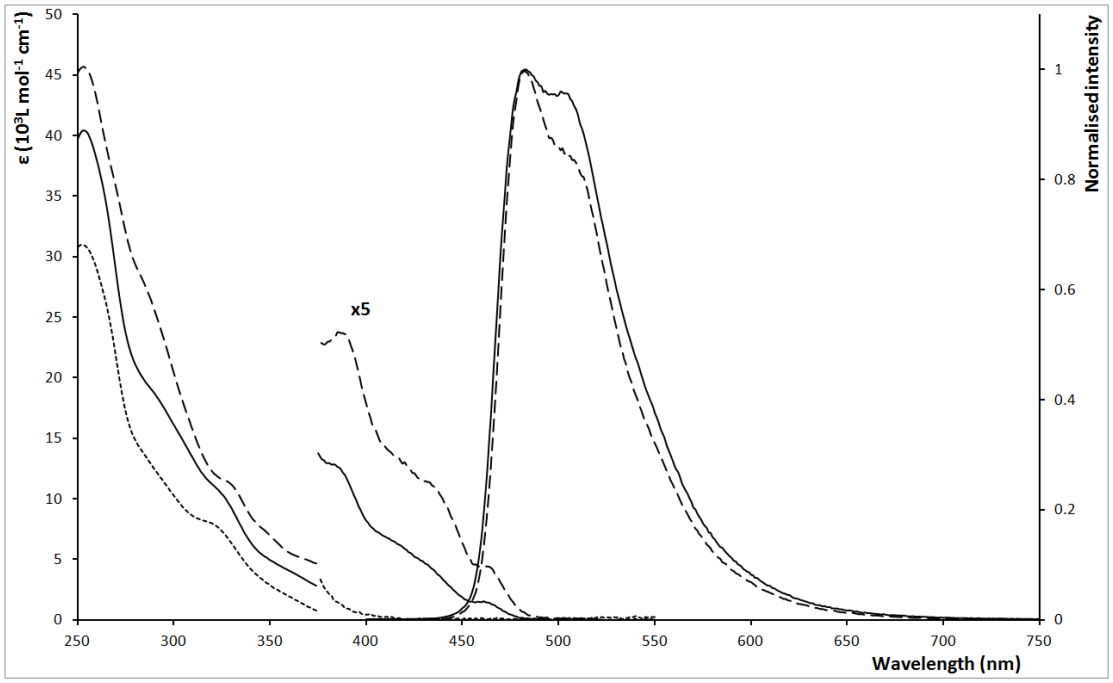

*Figure 3.4: Absorption (left) and emission (right) spectra of **2** (dashed line), **5** (dotted line) and **8** (solid line) measured in aerated DCM (abs.) and deaerated DCM (em.) solutions.*

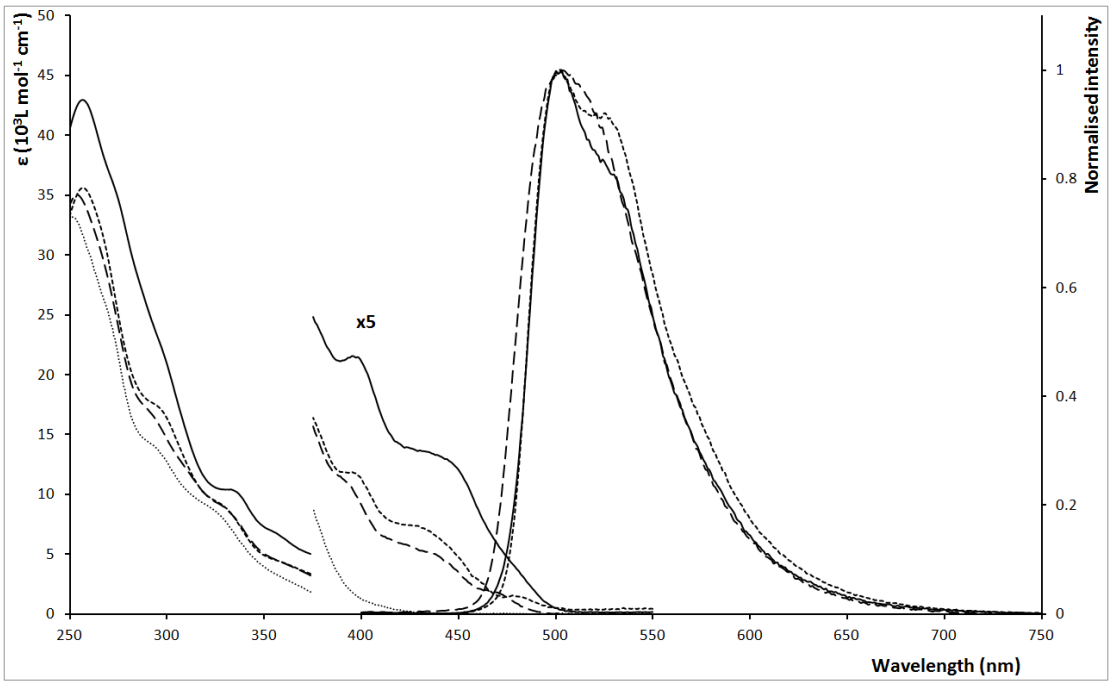

*Figure 3.5: Absorption (left) and emission (right) spectra of **3** (solid line), **6** (small dotted line), **9** (dashed line) and **10** (dotted line) measured in aerated DCM (abs.) and deaerated DCM (em.) solutions.*

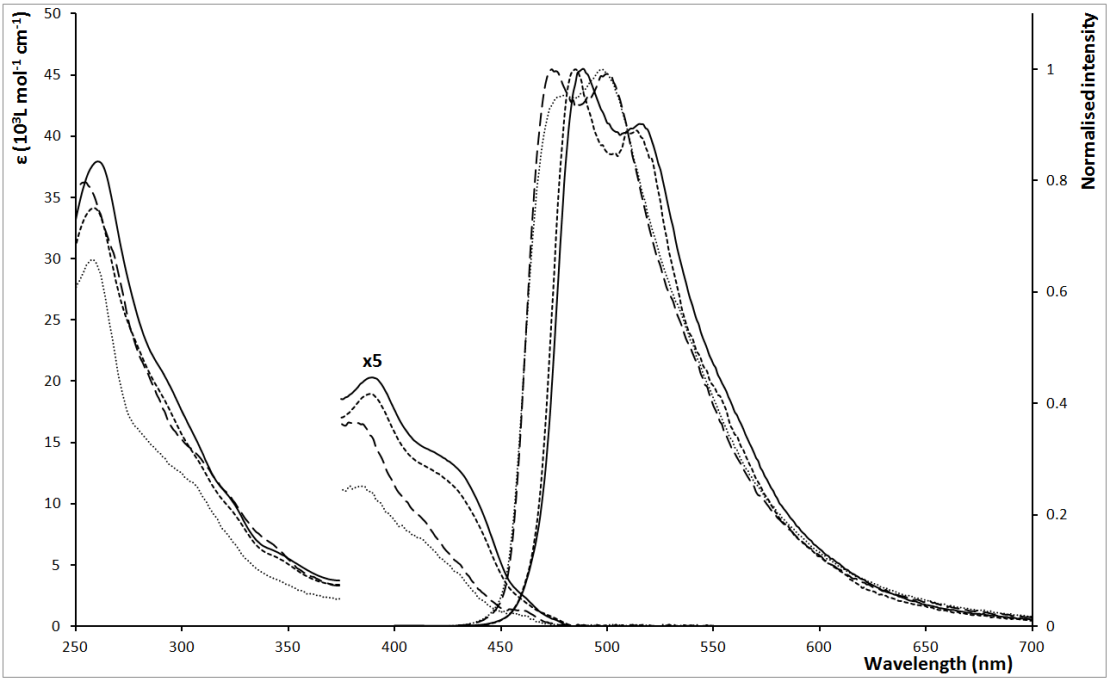

*Figure 3.6: Absorption (left) and emission (right) spectra of **3a** (solid line), **3b** (dotted line), **9a** (dashed line) and **9b** (small dotted line) measured in aerated DCM (abs.) and deaerated DCM (em.) solutions.*

The UV-visible spectra of pic complexes **3a-b** and **9a-b** follow the general trends of similar complexes. The molar absorptivity values of **9a-b** are decreased compared to those of **3a-b** due to the presence of the ppz ligand. Interestingly, the molar absorptivity values of the isomers b are also decreased compared to isomers a without easy explanation. This difference is more pronounced between **9a** and **9b** (with an ε_{max} value difference of 6300 L mol^{-1} cm^{-1}) than between **3a** and **3b** (with an ε_{max} value difference of 3800 L mol^{-1} cm^{-1}). These differences attenuate at higher wavelength and both isomers show similar onset absorptions.

The UV-visible and emission spectra are used to calculate an approximate HOMO-LUMO energy gap as the $E_{0\text{-}0}$ energy.[59,142] Converted into eV and normalised, the intersection of the spectra gives a good approximation of the $E_{0\text{-}0}$ energy (the energy separating the most stable excited state from the ground state). Therefore, this value is added to the previously calculated HOMO energy to find an approximate optical LUMO energy. These values follow the trends

observed with the reduction potentials but present the advantage of providing data when the reduction potential is not available (e.g. ppz complexes) or difficult to calculate due to a low reversibility of the reduction peak.

The emission profiles of the tris-heteroleptic complexes follow the trend of the oxidation potentials and strongly denote ppy based LUMO made of pyridine π^* orbitals. The emission maxima follow the ones of the corresponding bis-ppy complexes (Table 3.2). Therefore, complexes **1** and **7** or **2** and **8** display maxima at respectively 519 and 482/483 nm according to the number of fluorinated phenyl they carry. The same observation is made for **9** (503 nm) and **10** (502 nm) that both show emission maxima close to the one of **3** (503 nm).

The presence of the ppz ligand causes a slight broadening of the emission profile with FWHM values typically increased by 200 – 300 cm^{-1}. All tris-heteroleptic complexes with mixed ppy-ppz ligands experience this broadening compared to their all-ppy counterparts. Fluorination seem to slightly increase this effect, as **8** shows a difference of 30 1 cm^{-1} with **2,** while the difference between **7** and **1** is only 232 cm^{-1}. Even though they both display bigger FWHM values than **3**, the FWHM value of **9** is larger than the one of **10** by an additional 97 cm^{-1}, due to the broadening observed in the high energy part of its spectrum.

The emission spectra of **3a-b** and **9a-b** show blue shifted emission profiles compared to the acac complexes with emission maxima at 498/485 nm (**3a/3b**) and 499/498 (**9a/9b**). This is coherent with the stabilised HOMO and increased $E_{0\text{-}0}$ energies calculated for these complexes compared to their corresponding acac complexes. This is also coherent with observations made on the sky-blue emitter [$Ir(dFppy)_2(pic)$] (FIrpic) and other pic complexes.[38,59]

The emission profile broadness of pic complexes follows the trends observed for their corresponding acac complexes with an increase of the FWHM values induced by the introduction of the ppz ligand. It seems, however, that the presence of the pic ligand induces a further FWHM increase of around 200 and 350 cm^{-1} for **3a-b** and **9a-b** compared to **3** and **9** respectively. However, no coherent broadening is observed between isomers and **3a-b** show a slight 80 cm^{-1} FWHM decrease while **9a-b** show a small 69 cm^{-1} increase.

*Table 3.2: Photophysical properties of complexes **1** to **10** and **3a**, **3b**, **9a** and **9b**.*

	λ_{abs} (nm), (ε (10^3L mol^{-1} cm^{-1}))[a]	λ_{max} (nm), RT[b]	$E_{0\text{-}0}$ (eV)	HOMO (eV)	LUMO (eV)	FWHM (cm^{-1})
1	260 (39.15), 340 (9.15), 405 (4.02), 459 (2.88), 489 (1.32)	519 (520)[c]	2.58	-5.23	-2.65	2487
2	253 (45.72), 328 (11.44), 389 (4.72), 435 (2.23), 466 (0.82)	482 (484)[c]	2.74	-5.53	-2.79	2525
3	256 (42.97), 334 (10.34), 398 (4.29), 449 (2.44), 479 (0.79)	503 (503)[c]	2.65	-5.38	-2.73	2526
4	252 (34.04), 275 (23.69), 297 (15.15), 330 (8.57), 377 (2.77), 418 (0.19)	-	-	-5.29	-	-
5	253 (31.19), 321 (8.06), 359 (2.23), 400 (0.29)	-	-	-5.59	-	-
6	251 (33.18), 269 (25.53), 294 (13.89), 325 (8.61), 370 (2.21), 408 (0.15)	-	-	-5.44	-	-
7	256 (36.36), 295 (17.76), 335 (8.81), 374 (4.14), 405 (2.35), 456 (1.27), 487 (0.38)	519	2.61	-5.25	-2.64	2719
8	253 (40.40), 289 (18.86), 325 (10.349), 361 (3.95), 385 (2.52), 430 (0.95), 461 (0.31)	483	2.78	-5.55	-2.77	2826
9	254 (35.00), 291 (16.91), 330 (8.85), 369 (3.63), 392 (2.21), 437 (1.01), 469 (0.37)	503	2.72	-5.41	-2.69	2826
10	257 (35.63), 295 (17.39), 328 (9.17), 360 (4.28), 396 (2.36), 430 (1.46), 478 (0.32)	502	2.67	-5.40	-2.73	2729
3a	261 (37.55), 289 (20.99), 323 (10.15), 345 (5.81), 390 (3.87), 431 (2.33), 462 (0.27)	489	2.73	-5.53	-2.80	2771
3b	259 (32.69), 289 (18.54), 305 (13.67), 322 (9.37), 345 (5.39), 389 (3.66), 430 (2.14), 470 (0.23)	485	2.73	-5.52	-2.79	2691
9a	253 (36.20), 283 (20.92), 303 (14.62), 321 (10.91), 341 (6.86), 383 (3.28), 415 (1.65), 432 (0.93), 460 (0.24)	499	2.80	-5.56	-2.76	3139
9b	258 (31.18), 281 (16.35), 302 (12.57), 322 (7.66), 341 (4.18), 384 (2.34), 414 (1.42), 431 (0.84), 458 (0.19)	498	2.80	-5.53	-2.73	3208

[a]aerated DCM, [b]deaerated DCM, [c]according to literature,[61] the emission spectra were recorded with excitation wavelength of 350 nm. $E_{0\text{-}0}$ was calculated as the crossing of the normalised absorption and emission spectra expressed on an energy scale, HOMO = - (E_{ox} + 4.8eV), LUMO = HOMO + $E_{0\text{-}0}$.

3.2.3 Excited state lifetimes and quantum yields

The luminescence lifetime measurement was performed in solution using DCM as solvent. The solution was deaerated by bubbling argon for 40 minutes to remove a maximum of the oxygen. Due to the low boiling point of the solvent used, the concentration was not determined precisely.

The quantum yield (Φ_{PL}) measurements were performed on DCM solutions deaerated by freeze-pump-thaw cycles and calculated using quinine sulphate as a reference (in aqueous H_2SO_4 0.5M: $\Phi_{PL} = 0.546$).[143–146]

From the quantum yield, the radiative (k_r) and non radiative (k_{nr}) constants are calculated assuming unitary intersystem crossing.

Excited state lifetimes measured for complexes **1** to **3** show similar results than previously reported in literature.[61] In comparison with these values, quantum yields for complexes **7** to **10** are lowered by approximately a factor of two. Therefore, the radiative constants are significantly lowered as well. Complexes **7** and **8** show lifetime values in agreement with their number of fluorine substituents as they display similar values than **1** and **2** respectively. However, the significantly lowered quantum yield of **7** in comparison with **1** is pointing towards a less efficient emission, influenced by less efficient radiative (decrease of k_r) deactivation.

In the case of **8**, the reduced lifetime and quantum yields compared to **2** also lead to a decreased radiative constant. More importantly, results show a drastic increase of the non radiative constant. Therefore, unlike **2**, the low lifetime of **8** is explained by favoured non radiative processes.

*Table 3.3: Photophysical data measured on complexes **1** to **10** and **3a**, **3b**, **9a** and **9b**.*

	τ (ns), RT[a]	Φ_{PL} [a]	k_r (10^5 s^{-1})	k_{nr} (10^5 s^{-1})
1	1511 (1227)[b]	0.47[b]	3.83	4.32
2	898 (872)[b]	0.63[b]	7.22	4.24
3	1413 (1224)[b]	0.69[b]	5.64	2.53
7	1592	0.26	1.63	4.65
8	619	0.22	3.55	12.60
9	837	0.32	3.82	8.12
10	1575	0.30	1.90	4.44
3a	1850	0.49	2.65	2.76
3b	1559	0.43	2.76	3.66
9a	1004	0.42	4.18	5.78
9b	971	0.38	3.91	6.39

[a]deaerated DCM, [b]according to literature,[61] $k_r = \Phi_{PL} / \tau$, $k_{nr} = (1 - \Phi_{PL}) / \tau$.

Complexes **9** and **10** share similar structural properties, as they both have one pyridine and one fluorinated ligand. They also share quasi identical oxidation potential, emission maxima and quantum yield. Their emission profiles are similar and so are their absorption profiles. In these conditions, one would expect the two complexes to share similar excited state lifetime values as well. But **9** has a much lower value than **10** (837 vs 1537 ns). This unexpected result highlights the possibility of obtaining complexes with similar overall properties but differing only by one photophysical parameter, allowing a fine tuning of photophysical properties.

3.3 Second series: complexes with methoxylated ligands

3.3.1 Cyclic voltammetry

Cyclic voltammograms of complexes **11** to **19** were recorded vs Fc^{+}/Fc with all platinum electrodes. However, due to the poor solubility of some complexes, the MeCN had to be replaced with DMF. This change does not affect the data obtained and the redox potentials can still be compared with the data from the 1st series.

The cyclic voltammograms of these complexes (Figure 3.7) are characterised by oxidation peaks with decreased reversibility, causing a lowering of the cathodic current peak. This effect is already observed bis-heteroleptic complexes **11** to **13** but becomes more important for tris-heteroleptic complexes **14** to **19**.

Reduction profiles of complexes **11** to **13** also show low reversibility and only the cathodic potentials are reported (Table 3.4) for **12** and **13**. Nevertheless the signal is pushed to more negative values as the LUMO is becoming increasingly destabilised by the influence of the methyl (**12**) and methoxy substituents (**13**, a schematic view of HOMO-LUMO energies is presented in Figure 3.8).

This destabilisation translates into increasing $E_{0\text{-}0}$ energies going from 2.69 to 2.75 eV which in turns translates into increasing calculated LUMO energies going from -2.51 to -2.38 eV.

These $E_{0\text{-}0}$ values are very close to the one calculated for **2** which are what is expected with MeO substituents, as they provide a HOMO-LUMO energy gap similar to fluorine.

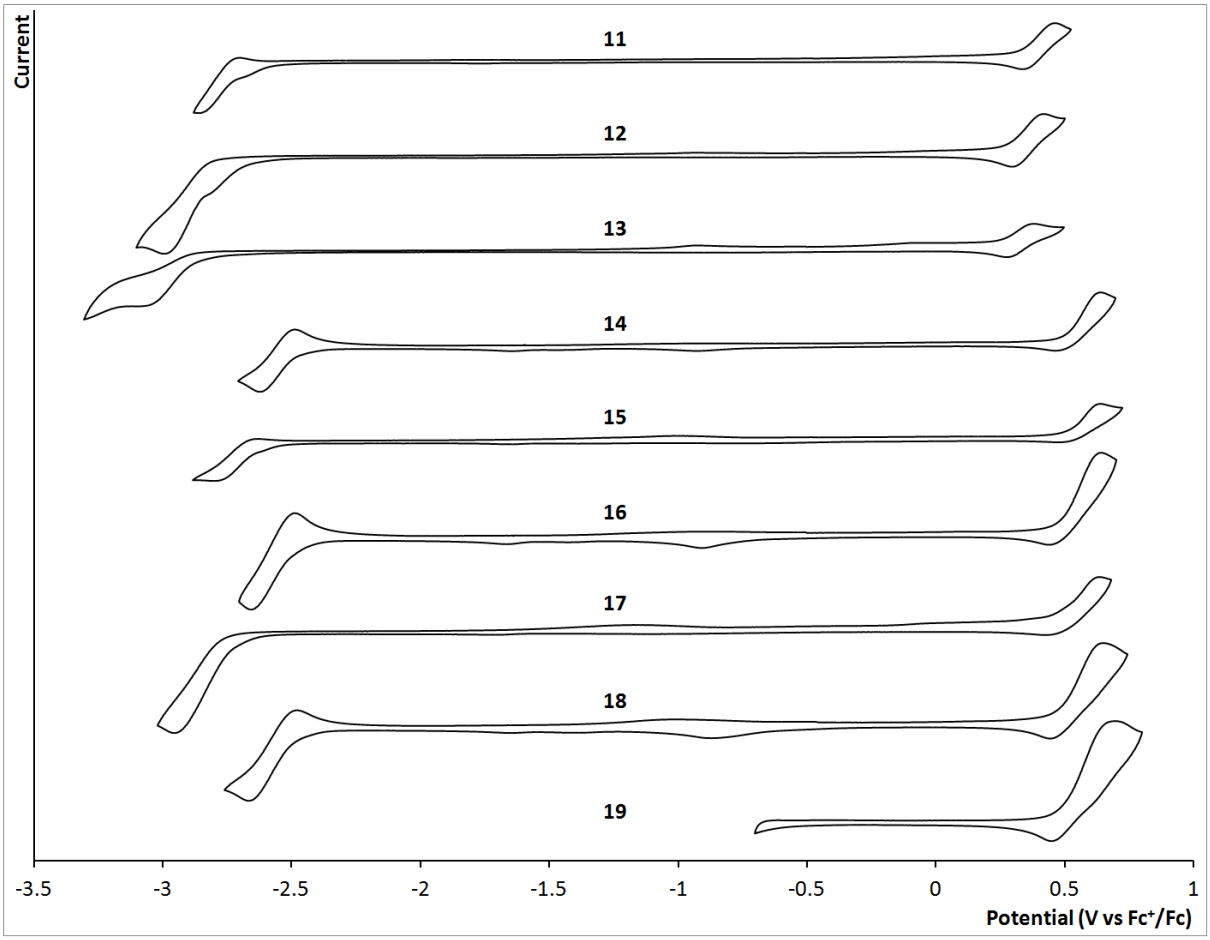

*Figure 3.7: Cyclic voltammograms of **11** to **19** (top to bottom), measured in DMF (0.1 M $TBAPF_6$) vs Fc^+/Fc at 1 V/s scan rate.*

The effect of the methyl/methoxy substituent on the oxidation potential is less striking. The oxidation potential of **12** is reduced by 0.04 V compared to the one of **11**, in agreement with Hammett parameter analysis predicting a slight destabilising effect of the methyl group on the meta position (here: on the phenyl ring, on the HOMO).[147,148] On the other hand, the oxidation potential of **13** is decreased by 0.07 V compared to the one of **11**, suggesting a HOMO destabilisation which goes against the predictions based on Hammett parameters for methoxy substituents. When looking at the oxidation potentials of complexes **14** to **19**, no significant effect or trend can be detected according to these effects.

*Table 3.4: Redox potential and photophysical data measured on complexes **2**, **5** and **11** to **19***

	E_{ox} (V)	E_{red} (V)	$E_{0\text{-}0}$ (eV)	HOMO (eV)	LUMO (eV)
2	0.73[a]	-2.45[a]	2.74	-5.53	-2.79
5	0.79[a]	-	-	-5.59	-
11	0.40 (0.42)[b]	-2.78	2.69	-5.20	-2.51
12	0.36	-3.04[c]	2.71	-5.16	-2.45
13	0.33	-3.10[c]	2.75	-5.13	-2.38
14	0.55	-2.56	2.68	-5.35	-2.67
15	0.56	-2.72	2.74	-5.36	-2.62
16	0.54	-2.58	2.67	-5.34	-2.67
17	0.54	-3.02[c]	2.81	-5.34	-2.53
18	0.54	-2.58	2.67	-5.34	-2.67
19	0.57	-	2.83	-5.37	-2.54

Redox potentials measured in DMF (0.1 M $TBAPF_6$) vs Fc^+/Fc, [a]measured in MeCN, [b]according to literature,[147] [c]cathodic peak only, $E_{0\text{-}0}$ was calculated as the crossing of the normalised absorption and emission spectra expressed on an energy scale, HOMO = - (E_{ox} + 4.8) eV, LUMO = HOMO + $E_{0\text{-}0}$.

This is expectable considering the relatively high distance separating the pyridine-4 position from the M-C bond.

Generally speaking, the oxidation potentials of the tris-heteroleptic complexes are all comprised between 0.54 and 0.57 V which corresponds roughly to the average oxidation potential between the bis-dMeOppy and the bis-dFppy/dFppz complexes.

This is coherent with HOMO orbitals being delocalised over the d orbitals of the iridium centre and π orbitals of the phenyl rings of both ligands.

Reduction profiles of complexes **14**, **16** and **18** exhibit the quasi reversible peaks of bis-dFppy complex (**2**) but with a shift towards more negative voltage of around 0.12 V.

According to the model considered here, HOMOs of these complexes are expected to be destabilised compared to the HOMO of **2,** due to the lower withdrawing influence of the methoxy substituents in comparison with the fluorines (this point fits with the oxidation potential values). On the other hand, the LUMO orbital of such tris-heteroleptic complexes is

expected to be located on the pyridine ring providing the most stable π^* orbitals. In other words, the LUMO is expected to be located solely on the dFppy pyridine. Therefore, the $E_{0\text{-}0}$ energy should be decreased and the reduction potential and calculated LUMO energy are expected to be close to the values obtained for **2**. Surprisingly, stable reduction potentials (-2.56/-2.58 V) and LUMO energies of (-2.68/-2.67 eV) are observed instead, which are significantly lower/higher than the values of **2** (-2.45 V/-2.79 eV). It seems that the LUMO energies reach a compromise value in between the energies of the two ligands.

Similarly to complexes **14**, **16** and **18**, the oxidation potentials obtained for complexes **15**, **17** and **19** are very close. A small variation ±0.01 V is observed around the value of **15**. The potential is increased for **17** and decreased for **19**. Even if these changes fit the model of HOMO destabilisation/stabilisation by the pyridine methyl/methoxy substituents, they are of very low magnitude and could as well be due to measurement uncertainties.

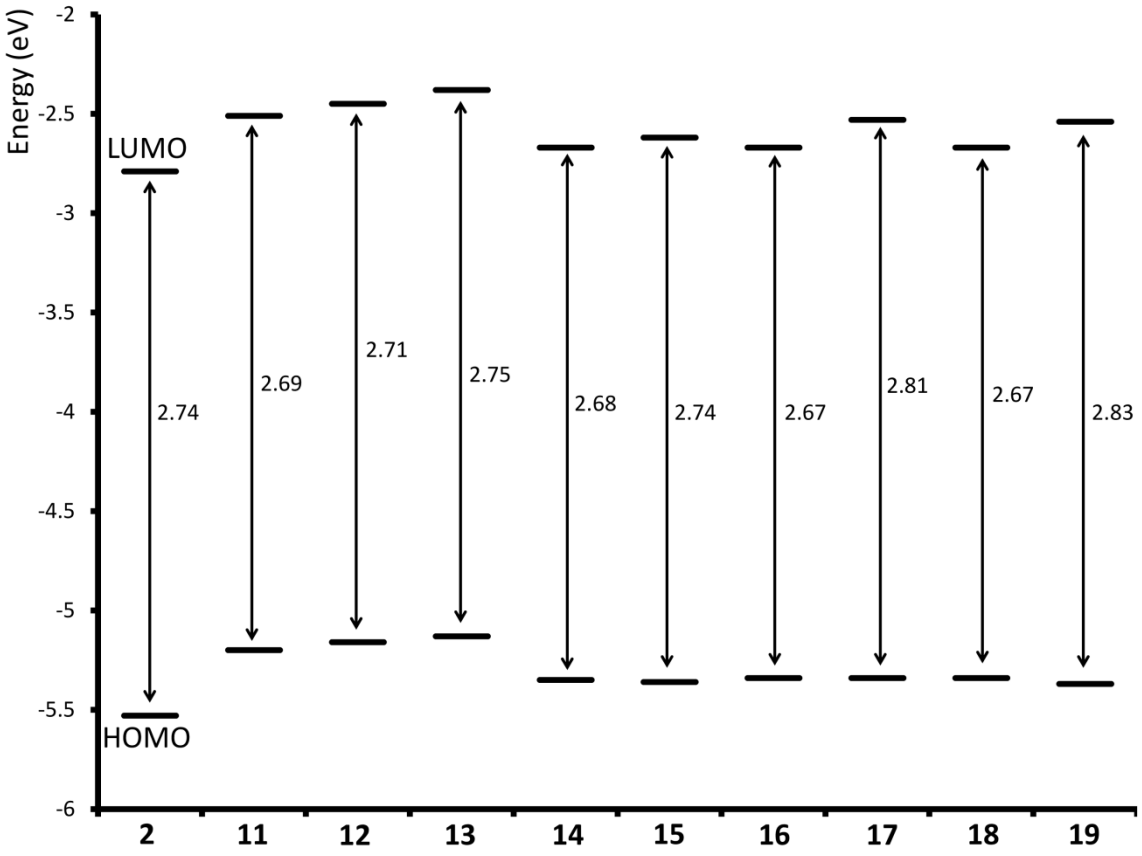

*Figure 3.8: Representation of HOMO-LUMO energy levels and optical energy gaps $E_{0\text{-}0}$ for complexes **2** and **11** to **19**.*

The reduction curves of these complexes show a decrease in the reversibility, coupled to a decrease in the peaks potential. Therefore, the reduction potential of **19** is not detectable with the conditions used.

Due to low reversibility or low measurability, it is not possible to rely on reduction potentials, for the present discussion. However, as these complexes are luminescent at room temperature (unlike **4**, **5** and **6**), their $E_{0\text{-}0}$ and calculated LUMO values offer a good alternative.

In this regard, $E_{0\text{-}0}$ energies of **15** (2.74 eV), **17** (2.81 eV) and **19** (2.83 eV) are gradually increased. This is coherent with the increasing LUMO destabilisation induced by the methyl and methoxy influences. Therefore, because of the large $E_{0\text{-}0}$ difference, the LUMO energy of **17** (-2.52 eV) is significantly higher than the one of **15** (-2.63 eV). Due to the higher oxidation

potential measured for **19** and despites a larger E_{0-0} energy, the calculated LUMO energy of **19** (-2.54 eV) is very close to the one of **17**. These values are found to be significantly stabilised (by respectively -0.11, -0.08 and -0.16 eV) compared to the calculated LUMO energies obtained for the corresponding bis-heteroleptic complexes **11**, **12** and **13**.

In the first series, the LUMO energy trends are following the number of fluorine substituents with little influence from the nature of the second heterocycle and its location around the iridium centre.

In the second series, this behaviour seems to be repeated. DFppy complexes (**14**, **16** and **18**) can then be understood as bearing a dFppy based LUMO which is destabilised to an extent by the presence of the dimethoxylated phenyl ring of the second ligand. For these complexes, no influence of the second pyridine ring on the LUMO energy is observed.

In the case of dFppz complexes (**15**, **17** and **19**), the LUMO bearing ligand is also the one with the pyridine and as this pyridine is being substituted, a direct influence on the LUMO energy is observed. However, the LUMO energies of these complexes also feel a sort of stabilisation from the difluorinated phenyl ring. Again, the influence of the second aromatic heterocycle (pyrazole) is not observed.

3.3.2 UV-visible and luminescence spectroscopy

UV-visible spectra of complexes **11**, **12** and **13** (Figure 3.9) are characterised by strong bands in the LC region (275 nm, $\varepsilon \approx 35 - 40 \times 10^3$ M^{-1} cm^{-1}) that are red shifted compared to **2**. They also show strong bands around 320 nm ($\varepsilon \approx 26 \times 10^3$ M^{-1} cm^{-1}). In the MLCT region, the profile of **13** is slightly blue shifted compared to **11** and **12**.

The dFppz complexes show systematically lower molar absorptivity values than their dFppy equivalents, as it was already observed for the first series. All complexes show high molar absorptivity values in the 310 to 360 nm region where all complexes (**11** to **19**) show significantly higher molar absorptivity values than **2**.

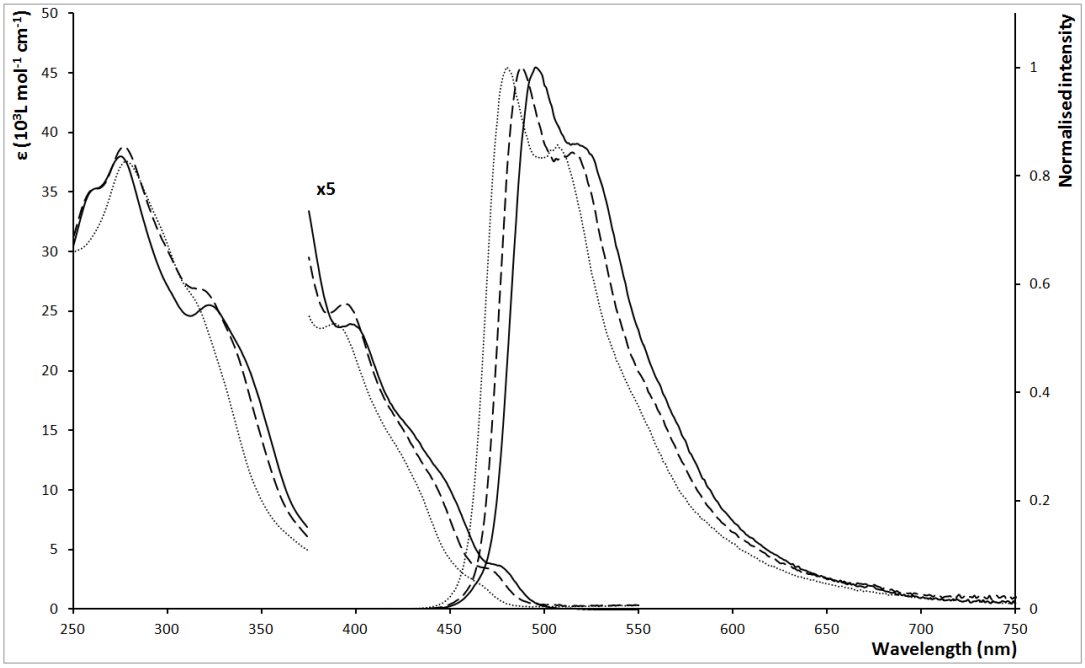

*Figure 3.9: Absorption (left) and emission (right) spectra of **11** (solid line), **12** (dashed line) and **13** (dotted line) measured in aerated DCM (abs.) and deaerated DCM (em.) solutions.*

The luminescence spectra of **11**, **12** and **13** (Figure 3.9) show standard profile shapes for iridium complexes with ppy ligands. Blue shifted emission maxima at 495, 488 and 480 nm

respectively (Table 3.5) are obtained as in agreement with LUMO destabilisation induced by the addition of the methyl and methoxy substituents.

Complexes with dFppy show less structured profiles with very similar onset emissions. Their maxima are measured at 500 (**14**), 504 (**16**) and 509 nm (**18**).

Assuming a LUMO located on the pyridine of the dFppy ligand, and following the Hammett parameter model, an emission red shift should be observed between **14** and **16** due to the meta-directing electron donating properties of the methyl substituent, which slightly destabilise the HOMO. Furthermore, a blue shift should be observed between **14** and **16,** as meta electron withdrawing character of the methoxy substituent is stabilising the HOMO. However, the similar oxidation potential values and onset emission values suggest a negligible influence of the pyridine substituent on the HOMO energy.

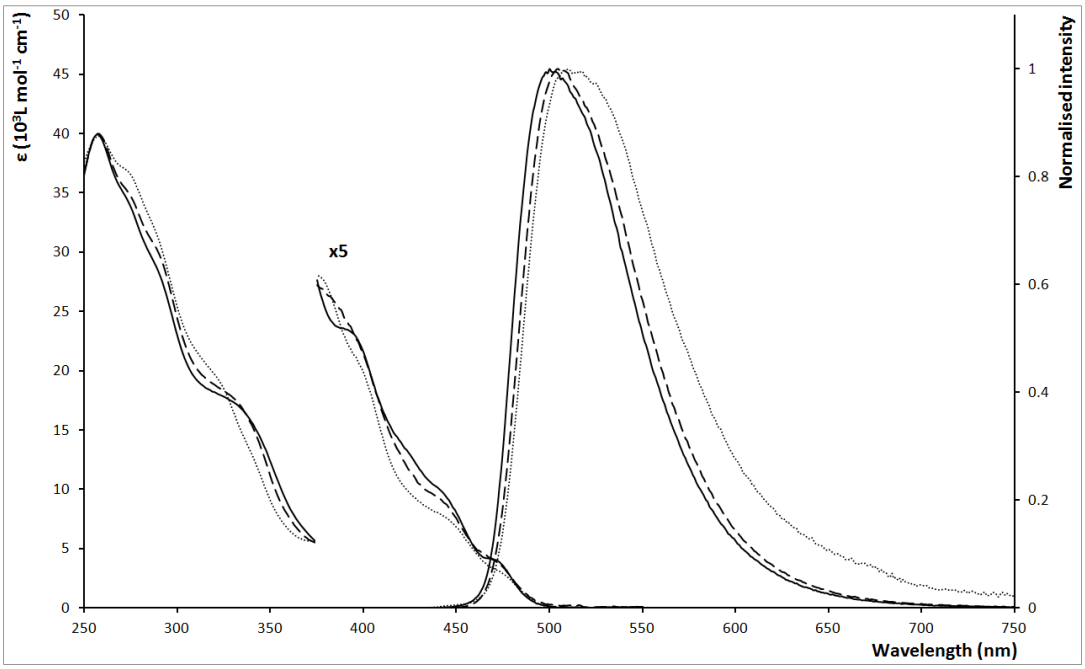

*Figure 3.10: Absorption (left) and emission (right) spectra of **14** (solid line), **16** (dashed line) and **18** (dotted line) measured in aerated DCM (abs.) and deaerated DCM (em.) solutions.*

The reason behind the observed red shift should then be looked for in differences in transitions probabilities between the excited state and vibrational levels of the ground state. The pyridine methoxy substituent seems to influence the spectrum shape by causing a broadening of the entire low energy half of the profile. This effect translates into a FWHM value that is significantly increased for **18** (+291 cm^{-1}) compared to **14** (Table 3.5).

However, the significant red shift observed compared to **2** (around 20 nm) reflects the calculations well and is coherent with a decreased $E_{0\text{-}0}$ energy.

The absence of a significant blue shift also suggests that the LUMO is not directly influenced by the pyridine substituents and is therefore located solely on the dFppy ligand.

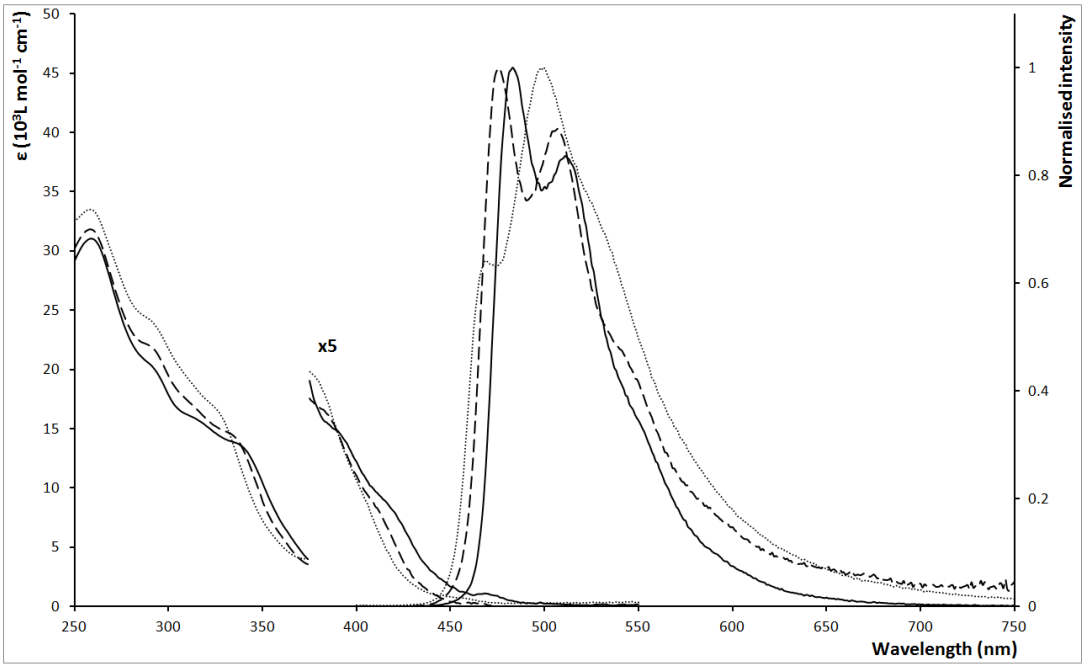

*Figure 3.11: Absorption (left) and emission (right) spectra of **15** (solid line), **17** (dashed line) and **19** (dotted line) measured in aerated DCM (abs.) and deaerated DCM (em.) solutions.*

The emission profiles of complexes **15**, **17** and **19** show an increasingly blue shifted onset emission, as expected in a situation where the HOMO-LUMO energy gap is gradually increased. The emission maxima of **17** is blue shifted by 7 nm compared to the one of **15**,

which is the same blue shift than between the corresponding bis-heteroleptic complexes (**11** and **12**). A new feature of the profiles is the increasing intensity of the second emission peak at 512 and 507 nm. In the case of complex **19**, this peak becomes the major peak and the emission maximum is red shifted to 498 nm. However, the first peak of the emission profile can still be measured at 469 nm. The 14 nm blue shift observed between this peak and the emission maximum of **15** is very close from the 15 nm separating the emission maxima of the bis-heteroleptic complexes **11** and **13**. In other words, the increments in the blue shift of the emission spectra are believed to be caused by the direct influence of the pyridine substituents on the LUMO energy which is located on the pyridine ring.

In this situation, the pyrazole is believed to be only playing a disruptive role on the emission profile. It does not influence the HOMO or LUMO energies directly but still has an influence on the emission spectra by influencing the spectra vibronic progression. Therefore, as the second and third emission bands are gradually increased, the emission profile is broaden with FWHM values increasing form 2425 cm^{-1} (**15**) to 3463 cm^{-1} (**19**).

*Table 3.5: Photophysical data measured on complexes **11** to **19**.*

	λ_{abs} (nm), (ε 10^3 L mol^{-1} cm^{-1})[a]	λ_{em} (nm), RT[b]	τ (ns), RT[b]	Φ_{PL}[b]	k_r (10^5 s^{-1})	k_{nr} (10^5 s^{-1})	FWHM (cm^{-1})
11	260 (37.25), 275 (40.09), 322 (26.49), 339 (21.64), 400 (5.20), 426 (3.03), 445 (2.20), 475 (0.70)	495	997	0.39	3.91	6.12	2641
12	260 (35.17), 277 (38.76), 318 (26.84), 335 (22.19), 395 (5.12), 420 (3.31), 440 (2.22), 470 (0.66)	488	368	0.20	5.43	21.74	2636
13	278 (37.56), 295 (32.47), 314 (26.07), 391 (4.75), 425 (2.65), 433 (2.12), 462 (0.5)	480	93	0.03	3.55	103.98	2641
14	257 (39.91), 270 (35.27), 288 (29.00), 330 (17.36), 390 (4.70), 418 (2.88), 440 (2.02), 470 (0.80),	500	1136	0.35	3.10	5.71	2772
15	259 (31.05), 288 (20.70), 312 (16.03), 336 (13.78), 387 (3.01), 415 (1.78), 439 (0.61), 471 (0.19)	483	682	0.19	2.75	11.91	2425
16	257 (40.03), 273 (35.15), 288 (30.51), 327 (18.08), 383 (5.23), 397 (4.50), 422 (2.50), 440 (1.90), 470 (0.82), 483 (0.38)	504	1053	0.52	4.89	4.60	2686
17	258 (31.80), 290 (21.99), 310 (17.38), 332 (14.65), 358 (6.88), 382 (3.33), 408 (1.98), 464 (0.14)	476	157	0.04	2.61	61.09	2849
18	258 (39.81), 273 (36.94), 287 (32.35), 318 (20.13), 340 (13.05), 376 (5.60), 400 (3.97), 442 (1.57), 473 (0.67)	509	1017	0.52	5.07	4.76	3063
19	258 (33.51), 290 (24.20), 309 (19.50), 325 (16.71), 353 (6.48), 376 (3.98), 400 (2.14), 458 (0.1)	498	43	0.01	1.95	230.61	3463

[a]aerated DCM, [b]deaerated DCM, the emission spectra were recorded with excitation wavelength of 350 nm, $E_{0\text{-}0}$ was calculated as the crossing of the normalised absorption and emission spectra expressed on an energy scale, $E_{HOMO} = -(E_{ox} + 4.8)$ eV, $E_{LUMO} = E_{HOMO} + E_{0\text{-}0}$, $k_r = \Phi_{PL} / \tau$, $k_{nr} = (1 - \Phi_{PL}) / \tau$.

3.3.3 Excited state lifetimes and quantum yields

The excited state lifetimes of the bis-heteroleptic complexes **11** to **13** show a drastic decrease. The initial measured value of 997 ns falls to 368 ns with the addition of the methyl substituent. When the methyl is replaced by a methoxy, the lifetime experiences an additional decrease falls down to 93 ns. These decreased lifetimes are coupled to a significant quantum yield decrease from 0.39 to 0.20 and down to 0.03. This seems to be due to an increase of non radiative deactivation mechanisms, as the radiative constants stay rather small, while the non radiative constants are increased from $6x10^5$ s^{-1} to $22x10^5$ s^{-1} and $104x10^5$ s^{-1}.

The same pattern is observed for the tris-heteroleptic dFppz complexes **15**, **17**, **19** (where the LUMO is believed to be located on the substituted pyridine) with lifetimes of 682, 157 and 43 ns respectively. Here again the quantum yields are decreased from 0.19 to 0.04 and 0.01 while the non radiative constants are significantly increased from $12x10^5$ s^{-1} to $61x10^5$ s^{-1} to $230x10^5$ s^{-1}.

Moreover, the tris-heteroleptic dFppy complexes **14**, **16** and **18** (where the LUMO is believed to be located on the non substituted pyridine of the dFppy ligand) show very close lifetimes with values of 1136, 1053 and 1017 ns. Quantum yields are comprised between 0.35 and 0.52 and the radiative and non radiative constants are stable (between $3x10^5$ and $5x10^5$ s^{-1}).

This observation strongly demonstrates the effect of the direct influence of the increasing LUMO destabilisation by the introduction of donor substituents on the pyridine. When the LUMO is located on the substituted pyridine, an effect is measured. When it is located on the other ligand, no effect is measured.

However, it is believed that the LUMO destabilisation induced by the pyridine methyl and methoxy substituents is not enough to cause these perturbations. Previous studies on

complexes bearing similarly substituted ppy type ligands do not show these tremendous decreases in lifetimes and quantum yields.

Measurements on bis-heteroleptic acac complexes with modified dFppy ligands such as 4-(tert-butyl)-2-(2,4-difluorophenyl)pyridine ($F_2{}^tBuppy$)[149] or 2-(2,4-difluorophenyl)-4-methoxypyridine ($F_2MeOppy$)[150] exhibited blue shifted emission maxima of 477 and 471 nm compared to **2** (482 nm) but did not show any decrease in lifetime and quantum yields (their quantum yields values were 0.89 and 0.60 respectively while the lifetime for the bis-$F_2MeOppy$ complex was measured at 590 ns).

Another study on an acac complex using the methylated ligand 4-methyl-2-phenylpyridine (Meppy)[151] reported a blue shifted emission maximum of 511 nm compared to **1** (519 nm), a quantum yield of 0.51 and a lifetime of 1400 ns. Another study looked at cationic bpy complexes with ppy main ligand and observed significant decrease in quantum yields and excited state lifetimes when the methoxy group was placed on the phenyl-3 instead of phenyl-4 carbon.[152] In this example the LUMO of such a complex is located on the ancillary ligand so the observed perturbation of the photophysical properties is not due to LUMO destabilisation.

In the context of this work, it appears that the increased perturbations are encountered as a result of mixing the 2,4-dimethoxylation of the phenyl and substitution of the pyridine-4 position. 2,4-dimethoxylation alone does not cause these effects (as revealed with **11**) and neither does the substituted pyridine alone. Furthermore, the present work reveals that the perturbation is observed only when other results strongly suggest a direct involvement of the modified pyridine as the LUMO bearer.

An explanation for the drastic decrease in quantum yield is the population of thermally accessible MC state (d-d* transitions). This phenomenon is a well known deactivation

pathway for organometallic complexes[41,44] and for iridium complexes with high LUMO energies such as ppz complexes[45]. It is also observed for complexes with dFppy ligands such as the sky blue emitter FIrpic.[38]

The population of such states would have been made possible by the joint LUMO destabilisation induced by the phenyl and pyridine substituents and would explain the higher performances observed for the dFppy complexes **14**, **16** and **18** where this destabilisation do not matter.

Another possible explanation for the excited state non radiative deactivation is a more favoured vibrational decay mechanism as vibronic coupling between the excited state isoenergetic vibrational states of the ground state is increased. This effect is a long-known source of non radiative decay in luminescent complexes in general and in iridium complexes in particular.[153,154]

This series of complexes **11** to **19** studied the effect of ligands with increasingly destabilised LUMO energies on the properties of tris-heteroleptic iridium complexes. The results show a broadening of the emission profile when the methoxylated ligand is used either with dFppy (FWHM: + 290-420 cm^{-1}) or dFppz (FWHM: + 820-1040 cm^{-1}). The modest increase of FWHM value of the dFppy complexes was not coupled with any photophysical performance decrease, while the large broadening of the dFppz complex goes with significant decreases in quantum yield and excited state lifetime values associated with favoured non radiative deactivation processes.

3.4 Third series: pim complexes

3.4.1 Cyclic voltammetry

The cyclic voltammetry measurements were performed in DMF (0.1 M $TBAPF_6$) with platinum counter and reference electrodes and a glassy carbon working electrode. All measurements were made vs Fc^+/Fc at 1 V/s scan rate.

The oxidation profiles (Figure 3.12) show quasi-reversible oxidation processes. The oxidation potential of the bis-mespim complex (**20**) is measured at 0.25 V (Table 3.6), in range with other iridium complexes bearing phenylimidazole ligands with non substituted phenyl rings.[55,115] Oxidation potentials values of **21**, **22** and **24** are measured close to the average of their respective corresponding bis-heteroleptic complexes (**2**/**20** and **5**/**20** and **20**/**23**).

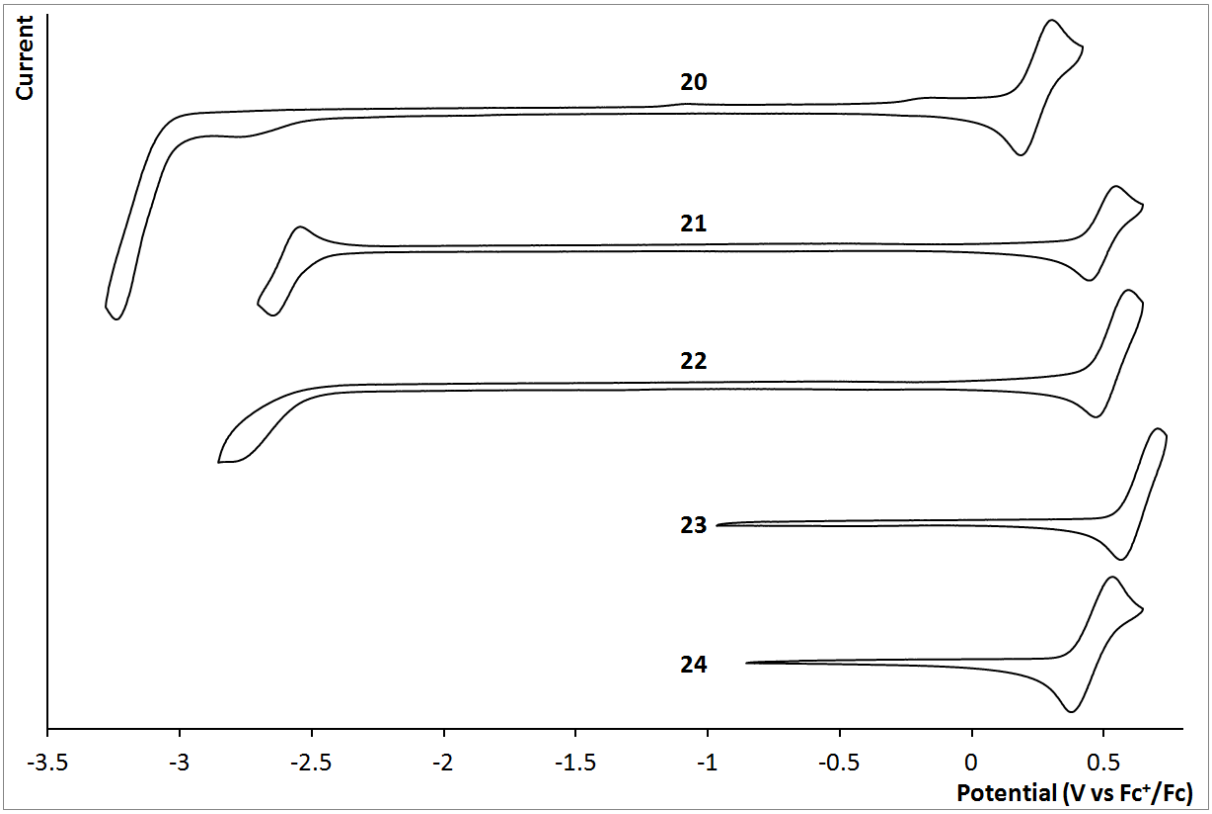

*Figure 3.12: Cyclic voltammograms of **20** to **24** (top to bottom), measured in DMF (0.1 M $TBAPF_6$) vs Fc^+/Fc at 1 V/s scan rate.*

The oxidation potential of **23** is increased by 0.14 V compared to complex **4**. This shift is coherent with the strong electron withdrawing effect of the trifluoromethyl substituent that stabilises both the HOMO and the LUMO.

The reduction potential of **20** is measured as an irreversible current at -3.25 V. The value is in agreement with reported complexes with similar ligands. The replacement of one mespim ligand with a dFppy ligand induces a significant positive shift with the reduction potential of complex **21** being measured at -2.60 V. In addition, the reduction current signal is quasi reversible and the $E_{0\text{-}0}$ value (2.64 eV) is very close to the one calculated for **3** (2.65 eV). These results are coherent with a HOMO located on the iridium centre and phenyl rings of the ligands while the LUMO stays mainly on the pyridine of the dFppy ligand. This situation is similar to what was described for complexes **14**, **16** and **18**.

*Table 3.6: Redox potential and photophysical data measured on complexes **20** to **24**.*

	E_{ox} (V)	E_{red} (V)	$E_{0\text{-}0}$ (eV)	HOMO (eV)	LUMO (eV)
20	0.25	-3.25[a]	2.75	-5.05	-2.30
21	0.50	-2.60	2.64	-5.30	-2.66
22	0.53	-2.80[a]	2.94	-5.33	-2.39
23	0.63	-	-	-5.43	-
24	0.45	-	2.90	-5.25	-2.35

Potentials were measured in DMF (0.1 M $TBAPF_6$) vs Fc^+/Fc, [a]cathodic peak only, $E_{0\text{-}0}$ was calculated as the crossing of the normalised absorption and emission spectra expressed on an energy scale, $E_{HOMO} = -(E_{ox} + 4.8)$ eV, $E_{LUMO} = E_{HOMO} + E_{0\text{-}0}$.

In the same way, observations made on **22** match with the ones made on **19**. As dFppy is replaced with dFppz, the LUMO is transferred to the second ligand and the reduction potential and $E_{0\text{-}0}$ energy are significantly increased but the LUMO energies are stabilised in comparison with the corresponding bis-heteroleptic complex. For **19**, this stabilisation of the LUMO energy is calculated at 0.16 eV (below **13**) while in the case of **22**, the stabilisation is only 0.09 eV (below **20**).

The oxidation potential of **24** is measured at 0.45 V, slightly lower than the one of **22**. This is due to the larger HOMO stabilisation induced by the phenyl 2,4-difluorination compared to the pyrazole trifluoromethyl substituent. The $E_{0\text{-}0}$ values and calculated LUMOs are similar, despites the non measureable reduction potential that suggested a more destabilised LUMO.

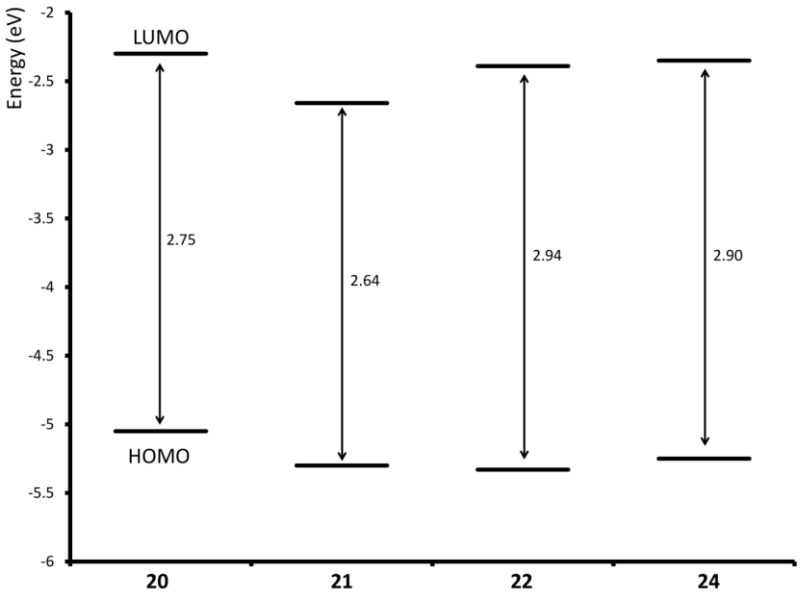

*Figure 3.13: Representation of HOMO-LUMO energy levels and optical energy gaps $E_{0\text{-}0}$ for complexes **20**, **21**, **22** and **24**.*

3.4.2 UV-visible, luminescence spectroscopy and excited state lifetimes

The UV-visible spectra of complexes **20** to **24** are characterised by intense peaks between 248 and 260 nm attributed to LC transitions. The peak of complex **20** is red shifted (260 nm) compared to the other three profiles (peak at 255 nm) and followed by a second marked peak at 268 nm. The profile exhibiting the highest molar absorptivity values is **21** and the lowest epsilons are obtained with **22**. This corresponds to what is expected when replacing dFppy with dFppz. In the MLCT region (300 to 375 nm), the profiles are mixed and if some peaks are distinguishable, the overall epsilon values are similar for **20**, **21** and **24** while the absorptivity of **22** is lowered. It is interesting to note the increased absorptivity of the CF_3ppz ligand (**24**) compared to the dFppz ligand (**22**) over the entire spectrum.

The low absorptivity region (425 to 500) is marked by the higher epsilon values of **21** over the other complexes. Its onset absorption appears at a significantly lower energy (500 nm) than for the other complexes of the series: **20** (475 nm), **24** (440 nm) and **22** (430 nm). These increased and decreased molar absorptivities of the dFppy and dFppz complexes are in agreement with observations of the first and second series.

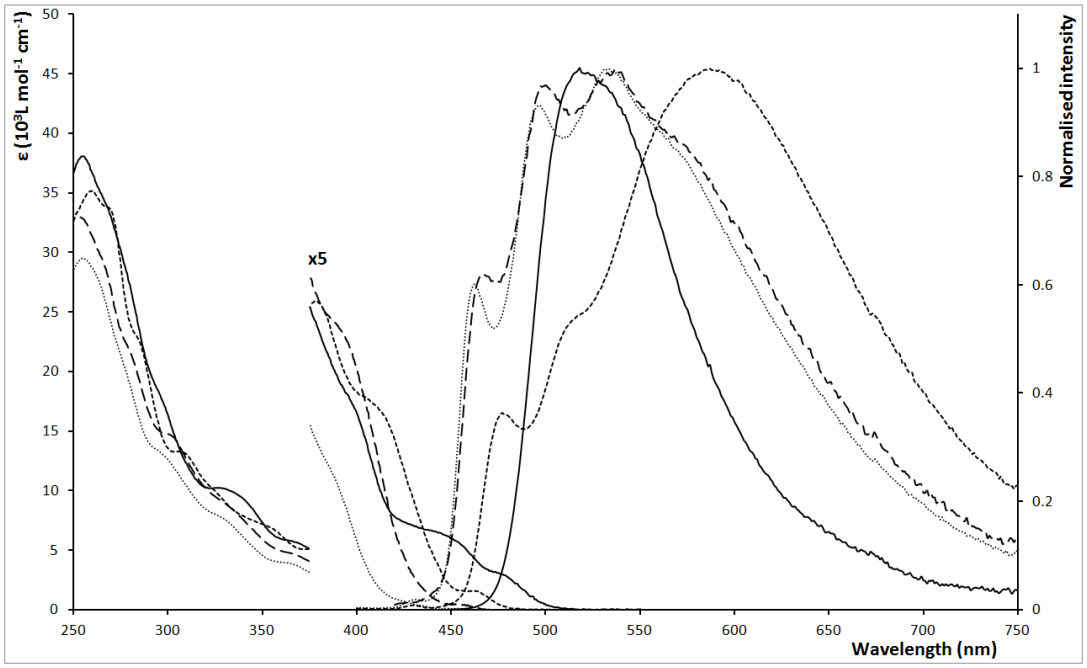

*Figure 3.14: Absorption (left) and emission (right) spectra of **20** (small dashed line), **21** (solid line), **22** (dotted line) and **24** (dashed line) measured in aerated DCM (abs.) and deaerated DCM (em.) solutions.*

The emission spectrum of complex **20** (in DCM) is defined by broad partly structured profile with three visible main peaks at 477, 515 and 587 nm with the emission maximum appearing at 587 nm (Table 3.7). The profile is very similar in shape to what was measured for the white emitting complex N966 that exhibited a maximum intensity at 570 nm.[115] The radiative lifetime is measured at 36 ns. This significantly shorter than the 1.96 µs measured for N966. Short lifetimes have been reported for all complexes of the series except **21**, suggesting that non radiative deactivation pathways are favoured.

The replacement of one mespim ligand by a dFppz or CF_3ppz ligand (**22** and **24**) caused a large broadening of the spectrum by increasing the intensity of the low wavelength peaks. The areas where the maximum intensity of **20** was recorded also show a decreased intensity for both **22** and **24** and the broad signal is replaced by a shoulder at 570 nm. The emission

maximum is now measured at 533 and 537 nm on a peak that was absent from the spectrum of **20**.

Due to the significantly more intense signal arising from the high energy part of the spectra, the FWHM values for **22** and **24** are calculated at 5933 and 5991 cm^{-1}. They are increased by roughly 910 and 970 cm^{-1} compared to the FWHM of **20**.

*Table 3.7: Photophysical data measured on complexes **20** to **24**.*

	λ_{abs} (nm), (ε 10^3 L mol^{-1} cm^{-1})[a]	λ_{em} (DCM, nm), RT[b]	τ (ns), RT[b]	FWHM (cm^{-1})
20	260 (35.16), 268 (33.79), 284 (22.80), 307 (13.27), 325 (9.95), 353 (6.99), 379 (5.18), 411 (3.40), 463 (0.32)	587	36	5022
21	255 (38.05), 268 (33.75), 296 (17.94), 327 (10.23), 337 (9.64), 364 (5.80), 396 (3.54), 440 (1.32), 474 (0.61)	518	1169	3072
22	255 (29.52), 274 (21.77), 296 (13.21), 326 (7.94), 362 (3.95), 387 (2.29), 420 (0.19)	533	28	5933
23	243 (31.21), 251 (30.92), 268 (22.81), 277 (20.61), 296 (13.36), 320 (9.47), 377 (3.06), 419 (0.16)	-	-	-
24	248 (32.62), 254 (32.90), 266 (29.09), 279 (21.89), 300 (14.74), 328 (98.15), 364 (4.77), 392 (3.37), 430 (0.38)	537	10	5991

[a]aerated DCM, [b]deaerated DCM, the emission spectra were recorded with an excitation wavelength of 380 nm, Lifetimes were measured at the λ_{max} of emission and no differences were observed with lifetimes measured at shoulder peaks.

By comparison, the replacement of a mespim ligand by a dFppy ligand is narrowing the emission profile and the FWHM is decreased by 1950 cm^{-1}. It is interesting to note that emission profiles from complexes **18** and **21** are very similar (Figure 3.15) due to close photophysical properties such as FWHM (3063 vs 3072 cm^{-1}), lifetime (1017 vs 1169 ns), emission maxima (509 vs 518) and $E_{0\text{-}0}$ energies (2.67 vs 2.64 eV).

This underlines the important role played by the dFppy ligand in the emission process of both complexes. The structure of the second ligand does not matter too much as long as the orbitals of its heteroaromatic ring are higher in energy than the pyridine π^*-orbitals of the dFppy. In

this situation, the second ligand is only responsible for a slight increase of the vibronic progression (inducing a small broadening of the emission profile in comparison to all-ppy complexes) and for a shift in the HOMO-LUMO energy gap (therefore in $E_{0\text{-}0}$ energies and emission maxima) mainly through stabilisation/destabilisation of its phenyl π-orbitals that participate in the HOMO.

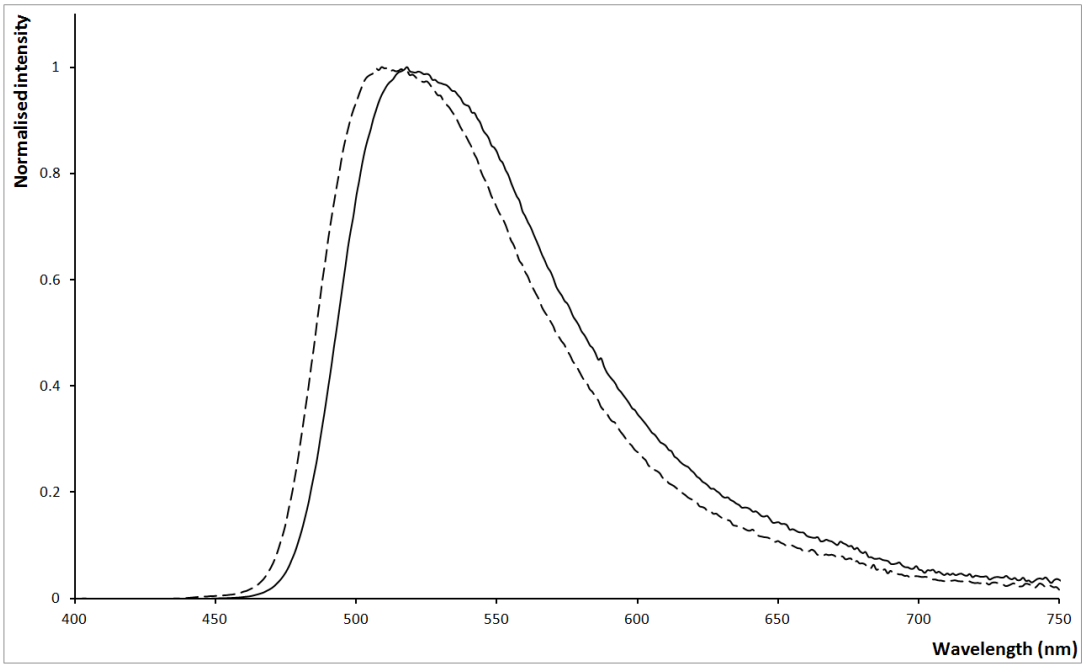

*Figure 3.15: Emission spectra of, **18** (dashed line) and **21** (solid line) measured in deaerated DCM.*

Additionally, observation of the emission profiles of **19** and **22** emphasises the important role played by dFppz in broadening the emission profiles. The FWHM values of these complexes are significantly increased by respectively 822 and 911 cm^{-1} (compared to the FWHM of the corresponding bis-heteroleptic complexes **13** and **20**).

In both cases, the first emission peaks are blue shifted due to the stabilising effect of the 2,4-difluorination on the HOMO energy. The first emission peak is then shifted from 476 to 469 nm between **13** and **19** and from 477 to 462 nm between **20** and **22**.

In **19**, the presence of dFppz induced an increase of the low energy peaks of the emission spectrum and an emission maximum shift from the first to the second peak. The high energy, more structured peaks are assigned to ligand centred (^{3}LC) transitions and the lower energy, broader peaks are assigned to charge transfer (^{3}MLCT) transitions.[155,156] Therefore, the change in emission profiles can be understood by a change in the nature of the excited state containing more or less of the LC/MLCT characters.

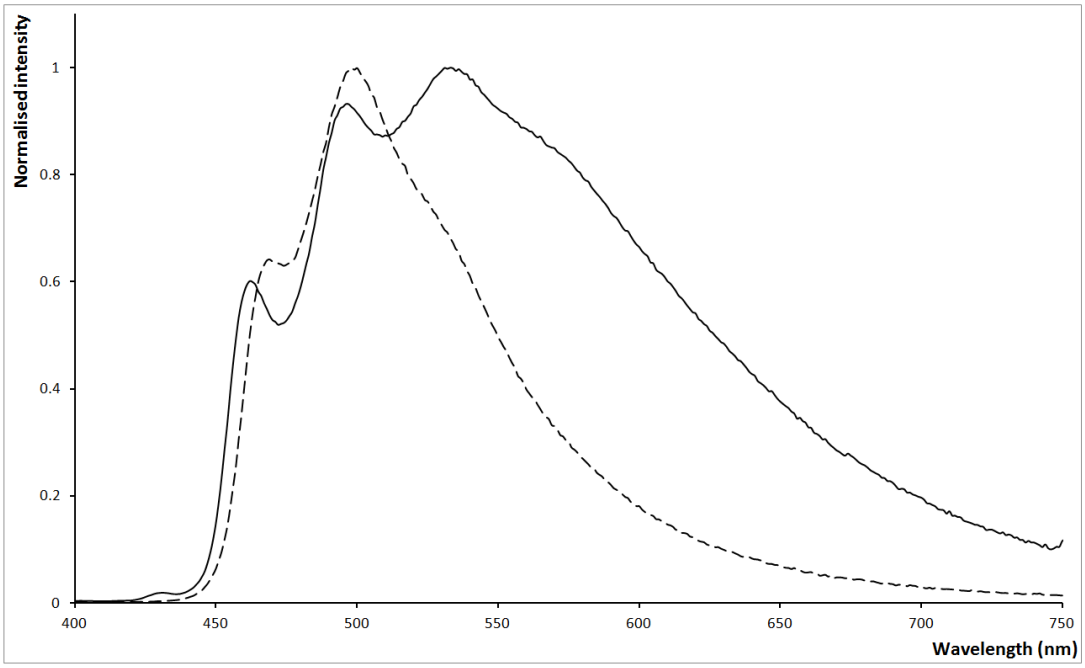

*Figure 3.16: Emission spectra of, **19** (dashed line) and **22** (solid line) measured in deaerated DCM.*

The situation is inverted for **20** and **22** as the low energy part of the spectrum becomes less intense when dFppz replaces one mespim ligand. The emission maximum is significantly blue shifted from 587 to 533 nm.

In order to estimate these changes, the emission profiles have been fitted with Gaussian curves (Figure 9.26 to Figure 9.29). Even though the results presented below (Table 3.8) are

very basic and qualitative, they provide a good comparative tool to observe changes between the spectra.

*Table 3.8: Result of the Gaussian fitting for the emission spectra of **13**, **19**, **20** and **22**.*

	Gaussian	max (eV)	intensity	broadness index.
13	1	2.60	0.80	0.051
	2	2.46	0.61	0.075
	3	2.33	0.28	0.113
	4	2.24	0.12	0.245
19	1	2.66	0.45	0.042
	2	2.52	0.45	0.067
	3	2.40	0.58	0.135
	4	2.23	0.19	0.227
20	1	2.61	0.32	0.052
	2	2.45	0.27	0.067
	3	2.26	0.45	0.140
	4	2.07	0.62	0.161
	5	1.85	0.30	0.207
22	1	2.68	0.56	0.048
	2	2.53	0.64	0.063
	3	2.37	0.64	0.098
	4	2.18	0.40	0.126
	5	2.05	0.40	0.228

The emission spectra of **13** and **19** are fitted using 4 Gaussians. The blue shift discussed above is observed with the Gaussians as the three first curves are calculated with blue shifted maximum intensities in **19** (higher energies). However, it also reveals a significant intensity decrease in the high energy curves (1 & 2) falling from 0.8 and 0.61 to 0.45 (on the normalised intensity scale). Therefore, this shows that the apparent increase of the second peak on the emission spectrum of **19** is probably not due to more intense high energy transitions with LC character but to the increase of the lower energy transitions of increased CT character represented by Gaussians 3 and 4.

The emission profile of complexes **20** and **22** was simulated using five Gaussian curves. The result confirms the effect suspected above. The emission of **20** is dominated by a broad Gaussian centred in the lower energy region of the spectra (2.07 eV) and followed in intensity by another broad curve of higher energy (2.26 eV). The two higher energy curves centred at 2.45 and 2.61 eV show only low intensities. The profile of **22** is marked by a significant intensity increase of the three higher energy Gaussians (at 2.37, 2.53 and 2.68 eV) at the expense of the lower energy one (centred at 2.18 eV).

From these results, it is difficult to clearly establish the role played by the dFppz ligand in broadening the emission profile and the exact mechanism taking place. Nonetheless, it is possible to underline a few noteworthy observations.

The broadening of the emission profile is achieved when combining high LUMO ligands with dFppz. Results from the first and second series show only a small increase in FWHM values except when a more destabilised LUMO is introduced by using the dMeOMeOppy ligand. This result is confirmed in the third series where the replacement of dFppz by dFppy leads to a drop in FWHM value.

The shape of the emission spectra suggests that the electron transfer associated with light emission arises from the other main ligand (mespim or dMeOMeOppy). The dFppz ligand plays a role in favouring/disfavouring some transitions probably by stabilisation/destabilisation of the LC/MLCT exited states.

The photophysical properties obtained for bis-heteroleptic complexes **13** and **20** indicates that the introduction of a dFppz ligand is not responsible for the low emission lifetime and quantum yields. These properties are inherent to the mespim and dMeOMeOppy ligands used. However, the presence of a dFppz ligand only makes things worse by introducing more non

radiative deactivation pathways, especially in complexes with increased HOMO-LUMO energy gaps.[157] The increase of the FWHM value is then achieved at the expense of the emission intensity.

3.4.3 Different solvents

The emission spectra were measured in different media as a way to test the consistency of the emission profile in different environments.

The first tests were performed on **22** to test the influence of solvent polarity on the emission profile. If the polarity of the solvent is increased, a red shift in the emission maximum is expected, due to the enhanced stabilisation of the excited state in polar solvents.[158–160] For the mixed LC/MLCT excited states of interest here, an increased polarity would accommodate the CT character more than the LC as it is more polar.[155]

Tests were performed in DCM/hexane (50/50) mixture for a lower polarity solvent (pure hexane was not suitable because of the low solubility of most complexes in this solvent), in MeCN for a higher polarity solvent and in CCl_4 for a low polarity halogenated solvent. In order to test solid state emission in thin films, pmma solutions were prepared and deposited on quartz plates (the films were prepared to contain 5-10 % of complex).

The results (Figure 3.17) show almost no changes in emission profile shape between DCM and MeCN. The DCM/hexane profile displays a slight decrease in the low energy transitions but it is rather small.

The pmma thin film emission exhibits a significant loss of low energy intensity and presents a more structured profile with a maximum of emission blue shifted by 38 nm. This suggests an increase of the LC character of the excited state probably due to the rigidity of the matrix. This effect is expected as the geometry changes and vibrations induced by the more polar

MLCT states are restricted by the rigidity of the matrix. Therefore, the LC transitions are favoured. Even if such effects are expected, their amplitude in the present context is surprising, especially when considering the almost unchanged profile of the N966 complex in thin films. Here, the loss of the low energy emission peaks is apparently inherent to the mespim ligand, since the same effect was observed for **20** (em. max. blue shift of 76 nm), **22** and **24** (em. max. blue shift of 40 nm. Figure 3.17 and Figure 3.18 and Table 3.9)

Moreover, the CCl_4 profiles show a quasi total shut down of the high energy transitions associated with a LC character of the excited state. Therefore, the emission maxima of **20**, **22** and **24** are red shifted by respectively 18, 52 and 44 nm.

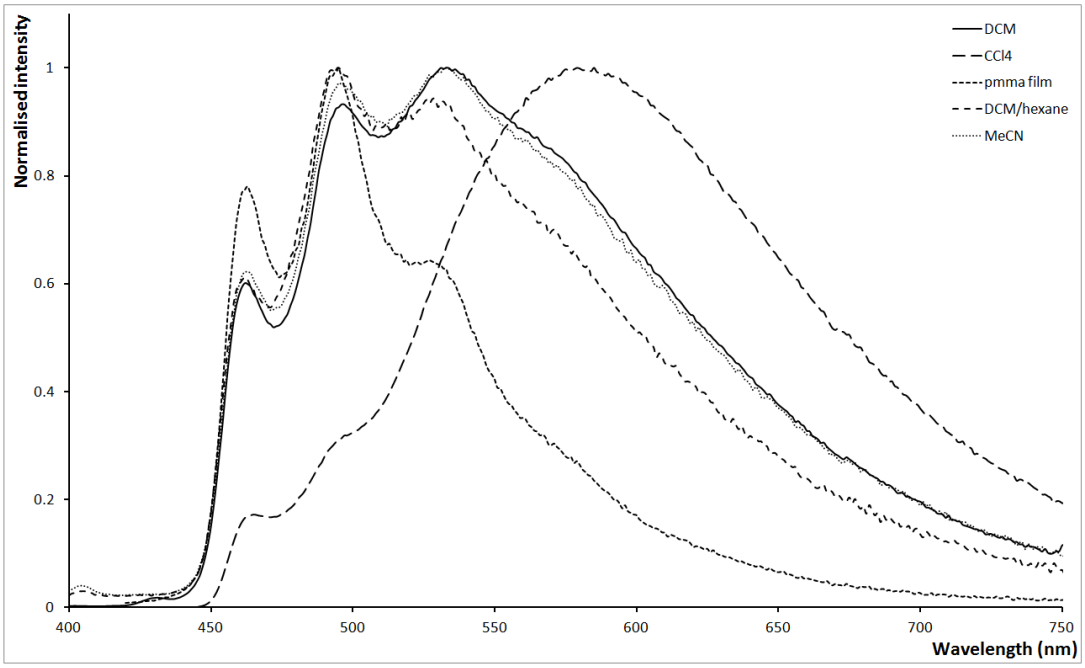

*Figure 3.17: Emission spectra of **22** measured in deaerated DCM, CCl_4, hexane/DCM mixture, MeCN and pmma film under normal atmosphere.*

Again, this effect can be assigned to the use of the mespim ligand as it has been observed in all the complexes where it is present except **21**. More precisely, these effects are observed in complexes where the light emission is arising from the mespim ligand. Complexes where the

LUMO is located on the ppy ligand do not show such drastic perturbations of the emission profiles. Therefore, the profile of **21** is barely modified in pmma film with only a 2 nm red shift of its maximum intensity. The modifications induced by CCl_4 are opposed to what is observed for the rest of the series with an emission profile actually becoming more structured and blue shifted. The emission maximum is observed at 499 nm (19 nm blue shift) with a second peak at 529 nm and a shoulder at 580 nm.

Generally speaking, **21** behaves like most other ppy complexes from the first and second series where the pmma only induces minor changes in emission maxima and profile shapes while CCl_4 generates a more structured and blue shifted profile (Figure 9.2 to Figure 9.17). It is interesting to note that, for these complexes the changes observed in CCl_4 are the ones normally expected from a solvent with low polarity (blue shift of emission maximum, more structured emission profile).

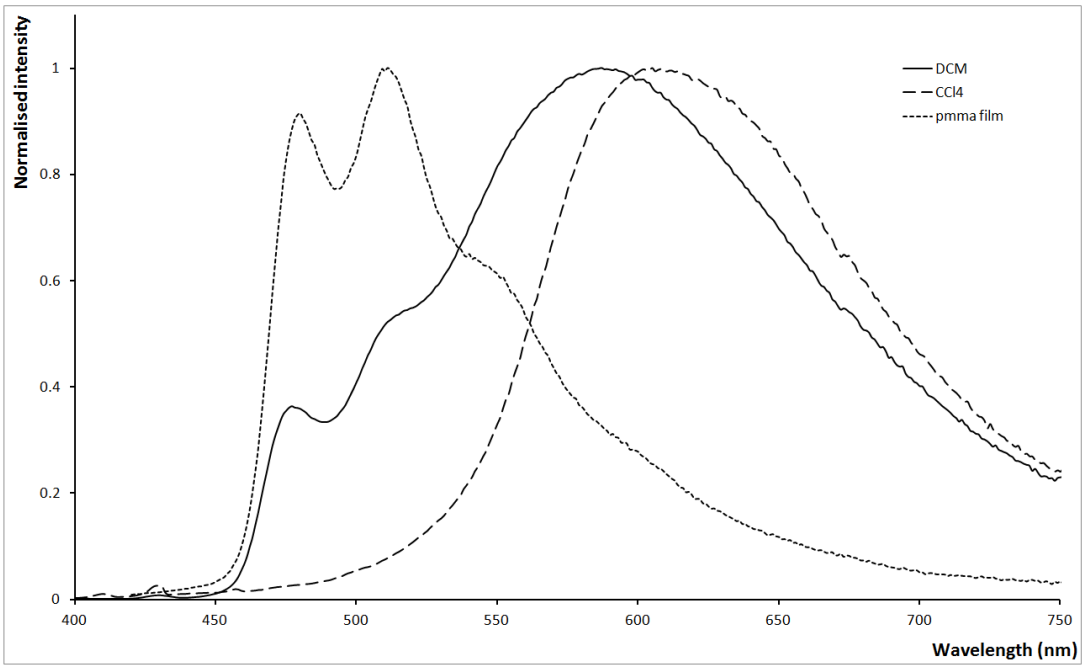

*Figure 3.18: Emission spectra of **20** measured in deaerated DCM, deaerated CCl_4 and pmma film under normal atmosphere.*

The CCl_4 emission spectra obtained from **20**, **22** and **24** are unexpected in the sense that they do not fit with standard solvatochromic shifts attributed to solvent polarity. Nevertheless, the effect of solvent interaction on the emission spectra is manifest. Therefore, one possibility would be to consider other solvent properties than the polarity, such as the higher polarizability of CCl_4.[161] A similar effect has been described for some organic dye (oxazine) and may apply in the present context.[162]

*Table 3.9: Emission maxima of the different peaks observed on the emission spectra of complexes **20**, **21**, **22** and **24**.*

complex	medium	peak 1	peak 2	peak 3	peak 4
20	DCM	477	515	-	587 (max)
	CCl_4	-	-	-	605
	pmma	480	511 (max)	547 (sh)	597 (sh)
21	DCM	518	-	-	-
	CCl_4	499 (max)	529	580 (sh)	-
	pmma	520			-
22	DCM	462	496	533 (max)	570 (sh)
	CCl_4	465	496 (sh)	-	585 (max)
	pmma	463	495 (max)	528 (sh)	572 (sh)
24	DCM	467	500	537 (max)	570 (sh)
	CCl_4	465	500	540 (sh)	581 (max)
	pmma	464	497 (max)	532 (sh)	578 (sh)

Data measured in DCM, CCl4 and in pmma films, the values are expressed in nm, max denotes the maximum intensity of the spectrum, sh denotes a shoulder signal.

Another factor that could influence the emission profile in CCl_4 is the complex solubility in the solvent. Indeed, a slightly decreased solubility in CCl_4 compared to DCM can induce the formation of aggregates and appearance of π-stacking interactions, leading to a red shift in the emission profile.

In the current state of the present research, it is believed that further investigations would be necessary to determine the exact nature of the emission mechanisms of these complexes. An extended solvent analysis would be useful to determine the exact solvent parameters inducing

the observed changes. Studies of different complex/pmma ratios could also be tested to optimise the emission profile in thin films and in different polymers and host materials.

Finally, theoretical calculations would be extremely helpful in understanding the nature of the excited state involved in the light emission process as well as in explaining the reason behind the emission broadness and solvent sensitivity of the emission profiles.

4 CONCLUSION

The present work focused on the design, synthesis and characterisation of new tris-heteroleptic iridium complexes for electroluminescent application. The aim was to study these complexes and their photophysical properties to develop a broad emitting molecule with white emission. The complexes were divided in four series corresponding to the type of ligands used. All complexes were characterised in great details by NMR analyses using ^{1}H, ^{13}C and ^{19}F spectroscopy as well as 2D techniques.

The first series with ppy/ppz type ligands showed challenging purification processes. It highlighted the possibility to play on ligand combinations to ease the purification process without drastically changing the complexes physical and photophysical properties. Even though these complexes showed limited emission broadening, they were useful to study reaction yields and observe reactivity differences, between ligands, and depending on the iridium starting material used. The second series using dimethoxylated ppy ligands with increasing LUMO energies in combination to dFppy or dFppz ligands offered much easier purification processes as the polarity differences between the complexes formed are increased by the presence of the methoxy substituents. Their photophysical properties displayed a significant broadening when high LUMO ligands were mixed with dFppz. Unfortunately, the low quantum yield observed with the corresponding bis-heteroleptic complex was conserved. This series also underlined the dominant role of the dFppy ligand in the emission process, if the energy of the second LUMO is increased. In this case, redox potentials and emission spectra pointed to a dFppy based emission, with the second ligand only playing a secondary role in influencing the photophysical properties of the complex.

The fourth series used a mespim ligand in combination with dFppy, dFppz and CF_3ppz. The photophysical properties confirmed the importance played by the dFppz in the emission broadening with an increase of FWHM values of nearly 1000 cm^{-1} between bis-mespim, the tris-heteroleptic dFppz and CF_3ppz complexes. The emission lifetime values of the bis-mespim and tris-heteroleptic complexes were similarly short (below 50 ns), indicating fast nonradiative processes generated by the mespim ligand.

Finally, the synthesis and separation of isomers of pic complexes was successfully achieved, using two main ligand combinations to obtain two pairs of structural isomers. These isomers were characterised in details by NMR spectroscopy, X-ray christallography, and by their photophysical properties. Even though the pic orientation induced little effect on the photophysical properties of these complexes, it opens the way to interesting synthesis possibilities, increasing the number of available parameters for the design of new iridium emitters.

In general, this work demonstrated the concept of using tris-heteroleptic complexes to develop broad emitting molecules. Moreover, by investigating different types of ligands, it highlighted clues on how to achieve this goal. Unfortunately, these broad emitting molecules obtained suffer from low emission lifetimes due to fast radiationless deactivation processes. However, this work also highlighted ways to improve the research methodology of tris-heterolpectic complexes and opened interesting possibilities for future research.

5 FUTURE PROSPECTS

The future work focused on the synthesis and purification of tris-heteroleptic iridium complexes with acac ancillary ligands in an effort to broaden the shape of the emission spectra to obtain white emission. The results obtained show a significant increase of the FWHM but always at the expense of the emission intensity. Effort should be made to correct this drawback. In this prospect, it is believed that the use of the dFppz ligand as a high LUMO bearer should be avoided. Since the use of pim ligands seem to generate broad spectra, it would be interesting to mix them with more emissive ligands that have high LUMO energies, such as pim-based carbene ligands or ppy with destabilised LUMOs (but not dMeOMeOppy as this ligand induces too much non radiative decay). Investigation on the ancillary ligand also needs to be done, opening infinite possibilities. Many interesting classes of symmetrical ancillary ligands such as amidinates[163] or diketiminates[164] have been used to tune the photophysical properties. The use of non-symmetrical ancillary ligands can also be investigated as the resulting isomers can be isolated by HPLC. In this regard, the field is also infinite with examples as wide as asymmetrical acac[165], ketoiminate and diketiminates, pic derivatives, and all the neutral aromatic ring combinations. The screening methodologies briefly described above can be developed to investigate rapidly the effect of a large number of ancillary ligands on many dimers or bis-MeCN precursors with minimal effort and cost.

Finally, the synthesis of tris-cyclometalated tris-heteroleptic complexes of the type [Ir(C^1^N^1)(C^2^N^2)(C^3^N^3)] could be attempted as it has already been explored for bis-heteroleptic complexes[45,157] and as a new synthetic methodology[108,109] drastically reduces the number of isomers formed.

6 EXPERIMENTAL PROCEDURES

6.1 General considerations

All the starting materials and solvents were commercially available and used as received except ethyl acetate that was distillated using a rotary evaporator before use. Solvent and acids were generally purchased from Fisher except for diethyl ether (Sigma-Aldrich), acetone (VWR), ethyl acetate (VWR) and ethoxyethanol (Acros Organics). Silica gel (60, 0.040-0.063mm, 230-400 mesh) was ordered from Alfa Aesar.

^{1}H spectra were recorded using a Bruker AVIII 300, a Bruker AVIII 400 or a Brucker DRX 500 spectrometer; ^{13}C spectra were recorded using a Bruker AVIII 400 or a Brucker DRX 500 spectrometer; ^{19}F were recorded using on a Bruker AVIII 300 spectrometer. Chemical shifts (δ) are expressed in ppm and referenced to the $CHCl_3$ residual peak (^{1}H: 7.26 ppm, ^{13}C: 77.16 ppm). Coupling constants (J) are in hertz (Hz).

Mass spectrometry experiments were performed by means of electrospray ionisation on a Synapt G2-S HDMS mass spectrometer (Waters LTD, Manchester, UK).

Elemental microanalyses were measured with a CE instruments elemental analyser EA1110, CHNS version.

Analytical HPLC chromatograms were recorded on a Shimadzu LC-20AD/T device, using a Phenomenex Kinetex 5 µ, C18, 100 Å column at a constant temperature of 35 C (isocratic solution of ACN/water at 1mL/min).

Preparative HPLC was performed with a Phenomenex Kinetex 5micron, C18, 100 Angstrom, AXIA packed column equipped with a SecurityGuard PREP cartridge Core-Shell C18.

Cyclic voltammetry was measured using a Metrohm Autolab PGSTAT101 potentiostat. All samples were measured in a degassed acetonitrile/$TBAPF_6$ 0.1M solution at RT, using a Pt working, counter and reference electrodes. The potentials were measured vs ferrocenium/ferrocene (Fc^+/Fc).

FT-IR analyses were made on a Perkin Elmer Spectrum100 FT-IR spectrometer

UV-Visible spectra were measured in aerated dichloromethane on a CARY5000 spectrometer.

Emission spectra and excited state lifetimes were measured using an Edinburgh Instruments FLSP920 spectrometer. All samples were prepared with dichloromethane degassed by careful argon bubbling for 40 minutes.

Quantum yield measurements were performed using a JobinYvon–Horiba Fluorolog spectrometer to record emission spectra and a Jasco V-650 spectrophotometer for the UV-vis spectra.

6.2 Syntheses of Ligands

6.2.1 Synthesis of 2-(2,4-difluorophenyl)pyridine (dFppy)

2-Bromopyridine (1 g, 0.6 mL, 6.33 mmol, 1 equiv.), 2,4-difluorophenylboronicacid (1.4 g, 8.862 mmol, 1.4 equiv.) were added to a round bottomed flask and dissolved in a 7:3 (v/v) THF : 2M aqueous Na_2CO_3 (anhydrous, VWR) solution 32 mL) and degassed with argon. Tetrakis(triphenylphosphine)palladium(0) (Aldrich, 0.315 g, 0.308 mmol, 5 mol%) was then added. After more degassing, the mixture was heated to reflux (70 °C) overnight under argon atmosphere. The mixture was poured into water and extracted with CH_2Cl_2 (150 mL). The organic phases were combined and dried over magnesium sulfate. After filtration of $MgSO_4$ (anhydrous, Sigma-Aldrich), CH_2Cl_2 was evaporated under vacuum. DFppy was purified by a first silica gel chromatography column using an n-hexane and Et_2O eluent (80 : 20) to remove the remaining catalyst and purified further by a pure CH_2Cl_2 column on silica.

The product obtained was a slightly yellow oil at room temperature and a white solid when stored in the freezer (melting point ≈ 20°C). Yield: 98%.

The NMR spectra are in agreement with previously published data.[116,166]

^{1}H NMR (400 MHz, $CDCl_3$) δ 8.63 (d, *J* = 4.8 Hz, 1H, 6), 7.96 (td, *J* = 8.9, 6.7 Hz, 1H, 6'), 7.72 – 7.55 (m, 2H, 3/4), 7.20 – 7.07 (m, 1H, 5), 6.97 – 6.88 (m, 1H, 5'), 6.83 (ddd, *J* = 11.3, 8.8, 2.5 Hz, 1H, 3').

^{13}C NMR (101 MHz, $CDCl_3$) δ 164.75 – 159.13 (m, 2'/4'), 152.67 (d, J = 1.8 Hz, 2), 149.90 (6), 136.62 (4), 132.27 (dd, *J* = 9.6, 4.4 Hz, 6'), 124.35 (d, *J* = 9.3 Hz, 3), 123.92 (dd, *J* = 11.8, 3.4 Hz, 1'), 122.56 (5), 112.01 (dd, *J* = 21.1, 3.4 Hz, 5'), 104.49 (t, *J* = 26.2 Hz, 3').

^{19}F NMR (282 MHz, Chloroform-*d*) δ -109.25 (d, *J* = 8.6 Hz), -112.87 (d, *J* = 8.6 Hz).

6.2.2 Synthesis of 1-(2,4-Difluorophenyl)pyrazole (dFppz)

1,1,3,3-tetramethoxypropane (2 g, 2 mL 12 mmol, 1 equiv.) was dissolved in 95% ethanol (20 mL) and an aqueous solution of concentrated HCl (37%) was added (2 mL). 1-(2,4-difluorophenyl)hydrazine hydrochloride (2.15 g, 12 mmol, 1 equiv.) was added to the solution with 40 mL of 95% ethanol. The mixture was then refluxed for 4 hours and cooled down to room temperature.

The reaction mixture was then dried under vacuum, dissolved again in ethanol and neutralized with a saturated aqueous solution of Na_2CO_3. The remaining Na_2CO_3 was removed by filtration. After evaporation of the solvent under vacuum, the product was purified by column chromatography (hexane : ethyl acetate, 20 : 1). The product obtained was a slightly yellow oil .Yield: 62%.

The NMR spectra are in agreement with previously published data.[119,167]

^{1}H NMR (400 MHz, $CDCl_3$) δ 7.88 (t, *J* = 2.8 Hz, 1H, 5), 7.86 – 7.76 (m, 1H, 6'), 7.69 (d, *J* = 1.7 Hz, 1H, 3), 6.99 – 6.87 (m, 2H, 3'/5'), 6.41 (dd, *J* = 2.4, 1.9 Hz, 1H, 4).

^{13}C NMR (101 MHz, $CDCl_3$) δ 160.76 (dd, *J* = 249.3, 11.3 Hz, 4'), 153.56 (dd, *J* = 251.6, 12.1 Hz, 2') 140.82 (3), 130.49 (d, *J* = 9.4 Hz, 5), 125.47 (d, *J* = 10.8 Hz, 6'), 111.96 (dd, *J* = 22.4, 3.7 Hz, 5'), 107.45 (4), 105.22 – 104.54 (m, 3').

^{19}F NMR (282 MHz, $CDCl_3$) δ -111.69 (d, *J* = 6.3 Hz), -120.88 (d, *J* = 6.2 Hz).

6.2.3 Synthesis of 2-(2,4-dimethoxyphenyl)pyridine (dMeOppy)

2-Bromopyridine (0.95 mL, 19 mmol, 1 equiv.), (2,4-dimethoxyphenyl)boronic acid (2.73 g, 15 mmol, 1.5 equiv.) were added to a round bottomed flask and dissolved in a 6:4 (v/v) THF : 2M aqueous Na_2CO_3 (anhydrous, VWR) solution 70 mL) and degassed by bubbling argon. Tetrakis(triphenylphosphine)palladium(0) (Aldrich, 0.115 g, 0.1 mmol, 1 mol%) was then added. After more degassing, the mixture was heated to reflux (70 °C) overnight under argon atmosphere. The mixture was poured into water and extracted with CH_2Cl_2 (150 mL). The organic phases were combined and dried over magnesium sulfate. After filtration of $MgSO_4$ (anhydrous, Sigma-Aldrich), CH_2Cl_2 was evaporated under vacuum. DMeOppy was purified by two silica gel columns following a literature procedure.[57]

Product: 1.627 g, 7.563 mmol, yield: 75 %

The NMR spectra are in agreement with previously published data.[147]

^{1}H NMR (400 MHz, $CDCl_3$) δ 8.64 (ddd, *J* = 4.9, 1.9, 1.0 Hz, 1H, 6), 7.82 – 7.71 (m, 2H, 3/6’), 7.63 (ddd, *J* = 8.0, 7.4, 1.9 Hz, 1H, 4), 7.12 (ddd, *J* = 7.4, 4.9, 1.2 Hz, 1H, 5), 6.61 (dd, *J* = 8.5, 2.4 Hz, 1H, 5’), 6.54 (d, *J* = 2.4 Hz, 1H, 3’), 3.82 (s, 3H, 10’), 3.81 (s, 3H, 8’).

^{13}C NMR (101 MHz, $CDCl_3$) δ 161.35 (4‘), 158.13 (2‘), 155.88 (2), 149.25 (6), 135.60 (4), 131.96 (6‘), 124.73 (3), 122.07 (1‘), 121.13 (5), 105.12 (5‘), 98.89 (3‘), 55.56 (8‘/10‘), 55.42 (8‘/10‘).

6.2.4 2-(2,4-dimethoxyphenyl)-4-methylpyridine (dMeOMeppy)

The same reaction conditions were used than for dMeOppy.

2-bromo-4-methylpyridine: 1.720 g, 10 mmol, 1 equiv.

2,4-dimethoxyphenyl)boronic acid: 2.377 g, 13 mmol, 1.3 equiv.

The product was purified by column chromatography on silica gel using hexane/THF (80/20) as eluent. Product: 1.684 g, 7.345 mmol, yield: 73 %

^{1}H NMR (400 MHz, $CDCl_3$) δ 8.51 (dd, *J* = 5.0, 0.8 Hz, 1H, 6), 7.71 (d, *J* = 8.5 Hz, 1H, 6‘), 7.58 (dt, *J* = 1.7, 0.8 Hz, 1H, 3), 6.97 (ddd, *J* = 5.0, 1.7, 0.8 Hz, 1H, 5), 6.59 (dd, *J* = 8.5, 2.4 Hz, 1H, 5‘), 6.54 (d, *J* = 2.4 Hz, 1H, 3‘), 3.83 (s, 3H, 8‘/10‘), 3.82 (s, 3H, 8‘/10‘), 2.35 (s, 3H, 7).

^{13}C NMR (101 MHz, $CDCl_3$) δ 161.23 (4‘), 158.07 (2‘), 155.82 (2), 149.02 (6), 146.54 (4), 132.01 (6‘), 125.54 (3), 122.29 (5), 105.03 (5‘), 98.91 (3‘), 55.62 (8‘/10‘), 55.42 (8‘/10‘), 21.24 (7).

6.2.5 2-(2,4-dimethoxyphenyl)-4-methoxypyridine (dMeOMeOppy)

The same reaction conditions were used than for dMeOppy and dMeOMeppy.

2-bromo-4-methoxypyridine: 1 g, 5.32 mmol, 1 equiv.

2,4-dimethoxyphenyl)boronic acid: 1.94 g, 10.64 mmol, 2 equiv.

Pd(cat): 0.3 g, 5 mol%

The product was purified by column chromatography on silica gel using hexane/THF (80/20) as eluent. Product: 1.190 g, 4.851 mmol, yield: 91 %

^{1}H NMR (400 MHz, $CDCl_3$) δ 8.46 (d, *J* = 5.7 Hz, 1H, 6), 7.77 (d, *J* = 8.5 Hz, 1H, 6'), 7.35 (d, *J* = 2.5 Hz, 1H, 3), 6.68 (dd, *J* = 5.7, 2.5 Hz, 1H, 5), 6.58 (dd, *J* = 8.6, 2.4 Hz, 1H, 5'), 6.52 (d, *J* = 2.4 Hz, 1H, 3'), 3.81 (s, 3H, 8/8'/10'), 3.81 (s, 6H, 8/8'/10').

^{13}C NMR (101 MHz, $CDCl_3$) δ 165.41 (4), 161.30 (4'), 158.08 (2'), 157.27 (2), 150.28 (6), 131.91 (6'), 121.96 (1'), 110.72 (3), 107.41 (5), 105.00 (5'), 98.86 (3'), 55.57 (8/8'/10'), 55.37 (8/8'/10'), 54.98 (8/8'/10').

6.2.6 1-phenyl-4-(trifluoromethyl)pyrazole (CF_3ppz)

In a dry 50 mL RB flask, 3,3,3-trifluoropropanoic acid (1.280 g, 10 mmol, 1 equiv.) was dissolved in 10 mL of dry DMF and the mixture was heated at 70ºC. Phosphorus oxychloride ($POCl_3$, 4.600 g, 30 mmol, 3 equiv.) was carefully added and the mixture was allowed to react at 70ºC for 1 hour. The mixture was cooled down to room temperature and slowly poured into 50 mL of an ice cold aqueous KPF_6 solution. The precipitate was filtered, washed with ice cold water and dried under vacuum.

The dried solid was dissolved to 30 mL of MeCN contained in a 250 mL RB flask. Phenyl hydrazine (1.5 mL, around 15 mmol) was added and the mixture was stirred for 1 hour at room temperature. Trifluoroacetic acid (TFA, 2 mL, 26 mmol) was added and the closed flask was heated at 70ºC for 4 hours. The reaction was stopped and the MeCN volume was reduced under vacuum. The mixture was poured in water and extracted with DCM. The organic phase was dried over $MgSO_4$ and the DCM volume was reduced under vacuum. Silica was added to the flask to adsorb the mixture and dried under vacuum. Hexane was added to wet the silica and it was deposited on top of a silica gel column prepared with hexane. The mixture was then eluted with hexane/EtOAc 90/10 as eluent to obtain the pure product.

1.099 g, 5.180 mmol, yield: 51%.

^{1}H NMR (400 MHz, $CDCl_3$) δ 8.18 (t, *J* = 1.0 Hz, 1H, 3), 7.91 (s, 1H, 5), 7.72 – 7.64 (m, 2H, 2'/6'), 7.54 – 7.44 (m, 2H, 3'/5'), 7.42 – 7.33 (m, 1H, 4').

^{13}C NMR (101 MHz, $CDCl_3$) δ 139.45 (1'), 138.33 (q, *J* = 3.1 Hz, 5), 129.79 (2'/6'), 127.89 (4'), 126.42 (d, *J* = 3.7 Hz, 3), 122.61 (q, *J* = 266.2 Hz, 6), 119.90 (3'/5'), 115.63 (q, *J* = 37.9 Hz, 4).

^{19}F NMR (282 MHz, $CDCl_3$) δ -56.68.

6.2.7 1-mesityl-2-phenylimidazole (mespim)

2,4,6-trimethylaniline (2 g, 14.79 mmol, 2.1 mL, 1 equiv.) and glyoxal 40% w./w. aq.(2.146 g, 14.79 mmol, 1.7 mL, 1 equiv.) were mixed in a 500 mL round bottomed flask filed with 40 mL of methanol degassed by argon bubbling. The mixture was stirred for 1 hour and a yellow precipitate formed. Additional degassed methanol 40 mL was added. Benzaldehyde (3.29 g, 31.06 mmol, 3.3 mL, 2.1 equiv.) was added, followed by ammonium chloride (1.58 g, 29.58 mmol, 2 equiv.). The mixture was heated to reflux for 1 hour and phosphoric acid (14 mL) was slowly added. The mixture was heated to reflux for 8 hours.

The heating was stopped and the cooled solution was neutralized with a sodium carbonate aqueous solution. The product was extracted with DCM and the organic phse dried over $MgSO_4$. After evaporation of the solvent (to dryness, to remove all traces of methanol), the crude was dissolved in the minimum amount of DCM and adsorbed on silica. The silica was dried under vacuum and hexane was added for deposition on top of a hexane packed silica gel column. The product was eluted with hexane/EtOAc (60/40) and obtained as a brown solid.

0.434 g, 1.654 mmol, yield: 11%

^{1}H NMR (400 MHz, $CDCl_3$) δ 7.43 – 7.39 (m, 2H, 2’/6’), 7.30 (d, *J* = 1.2 Hz, 1H, 4), 7.23 – 7.18 (m, 3H, 3’/4’/5’), 6.95 (q, *J* = 0.8 Hz, 2H, 3’’/5’’), 6.88 (d, *J* = 1.2 Hz, 1H, 5), 2.34 (s, 3H, 8’’), 1.92 (s, 6H, 7’’/9’’).

^{13}C NMR (101 MHz, $CDCl_3$) δ 146.44 (2), 138.91 (4‘‘), 135.34 (2‘‘/6‘‘), 134.77 (1‘‘), 130.85 (1‘), 129.50 (4), 129.45 (3‘‘/5‘‘), 128.41 (3‘/5‘), 128.26 (4‘), 126.83 (2‘/6‘), 122.03 (5), 21.22 (8‘‘), 17.74 (7‘‘/9‘‘).

6.3 First series of complexes: 1 to 10

6.3.1 Synthesis of Chloro-bridged dimers

Three reactions A, B and C were made using different methodologies[55,61]. Each of them used two different ligands (1 equiv each). A was made using $IrCl_3xH_2O$ (1 equiv), B and C were made using $\{Ir(COD)Cl\}_2$ (0.5 equiv).

A: $IrCl_3xH_2O$ was added to a round bottomed flask containing 10 mL of a 7:3 (v/v) ethoxyethanol/water mixture. The solution was degassed by bubbling argon and the ligands were added together with 10 more mL of the ethoxyethanol/water mixture. After further degassing, the solution was placed under argon atmosphere and heated at 130°C overnight while stirring (a reflux condenser was used).

B: $[\{Ir(COD)Cl\}_2]$ was weighted in a 25 mL round bottomed flask and solubilized in 2 mL of ethoxyethanol. The solution was degassed. The two ligands and 1 mL of ethoxyethanol were added. After further degassing, the flask was sealed under argon atmosphere and the mixture was heated at 130°C for 3h under stirring.

C: $[\{Ir(COD)Cl\}_2]$ was weighted in a 25 mL round bottomed flask and solubilized in 2 mL of xylenes. The solution was degassed. The two ligands and 1 mL of xylenes were added. After further degassing, the flask was sealed under argon atmosphere and the mixture was heated at 130°C for 3h while stirring.

The reaction mixtures were cooled down to room temperature. Water was added to **A** and B and hexane was added to C. The three mixtures were kept in the fridge for two hours and filtered. The solid from reactions A and B were washed with cold MeOH. The solid from reaction C was washed with hexane.

6.3.2 Syntheses of the acac complexes

The solids obtained with reactions A, B, and C were reacted separately with sodium acetylacetonate.[61]

The dimer mixture was added to a round bottomed flask and dissolved in 20 mL of DCM/MeOH (9:1). AcacNa was added and the solution was degassed with argon and heated to reflux (40°C) under stirring and argon atmosphere overnight.

After the reaction ended, the solvent was evaporated under vacuum and a MeOH/water mixture was added (the proportion was not really important but a better precipitation was obtained when adding more MeOH than water). The solution was cooled in the fridge for 2 hours and filtered. The residue was washed with a minimal amount of cold MeOH. The residue was added to a flask by dissolving in CH_2Cl_2 and dried under vacuum.

^{1}H NMR spectra of the four crudes were made and products of reactions A, B and C were purified together on a silica gel chromatography column using pure CH_2Cl_2.

As the products tended to be degraded by the acidic silica, 1 mL of triethylamine was added to the silica when preparing the column.

6.3.3 Synthesis of [Ir(dFppy)(ppy)(acac)] (3)

The three reactions, A, B and C were made following the general procedure with 2-phenylpyridine (ppy, 0.1 g, 0.64 mmol, 1 equiv), 2-(2,4-difluorophenyl)pyridine (dFppy, 0.123 g, 0.64 mmol, 1 equiv), $\{Ir(COD)Cl\}_2$ (0.216 g, 0.32 mmol, 0.5 equiv) and $IrCl_3xH_2O$ (0.227 g, 0.64 mmol, 1 equiv).

The solids obtained were reacted separately with sodium acetylacetonate (acacNa, 0.225 g, 1.61 mmol) following the general procedure to obtain yellow crude powders: A: 0.275 g B: 0.255 g, C: 0.294 g.

Once analysed, the different crude were mixed and purified all together. The product was purified according to the procedure and isolated as a yellow solid: 0.237 g. m/z: calc 636.0 found 636.1207. Anal Calcd. For $C_{27}H_{21}F_2IrN_2O_2$: C, 51.01; H, 3.33; N, 4.41. Found: C, 50.86; H, 3.19; N, 4.55.

^{1}H NMR (500 MHz, $CDCl_3$) δ 8.51 (dd, *J* = 5.7, 0.8 Hz, 1H, 6b), 8.44 (dd, *J* = 5.7, 0.7 Hz, 1H, 6a), 8.23 (d, *J* = 8.3 Hz, 1H, 3a), 7.87 (d, *J* = 8.1 Hz, 1H3b), 7.78 – 7.74 (m, 2H, 4a/4b), 7.56 (dd, *J* = 7.8, 1.0 Hz, 1H, 2'b), 7.19 – 7.14 (m, 2H, 5a/5b), 6.86 (td, *J* = 7.7, 1.2 Hz, 1H, 3'b), 6.73 (td, *J* = 7.4, 1.3 Hz, 1H, 4'b), 6.27 (ddd, *J* = 12.2, 9.3, 2.4 Hz, 1H, 3'a), 6.21 (dd, *J* = 7.6, 0.8 Hz, 1H, 5'b), 5.71 (dd, *J* = 9.0, 2.3 Hz, 1H, 5'a), 5.23 (s, 1H, 3c), 1.81 (s, 3H, 1c/5c), 1.78 (s, 3H, 1c/5c).

^{13}C NMR (101 MHz, $CDCl_3$*d*) δ 184.99 (2c/4c), 184.92 (2c/4c) , 168.54 (2b), 152.80 (d, *J* = 6.9 Hz, 1'a), 148.27 (6a/6b), 146.47 (1'b), 144.78 (6'b), 137.50 (4a/4b), 137.40 (4a/4b), 133.05 (5'b), 129.31 (4'b), 124.06 (2'b), 122.49 (d, *J* = 18.8 Hz, 3a), 121.79 (5a/5b/3'b), 121.43 (d, *J* = 8.8 Hz, 5a/5b/3'b), 118.78 (3b), 115.52 – 115.10 (m, 5'a), 100.66 (3c), 96.91 (t, *J* = 26.9 Hz, 3'a), 28.92 (1c/5c), 28.81 (1c/5c).

^{19}F NMR (282 MHz, $CDCl_3$) δ -109.40 (d, *J* = 10.1 Hz), -111.68 (d, *J* = 9.9 Hz).

6.3.3.1 [Ir(ppy)$_2$(acac)] (1)

Anal Calcd. For $C_{27}H_{23}IrN_2O_2$: C, 54.08; H, 3.87; N, 4.67. Found: C, 54.36; H, 3.63; N, 4.93.

1H NMR (400 MHz, $CDCl_3$) δ 8.52 (ddd, J = 5.8, 1.6, 0.8 Hz, 2H, 6a), 7.84 (dt, J = 8.1, 1.1 Hz, 2H, 3a), 7.71 (ddd, J = 8.1, 7.4, 1.6 Hz, 2H, 4a), 7.54 (dd, J = 7.7, 1.4 Hz, 2H, 2'a), 7.13 (ddd, J = 7.3, 5.7, 1.4 Hz, 2H, 5a), 6.81 (td, J = 7.5, 1.3 Hz, 2H, 3'a), 6.69 (td, J = 7.4, 1.4 Hz, 2H, 4'a), 6.27 (dd, J = 7.5, 1.2 Hz, 2H, 5'a), 5.22 (s, 1H, 3c), 1.79 (s, 6H, 1c/5c).

^{13}C NMR (101 MHz, $CDCl_3$) δ 184.71 (2c/4c), 168.72 (2a), 148.28 (6a), 147.72 (1'a), 144.86 (6'a), 136.91 (4a), 133.17 (5'a), 129.21 (4'a), 123.92 (2'a), 121.52 (5a), 120.83 (3'a), 118.50 (3a), 100.49 (3c), 28.89 (1c/5c).

6.3.3.2 [Ir(dFppy)$_2$(acac)] (2)

m/z: calc 672.1012, found 672.1017. Anal Calcd. For $C_{27}H_{19}F_4IrN_2O_2$: C, 48.28; H, 2.85; N, 4.17. Found: C, 48.12; H, 2.84; N, 4.28.

^{1}H NMR (500 MHz, $CDCl_3$) δ 8.44 (dd, *J* = 5.7, 0.8 Hz, 2H, 6a), 8.25 (d, *J* = 8.4 Hz, 2H, 3a), 7.79 (td, *J* = 8.0, 1.1 Hz, 2H, 4a), 7.19 (ddd, *J* = 7.2, 5.8, 1.2 Hz, 2H, 5a), 6.33 (ddd, *J* = 12.2, 9.3, 2.3 Hz, 2H, 3'a), 5.65 (dd, *J* = 8.8, 2.3 Hz, 2H, 5'a), 5.26 (s, 1H, 3c), 1.81 (s, 6H, 1c/5c).

^{13}C NMR (101 MHz, $CDCl_3$) δ 185.16 (2c/4c), 165.49 (d, *J* = 6.8 Hz, 2a), 164.24 – 159.52 (m, 2'a/4'a), 151.43 (d, *J* = 6.9 Hz, 1'a), 148.20 (6a), 138.00 (4a), 128.77 (6'a), 122.76 (d, *J* = 19.1 Hz, 3a), 121.74 (5a), 115.23 (dd, *J* = 16.9, 2.5 Hz, 5'a), 100.83 (3c), 97.45 (t, *J* = 26.9 Hz, 3'a), 28.81 (1c/5c).

^{19}F NMR (282 MHz, $CDCl_3$) δ -108.86 (d, *J* = 10.2 Hz), -111.11 (d, *J* = 10.2 Hz).

6.3.4 Synthesis of [Ir(dFppz)(ppz)(acac)] (6)

The three reactions, A, B and C were made following the general procedure with 2-phenylpyrazole (ppz, 0.1 g, 0.69 mmol, 1 equiv), and 1-(2,4-Difluorophenyl)pyrazole (dFppz , 0.125 g, 0.69 mmol, 1 equiv), $\{Ir(COD)Cl\}_2$ (0.233 g, 0.35 mmol, 0.5 equiv) and $IrCl_3xH_2O$ (0.245 g, 0.69 mmol, 1 equiv).

The solids obtained were reacted separately with acacNa (0.243 g, 1.73 mmol) following the general procedure to obtain yellow crude powders: A: 0.284 g, B: 0.101 g, C: 0.150 g.

The product was purified according to the procedure and obtained as a grey solid: 0.1577 g. m/z: calc 635.0980, found 635.0986. Anal Calcd. For $C_{23}H_{19}F_2IrN_4O_2$: C, 45.02; H, 3.12; N, 9.13. Found: C, 45.05; H, 3.27; N, 8.86.

^{1}H NMR (500 MHz, $CDCl_3$) δ 8.32 (d, *J* = 2.7 Hz, 1H, 5a), 8.05 (d, *J* = 2.8 Hz, 1H,5b), 7.59 (dd, *J* = 3.6, 2.3 Hz, 2H, 3a/3b), 7.16 (d, *J* = 7.9 Hz, 1H, 2'b), 6.86 (td, *J* = 7.7, 1.1 Hz, 1H, 3'b), 6.68 (td, *J* = 7.4, 1.0 Hz, 1H, 4'b), 6.66 – 6.63 (m, 3H, 4a/4b), 6.38 (ddd, *J* = 11.8, 8.9, 2.4 Hz, 1H, 3'a), 6.20 (dd, *J* = 7.5, 1.0 Hz, 1H, 5'b), 5.69 (dd, *J* = 8.6, 2.4 Hz, 1H, 5'a), 5.24 (s, 1H, 3c), 1.83 (s, 3H, 1c/5c), 1.81 (s, 3H, 1c/5c).

^{13}C NMR (101 MHz, $CDCl_3$) δ 185.47 (2c/4c), 185.38 (2c/4c), 159.42 (dd, *J* = 249.3, 10.8 Hz, 4'a), 148.53 (dd, *J* = 251.1, 13.1 Hz, 2'a), 144.41 (6'b), 138.03 (3a/3b), 137.53 (3a/3b), 134.86 (5'b), 134.46 (d, *J* = 5.2 Hz, 1'a), 130.37 (d, *J* = 14.6 Hz, 5a), 128.90 – 128.35 (m, 6'a), 127.27 (1'b), 126.06 (5b), 125.55 (4'b), 121.98 (3'b), 116.85 (dd, *J* = 18.5, 2.0 Hz, 5'a), 110.74 (2'b), 107.74 – 107.10 (m, 4a/4b), 107.04 (4a/4b), 100.33 (3c), 97.31 (dd, *J* = 28.1, 23.6 Hz, 3'a), 28.48 (1c/5c), 28.40 (1c/5c).

^{19}F NMR (282 MHz, $CDCl_3$) δ -115.02 (d, J = 5.4 Hz), -126.28 (d, J = 5.3 Hz).

6.3.4.1 [Ir(ppz)$_2$(acac)] (4)

m/z: calc 578.1294, found 578.1293. Anal Calcd. For $C_{23}H_{21}IrN_4O_2$: C, 47.82; H, 3.66; N, 9.70. Found: C, 47.61; H, 3.67; N, 9.86.

^{1}H NMR (500 MHz, $CDCl_3$) δ 8.04 (d, *J* = 2.4 Hz, 2H, 5a), 7.61 (dd, *J* = 2.1, 0.4 Hz, 2H, 3a), 7.13 (dd, *J* = 7.9, 1.0 Hz, 2H, 2'a), 6.81 (td, *J* = 7.7, 1.3 Hz, 2H, 3'a), 6.66 – 6.61 (m, 4H, 4'a/4a), 6.25 (dd, *J* = 7.5, 1.2 Hz, 2H, 5'a), 5.22 (s, 1H, 3c), 1.81 (s, 6H, 1c/5c).

^{13}C NMR (101 MHz, $CDCl_3$) δ 185.25 (2c/4c), 144.61 (6'a), 137.90 (3a), 135.02 (5'a), 128.46 (1'a), 125.73 (5a/4'a), 125.47 (5a/4'a), 121.42 (3'a), 110.55 (2'a), 106.76 (4a), 100.16 (3c), 28.49 (1c/5c).

6.3.4.2 [Ir(dFppz)$_2$(acac)] (5)

m/z: calc 650.0917, found 650.0912. Anal Calcd. For $C_{23}H_{17}F_4IrN_4O_2$: C, 42.52; H, 2.64; N, 8.62. Found: C, 42.43; H, 2.53; N, 8.80.

^{1}H NMR (500 MHz, $CDCl_3$) δ 8.33 (d, *J* = 2.9 Hz, 2H, 5a), 7.58 (d, *J* = 2.2 Hz, 2H, 3a), 6.66 (t, 2H, 4a), 6.44 (ddd, *J* = 11.7, 8.9, 2.5 Hz, 2H, 3'a), 5.65 (dd, *J* = 8.4, 2.5 Hz, 2H, 5'a), 5.26 (s, 1H, 3c), 1.84 (s, 6H, 1c/5c).

^{13}C NMR (101 MHz, $CDCl_3$) δ 185.64 (2c/4c), 159.41 (dd, *J* = 250.0, 10.7 Hz, 4'a), 148.56 (dd, *J* = 251.7, 13.1 Hz, 2'a), 137.69 (3a), 133.18 (d, *J* = 5.9 Hz, 1'a), 130.70 (d, *J* = 14.7 Hz, 5a), 128.80 – 128.38 (m, 6'a), 116.78 (dd, *J* = 18.9, 2.9 Hz, 5'a), 107.49 (4a), 100.52 (3c), 97.87 (dd, *J* = 28.2, 23.5 Hz, 3'a), 28.37 (1c/5c).

^{19}F NMR (282 MHz, $CDCl_3$) δ -114.52 (d, *J* = 5.5 Hz), -125.72 (d, *J* = 5.6 Hz).

6.3.5 Synthesis of [Ir(ppy)(ppz)(acac)] (7)

The three reactions, A, B and C were made following the general procedure with ppz (0.1 g, 0.69 mmol, 1 equiv), ppy (0.108 g, 0.69 mmol, 1 equiv), $\{Ir(COD)Cl\}_2$ (0.233 g, 0.35 mmol, 0.5 equiv) and $IrCl_3xH_2O$ (0.245 g, 0.69 mmol, 1 equiv).

The solids obtained were reacted separately with acacNa (0.243 g, 1.73 mmol) following the general procedure to obtain yellow crude powders: **A**: 0.237 g, B: 0.288 g, C: 0.164 g.

The product was separated according to the procedure, obtained as a yellow solid: 0.0612 g. m/z: calc 610.1216, found 610.1248. Anal Calcd. For $C_{25}H_{22}IrN_3O_2$: C, 51.01; H, 3.77; N, 7.14. Found: C, 51.09; H, 3.57; N, 7.32.

^{1}H NMR (500 MHz, $CDCl_3$) δ 8.56 (d, *J* = 5.7 Hz, 1H, 6a), 8.04 (d, *J* = 2.8 Hz, 1H, 5b), 7.83 (d, *J* = 8.1 Hz, 1H, 3a), 7.72 (td, *J* = 7.9, 1.5 Hz, 1H, 4a), 7.59 (d, *J* = 2.0 Hz, 1H, 3b), 7.54 (d, *J* = 7.7 Hz, 1H, 2'a), 7.15 – 7.11 (m, 2H, 5a/2'b), 6.84 – 6.77 (m, 2H, 3'a/3'b), 6.72 (td, *J* = 7.5, 1.2 Hz, 1H, 4'a), 6.65 – 6.60 (m, 2H, 4b/4'b), 6.28 (d, *J* = 7.6 Hz, 1H, 5'a), 6.22 (dd, *J* = 7.5, 1.0 Hz, 1H, 5'b), 5.22 (s, 1H, 3c), 1.81 (s, 3H, 1c/5c), 1.79 (s, 3H, 1c/5c).

^{13}C NMR (101 MHz, $CDCl_3$) δ 185.37 (2c/4c), 184.69 (2c/4c), 169.31 (2a), 148.49 (6a), 146.91 (1'a), 144.72 (6'a/6'b), 137.80 (3b), 137.04 (4a), 134.29 (5'a/5'b), 133.81 (5'a/5'b), 129.42 (4'a), 129.21 (1'b), 125.65 (5b/4'b), 125.34 (5b/4'b), 123.91 (2'a), 121.50 (5a/3'a/3'b), 121.26 (5a/3'a/3'b), 120.94 (5a/3'a/3'b), 118.50 (3a), 110.60 (2'b), 106.79 (4b), 100.31 (3c), 28.77 (1c/5c), 28.60 (1c/5c).

6.3.6 Synthesis of [Ir(dFppy)(dFppz)(acac)] (8)

The three reactions, A, B, and C were made following the general procedure with dFppy (0.14 g, 0.73 mmol, 1 equiv), dFppz (0.132 g, 0.73 mmol, 1 equiv), $\{Ir(COD)Cl\}_2$ (0.246 g, 0.34 mmol, 0.5 equiv) and $IrCl_3xH_2O$ (0.257 g, 0.73 mmol, 1 equiv).

The solids obtained were reacted separately with acacNa (0.256 g, 1.83 mmol) following the general procedure to obtain yellow crude powders: A: 0.330 g, B: 0.296 g, C: 0.264 g, .

The product was separated according to the procedure, obtained as a yellow solid: 0.1586 g. m/z: calc 682.0839, found 682.0843. Anal Calcd. For $C_{26}H_{19}F_4IrN_2O_2$: C, 45.45; H, 2.75; N, 6.36. Found: C, 45.61; H, 2.67; N, 6.50.

^{1}H NMR (500 MHz, $CDCl_3$) δ 8.49 (dd, *J* = 5.7, 0.9 Hz, 1H, 6a), 8.34 (d, *J* = 2.9 Hz, 1H, 3b), 8.24 (d, *J* = 8.3 Hz, 1H, 3a), 7.79 (td, *J* = 8.1, 1.2 Hz, 1H, 4a), 7.55 (d, *J* = 2.2 Hz, 1H, 5b), 7.18 (ddd, *J* = 7.3, 5.8, 1.3 Hz, 1H, 5a), 6.66 (t, *J* = 2.6 Hz, 1H, 4b), 6.42 (ddd, *J* = 11.8, 8.9, 2.5 Hz, 1H, 3'b), 6.34 (ddd, *J* = 12.3, 9.3, 2.3 Hz, 1H, 3'a), 5.68 (dd, *J* = 8.7, 2.4 Hz, 1H, 5'a), 5.61 (dd, *J* = 8.5, 2.5 Hz, 1H, 5'b), 5.27 (s, 1H, 3c), 1.84 (s, 3H, 1c/5c), 1.83 (s, 3H, 1c/5c).

^{13}C NMR (101 MHz, $CDCl_3$) δ 185.79 (2c/4c), 185.13 (2a), 166.03 (d, *J* = 7.0 Hz, 2'a/4'a/4'b), 163.18 (dd, *J* = 200.0, 13.5 Hz, 2'a/4'a/4'b), 161.81 – 159.39 (m, 2'a/4'a/4'b), 159.37 (dd, *J* = 249.6, 10.6 Hz, 2'a/4'a/4'b), 150.39 (d, *J* = 6.9 Hz, 1'a), 148.66 (dd, *J* = 251.7, 13.3 Hz, 2'b), 148.37 (6a), 138.14 (4a/5b), 137.64 (4a/5b), 134.12 (d, *J* = 4.4 Hz, 1'b), 130.66 (d, *J* = 14.9 Hz, 3b), 128.95 – 128.47 (m, 6'a/6'b), 122.74 (d, *J* = 19.0 Hz, 3a), 121.74 (5a), 116.47 – 115.58 (m, 5'a/5'b), 107.51 (4b), 100.68 (3c), 98.28 – 97.12 (m, 3'a/3'b), 28.59 (d, *J* = 15.7 Hz, 1c/5c).

^{19}F NMR (282 MHz, $CDCl_3$) δ -108.45 (d, *J* = 10.2 Hz), -111.15 (d, *J* = 10.2 Hz), -114.81 (d, *J* = 5.5 Hz), -125.68 (d, *J* = 5.5 Hz).

6.3.7 Synthesis of [Ir(dFppy)(ppz)(acac)] (9)

The three reactions, A, B and C were made following the general procedure with ppz (0.1 g, 0.69 mmol, 1 equiv), dFppy (0.132 g, 0.69 mmol, 1 equiv), $\{Ir(COD)Cl\}_2$ (0.233 g, 0.35 mmol, 0.5 equiv) and $IrCl_3xH_2O$ (0.245 g, 0.69 mmol, 1 equiv).

The solids obtained were reacted separately with acacNa (0.243 g, 1.73 mmol) following the general procedure to obtain yellow crude powders: A: 0.307 g, B: 0.247 g, C: 0. 246 g.

The product was purified according to the procedure obtained as a yellow solid: 0.1870 g. m/z: calc .1153, found 625.1157. Anal Calcd. For $C_{25}H_{20}F_2IrN_3O_2$: C, 48.07; H, 3.23 N, 6.73. Found: C, 48.03; H, 3.15; N, 6.73

^{1}H NMR (500 MHz, $CDCl_3$) δ 8.55 (dd, *J* = 5.7, 0.9 Hz, 1H, 6a), 8.22 (d, *J* = 8.3 Hz, 1H, 3a), 8.06 (d, *J* = 2.7 Hz, 1H, 5b), 7.77 (td, *J* = 8.3, 1.2 Hz, 1H, 4a), 7.56 (d, *J* = 2.0 Hz, 1H, 3b), 7.18 – 7.14 (m, 2H, 2'b/5a), 6.85 (td, *J* = 7.7, 1.3 Hz, 1H, 3'b), 6.68 – 6.64 (m, 2H, 4b/4'b), 6.29 (ddd, *J* = 12.1, 9.3, 2.4 Hz, 1H, 3'a), 6.17 (dd, *J* = 7.5, 1.2 Hz, 1H, 5'b), 5.72 (dd, *J* = 8.9, 2.4 Hz, 1H, 5'a), 5.24 (s, 1H, 3c), 1.82 (s, 3H, 1c/5c), 1.80 (s, 3H, 1c/5c).

^{13}C NMR (101 MHz, $CDCl_3$) δ 185.56 (2c/4c), 184.97 (2c/4c), 166.25 (d, *J* = 7.6 Hz, 2a), 151.84 (d, *J* = 7.2 Hz, 1'a), 148.45 (6a), 144.55 (6'b), 137.98 (3b), 137.65 (4a), 134.14 (5'b), 128.12 (1'b), 125.99 (5b/4'b), 125.43 (5b/4'b), 122.48 (d, *J* = 18.7 Hz, 3a), 121.84 (3'b), 121.48 (5a), 115.84 (d, *J* = 16.8 Hz, 5'a), 110.81 (2'b), 107.08 (4b), 100.50 (3c), 97.04 (t, *J* = 27.1 Hz, 3'a), 28.67 (1c/5c), 28.61 (1c/5c).

^{19}F NMR (282 MHz, $CDCl_3$) δ -109.02 (d, *J* = 9.9 Hz), -111.72 (d, *J* = 9.9 Hz).

6.3.8 Synthesis of [Ir(dFppz)(ppy)(acac)] (10)

The three reactions, A, B and C were made following the general procedure with ppy (0.1 g, 0.64 mmol, 1 equiv), dFppz (0.116 g, 0.64 mmol, 1 equiv), $\{Ir(COD)Cl\}_2$ (0.216 g, 0.32 mmol, 0.5 equiv) and $IrCl_3xH_2O$ (0.227 g, 0.64 mmol, 1 equiv).

The solids obtained were reacted separately with acacNa (0.225 g, 1.61 mmol) following the general procedure to obtain yellow crude powders: A: 0.236 g, B: 0.150 g, C: 0.164 g.

The product was purified according to the procedure, obtained as a yellow solid: 0.1266 g. m/z: 625.1153, found 625.1157. Anal Calcd. For $C_{25}H_{20}F_2IrN_3O_2$: C, 48.07; H, 3.23; N, 6.73. Found: C, 48.05; H, 3.12; N, 6.65.

^{1}H NMR (500 MHz, $CDCl_3$) δ 8.50 (d, *J* = 5.3 Hz, 1H, 6a), 8.33 (d, *J* = 2.8 Hz, 1H, 5b), 7.85 (d, *J* = 8.1 Hz, 1H, 3a), 7.75 (td, *J* = 8.0, 1.5 Hz, 1H, 4a), 7.58 (d, *J* = 2.1 Hz, 1H, 2'a/3b), 7.56 (d, *J* = 7.7 Hz, 1H, 2'a/3b), 7.16 (ddd, *J* = 7.2, 5.8, 1.3 Hz, 1H, 5a), 6.88 (td, *J* = 7.7, 1.0 Hz, 1H, 3'a), 6.77 (td, *J* = 7.5, 1.2 Hz, 1H, 4'a), 6.65 (t, *J* = 2.5 Hz, 1H, 4b), 6.37 (ddd, *J* = 11.7, 8.9, 2.5 Hz, 1H, 3'b), 6.24 (d, *J* = 7.5 Hz, 1H, 5'a), 5.67 (dd, *J* = 8.6, 2.4 Hz, 1H, 5'b), 5.25 (s, 1H, 3c), 1.85 (s, 3H, 1c/5c), 1.80 (s, 3H, 1c/5c).

^{13}C NMR (101 MHz, $CDCl_3$) δ 185.61 (2c/4c), 184.87 (2c/4c), 169.07 (2a), 159.39 (dd, *J* = 249.3, 11.0 Hz, 4'b), 148.62 (dd, *J* = 250.9, 13.3 Hz, 2'b), 148.40 (6a), 145.49 (1'a/6'a), 144.65 (1'a/6'a), 137.52 (4a/3b), 137.46 (4a/3b), 135.30 (d, *J* = 4.9 Hz, 1'b), 133.68 (5'a), 130.33 (d, *J* = 14.9 Hz, 5b), 129.51 (4'a), 128.77 (6'b), 124.02 (2'a), 121.76 (5a/3'a), 121.49 (5a/3'a), 118.77 (3a), 116.20 (dd, *J* = 18.3, 2.1 Hz, 5'b), 107.33 – 107.12 (m, 4b), 100.49 (3c), 97.50 – 77.38 (m, 3'b), 28.78 (1c/5c), 28.52 (1c/5c).

^{19}F NMR (282 MHz, $CDCl_3$) δ -115.32 (d, *J* = 5.5 Hz), -126.28 (d, *J* = 5.3 Hz).

6.4 Second series of complexes: 11 to 19

6.4.1 Dimers of 14, 16 and 18

$[\{Ir(COD)Cl\}_2]$ (0.222 g, 0.330 mmol, 0.5 equiv.) was weighted in a 25 mL round bottomed flask and solubilized in 2 mL of ethoxyethanol. The solution was degassed. The two ligands (0.726 mmol, 1.1 equiv.) and 1 mL of ethoxyethanol were added. After further degassing, the flask was sealed under argon atmosphere and the mixture was heated at 130°C for 3h under stirring.

*Table 6.1: Quantity of ligands used for the syntheses of **14**, **16** and **18**.*

	14 (g)	**16** (g)	**18** (g)
dFppy	0.139	0.139	0.139
dMeOppy	0.156	-	-
dMeOMeppy	-	0.166	-
dMeOMeOppy	-	-	0.178

6.4.2 Dimers of 7, 9 and 11

$IrCl_3xH_2O$ (0.233 g, 0.660 mmol, 1 equiv.) was added to a round bottomed flask containing 10 mL of a 7:3 (v/v) ethoxyethanol/water mixture. The solution was degassed by bubbling argon and the ligands (0.726 mmol, 1.1 equiv.) were added together with 10 more mL of the ethoxyethanol/water mixture. After further degassing, the solution was placed under argon atmosphere and heated at 130°C overnight while stirring (a reflux condenser was used).

*Table 6.2: Quantity of ligands used for the syntheses of **15**, **17** and **19**.*

	15 (g)	**17** (g)	**19** (g)
dFppz	0.131	0.131	0.131
dMeOppy	0.156	-	-
dMeOMeppy	-	0.166	-
dMeOMeOppy	-	-	0.178

6.4.3 Acac complexes 14 to 19

The dimer mixture was added to a round bottomed flask and dissolved in 40 mL of DCM/MeOH (9:1). AcacNa was added and the solution was degassed with argon and heated to reflux (40°C) under stirring and argon atmosphere overnight.

After the reaction ended, the solvent was evaporated under vacuum and a MeOH/water mixture was added (the proportion was not really important but a better precipitation was obtained when adding more water than MeOH). The solution was cooled in the fridge for 2 hours and filtered. The residue was washed with a minimal amount of cold MeOH. The residue was added to a flask by dissolving in CH_2Cl_2 and dried under vacuum.

The product was purified by column chromatography on silica gel using pure CH_2Cl_2 as eluent. As the products tended to be degraded by the acidic silica, 1 mL of triethylamine was added to the silica when preparing the column.

Complexes **11**, **12** and **13** were harvested as by-products of the reactions.

6.4.4 [Ir(dMeOppy)$_2$(acac)] (11)

m/z: calc 743.1709, found 743.1716. Anal Calcd. For $C_{31}H_{31}IrN_2O_6$: C, 51.73; H, 4.34; N, 3.89. Found: C, 50.34; H, 4.21; N, 3.81.

^{1}H NMR (500 MHz, $CDCl_3$) δ 8.53 (dt, *J* = 8.5, 1.2 Hz, 2H, 3a), 8.45 (ddd, *J* = 5.7, 1.7, 0.7 Hz, 2H, 6a), 7.63 (ddd, *J* = 8.6, 7.3, 1.7 Hz, 2H, 4a), 6.98 (ddd, *J* = 7.3, 5.8, 1.5 Hz, 2H, 5a), 5.96 (d, *J* = 2.3 Hz, 2H, 3'a), 5.39 (d, *J* = 2.2 Hz, 2H, 5'a), 5.19 (s, 1H, 3c), 3.86 (s, 6H, 8'a), 3.47 (s, 6H, 10'a), 1.77 (s, 6H, 1c/5c).

^{13}C NMR (101 MHz, $CDCl_3$) δ 184.53 (2c/4c), 167.84 (2a), 160.47 (4'a), 159.40 (2'a), 152.86 (1'a/6'a), 147.78 (6a), 136.58 (4a), 126.19 (1'a/6'a), 122.34 (3a), 119.21 (5a), 109.82 (5'a), 100.41 (3c), 91.99 (3'a), 54.93 (8'a), 54.56 (10'a), 28.92 (1c/5c).

6.4.5 [Ir(dMeOMeppy)$_2$(acac)] (12)

m/z: calc 771.7022, found 771.2023. Anal Calcd. For $C_{33}H_{35}IrN_2O_6$: C, 53.00; H, 4.72; N, 3.75. Found: C, 53.39; H, 4.45; N, 3.59.

^{1}H NMR (500 MHz, $CDCl_3$) δ 8.35 (d, *J* = 1.9 Hz, 2H, 3a), 8.28 (d, *J* = 5.8 Hz, 2H, 6a), 6.84 – 6.79 (m, 2H, 5a), 5.96 (d, *J* = 2.2 Hz, 2H, 3'a), 5.43 (d, *J* = 2.2 Hz, 2H, 5'a), 5.16 (s, 1H, 3c), 3.87 (s, 6H, 8'a), 3.49 (s, 6H, 10'a), 2.52 (s, 6H, 7), 1.75 (s, 6H, 1c/5c).

^{13}C NMR (126 MHz, $CDCl_3$) δ 184.39 (2c/4c), 167.15 (2a), 160.21 (4'a), 159.20 (2'a), 152.88 (1'a/6'a), 147.81 (4a), 147.18 (6a), 126.33 (1'a/6'a), 123.01 (3a), 120.48 (5a), 110.29 (5'a), 100.30 (3c), 91.75 (3'a), 54.92 (8'a), 54.56 (10'a), 28.91 (1c/5c), 21.79 (7a).

6.4.6 [Ir(dMeOMeOppy)$_2$(acac)] (13)

m/z: calc 803.1920, found 803.1927. Anal Calcd. For $C_{33}H_{35}IrN_2O_8$: C, 50.82; H, 4.52; N, 3.59. Found: C, 50.58; H, 4.36; N, 3.41.

^{1}H NMR (500 MHz, $CDCl_3$) δ 8.22 (d, *J* = 6.5 Hz, 2H, 6a), 8.12 (d, *J* = 2.8 Hz, 2H, 3a), 6.60 (dd, *J* = 6.6, 2.9 Hz, 2H, 5a), 5.95 (d, *J* = 2.3 Hz, 2H, 3'a), 5.46 (d, *J* = 2.2 Hz, 2H, 5'a), 5.15 (s, 1H, 3c), 3.96 (s, 6H, 8'a), 3.86 (s, 6H, 8a), 3.51 (s, 6H, 10'a), 1.75 (s, 6H, 1c/5c).

^{13}C NMR (126 MHz, $CDCl_3$) δ 184.34 (2c/4c), 168.69 (2a), 166.42 (4a), 160.28 (4'a), 159.25 (2'a), 153.05 (1'a/6'a), 148.44 (6a), 126.62 (1'a/6'a), 110.47 (5'a), 107.51 (3a), 106.33 (5a), 100.33 (3c), 91.74 (3'a), 55.39 (8a), 55.00 (8'a), 54.63 (10'a), 28.92 (1c/5c).

6.4.7 [Ir(dMeOppy)(dFppy)(acac)] (14)

0.177 g, 0.254 mmol, yield: 38 %, m/z: calc 719.1309, found 719.1307. Anal Calcd. For $C_{29}H_{25}F_2IrN_2O_4$: C, 50.06; H, 3.62; N, 4.03. Found: C, 49.74; H, 3.34; N, 4.43.

^{1}H NMR (500 MHz, $CDCl_3$) δ 8.56 (d, *J* = 8.4 Hz, 1H, 3a), 8.50 (dd, *J* = 5.7, 0.8 Hz, 1H, 6b), 8.38 (dd, *J* = 5.7, 0.9 Hz, 1H, 6a), 8.22 (d, *J* = 8.4 Hz, 1H, 3b), 7.78 – 7.72 (m, 1H, 4b), 7.67 (ddd, *J* = 8.8, 7.5, 1.7 Hz, 1H, 4a), 7.14 (ddd, *J* = 7.2, 5.8, 1.2 Hz, 1H, 5b), 7.02 (ddd, *J* = 7.2, 5.8, 1.4 Hz, 1H, 5a), 6.32 – 6.24 (m, 1H, 3'b), 6.00 (d, *J* = 2.2 Hz, 1H, 3'a), 5.70 (dd, *J* = 9.0, 2.3 Hz, 1H, 5'b), 5.33 (d, *J* = 2.2 Hz, 1H, 5'a), 5.22 (s, 1H, 3c), 3.88 (s, 3H, 8'a), 3.50 (s, 3H, 10'a), 1.79 (s, 6H, 1c/5c).

^{13}C NMR (101 MHz, $CDCl_3$) δ 184.91 (2c/4c), 184.78 (2c/4c), 167.55 (2a), 165.76 (d, *J* = 7.1 Hz, 2b), 163.20 (dd, *J* = 183.4, 13.0 Hz, 4'b), 160.66 (dd, *J* = 187.0, 12.6 Hz, 2'b), 160.57 (4'a), 159.47 (2'a), 153.12 (d, J = 6.9 Hz, 1'b/6'b),151.15 (1'a/6'a), 148.34 (6b), 147.60 (6a), 137.44 (4b), 137.13 (4a), 128.99 – 128.74 (m, 1'b/6'b), 125.97 (1'a/6'a), 122.69 (3a), 122.41 (d, *J* = 19.1 Hz, 3b), 121.32 (5b), 119.66 (5a), 115.36 (dd, *J* = 16.7, 2.1 Hz, 5'b), 109.96 (5'a), 100.63 (3c), 96.90 (t, *J* = 26.9 Hz, 3'b), 92.08 (3'a), 55.00 (8'a), 54.63 (10'a), 28.89 (1c/5c).

^{19}F NMR (282 MHz, $CDCl_3$) δ -109.34 (d, *J* = 9.9 Hz), -111.83 (d, *J* = 9.8 Hz).

6.4.8 [Ir(dMeOppy)(dFppz)(acac)] (15)

0.142 g, 0.207 mmol, yield: 31 %, m/z: calc 708.1262, found 708.1267. Anal Calcd. For $C_{27}H_{24}F_2IrN_3O_4$: C, 47.54; H, 3.64; N, 6.12. Found: C, 47.36; H, 3.53; N, 6.14.

^{1}H NMR (500 MHz, $CDCl_3$) δ 8.55 (d, *J* = 8.5 Hz, 1H, 3a), 8.43 (dd, *J* = 5.7, 0.9 Hz, 1H, 6a), 8.31 (d, *J* = 2.8 Hz, 1H, 5b), 7.70 – 7.64 (m, 1H, 4a), 7.57 (d, *J* = 2.1 Hz, 1H, 3b), 7.01 (ddd, *J* = 7.2, 5.9, 1.3 Hz, 1H, 5a), 6.63 (t, *J* = 2.5 Hz, 1H, 4b), 6.37 (ddd, *J* = 11.6, 8.9, 2.5 Hz, 1H, 3'b), 6.01 (d, *J* = 2.2 Hz, 1H, 3'a), 5.66 (dd, *J* = 8.7, 2.3 Hz, 1H, 5'b), 5.34 (d, *J* = 2.2 Hz, 1H, 5'a), 5.23 (s, 1H, 3c), 3.88 (s, 3H, 8'a), 3.56 (s, 3H, 10'a), 1.82 (s, 3H, 1c/5c), 1.81 (s, 3H, 1c/5c).

^{13}C NMR (101 MHz, $CDCl_3$) δ 185.53 (2c/4c), 184.74 (2c/4c), 168.11 (2a), 160.81 (4'a), 159.42 (2'a), 159.40 (dd, *J* = 249.3, 11.0 Hz, 4'b), 150.25 (1'a/6'a), 149.89 (d, *J* = 13.1 Hz, 2'b), 147.76 (6a), 137.47 (3b), 137.25 (4a), 135.67 (d, *J* = 5.1 Hz, 1'b/6'b), 130.23 (d, *J* = 15.0 Hz, 5b), 128.81 (1'b/6'b), 125.89 (1'a/6'a), 122.68 (3a), 119.61 (5a), 116.61 – 116.00 (m, 5'b), 110.31 (5'a), 107.16 (4b), 100.46 (3c), 97.12 (dd, *J* = 28.1, 23.7 Hz, 3'b), 92.25 (3'a), 54.98 (8'a), 54.75 (10'a), 28.75 (1c/5c), 28.58 (1c/5c).

^{19}F NMR (282 MHz, $CDCl_3$) δ -115.24 (d, *J* = 5.5 Hz), -126.40 (d, *J* = 5.5 Hz).

6.4.9 [Ir(dMeOMeppy)(dFppy)(acac)] (16)

0.245 g, 0.371 mmol, yield: 56 %, m/z: calc 733.1466, found 733.1465. Anal Calcd. For $C_{30}H_{27}F_2IrN_2O_4$: C, 50.77; H, 3.83; N, 3.95. Found: C, 46.69; H, 3.54; N, 3.91.

^{1}H NMR (500 MHz, $CDCl_3$) δ 8.50 (dd, *J* = 5.7, 0.9 Hz, 1H, 6b), 8.38 (d, *J* = 0.6 Hz, 1H, 3a), 8.21 (d, *J* = 6.0 Hz, 2H, 6a/3b), 7.76 – 7.71 (m, 1H, 4b), 7.13 (ddd, *J* = 7.2, 5.8, 1.2 Hz, 1H, 5b), 6.87 (dd, *J* = 5.9, 1.5 Hz, 1H, 5a), 6.28 (ddd, *J* = 12.3, 9.3, 2.3 Hz, 1H, 3'b), 6.00 (d, *J* = 2.2 Hz, 1H, 3'a), 5.74 (dd, *J* = 9.0, 2.3 Hz, 1H, 5'b), 5.32 (d, *J* = 2.3 Hz, 1H, 5'a), 5.21 (s, 1H, 3c), 3.89 (s, 3H, 8'a), 3.49 (s, 3H, 10'a), 2.56 (s, 3H, 7a), 1.78 (s, *J* = 1.8 Hz, 3H, 1c/5c), 1.78 (s, 3H, 1c/5c).

^{13}C NMR (101 MHz, $CDCl_3$) δ 184.84 (2c/4c), 184.67 (2c/4c), 166.80 (2a), 165.83 (d, *J* = 7.2 Hz, 2b), 163.20 (dd, *J* = 183.2, 12.7 Hz, 4'b), 160.66 (dd, *J* = 186.7, 13.1 Hz, 2'b), 160.34 (4'a), 159.25 (2'a), 153.40 (d, *J* = 7.0 Hz, 1'b/6'b), 151.06 (1'a/6'a), 148.57 (4a), 148.37 (6b), 146.93 (6a), 137.34 (4b), 128.90 (1'b/6'b), 125.99 (1'a/6'a), 123.38 (3a), 122.35 (d, *J* = 19.4 Hz, 3b), 121.28 (5b), 120.92 (5a), 115.39 (d, *J* = 15.9 Hz, 5'b), 110.00 (5'a), 100.56 (3c), 96.77 (t, *J* = 27.0 Hz, 3'b), 92.10 (3'a), 54.99 (8'a), 54.59 (10'a), 28.89 (1c/5c), 21.83 (7a).

^{19}F NMR (282 MHz, $CDCl_3$) δ -109.51 (d, *J* = 9.9 Hz), -111.93 (d, *J* = 9.9 Hz).

6.4.10 [Ir(dMeOMeppy)(dFppz)(acac)] (17)

0.0948 g, 0.136 mmol, yield: 20 %, m/z: calc 722.1418, found 722.1423. Anal Calcd. For $C_{28}H_{26}F_2IrN_3O_4$: C, 48.13; H, 3.75; N, 6.01. Found: C, 47.56; H, 3.77; N, 5.78.

^{1}H NMR (500 MHz, $CDCl_3$) δ 8.36 (s, 1H, 3a), 8.31 (d, *J* = 2.8 Hz, 1H, 5b), 8.25 (d, *J* = 5.9 Hz, 1H, 6a), 7.56 (d, *J* = 2.1 Hz, 1H, 3b), 6.86 (dd, *J* = 5.9, 1.5 Hz, 1H, 5a), 6.62 (t, *J* = 2.5 Hz, 1H, 4b), 6.37 (ddd, *J* = 11.7, 8.9, 2.5 Hz, 1H, 3'b), 6.00 (d, *J* = 2.2 Hz, 1H, 3'a), 5.68 (dd, *J* = 8.7, 2.3 Hz, 1H, 5'b), 5.32 (d, *J* = 2.2 Hz, 1H, 5'a), 5.21 (s, 1H, 3c), 3.88 (s, 3H, 8'a), 3.55 (s, 3H, 10'a), 2.55 (s, 3H, 7a), 1.81 (s, 3H, 1c/5c), 1.80 (s, 3H, 1c/5c).

^{13}C NMR (126 MHz, $CDCl_3$) δ 185.44 (2c/4c), 184.71 (2c/4c), 167.32 (2a), 160.57 (4'a), 159.20 (2'a), 150.10 (1'a/6'a), 148.77 (4a), 147.09 (6a), 137.48 (3b), 135.85 (1'b/6'b), 130.20 (d, *J* = 15.0 Hz, 5b), 128.85 (1'b/6'b), 125.93 (1'a/6'a), 123.39 (3a), 120.92 (5a), 116.31 (d, J = 18.1 Hz, 5'b), 110.33 (5'a), 107.14 (4b), 100.45 (3c), 98.21 – 95.77 (m, 3'b), 92.30 (3'a), 55.00 (8'a), 54.74 (10'a), 28.75 (1c/5c), 28.57 (1c/5c), 21.85 (7a).

^{19}F NMR (282 MHz, $CDCl_3$) δ -115.42 (d, *J* = 5.4 Hz), -126.51 (d, *J* = 5.3 Hz).

6.4.11 [Ir(dMeOMeOppy)(dFppy)(acac)] (18)

0.233 g, 0.321 mmol, yield: 48 %, m/z: calc 749.1415, found 749.1417. Anal Calcd. For $C_{30}H_{27}F_2IrN_2O_5$: C, 49.65; H, 3.75; N, 3.86. Found: C, 49.60; H, 3.84; N, 4.14.

^{1}H NMR (500 MHz, $CDCl_3$) δ 8.51 (dd, *J* = 5.7, 0.9 Hz, 1H, 6b), 8.21 (d, *J* = 8.3 Hz, 1H, 3b), 8.17 – 8.14 (m, 2H, 3a/6a), 7.76 – 7.71 (m, 1H, 4b), 7.13 (ddd, *J* = 7.2, 5.8, 1.3 Hz, 1H, 5b), 6.65 (dd, *J* = 6.6, 2.8 Hz, 1H, 5a), 6.28 (ddd, *J* = 12.3, 9.3, 2.3 Hz, 1H, 3'b), 5.99 (d, *J* = 2.2 Hz, 1H, 3'a), 5.78 (dd, *J* = 9.0, 2.4 Hz, 1H, 5'b), 5.31 (d, *J* = 2.3 Hz, 1H, 5'a), 5.21 (s, 1H, 3c), 3.98 (s, 3H, 8a), 3.88 (s, 3H, 8'a), 3.49 (s, 3H, 10'a), 1.80 (s, 3H, 1c/5c), 1.78 (s, 3H, 1c/5c).

^{13}C NMR (126 MHz, $CDCl_3$) δ 184.87 (2c/4c), 184.66 (2c/4c), 168.15 (2a), 166.79 (4a), 165.96 (d, *J* = 6.6 Hz, 2b), 162.93 (dd, *J* = 230.0, 13.0 Hz, 4'b), 160.90 (dd, *J* = 233.7, 12.9 Hz, 2'b), 160.40 (4'a), 159.28 (2'a), 153.35 (d, *J* = 6.9 Hz, 1'b/6'b), 151.02 (1'a/6'a), 148.45 (6b), 148.14 (6a), 137.33 (4b), 129.13 – 128.85 (m, 1'b/6'b), 126.19 (1'a/6'a), 122.35 (d, *J* = 18.9 Hz, 3b), 121.30 (5b), 115.48 (d, *J* = 16.5 Hz, 5'b), 110.05 (5'a), 107.95 (3a), 106.81 (5a), 100.61 (3c), 96.76 (t, *J* = 27.0 Hz, 3'b), 92.12 (3'a), 55.49 (8a), 55.06 (8'a), 54.61 (10'a), 28.86 (1c/5c).

^{19}F NMR (282 MHz, $CDCl_3$) δ -109.45 (d, *J* = 10.1 Hz), -111.95 (d, *J* = 10.1 Hz).

6.4.12 [Ir(dMeOMeOppy)(dFppz)(acac)] (19)

0.057 g, 0.080 mmol, yield; 12%, m/z: calc 738.1367, found 738.1370. Anal Calcd. For $C_{28}H_{26}F_2IrN_3O_5$: C, 47.05; H, 3.67; N, 5.88. Found: C, 46.75; H, 3.71; N, 5.58.

^{1}H NMR (400 MHz, $CDCl_3$) δ 8.30 (d, *J* = 2.8 Hz, 1H, 5b), 8.20 (d, *J* = 6.6 Hz, 1H, 6a), 8.14 (d, *J* = 2.9 Hz, 1H, 3a), 7.57 (d, *J* = 2.2 Hz, 1H, 3b), 6.64 (dd, J = 6.6, 2.9 Hz, 1H, 5a), 6.62 (t, J = 2.5 Hz, 1H, 4b), 6.37 (ddd, *J* = 11.8, 9.0, 2.5 Hz, 1H, 3'b), 5.99 (d, *J* = 2.3 Hz, 1H, 3'a), 5.73 (dd, *J* = 8.7, 2.2 Hz, 1H, 5'b), 5.31 (d, *J* = 2.3 Hz, 1H, 5'a), 5.22 (s, 1H, 3c), 3.98 (s, 3H, 8a), 3.87 (s, 3H, 8'a), 3.55 (s, 3H, 10'a), 1.81 (s, 3H, 1c/5c), 1.80 (s, 3H, 1c/5c).

^{13}C NMR (101 MHz, $CDCl_3$) δ 185.46 (2c/4c), 184.59 (2c/4c), 168.72 (2a), 166.86 (4a), 160.63 (4'a), 159.38 (dd, *J* = 248.5, 10.3 Hz, 4'b), 159.23 (2'a), 150.19 (1'a/6'a), 148.60 (dd, *J* = 250.7, 13.2 Hz, 2'b), 148.30 (6a), 137.50 (3b), 135.98 (d, *J* = 4.9 Hz, 1'b/6'b), 130.16 (d, *J* = 14.8 Hz, 5b), 129.14 – 128.69 (m, 1'b/6'b), 126.11 (6'a), 116.83 – 116.04 (m, 5'b), 110.42 (5'a), 107.88 (3a), 107.30 – 106.96 (m, 4b), 106.78 (5a), 100.43 (3c), 96.97 (dd, *J* = 28.2, 23.8 Hz, 3'b), 92.29 (3'a), 55.50 (8a), 55.05 (8'a), 54.72 (10'a), 28.73 (1c/5c), 28.59 (1c/5c).

^{19}F NMR (282 MHz, $CDCl_3$) δ -115.36 (d, *J* = 5.5 Hz), -126.53 (d, *J* = 5.4 Hz).

6.5 Third series of complexes: 20 to 24

$IrCl_3xH_2O$ was added to a round bottomed flask containing 10 mL of a 7:3 (v/v) ethoxyethanol/water mixture. The solution was degassed by bubbling argon and the ligands were added together with 10 more mL of the ethoxyethanol/water mixture. After further degassing, the solution was placed under argon atmosphere and heated at 130°C overnight while stirring (a reflux condenser was used).

*Table 6.3: Quantity of reagents used for the syntheses of **20**, **21**, **22**, **23** and **24**.*

ligands	**20** (g, mmol, eq.)	**21** (g, mmol, eq.)	**22** (g, mmol, eq.)	**23** (g, mmol, eq.)	**24** (g, mmol, eq.)
$IrCl_3xH_2O$	0.233, 0.660, 1	0.233, 0.660, 1	0.233, 0.660, 1	0.3, 0.851, 1	0.500, 1.418, 1
Mespim	0.381, 1.452, 2.2	0.190, 0.726, 1.1	0.190, 0.726, 1.1	-	0.409, 1.560, 1.1
dFppy	-	0.139, 0.726, 1.1	-	-	-
dFppz	-	-	0.131, 0.726, 1.1	-	-
CF3ppz	-	-	-	0.399, 1.870, 2.2	0.331, 1.560, 1.1

The acac complexes were synthesized according to the procedure described above.

Complex **20** was obtain with good purity after a filtration on silica gel but excellent purity was obtained by successive crystallisation in DCM/hexane were solvent was left to evaporate slowly. Complex **23** was obtained with excellent purity with no other purification than the standard precipitation.

Complexes **21**, **22** and **24** were purified by multiple chromatography columns on silica gel and preparative TLC plates.

6.5.1.1 Ir(mespim)$_2$(acac) (20)

0.410 g, 0.494 mmol, yield: 75%. Anal Calcd. For $C_{41}H_{41}IrN_4O_2$: C, 60.50; H, 5.08; N, 6.88. Found: C, 60.18; H, 5.15; N, 6.53.

^{1}H NMR (400 MHz, $CDCl_3$) δ 7.23 (d, *J* = 1.5 Hz, 2H, 4a), 7.07 (s, 4H, 3’’a/5’’a), 6.89 (d, *J* = 1.5 Hz, 2H, 5a), 6.61 – 6.50 (m, 4H, 4’a/5’a), 6.41 (ddd, *J* = 7.7, 6.2, 2.2 Hz, 2H, 3’a), 6.14 (dd, *J* = 7.5, 1.1 Hz, 2H, 2’a), 5.23 (s, 1H, 3c), 2.42 (s, 6H, 8’’a), 2.12 (s, 6H, 7’’a), 2.04 (s, 6H, 9’’a), 1.82 (s, 6H, 1c/5c).

^{13}C NMR (101 MHz, $CDCl_3$) δ 184.49 (2c/4c), 157.98 (2a), 145.42 (1‘a/6’a), 139.56 (4’’a), 136.63 (1’a/6’a/2’’a/6’’a), 136.22 (1’a/6’a/2’’a/6’’a), 135.91 (1’a/6’a/2’’a/6’’a), 134.29 (5’a), 133.36 (1’’a), 129.60 (3’’a/5’’a), 127.73 (4’a), 126.42 (4a), 121.04 (2’a), 120.03 (3’a), 119.34 (5a), 99.95 (3c), 28.50 (1c/5c), 21.34 (8’’a), 17.83 (7’’a), 17.50 (9’’a).

6.5.2 Ir(mespim)(dFppy)(acac) (21)

0.065 g, 0.087 mmol, yield: 13%. m/z: calc 766.1833, found 766.1821. Anal Calcd. For $C_{34}H_{30}IrF_2N_3O_2$: C, 54.97; H, 4.07; N, 5.66. Found: C, 55.05; H, 4.36; N, 5.45.

^{1}H NMR (400 MHz, $CDCl_3$) δ 8.64 (ddd, *J* = 5.8, 1.7, 0.8 Hz, 1H, 6b), 8.25 – 8.21 (m, 1H, 3b), 7.76 – 7.69 (m, 1H, 4b), 7.16 (d, *J* = 1.6 Hz, 1H, 4a), 7.12 (ddd, *J* = 7.3, 5.7, 1.4 Hz, 1H, 5b), 7.07 (d, *J* = 5.5 Hz, 2H, 3’’a/5’’a), 6.91 (d, *J* = 1.6 Hz, 1H, 5a), 6.55 (td, *J* = 7.4, 1.5 Hz, 1H, 4’a), 6.46 (td, *J* = 7.5, 1.3 Hz, 1H, 3’a), 6.29 (ddd, *J* = 12.6, 9.3, 2.4 Hz, 1H, 3’b), 6.14 (dd, *J* = 7.7, 1.1 Hz, 1H, 2’a), 6.10 (ddd, *J* = 9.1, 4.6, 1.6 Hz, 2H, 5’a/5’b), 5.25 (s, 1H, 3c), 2.42 (s, 3H, 8’’a), 2.12 (s, 3H, 7’’a), 2.00 (s, 3H, 9’’a), 1.85 (s, 3H1c), 1.80 (s, 3H, 5c).

^{13}C NMR (101 MHz, $CDCl_3$) δ 185.30 (2c/4c), 184.80 (2c/4c), 166.43 (d, *J* = 6.9 Hz, 2b), 163.27 (dd, *J* = 195.0, 12.9 Hz, 4’b), 160.72 (dd, *J* = 199.0, 13.0 Hz, 2’b), 157.06 (2a), 153.52 (d, *J* = 6.9 Hz, 1’b/6’b), 148.45 (6b), 143.42 (1’a/6’a), 139.88 (4’’a), 137.09 (4b), 136.19 (1’a/6’a/2’’a/6’’a), 136.00 (1’a/6’a/2’’a/6’’a), 135.75 (1’a/6’a/2’’a/6’’a), 133.21 (5’a), 133.04 (1’’a), 129.76 (3’’a/5’’a), 129.69 (3’’a/5’’a), 128.94 (1’b/6’b), 128.02 (4’a), 126.26 (4a), 122.36 (d, *J* = 18.7 Hz, 3b), 121.37 (2’a/5b), 121.07 (3’a), 119.88 (5a), 116.02 – 115.60 (m, 5’b), 100.44 (3c), 96.39 (t, *J* = 27.0 Hz, 3’b), 28.64 (1c/5c), 28.62 (1c/5c), 21.36 (8’’a), 17.79 (7’’a), 17.34 (9’’a).

^{19}F NMR (282 MHz, $CDCl_3$) δ -110.07 (q, *J* = 9.4 Hz), -112.07 – -112.25 (m).

6.5.3 Ir(mespim)(dFppz)(acac) (22)

0.133 g, 0.181 mmol, yield: 27%. m/z: calc 755.1786, found 755.1782. Anal Calcd. For $C_{32}H_{29}IrF_2N_4O_2$: C, 52.52; H, 3.99; N, 7.66. Found: C, 52.34; H, 4.47; N, 7.57.

^{1}H NMR (400 MHz, $CDCl_3$) δ 8.33 (d, *J* = 2.9 Hz, 1H, 5b), 7.63 (d, *J* = 2.2 Hz, 1H, 3b), 7.16 (d, *J* = 1.5 Hz, 1H, 4a), 7.07 (d, *J* = 3.3 Hz, 2H, 3’’a/5’’a), 6.90 (d, *J* = 1.6 Hz, 1H, 5a), 6.64 (t, *J* = 2.6 Hz, 1H, 4b), 6.58 (td, *J* = 7.4, 1.5 Hz, 1H, 4’a), 6.47 (td, *J* = 7.5, 1.3 Hz, 1H, 3’a), 6.37 (ddd, *J* = 11.8, 9.0, 2.5 Hz, 1H, 3’b), 6.14 (dd, *J* = 7.7, 1.3 Hz, 1H, 2’a), 6.11 (dd, *J* = 7.6, 1.2 Hz, 1H, 5’a), 6.02 (dd, *J* = 8.8, 2.5 Hz, 1H, 5’b), 5.25 (s, 1H, 3c), 2.42 (s, 3H, 8’’a), 2.11 (s, 3H, 7’’a), 2.00 (s, 3H, 9’’a), 1.87 (s, 3H, 1c), 1.80 (s, 3H, 5c).

^{13}C NMR (101 MHz, $CDCl_3$) δ 185.22 (2c/4c), 185.08 (2c/4c), 159.42 (dd, *J* = 248.6, 10.9 Hz, 4’b), 157.67 (2a), 148.53 (dd, *J* = 250.8, 13.3 Hz, 2’b), 142.59 (1’a/6’a), 139.91 (4’’a), 137.31 (3b), 136.14 (d, J = 1.8 Hz, 1’b/6’b), 136.01 (d, J = 6.3 Hz, 1’a/6’a/2’’a/6’’a), 135.71 (1’a/6’a/2’’a/6’’a), 134.05 (5’’a), 132.95 (1’’a), 130.21 (d, *J* = 14.5 Hz, 5b), 129.75 (3’’a/5’’a), 129.71 (3’’a/5’’a), 128.93 (1’b/6’b), 128.23 (4’a), 126.24 (4a), 121.33 (2’a), 121.19 (3’a), 119.83 (5a), 116.79 (d, *J* = 19.7 Hz, 5’b), 107.47 – 106.83 (m, 4b), 100.27 (3c), 96.67 (dd, *J* = 28.2, 23.8 Hz, 3’b), 28.53 (1c), 28.37 (5c), 21.35 (8’’a), 17.77 (7’’a), 17.38 (9’’a).

^{19}F NMR (282 MHz, $CDCl_3$) δ -116.04 (d, *J* = 5.3 Hz), -126.77 (d, *J* = 5.2 Hz).

6.5.3.1 Ir(CF$_3$ppz)$_2$(acac) (23)

0.509 g, 0.713 mmol, yield: 84%. m/z: calc 737.0939, found 737.0944. Anal Calcd. For $C_{25}H_{19}IrF_6N_4O_2$: C, 42.08; H, 2.68; N, 7.85. Found: C, 42.00; H, 2.51; N, 7.79.

^{1}H NMR (400 MHz, $CDCl_3$) δ 8.28 (s, 2H, 5a), 7.83 (s, 2H, 3a), 7.12 (dd, *J* = 7.9, 1.2 Hz, 2H, 2'a), 6.83 (td, *J* = 7.7, 1.4 Hz, 2H, 3'a), 6.72 (td, *J* = 7.4, 1.3 Hz, 2H, 4'a), 6.25 (dd, *J* = 7.5, 1.3 Hz, 2H, 5'a), 5.30 (s, 1H, 3c), 1.86 (s, 6H, 1c/5c).

^{13}C NMR (101 MHz, $CDCl_3$) δ 185.87 (2c/4c), 143.37 (1'a/6'a), 135.64 (q, *J* = 3.4 Hz, 3a), 134.98 (5'a), 128.25 (1'a/6'a), 126.76 (4'a), 124.89 (q, *J* = 3.9 Hz, 5a), 122.11 (3'a), 121.83 (q, *J* = 266.7 Hz, 6a), 114.65 (q, *J* = 39.8 Hz, 4a), 111.41 (2'a), 100.65 (3c), 28.45 (1c/5c).

^{19}F NMR (282 MHz, $CDCl_3$) δ -56.91 (s).

6.5.4 Ir(mespim)(CF_3ppz)(acac) (24)

0.224 g, 0.293 mmol, yield: 20%. m/z: calc 787.1848, found 787.1851. Anal Calcd. For $C_{33}H_{30}IrF_3N_4O_2$: C, 51.89; H, 3.96; N, 7.34. Found: C, 51.68; H, 3.96; N, 7.06.

^{1}H NMR (400 MHz, $CDCl_3$) δ 8.31 (s, 1H, 5b), 7.88 (s, 1H, 3b), 7.17 (dd, *J* = 9.4, 1.2 Hz, 2H, 4a/2'b), 7.08 (s, 2H, 3''a/5''a), 6.90 (d, *J* = 1.6 Hz, 1H, 5a), 6.83 (td, *J* = 7.6, 1.4 Hz, 1H, 3'b), 6.74 (td, *J* = 7.4, 1.3 Hz, 1H, 4'b), 6.62 (dd, *J* = 7.5, 1.4 Hz, 1H, 5'b), 6.57 (td, *J* = 7.4, 1.4 Hz, 1H, 4'a), 6.45 (td, *J* = 7.5, 1.3 Hz, 1H, 3'a), 6.14 (td, *J* = 7.7, 1.2 Hz, 2H, 2'a/5'a), 5.26 (s, 1H, 3c), 2.42 (s, 3H, 8''a), 2.11 (s, 3H, 7''a), 2.01 (s, 3H, 9''a), 1.86 (s, 3H, 1c), 1.81 (s, 3H, 5c).

^{13}C NMR (101 MHz, $CDCl_3$) δ 185.33 (2c/4c), 185.15 (2c/4c), 157.59 (2a), 143.93 (1'b/6'b), 142.95 (1'a/6'a), 139.89 (4''a), 136.05 (1'a/6'a/2''a/6''a), 135.99 (1'a/6'a/2''a/6''a), 135.65 (1'a/6'a/2''a/6''a), 135.41 (d, *J* = 5.7 Hz, 3b/4'b/5'b), 133.88 (5'a), 132.97 (1''a), 130.84 (1'b/6'b), 129.74 (3''a/5''a), 129.69 (3''a/5''a), 128.26 (4'a), 126.28 (4a/4'b), 126.18 (4a/4'b), 124.54 (q, *J* = 3.9 Hz, 5b), 122.10 (q, *J* = 266.7 Hz, 6b), 121.33 (2'a), 121.08 (3'b), 121.01 (3'a), 119.67 (5a), 114.28 (q, *J* = 39.5 Hz, 4b), 111.10 (2'b), 100.30 (3c), 28.49 (1c/5c), 28.44 (1c/5c), 21.34 (8''a), 17.77 (7''a), 17.37 (9''a).

^{19}F NMR (282 MHz, $CDCl_3$) δ -56.80 (s).

6.6 Fourth series of complexes: 3a/b and 9a/b

6.6.1 Synthesis of [Ir(dFppy)(ppy)(MeCN)$_2$][PF$_6$] (3MeCN)

In a 50 mL RB flask, complex **3** (0.050 g, 0.078 mmol) was dissolved in dry MeCN (10 mL) and the mixture was deaerated by bubbling argon for 15 minutes. The flask was sealed under argon atmosphere, BF_3 (0.1 mL) was added and the mixture was stirred at RT for 1 hour. The flask was open and an aqueous solution of KPF_6 (30 mL) was added carefully to the solution under vigorous stirring. The mixture was stirred for an additional half hour and the MeCN was slowly evaporated under vacuum until a yellow precipitate formed. The flask was left in the fridge for 2 hours and the precipitate was filtered and washed with water to remove the excess KPF_6. The yellow product was dried on the filter under vacuum and dissolved and removed from the filter by dissolution in DCM. The DCM was evaporated under vacuum and product was harvested as a yellow solid (0.055 g, 0.072 mmol, yield: 92%)

^{1}H NMR (400 MHz, CD_3CN) δ 9.15 (ddd, *J* = 5.7, 1.6, 0.8 Hz, 1H), 9.05 (ddd, *J* = 5.9, 1.4, 0.9 Hz, 1H), 8.32 (dt, *J* = 8.4, 2.2 Hz, 1H), 8.14 – 8.02 (m, 3H), 7.68 (dd, *J* = 7.7, 1.3 Hz, 1H), 7.53 – 7.43 (m, 2H), 6.94 (td, *J* = 7.6, 1.2 Hz, 1H), 6.78 (td, *J* = 7.5, 1.4 Hz, 1H), 6.51 (ddd, *J* = 12.8, 9.4, 2.4 Hz, 1H), 6.03 (dd, *J* = 7.6, 0.7 Hz, 1H), 5.56 (dd, *J* = 8.8, 2.4 Hz, 1H), 1.96 (s, 6H).

6.6.2 Synthesis of [Ir(dFppy)(ppy)(pic)] (3a & 3b)

In a 250 mL RB flask, **3MeCN** (0.3 g, 0.393 mmol, 1 equiv.) was dissolved in 50 mL of DCM and the mixture was deaerated by bubbling argon for 15 minutes. TBAOHx30H_2O (0.8 g, 1 mmol, 2.5 equiv.) was added. Picolinic acid (0.074 g, 0.6 mmol, 1.5 equiv.) was added and the mixture heated to reflux overnight under argon atmosphere.

The heating was stopped and the solvent was evaporated to dryness. The solid was suspended in 30 mL of MeOH, precipitated with water (100 mL) and left in the fridge for 2 hours. The precipitate was filtered and washed with water (200 mL) and freezer cold MeOH (20 mL). The isomers mixture was dried and harvested as a yellow solid (0.1819 g, 0.276 mmol, yield: 70%).

The diastereomers were separated by preparative HPLC. 0.5 mL of a MeCN solution of the **3a** & **3b** mixture (10mg/mL, 0.015 M) was injected in the column and eluted at RT with a MeCN/water (40/60) mixture. Four injections were made per method (one every 20 minutes) and the method was repeated. The products were harvested in the middle of the two peaks. Because the peaks are not well separated, a second round of purification was necessary to obtain the pure products.

6.6.3 [Ir(dFppy)(ppy)(pic)] (3a)

0.077 g, 0.119 mmol, yield: 30%, m/z: calc 682.0894, found 682.0884. Anal Calcd. For $C_{28}H_{18}F_2IrN_3O_2$: C, 51.06; H, 2.75; N, 6.38. Found: C, 50.97; H, 2.95; N, 6.34.

^{1}H NMR (400 MHz, $CDCl_3$) δ 8.74 – 8.71 (m, 1H, 6b), 8.33 (dt, *J* = 8.2, 1.0 Hz, 1H, 3c), 8.27 (dt, *J* = 7.5, 1.4 Hz, 1H, 3a), 7.90 (td, *J* = 7.7, 1.6 Hz, 1H, 4c), 7.86 (dt, *J* = 8.2, 1.0 Hz, 1H, 3b), 7.79 – 7.69 (m, 3H, 4a/4b/6c), 7.64 (dd, *J* = 7.8, 1.3 Hz, 1H, 2'b), 7.48 (dd, *J* = 5.8, 0.9 Hz, 1H, 6a), 7.34 (ddd, *J* = 7.3, 5.3, 1.4 Hz, 1H, 5c), 7.16 (ddd, *J* = 7.1, 5.8, 1.3 Hz, 1H, 5b), 6.99 (td, *J* = 7.5, 1.2 Hz, 1H, 3'b), 6.94 (ddd, *J* = 7.3, 5.8, 1.4 Hz, 1H, 5a), 6.85 (td, *J* = 7.4, 1.4 Hz, 1H, 4'b), 6.40 – 6.30 (m, 2H, 5'b/3'a), 5.63 (dd, *J* = 8.9, 2.4 Hz, 1H, 5'a).

^{13}C NMR (101 MHz, $CDCl_3$) δ 172.84 (7c), 167.54 (2b), 166.15 (d, *J* = 7.0 Hz, 2a), 163.61 (dd, *J* = 194.0, 12.9 Hz, 4'a), 161.05 (dd, *J* = 197.6, 12.5 Hz, 2'a), 154.15 (d, *J* = 6.7 Hz, 1'a/6'a), 152.14 (2c), 148.92 (6b), 148.41 (6c), 148.17 (6a), 146.43 (1'b/6'b), 144.06 (1'b/6'b), 138.05 (4a/4b/4c), 137.89 (4a/4b/4c), 137.75 (4a/4b/4c), 132.58 (5'b), 130.31 (4'b), 128.51 (3c), 128.24 (5c), 124.68 (2'b), 123.21 (d, *J* = 20.0 Hz, 3a), 122.66 (5b), 122.12 (5a), 121.79 (3'b), 118.88 (3'b), 114.57 (dd, *J* = 17.2, 2.6 Hz, 5'a), 97.73 (t, *J* = 26.9 Hz, 3'a).

^{19}F NMR (282 MHz, $CDCl_3$) δ -108.66 (d, *J* = 10.3 Hz), -110.97 (d, *J* = 10.3 Hz).

6.6.4 [Ir(dFppy)(ppy)(pic)] (3b)

0.047 g, 0.073 mmol, yield: 19%, m/z: calc 682.0894, found 682.0884. Anal Calcd. For $C_{28}H_{18}F_2IrN_3O_2$: C, 51.06; H, 2.75; N, 6.38. Found: C, 51.46; H, 3.29; N, 6.25.

^{1}H NMR (400 MHz, $CDCl_3$) δ 8.80 (ddd, *J* = 5.8, 1.7, 0.8 Hz, 1H, 6a), 8.33 (ddd, *J* = 7.8, 1.5, 0.8 Hz, 1H, 3c), 8.22 (dd, *J* = 8.4, 1.8 Hz, 1H, 3a), 7.96 – 7.88 (m, 2H, 3'b/4c), 7.81 (ddd, *J* = 5.3, 1.6, 0.8 Hz, 1H, 6c), 7.79 – 7.69 (m, 2H, 4a/4b), 7.60 (dd, *J* = 7.8, 1.4 Hz, 1H, 2'b), 7.44 – 7.38 (m, 2H, 6b/5c), 7.15 (ddd, *J* = 7.3, 5.8, 1.4 Hz, 1H, 5a), 6.97 – 6.88 (m, 2H, 5b/3'b), 6.79 (td, *J* = 7.5, 1.4 Hz, 1H, 4'b), 6.42 (ddd, *J* = 12.5, 9.2, 2.4 Hz, 1H, 3'a), 6.12 (dd, *J* = 7.6, 1.2 Hz, 1H, 5'b), 5.87 (dd, *J* = 8.9, 2.4 Hz, 1H, 5'a).

^{13}C NMR (101 MHz, $CDCl_3$) δ 172.95 (7c), 169.16 (2b), 164.68 (d, *J* = 6.5 Hz, 2a), 163.76 (dd, *J* = 221.1, 13.2 Hz, 4'a), 161.20 (dd, *J* = 224.4, 13.1 Hz, 2'a), 152.60 (d, *J* = 6.9 Hz, 1'a/6'a), 152.11 (2c), 149.06 (6a), 148.47 (6c), 148.02 (6b), 147.85 (1'b/6'b), 144.24 (1'b/6'b), 138.08 (4c), 137.83 (4a/4b), 137.77 (4a/4b), 132.47 (5'b), 129.86 (4'b), 128.54 (3c), 128.32 (5c), 124.39 (2'b), 122.58 (d, *J* = 18.7 Hz, 3a), 122.46 – 122.17 (m, 5a/5b/3'b), 119.49 (3b), 114.74 (d, *J* = 16.4 Hz, 5'a), 97.27 (t, *J* = 26.9 Hz, 3'a).

^{19}F NMR (282 MHz, $CDCl_3$) δ -107.84 (d, *J* = 10.5 Hz), -110.46 (d, *J* = 10.6 Hz).

6.6.5 Synthesis of [Ir(dFppy)(ppz)(MeCN)$_2$][PF$_6$] (9MeCN)

In a 250 mL RB flask, complex **9** (0.254 g, 0.407 mmol) was dissolved in dry MeCN (50 mL) and the mixture was deaerated by bubbling argon for 15 minutes. The flask was sealed under argon atmosphere, BF_3 (1 mL) was added and the mixture was stirred at RT for 1 hour. The flask was open and an aqueous solution of KPF_6 (100 mL) was added carefully to the solution under vigorous stirring. The mixture was stirred for an additional half hour and the MeCN was slowly evaporated under vacuum until a yellow precipitate formed. The flask was left in the fridge for 2 hours and the precipitate was filtered and washed with water to remove the excess KPF_6. The yellow product was dried on the filter under vacuum and dissolved and removed from the filter by dissolution in DCM. The DCM was evaporated under vacuum and the product was harvested as a yellow solid (0.366 g, 0.486 mmol, yield: quantitative)

^{1}H NMR (400 MHz, CD_3CN) δ 9.14 (ddd, *J* = 5.8, 1.6, 0.8 Hz, 1H), 8.44 (dd, *J* = 2.9, 0.6 Hz, 1H), 8.31 (dt, *J* = 8.4, 2.2 Hz, 1H), 8.15 (dd, *J* = 2.3, 0.6 Hz, 1H), 8.12 – 8.06 (m, 1H), 7.49 (ddd, *J* = 7.4, 5.8, 1.4 Hz, 1H), 7.39 (dd, *J* = 7.9, 1.2 Hz, 1H), 7.01 – 6.91 (m, 1H), 6.89 (dd, *J* = 2.9, 2.3 Hz, 1H), 6.70 (td, *J* = 7.5, 1.2 Hz, 1H), 6.53 (ddd, *J* = 12.7, 9.4, 2.4 Hz, 1H), 6.02 (dd, *J* = 7.6, 1.3 Hz, 1H), 5.54 (dd, *J* = 8.8, 2.4 Hz, 1H), 1.96 (s, 6H).

6.6.6 Synthesis of [Ir(dFppy)(ppz)(pic)] (9a & 9b)

In a 250 mL RB flask, **9MeCN** (0.1 g, 0.133 mmol, 1 equiv.) was dissolved in 50 mL of DCM and the mixture was deaerated by bubbling argon for 15 minutes. TBAOHx30H_2O (0.266 g, 0.332 mmol, 2.5 equiv.) was added. Picolinic acid (0.025 g, 0.12 mmol, 1.5 equiv.) was added and the mixture heated to reflux overnight under argon atmosphere.

The heating was stopped and the solvent was evaporated to dryness. The solid was suspended in 30 mL of MeOH, precipitated with water (100 mL) and left in the fridge for 2 hours. The precipitate was filtered and washed with water (200 mL) and freezer cold MeOH (20 mL). The diastereomer mixture was dried and harvested as a yellow solid (0.094 g, 0.145 mmol, yield: quantitative).

The diastereomers were separated by preparative HPLC. 0.5 mL of a MeCN solution of the **9a** & **9b** mixture (10mg/mL, 0.015 M) was injected in the column and eluted at RT with a MeCN/water (45/55) mixture. Up to twelve injections were made per method (one every 10 minutes) and the method was repeated.

6.6.7 [Ir(dFppy)(ppz)(pic)] (9a)

0.035 g, 0.054 mmol, yield: 41%, m/z: calc 671.0846, found 671.0833. Anal Calcd. For $C_{26}H_{17}F_2IrN_4O_2$: C, 48.22; H, 2.65; N, 8.65. Found: C, 46.57; H, 2.72; N, 7.96.

^{1}H NMR (400 MHz, $CDCl_3$) δ 8.34 (dd, *J* = 7.9, 1.0 Hz, 1H, 3c), 8.25 (dd, *J* = 8.6, 1.6 Hz, 1H, 3a), 8.07 (d, *J* = 2.6 Hz, 1H, 5b), 7.93 (td, *J* = 7.7, 1.6 Hz, 1H, 4c), 7.83 (dd, *J* = 5.3, 0.8 Hz, 1H, 6c), 7.79 – 7.70 (m, 2H, 4a/3b), 7.56 (dd, *J* = 5.9, 0.9 Hz, 1H, 6a), 7.37 (ddd, *J* = 7.0, 5.3, 1.4 Hz, 1H, 5c), 7.24 (dd, *J* = 8.0, 1.0 Hz, 1H, 2'b), 6.98 (td, *J* = 7.7, 1.3 Hz, 1H, 3'b), 6.94 (ddd, *J* = 7.3, 5.8, 1.4 Hz, 1H, 5a), 6.78 (td, *J* = 7.5, 1.2 Hz, 1H, 4'b), 6.63 – 6.57 (m, 1H, 4b), 6.41 – 6.29 (m, 2H, 3'a/5'b), 5.68 (dd, *J* = 8.8, 2.4 Hz, 1H, 5'a).

^{13}C NMR (101 MHz, $CDCl_3$) δ 173.02 (7c), 166.61 (d, *J* = 6.3 Hz, 2a), 163.61 (dd, *J* = 212.7, 12.9 Hz, 4'a), 161.06 (dd, *J* = 216.2, 12.7 Hz, 2'a), 153.30 (d, *J* = 6.7 Hz, 1'a/6'a), 152.20 (2c), 148.51 (6a), 148.06 (6c), 143.74 (1'b/6'b), 138.24 (4c), 138.00 (4a/3b), 137.97 (4a/3b), 133.70 (5'b), 128.57 (3c), 128.24 (1'b/6'b), 128.13 (5c), 126.29 (5b/4'b), 123.15 (d, *J* = 19.9 Hz, 3a), 122.33 (3'b), 122.04 (5a), 115.18 (dd, *J* = 17.3, 2.4 Hz, 5'a), 111.38 (2'b), 107.88 (4b), 97.84 (t, *J* = 27.0 Hz, 3'a).

^{19}F NMR (282 MHz, $CDCl_3$) δ -108.28 (d, *J* = 10.5 Hz), -111.10 (d, *J* = 10.3 Hz).

6.6.8 [Ir(dFppy)(ppz)(pic)] (9b)

0.041 g, 0.063 mmol, yield: 48%, m/z: calc 671.0846, found 671.0833. Anal Calcd. For $C_{26}H_{17}F_2IrN_4O_2$: C, 48.22; H, 2.65; N, 8.65. Found: C, 48.16; H, 2.70; N, 8.57.

^{1}H NMR (400 MHz, $CDCl_3$) δ 8.88 (dd, *J* = 5.8, 0.9 Hz, 1H, 6a), 8.32 (dt, *J* = 7.7, 1.1 Hz, 1H, 3c), 8.21 (d, *J* = 8.3 Hz, 1H, 3a), 8.08 (d, *J* = 2.8 Hz, 1H, 5b), 7.92 (td, *J* = 7.7, 1.6 Hz, 1H, 4c), 7.87 (d, *J* = 5.4 Hz, 1H, 6c), 7.80 – 7.71 (m, 1H, 4a), 7.38 (ddd, *J* = 7.4, 5.3, 1.5 Hz, 1H, 5c), 7.24 – 7.12 (m, 2H, 5a/2'b), 6.91 (td, *J* = 7.7, 1.4 Hz, 1H, 3'b), 6.76 – 6.66 (m, 2H, 4'b/3b), 6.51 (t, *J* = 2.5 Hz, 1H, 4b), 6.43 (ddd, *J* = 12.1, 9.2, 2.4 Hz, 1H, 3'a), 6.12 (dd, *J* = 7.5, 1.1 Hz, 1H, 5'b), 5.87 (dd, *J* = 8.8, 2.4 Hz, 1H, 5'a).

^{13}C NMR (101 MHz, $CDCl_3$) δ 173.02 (7c), 165.13 (d, *J* = 7.0 Hz, 2a), 163.74 (dd, *J* = 234.1, 13.0 Hz, 4'a), 161.18 (dd, *J* = 237.4, 12.7 Hz, 2'a), 152.64 (2c), 151.72 (d, *J* = 7.1 Hz, 1'a/6'a), 149.46 (6a), 149.26 (6c), 143.74 (1'b/6'b), 138.02 (4c), 137.89 (4a), 137.08 (3b), 133.60 (5'b), 130.27 (1'b/6'b), 128.18 (3c), 127.84 (5c), 126.49 (5b), 125.93 (4'b), 122.72 (3'b), 122.55 (d, *J* = 18.8 Hz, 3a), 122.23 (5a), 115.03 (dd, *J* = 17.0, 2.3 Hz, 5'a), 111.23 (2'b), 107.79 (4b), 97.44 (t, *J* = 26.8 Hz, 3'a).

^{19}F NMR (282 MHz, $CDCl_3$) δ -107.51 (d, *J* = 10.3 Hz), -110.54 (d, *J* = 10.5 Hz).

6.7 Screening experiments

The emission spectra were measured on a BMG LABTECH CLARIOstar microplate reader.

A chloro-bridged dimer or a bis-MeCN complex was weighted and transferred to a volumetric flask and dissolved in DCM. Each ligand was weighted in a 28 mL vial and dissolved in 15 mL of DCM. A solution of TBAOH was also prepared in a 100 mL volumetric flask.

In a 3 mL vial, 1mL of the dimer/bis-MeCN complex was added together with 1mL of the ligand solution and 1mL of DCM or of the TBAOH solution (depending on the ligand properties). The vial was close, shaked vigorously for a few seconds and left overnight at room temperature and protected from light.

The reaction solutions were then transferred to their corresponding microplate well and left to dry before recording the spectra.

7 ABBREVIATION LIST

acac	acetylacetonate
Na(acac)acacNa	sodium acetylacetonate
Alq_3	tris(8-hydroxyquinolinato)aluminium
BCP	bathocuproine
bpy	2,2'-bipyridine
BTZ	2-(2-(hydroxyphenyl)benzothiazole
CBP	4,4′-bis(*N*-carbazolyl)biphenyl
CF_3ppz	1-phenyl-4-(trifluoromethyl)pyrazole
CIE	commission internationale de l'éclairage
COD	cyclooctadiene
COSY	COrrelated SpectroscopY
DCM	dichloromethane, CH_2Cl_2
dFppy	2-(2,4-difluorophenyl)pyridine
dFppz	1-(2,4-difluorophenyl) pyrazole
DFT	density functional theory
DGME	diethylene glycol methyl ether
dMeOppy	2-(2,4-dimethoxyphenyl)pyridine
dMeOMeppy	2-(2,4-dimethoxyphenyl)-4-methylpyridine
dMeOMeOppy	2-(2,4-dimethoxyphenyl)-4-methoxypyridine
DMF	*N*,*N*-dimethylformamide
dtb-bpy	4,4'-di-tert-butyl-2,2'-bipyridine
EtOH	ethanol
eV	electronvolt
fac	facial

Fc^+/Fc	ferrocenium/ferrocene
HOMO	highest occupied molecular orbital
H2BC	Heteronuclear 2 Bond Correlation
HMBC	Heteronuclear Multiple Bond Correlation
HPLC	High Pressure Liquid Chromatography
HSQC	Heteronuclear Single Quantum Correlation
ISC	inter-system crossing
ITO	Indium Tin Oxide
LC	ligand centred
LEC/LEEC	light emitting electrochemical cell
LUMO	lowest unoccupied molecular orbital
MC	metal centred
MeCN	acetonitrile, CH_3CN
MeOH	methanol
mer	meridional
mespim	1-mesityl-2-phenylimidazole
MLCT	metal to ligand charge transfer
nm	nanometer
NMR	Nuclear Magnetic Resonance
NOESY	Nuclear Overhauser Effect SpectroscopY
OLED	organic light emitting diode
phen	1,10-phenanthroline
phi	phenanthrene-9,10-diimine
pic	picolinate
pmma	poly(methyl methacrylate)

piq-F	1-(4-fluorophenyl)isoquinoline
Ppy	phenylpyridine
Ppz	phenylpyrazole
R_f	retention factor (for TLC)
RT	room temperature
s	second
SOC	spin-orbit coupling
TBA	Tetrabutylammonium
TD-DFT	time-dependent density functional theory
TFA	2,2,2-trifluoroacetic acid
OTf	Triflate
TPD	N,N′-Bis(3-methylphenyl)-N,N′-diphenylbenzidine
TLC	thin layer chromatography
V	Volts

8 BIBLIOGRAPHY

(1) Fouquet, R.; Pearson, P. J. G. *Energy J.* **2006**, *27*, 139.

(2) Tsao, J. Y.; Waide, P. *Leukos* **2010**, *6*, 259.

(3) USDOE. *Buildings R & D Breakthroughs: Technologies and Products Supported by the Building Technologies Program*; **2012**.

(4) Takei, Y. *Sci. Technol. Trends–Quarterly Rev.* **2009**, *32*, 59.

(5) World Energy Council. *World Energy Resources: **2013** survey*; World Energy council: London, 2013.

(6) U.S. Energy Information Administration. *International Energy Outlook 2016*; **2016**.

(7) Tsao, J. Y.; Saunders, H. D.; Creighton, J. R.; Coltrin, M. E.; Simmons, J. A. *J. Phys. D Appl. Phys.* **2010**, *43*, 354001.

(8) Farinola, G. M.; Ragni, R. *Chem. Soc. Rev.* **2011**, *40*, 3467.

(9) Brütting, W.; Frischeisen, J.; Schmidt, T. D.; Scholz, B. J.; Mayr, C. *Phys. Status Solidi A* **2012**, *22*, 1.

(10) Hu, T.; He, L.; Duan, L.; Qiu, Y. *J. Mater. Chem.* **2012**, *22*, 4206.

(11) Miller, N. J.; Leon, F. A. *OLED Lighting Products: Capabilities, Challenges, Potential*; **2016**.

(12) Kappaun, S.; Slugovc, C.; List, E. J. W. *Int. J. Mol. Sci.* **2008**, *9*, 1527.

(13) Slinker, J. D.; Rivnay, J.; Moskowitz, J. S.; Parker, J. B.; Bernhard, S.; Abruña, H. D.; Malliaras, G. G. *J. Mater. Chem.* **2007**, *17*, 2976.

(14) Tordera, D.; Meier, S.; Lenes, M.; Costa, R. D.; Ortí, E.; Sarfert, W.; Bolink, H. J. *Adv. Mater.* **2012**, *24*, 897.

(15) Costa, R. D.; Ortí, E.; Bolink, H. J.; Monti, F.; Accorsi, G.; Armaroli, N. *Angew. Chem. Int. Ed.* **2012**, *51*, 8178.

(16) Pei, Q.; Yu, G.; Zhang, C.; Yang, Y.; Heeger, A. J. *Science* **1995**, *269*, 1086.

(17) Maness, K. M.; Terrill, R. H.; Meyer, T. J.; Murray, R. W.; Wightman, R. M. *J. Am. Chem. Soc.* **1996**, *118*, 10609.

(18) Rothe, C.; Chiang, C.-J.; Jankus, V.; Abdullah, K.; Zeng, X.; Jitchati, R.; Batsanov, A. S.; Bryce, M. R.; Monkman, A. P. *Adv. Funct. Mater.* **2009**, *19*, 2038.

(19) Sun, L.; Galan, A.; Ladouceur, S.; Slinker, J. D.; Zysman-Colman, E. *J. Mater. Chem.* **2011**, *21*, 18083.

(20) Scaiano, J. C.; Ramamurthy, V.; Turro, N. J. *Principles of Molecular Photochemistry: An Introduction*; 1st ed.; University Science Books: Sausalito, **2009**.

(21) *Higly Efficient OLEDs with Phosphorescent Materials*; Yersin, H., Ed.; 1st ed.; Wiley-VCH Verlag GmbH & Co. KGaA: Weinheim, **2008**.

(22) Baldo, M. A.; Forrest, S. R. *Nature* **1998**, *395*, 151.

(23) Shuai, Z.; Beljonne, D.; Silbey, R. J.; Brédas, J. L. *Phys. Rev. Lett.* **2000**, *84*, 131.

(24) Wohlgenannt, M.; Vardeny, Z. V. *J. Phys. Condens. Mater.* **2003**, *15*, 83.

(25) Yersin, H.; Rausch, A. F.; Czerwieniec, R.; Hofbeck, T.; Fischer, T. *Coord. Chem. Rev.* **2011**, *255*, 2622.

(26) Kozhevnikov, D. N.; Kozhevnikov, V. N.; Shafikov, M. Z.; Prokhorov, A. M.; Bruce, D. W.; Williams, J. A. G. *Inorg. Chem.* **2011**, *50*, 3804.

(27) Adachi, C.; Baldo, M. A.; Thompson, M. E.; Forrest, S. R. *J. Appl. Phys.* **2001**, *90*, 5048.

(28) Crabtree, R. H. *The Organometallic Chemistry of the Transition Metals*; John Wiley & Sons, I., Ed.; 4th ed.; John Wiley & Sons, Inc: New Haven, **2005**.

(29) Sprouse, S.; King, K. A.; Spellane, P. J.; Watts, R. J. *J. Am. Chem. Soc.* **1984**, *106*, 6647.

(30) Nonoyama, M. *J. Organomet. Chem.* **1975**, *86*, 263.

(31) Lamansky, S.; Djurovich, P.; Murphy, D.; Abdel-Razzaq, F.; Kwong, R.; Tsyba, I.; Bortz, M.; Mui, B.; Bau, R.; Thompson, M. E. *Inorg. Chem.* **2001**, *40*, 1704.

(32) Lamansky, S.; Djurovich, P.; Murphy, D.; Abdel-razzaq, F.; Lee, H.; Adachi, C.; Burrows, P. E.; Forrest, S. R.; Thompson, M. E. *J. Am. Chem. Soc.* **2001**, *123*, 4304.

(33) Ohsawa, Y.; Sprouse, S.; King, K. A.; DeArmond, M. K.; Hanck, K. W.; Watts, R. J. *J. Phys. Chem.* **1987**, *91*, 1047.

(34) Adachi, C.; Kwong, R. C.; Djurovich, P.; Adamovich, V.; Baldo, M. A.; Thompson, M. E.; Forrest, S. R. *Appl. Phys. Lett.* **2001**, *79*, 2082.

(35) Tamayo, A. B.; Alleyne, B. D.; Djurovich, P. I.; Lamansky, S.; Tsyba, I.; Ho, N. N.; Bau, R.; Thompson, M. E. *J. Am. Chem. Soc.* **2003**, *125*, 7377.

(36) Tsuchiya, K.; Ito, E.; Yagai, S.; Kitamura, A.; Karatsu, T. *Eur. J. Inorg. Chem.* **2009**, 2104.

(37) Chen, L. A.; Xu, W.; Huang, B.; Ma, J.; Wang, L.; Xi, J.; Harms, K.; Gong, L.; Meggers, E. *J. Am. Chem. Soc.* **2013**, *135*, 10598.

(38) Baranoff, E.; Curchod, B. F. E. *Dalton. Trans.* **2015**, *44*, 8318.

(39) Atkins, P.; Overton, T.; Rourke, J.; Weller, M.; Armstrong, F.; Hagerman, M. *Shriver & Atkins' Inorganic Chemistry*; Company, W. . F. and, Ed.; 5th ed.; Oxford University Press: New York, **2010**.

(40) Albright, A. *Tetrahedron* **1982**, *38*, 1339.

(41) Wagenknecht, P. S.; Ford, P. C. *Coord. Chem. Rev* **2011**, *255*, 591.

(42) Hay, P. J. *J. Phys. Chem. A* **2002**, *106*, 1634.

(43) You, Y.; Nam, W. *Chem Soc Rev* **2012**, *41*, 7061.

(44) Meyer, T. *Pure Appl. Chem.* **1986**, *58*, 1193.

(45) Sajoto, T.; Djurovich, P. I.; Tamayo, A. B.; Oxgaard, J.; Goddard, W. a; Thompson, M. E. *J. Am. Chem. Soc.* **2009**, *131*, 9813.

(46) Batagin-Neto, a; Assis, A. *J. Phys. Chem. A* **2014**, *118*, 3717.

(47) Gorodetsky, A. a.; Parker, S.; Slinker, J. D.; Bernards, D. a.; Wong, M. H.; Malliaras, G. G.; Flores-Torres, S.; Abruña, H. D. *Appl. Phys. Lett.* **2004**, *84*, 807.

(48) Zysman-colman, E.; Slinker, J. D.; Parker, J. B.; Malliaras, G. G.; Bernhard, S. *Chem. Mater.* **2008**, *20*, 388.

(49) Bernhard, S.; Gao, X.; Malliaras, G. G.; Abruña, H. D. *Adv. Mater.* **2002**, *14*, 433.

(50) Du, B.-S.; Liao, J.-L.; Huang, M.-H.; Lin, C.-H.; Lin, H.-W.; Chi, Y.; Pan, H.-A.; Fan, G.-L.; Wong, K.-T.; Lee, G.-H.; Chou, P.-T. *Adv. Funct. Mater.* **2012**, *22*, 3491.

(51) Chen, Y.-L.; Li, S.-W.; Chi, Y.; Cheng, Y.-M.; Pu, S.-C.; Yeh, Y.-S.; Chou, P.-T. *ChemPhysChem* **2005**, *6*, 2012.

(52) Zhang, Q.; Zhou, Q.; Cheng, Y.; Wang, L.; Ma, D.; Jing, X.; Wang, F. *Adv. Funct. Mater.* **2006**, *16*, 1203.

(53) Armaroli, N. *Chem. Soc. Rev.* **2001**, *30*, 113.

(54) Baranoff, E.; Yum, J.-H.; Graetzel, M.; Nazeeruddin, M. K. *J. Organomet. Chem.* **2009**, *694*, 2661.

(55) Baranoff, E.; Fantacci, S.; De Angelis, F.; Zhang, X.; Scopelliti, R.; Grätzel, M.; Nazeeruddin, M. K. *Inorg. Chem.* **2010**, *50*, 451.

(56) Tordera, D.; Delgado, M.; Ortí, E.; Bolink, H. J.; Frey, J.; Nazeeruddin, M. K.; Baranoff, E. *Chem. Mater.* **2012**, *24*, 1896.

(57) Frey, J.; Curchod, B. F. E.; Scopelliti, R.; Tavernelli, I.; Rothlisberger, U.; Nazeeruddin, M. K.; Baranoff, E. *Dalton Trans.* **2013**.

(58) Baranoff, E.; Jung, I.; Scopelliti, R.; Solari, E.; Grätzel, M.; Nazeeruddin, M. K. *Dalton Trans.* **2011**, *40*, 6860.

(59) Baranoff, E.; Curchod, B. F. E.; Monti, F.; Steimer, F.; Accorsi, G.; Tavernelli, I.; Rothlisberger, U.; Scopelliti, R.; Grätzel, M.; Nazeeruddin, M. K. *Inorg. Chem.* **2012**, *51*, 799.

(60) Costa, R. D.; Ortí, E.; Bolink, H. J.; Graber, S.; Schaffner, S.; Neuburger, M.; Housecroft, C. E.; Constable, E. C. *Adv. Funct. Mater.* **2009**, *19*, 3456.

(61) Baranoff, E.; Curchod, B. F. E.; Frey, J.; Scopelliti, R.; Kessler, F.; Tavernelli, I.; Rothlisberger, U.; Grätzel, M.; Nazeeruddin, M. K. *Inorg. Chem.* **2012**, *51*, 215.

(62) Chi, Y.; Chou, P.-T. *Chem. Soc. Rev.* **2010**, *39*, 638.

(63) Fu, H.; Cheng, Y. M.; Chou, P. T.; Chi, Y. *Mater. Today* **2011**, *14*, 472.

(64) Suzuri, Y.; Oshiyama, T.; Ito, H.; Hiyama, K.; Kita, H. *Sci. Technol. Adv. Mater.* **2014**, *15*, 54202.

(65) Holmes, R. J.; Forrest, S. R.; Tung, Y. J.; Kwong, R. C.; Brown, J. J.; Garon, S.; Thompson, M. E. *Appl. Phys. Lett.* **2003**, *82*, 2422.

(66) Rausch, A. F.; Thompson, M. E.; Yersin, H. *J. Phys. Chem. A* **2009**, *113*, 5927.

(67) Holmes, R. J.; D'Andrade, B. W.; Forrest, S. R.; Ren, X.; Li, J.; Thompson, M. E. *Appl. Phys. Lett.* **2003**, *83*, 3818.

(68) Li, J.; Djurovich, P. I.; Alleyne, B. D.; Tsyba, I.; Ho, N. N.; Bau, R.; Thompson, M. E.

Polyhedron **2004**, *23*, 419.

(69) Yeh, S.-J.; Wu, M.-F.; Chen, C.-T.; Song, Y.-H.; Chi, Y.; Ho, M.-H.; Hsu, S.-F.; Chen, C. H. *Adv. Mater.* **2005**, *17*, 285.

(70) Hung, J.-Y.; Chi, Y.; Pai, I.-H.; Yu, Y.-C.; Lee, G.-H.; Chou, P.-T.; Wong, K.-T.; Chen, C.-C.; Wu, C.-C. *Dalton. Trans.* **2009**, *115*, 6472.

(71) Chiu, Y. C.; Hung, J. Y.; Chi, Y.; Chen, C. C.; Chang, C. H.; Wu, C. C.; Cheng, Y. M.; Yu, Y. C.; Lee, G. H.; Chou, P. T. *Adv. Mater.* **2009**, *21*, 2221.

(72) Chiu, Y. C.; Chi, Y.; Hung, J. Y.; Cheng, Y. M.; Yu, Y. C.; Chung, M. W.; Lee, G. H.; Chou, P. T.; Chen, C. C.; Wu, C. C.; Hsieh, H. Y. *ACS appl. Mater. Inter.* **2009**, *1*, 433.

(73) Lo, S.; Shipley, C. P.; Bera, R. N.; Harding, R. E.; Cowley, A. R.; Burn, P. L.; Samuel, I. D. W.; Uni, V.; Haugh, N.; Andrews, S.; May, R. V; Re, V.; Recei, M.; July, V. *Chem. Mater.* **2006**, *18*, 5119.

(74) Lee, S. J.; Park, K. M.; Yang, K.; Kang, Y. *Inorg. Chem.* **2009**, *48*, 1030.

(75) Kessler, F.; Watanabe, Y.; Sasabe, H.; Katagiri, H.; Nazeeruddin, M. K.; Grätzel, M.; Kido, J. *J. Mater. Chem. C* **2013**, *1*, 1070.

(76) Yang, C. H.; Mauro, M.; Polo, F.; Watanabe, S.; Muenster, I.; Fröhlich, R.; De Cola, L. *Chem. Mater.* **2012**, *24*, 3684.

(77) Li, T. Y.; Liang, X.; Zhou, L.; Wu, C.; Zhang, S.; Liu, X.; Lu, G. Z.; Xue, L. S.; Zheng, Y. X.; Zuo, J. L. *Inorg. Chem.* **2015**, *54*, 161.

(78) Lu, K. Y.; Chou, H. H.; Hsieh, C. H.; Yang, Y. H. O.; Tsai, H. R.; Tsai, H. Y.; Hsu, L. C.; Chen, C. Y.; Chen, I. C.; Cheng, C. H. *Adv. Mater.* **2011**, *23*, 4933.

(79) Sajoto, T.; Djurovich, P. I.; Tamayo, A.; Yousufuddin, M.; Bau, R.; Thompson, M. E.; Holmes, R. J.; Forrest, S. R. *Inorg. Chem.* **2005**, *44*, 7992.

(80) Holmes, R. J.; Forrest, S. R.; Sajoto, T.; Tamayo, A.; Djurovich, P. I.; Thompson, M. E.; Brooks, J.; Tung, Y. J.; D'Andrade, B. W.; Weaver, M. S.; Kwong, R. C.; Brown, J. J. *Appl. Phys. Lett.* **2005**, *87*, 1.

(81) Chien, C.-H.; Fujita, S.; Yamoto, S.; Hara, T.; Yamagata, T.; Watanabe, M.; Mashima, K. *Dalton Trans.* **2008**, 916.

(82) Haneder, S.; Da Como, E.; Feldmann, J.; Lupton, J. M.; Lennartz, C.; Erk, P.; Fuchs, E.; Molt, O.; Münster, I.; Schildknecht, C.; Wagenblast, G. *Adv. Mater.* **2008**, *20*, 3325.

(83) Tsuchiya, K.; Yagai, S.; Kitamura, A.; Karatsu, T.; Endo, K.; Mizukami, J.; Akiyama, S.; Yabe, M. *Eur. J. Inorg. Chem.* **2010**, *2010*, 926.

(84) Yang, C.-H.; Beltran, J.; Lemaur, V.; Cornil, J.; Hartmann, D.; Sarfert, W.; Fröhlich, R.; Bizzarri, C.; De Cola, L. *Inorg. Chem.* **2010**, *49*, 9891.

(85) Chang, C. F.; Cheng, Y. M.; Chi, Y.; Chiu, Y. C.; Lin, C. C.; Lee, G. H.; Chou, P. T.; Chen, C. C.; Chang, C. H.; Wu, C. C. *Angew. Chem. Int. Ed.* **2008**, *47*, 4542.

(86) Li, H.; Yin, Y. M.; Cao, H. T.; Sun, H. Z.; Wang, L.; Shan, G. G.; Zhu, D. X.; Su, Z. M.; Xie, W. F. *J. Organomet. Chem.* **2014**, *753*, 55.

(87) Kessler, F.; Costa, R. D.; Di Censo, D.; Scopelliti, R.; Ortí, E.; Bolink, H. J.; Meier, S.;

Sarfert, W.; Grätzel, M.; Nazeeruddin, M. K.; Baranoff, E. *Dalton Trans.* **2012**, *41*, 180.

(88) Zhang, F.; Duan, L.; Qiao, J.; Dong, G.; Wang, L.; Qiu, Y. *Org. Electron.* **2012**, *13*, 1277.

(89) Meier, S. B.; Sarfert, W.; Junquera-Hernández, J. M.; Delgado, M.; Tordera, D.; Ortí, E.; Bolink, H. J.; Kessler, F.; Scopelliti, R.; Grätzel, M.; Nazeeruddin, M. K.; Baranoff, E. *J. Mater. Chem. C* **2013**, *1*, 58.

(90) Stringer, B. D.; Quan, L. M.; Barnard, P. J.; Wilson, D. J. D.; Hogan, C. F. *Organometallics* **2014**, *33*, 4860.

(91) Darmawan, N.; Yang, C. H.; Mauro, M.; Raynal, M.; Heun, S.; Pan, J.; Buchholz, H.; Braunstein, P.; De Cola, L. *Inorg. Chem.* **2013**, *52*, 10756.

(92) Monti, F.; La Placa, M. G. I.; Armaroli, N.; Scopelliti, R.; Grätzel, M.; Nazeeruddin, M. K.; Kessler, F. *Inorg. Chem.* **2015**, *54*, 3031.

(93) Monti, F.; Kessler, F.; Delgado, M.; Frey, J.; Bazzanini, F.; Accorsi, G.; Armaroli, N.; Bolink, H. J.; Ortí, E.; Scopelliti, R.; Nazeeruddin, M. K.; Baranoff, E. *Inorg. Chem.* **2013**, *52*, 10292.

(94) Stinner, C.; Wightman, M. D.; Kelley, S. O.; Hill, M. G.; Barton, J. K. *Inorg. Chem.* **2001**, *40*, 5245.

(95) Broomhead, J. A.; Grumley, W. *Inorg. Chem.* **1971**, *10*, 2002.

(96) Watts, R. J.; Harrington, J. S. *J. Inorg. Nucl. Chem.* **1975**, *37*, 1293.

(97) Mürner, H.; Jackson, B.; Barton, J. *Inorg. Chem.* **1998**, *37*, 3007.

(98) Park, G. Y.; Kim, Y.; Ha, Y. *Mol. Cryst. Liq. Cryst.* **2006**, *462*, 179.

(99) Dedeian, K.; Djurovich, P. I.; Garces, F. O.; Carlson, G.; Watts, R. J. *Inorg. Chem.* **1991**, *30*, 1685.

(100) Felici, M.; Contreras-Carballada, P.; Smits, J. M. M.; Nolte, R. J. M.; Williams, R. M.; De Cola, L.; Feiters, M. C. *Molecules* **2010**, *15*, 2039.

(101) Edkins, R. M.; Wriglesworth, A.; Fucke, K.; Bettington, S. L.; Beeby, A. *Dalton Trans.* **2011**, *40*, 9672.

(102) Xu, X.; Guo, H.; Zhao, J.; Liu, B.; Yang, X.; Zhou, G.; Wu, Z. *Chem. Mater.* **2016**, *28*, 8556.

(103) Lepeltier, M.; Graff, B.; Lalevée, J.; Wantz, G.; Ibrahim-Ouali, M.; Gigmes, D.; Dumur, F. *Org. Electron.* **2016**, *37*, 24.

(104) Liao, J. L.; Chi, Y.; Sie, Z. T.; Ku, C. H.; Chang, C. H.; Fox, M. A.; Low, P. J.; Tseng, M. R.; Lee, G. H. *Inorg. Chem.* **2015**, *54*, 10811.

(105) Sullivan, B. P.; Meyer, T. J. *J. Chem. Soc., Chem. Commun.* **1984**, 403.

(106) Yoshikawa, N.; Sakamoto, J.; Matsumura-Inoue, T.; Takashima, H.; Tsukahara, K.; Kanehisa, N.; Kai, Y. *anal. Sci.* **2004**, *20*, 711.

(107) Soman, S.; Manton, J. C.; Inglis, J. L.; Halpin, Y.; Twamley, B.; Otten, E.; Browne, W. R.; De Cola, L.; Vos, J. G.; Pryce, M. T. *Chem. Commun.* **2014**, *50*, 6461.

(108) Tamura, Y.; Hisamatsu, Y.; Kumar, S.; Itoh, T.; Sato, K.; Kuroda, R.; Aoki, S. *Inorg. Chem.* **2017**, *56*, 812.

(109) Hisamatsu, Y.; Kumar, S.; Aoki, S. *Inorg. Chem.* **2017**, *56*, 886.

(110) Zhou, G.; Wong, W.-Y.; Suo, S. *J. Photoch. Photobio. C* **2010**, *11*, 133.

(111) Coppo, P.; Duati, M.; Kozhevnikov, V. N.; Hofstraat, J. W.; De Cola, L. *Angew. Chem. Int. Ed.* **2005**, *44*, 1806.

(112) Mazzeo, M.; Vitale, V.; Della Sala, F.; Anni, M.; Barbarella, G.; Favaretto, L.; Sotgiu, G.; Cingolani, R.; Gigli, G. *Adv. Mater.* **2005**, *17*, 34.

(113) Hamada, Y.; Sano, T.; Fujii, H.; Nishio, Y.; Takahashi, H.; Shibata, K. *Jpn. J. Appl. Phys.* **1996**, *35*, 1339.

(114) Xu, X.; Liao, Y.; Yu, G.; You, H.; Di, C.; Su, Z.; Ma, D.; Wang, Q.; Li, S.; Wang, S.; Ye, J.; Liu, Y. *Chem. Mater.* **2007**, *19*, 1740.

(115) Bolink, H. J.; De Angelis, F.; Baranoff, E.; Klein, C.; Fantacci, S.; Coronado, E.; Sessolo, M.; Kalyanasundaram, K.; Grätzel, M.; Nazeeruddin, M. K. *Chem. Commun.* **2009**, 4672.

(116) You, Y.; Park, S. Y. *J. Am. Chem. Soc.* **2005**, *127*, 12438.

(117) Knorr, L. *Ber. Dtsch. Chem. Ges.* **1883**, *16*, 2597.

(118) Finar, I. L.; Rackham, D. M. *J. Chem. Soc. B* **1968**, 211.

(119) He, L.; Duan, L.; Qiao, J.; Dong, G.; Wang, L.; Qiu, Y. *Chem. Mater.* **2010**, *22*, 3535.

(120) Yamanaka, H.; Takekawa, T.; Morita, K.; Ishihara, T. *Tetr. Lett.* **1996**, *37*, 1829.

(121) Davies, I. W.; Marcoux, J.; Wu, J.; Palucki, M.; Corley, E. G.; Robbins, M. A.; Tsou, N.; Ball, R. G.; Dormer, P.; Larsen, R. D.; Reider, P. J. *J. Org. Chem.* **2000**, 4571.

(122) Tordera, D.; Pertegás, A.; Shavaleev, N. M.; Scopelliti, R.; Ortí, E.; Bolink, H. J.; Baranoff, E.; Grätzel, M.; Nazeeruddin, M. K. *J. Mater. Chem.* **2012**, *22*, 19264.

(123) Wu, L.-L.; Sun, I.-W.; Yang, C.-H. *Polyhedron* **2007**, *26*, 2679.

(124) Parshall, G. W. *Acc. Chem. Res.* **1970**, *3*, 139.

(125) Ryabov, A. D. *Chem. Rev.* **1990**, *90*, 403.

(126) Canty, A. J.; van Koten, G. *Acc. Chem. Res.* **1995**, *28*, 406.

(127) Albrecht, M. *Chem. Rev.* **2010**, *110*, 576.

(128) Huang, W. S.; Lin, J. T.; Chien, C. H.; Tao, Y. T.; Sun, S. S.; Wen, Y. S. *Chem. Mater.* **2004**, *16*, 2480.

(129) Chen, L.; Yang, C.; Qin, J.; Gao, J.; Ma, D. *Inorg. Chim. Acta* **2006**, *359*, 4207.

(130) Ding, J.; Gao, J.; Cheng, Y.; Xie, Z.; Wang, L.; Ma, D.; Jing, X.; Wang, F. *Adv. Funct. Mater.* **2006**, *16*, 575.

(131) Velusamy, M.; Thomas, K. R. J.; Chen, C.-H.; Lin, J. T.; Wen, Y. S.; Hsieh, W.-T.; Lai, C.-H.; Chou, P.-T. *Dalton Trans.* **2007**, 3025.

(132) Wei, X.; Peng, J.; Cheng, J.; Xie, M.; Lu, Z.; Li, C.; Cao, Y. *Adv. Funct. Mater.* **2007**,

17, 3319.

(133) Karatsu, T.; Takahashi, M.; Yagai, S.; Kitamura, A. *Inorg. Chem.* **2013**, *52*, 12338.

(134) Chen, X.; Okamoto, Y.; Yano, T.; Otsuki, J. *J. Sep. Sci.* **2007**, *30*, 713.

(135) Coughlin, F. J.; Westrol, M. S.; Oyler, K. D.; Byrne, N.; Kraml, C.; Zysman-colman, E.; Lowry, M. S.; Bernhard, S. *Inorg. Chem.* **2008**, *47*, 2039.

(136) Marchi, E.; Sinisi, R.; Bergamini, G.; Tragni, M.; Monari, M.; Bandini, M.; Ceroni, P. *Chem. Eur. J.* **2012**, *18*, 8765.

(137) Citti, C.; Battisti, U. M.; Ciccarella, G.; Maiorano, V.; Gigli, G.; Abbate, S.; Mazzeo, G.; Castiglioni, E.; Longhi, G.; Cannazza, G. *J. Chromatogr. A* **2016**, *1467*, 335.

(138) Pommerehne, J.; Vestweber, H.; Guss, W.; Mahrt, R. F.; Bässler, H.; Porsch, M.; Daub, J. *Adv. Mater.* **1995**, *7*, 551.

(139) Cardona, C. M.; Li, W.; Kaifer, A. E.; Stockdale, D.; Bazan, G. C. *Adv. Mater.* **2011**, *23*, 2367.

(140) Fei, T.; Gu, X.; Zhang, M.; Wang, C.; Hanif, M.; Zhang, H.; Ma, Y. *Synth. Met.* **2009**, *159*, 113.

(141) B. Schmid, F. O. Garces, and R. J. W. *Inorg. Chem.* **1994**, *33*, 9.

(142) Djurovich, P. I.; Mayo, E. I.; Forrest, S. R.; Thompson, M. E. *Org. Electron. 10* **2009**, *10*, 515.

(143) Brouwer, A. M. *Pure Appl. Chem.* **2011**, *83*, 2213.

(144) Melhuish, W. H. *J. Phys. Chem.* **1961**, *65*, 229.

(145) Sjöback, R.; Nygren, J.; Kubista, M. Absorption and fluorescence properties of fluorescein. *Spectrochim. Acta A*, **1995**, *51*, L7.

(146) Würth, C.; Grabolle, M.; Pauli, J.; Spieles, M.; Resch-genger, U. *Nat. Protoc.* **2013**, *8*, 1535.

(147) Frey, J.; Curchod, B. F. E.; Scopelliti, R.; Tavernelli, I.; Rothlisberger, U.; Nazeeruddin, M. K.; Baranoff, E. *Dalton Trans.* **2014**, *43*, 5667.

(148) Hansch, C.; Leo, A.; Taft, R. W. *Chem. Rev.* **1991**, *91*, 165.

(149) Laskar, I. R.; Hsu, S. F.; Chen, T. M. *Polyhedron* **2006**, *25*, 1167.

(150) Laskar, I. R.; Hsu, S. F.; Chen, T. M. *Polyhedron* **2005**, *24*, 189.

(151) Lepeltier, M.; Lee, T. K. M.; Lo, K. K. W.; Toupet, L.; Le Bozec, H.; Guerchais, V. *Eur. J. Inorg. Chem.* **2007**, *2*, 2734.

(152) Hasan, K.; Bansal, A. K.; Samuel, I. D. W.; Roldán-Carmona, C.; Bolink, H. J.; Zysman-Colman, E. *Sci. Rep.* **2015**, *5*, 1.

(153) Treadway, J. A.; Loeb, B.; Lopez, R.; Anderson, P. A.; Keene, F. R.; Meyer, T. J. *Inorg. Chem.* **1996**, *35*, 2242.

(154) Harding, R. E.; Lo, S.-C.; Burn, P. L.; Samuel, I. D. W. *Org. Electron.* **2008**, *9*, 377.

(155) Colombo, M. G.; Güedel, H. U. *Inorg. Chem.* **1993**, *32*, 3081.

(156) Li, J.; Djurovich, P. I.; Alleyne, B. D.; Yousufuddin, M.; Ho, N. N.; Thomas, J. C.; Peters, J. C.; Bau, R.; Thompson, M. E. *Inorg. Chem.* **2005**, *44*, 1713.

(157) Dedeian, K.; Shi, J.; Shepherd, N.; Forsythe, E.; Morton, D. C. *Inorg. Chem.* **2005**, *44*, 4445.

(158) Jayabharathi, J.; Thanikachalam, V.; Srinivasan, N.; Perumal, M. V. *Spectrochim. Acta A* **2011**, *79*, 338.

(159) Jayabharathi, J.; Thanikachalam, V.; Srinivasan, N.; Jayamoorthy, K. *Spectrochim. Acta A* **2012**, *93*, 240.

(160) Beeby, A.; Bettington, S.; Samuel, I. D. W.; Wang, Z. *J. Mater. Chem.* **2003**, *13*, 80.

(161) Bosque, R.; Sales, J. *J. Chem. Inf. Comput. Sci.* **2002**, *42*, 1154.

(162) Ghanadzadeh, A.; Zeini, A.; Kashef, A.; Moghadam, M. *Spectrochim. Acta A* **2009**, *73*, 324.

(163) Liu, Y.; Ye, K.; Fan, Y.; Song, W.; Wang, Y.; Hou, Z. *Chem. Commun.* **2009**, 3699.

(164) Radwan, Y. K.; Maity, A.; Teets, T. S. *Inorg. Chem.* **2015**, *54*, 7122.

(165) Zhou, Y.; Gao, H.; Wang, X.; Qi, H. *Inorg. Chem.* **2015**, *54*, 1446.

(166) Henwood, A. F.; Bansal, A. K.; Cordes, D. B.; Slawin, A. M. Z.; Samuel, I. D. W.; Zysman-Colman, E. *J. Mater. Chem. C* **2016**, *4*, 3726.

(167) Jitchati, R.; Batsanov, A. S.; Bryce, M. R. *Tetrahedron* **2009**, *65*, 855.

9 SUPPORTING INFORMATION

9.1 SCREENING LIGANDS

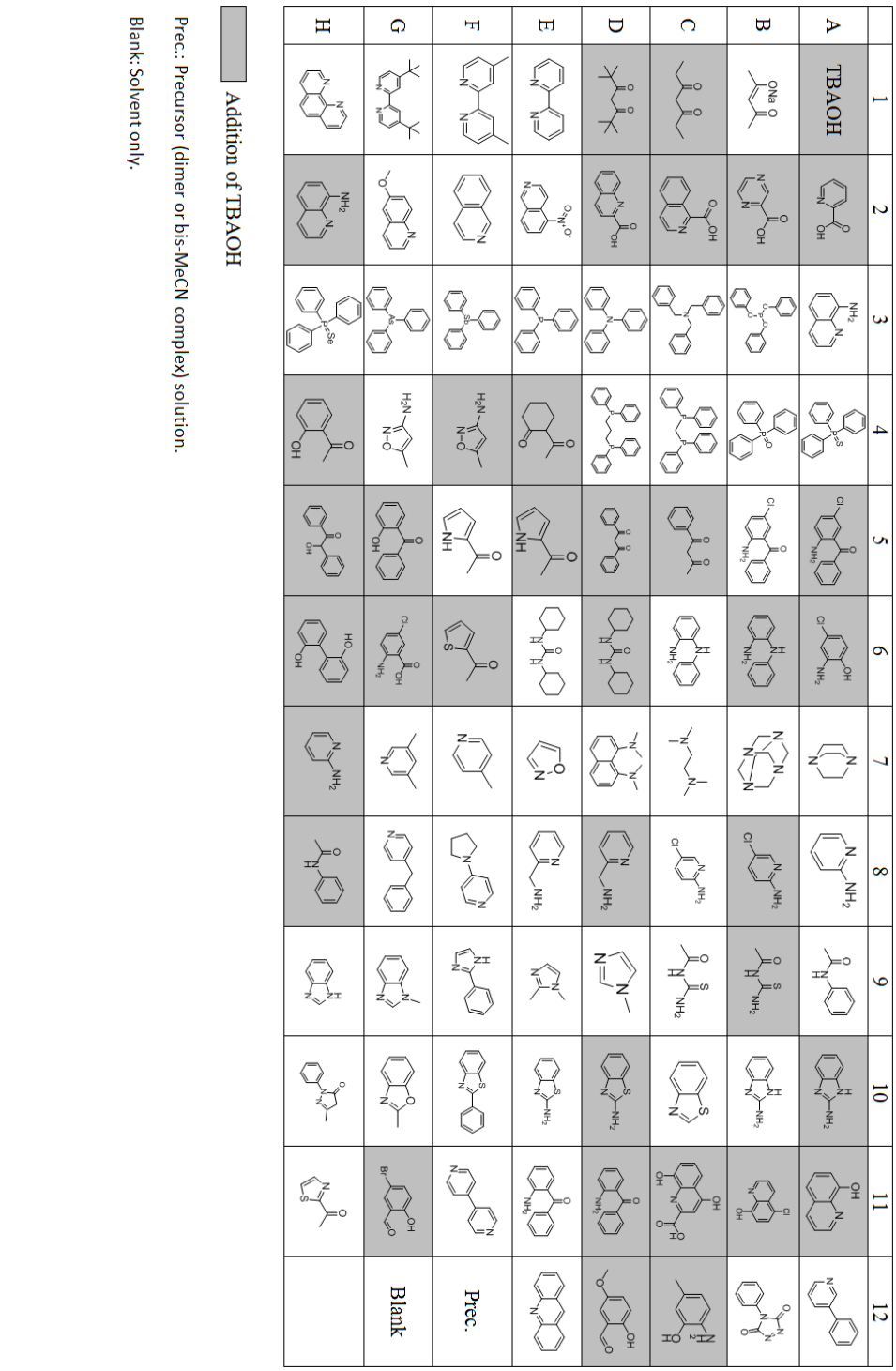

Figure 9.1: List of ligands used for screening experiments according to their microplate location.

9.2 CRYSTALLOGRAPHIC DATA

9.2.1 1st series

*Table 9.1: Crystal data and structure refinement for [Ir(dFppz)(ppz)(acac)] (**6**).*

Empirical formula	$C_{25}D_2Cl_6F_2H_{19}IrN_4O_2$
Formula weight	854.38
Temperature/K	100.01(10)
Crystal system	triclinic
Space group	P-1
a/Å	9.0515(4)
b/Å	10.4003(4)
c/Å	15.5704(6)
α/°	83.634(3)
β/°	87.937(3)
γ/°	89.965(3)
Volume/Å^3	1455.78(10)
Z	2
ρ_{calc}g/cm^3	1.949
μ/mm^{-1}	14.342
F(000)	824.0
Crystal size/mm^3	0.2387 × 0.1552 × 0.1321
Radiation	CuKα (λ = 1.5418)
2Θ range for data collection/°	5.714 to 140.116
Index ranges	$-11 \leq h \leq 11$, $-12 \leq k \leq 11$, $-12 \leq l \leq 18$
Reflections collected	10147
Independent reflections	5471 [R_{int} = 0.0253, R_{sigma} = 0.0286]
Data/restraints/parameters	5471/1/369
Goodness-of-fit on F^2	1.053
Final R indexes [I>=2σ (I)]	R_1 = 0.0253, wR_2 = 0.0644
Final R indexes [all data]	R_1 = 0.0258, wR_2 = 0.0649
Largest diff. peak/hole / e Å^{-3}	1.11/-1.55

Table 9.2: Crystal data and structure refinement for [Ir(ppy)(ppz)(acac)] (7)

Empirical formula	$C_{25}H_{22}IrN_3O_2$
Formula weight	588.65
Temperature/K	100.01(10)
Crystal system	monoclinic
Space group	P 2_1/n
a/Å	10.2570(4)
b/Å	17.4474(6)
c/Å	11.9101(6)
α/°	90
β/°	93.275(4)
γ/°	90
Volume/Å^3	2127.92(16)
Z	4
Pcalc/ g/cm^3	1.837
μ/mm^{-1}	12.367
F(000)	1144.0
Crystal size/mm^3	0.1511 × 0.111 × 0.0671
Radiation	CuKα (λ = 1.54184)
2Θ range for data collection/°	9 to 140.114
Index ranges	$-12 \leq h \leq 8$, $-21 \leq k \leq 20$, $-14 \leq l \leq 12$
Reflections collected	8569
Independent reflections	4026 [R_{int} = 0.0299, R_{sigma} = 0.0359]
Data/restraints/parameters	4026/0/282
Goodness-of-fit on F^2	1.044
Final R indexes [I>=2σ (I)]	R_1 = 0.0284, wR_2 = 0.0664
Final R indexes [all data]	R_1 = 0.0373, wR_2 = 0.0726
Largest diff. peak/hole / e Å^{-3}	2.49/-0.91

*Table 9.3: Crystal data and structure refinement for [Ir(dFppy)(dFppz)(acac)] (**8**)*

Empirical formula	$C_{25}H_{18}F_4IrN_3O_2$
Formula weight	660.62
Temperature/K	100.01(10)
Crystal system	orthorhombic
Space group	Pbca
a/Å	16.0919(3)
b/Å	15.6229(2)
c/Å	17.9006(3)
α/°	90
β/°	90
γ/°	90
Volume/Å^3	4500.23(12)
Z	8
ρ_{calc}g/cm^3	1.950
μ/mm^{-1}	12.049
F(000)	2544.0
Crystal size/mm^3	0.2052 × 0.1163 × 0.1047
Radiation	CuKα (λ = 1.54184)
2Θ range for data collection/°	9.31 to 140.126
Index ranges	$-12 \leq h \leq 19$, $-12 \leq k \leq 18$, $-21 \leq l \leq 19$
Reflections collected	11194
Independent reflections	4232 [R_{int} = 0.0216, R_{sigma} = 0.0221]
Data/restraints/parameters	4232/0/318
Goodness-of-fit on F^2	1.075
Final R indexes [I>=2σ (I)]	R_1 = 0.0259, wR_2 = 0.0601
Final R indexes [all data]	R_1 = 0.0309, wR_2 = 0.0631
Largest diff. peak/hole / e Å^{-3}	0.78/-1.03

*Table 9.4: Crystal data and structure refinement for [Ir(dFppy)(ppz)(acac)] (**9**)*

Empirical formula	$C_{25}H_{20}F_2IrN_3O_2$
Formula weight	624.64
Temperature/K	100.00(10)
Wavelength/Å	1.5418
Crystal system	Monoclinic
Space group	P 2_1/n
Unit cell dimensions	
a/Å	10.24834(14)
b/Å	17.7056(2)
c/Å	11.91514(18)
α/°	90
β/°	92.6012(13)
γ/°	90
Volume/Å^3	2159.80(5)
Z	4
Density (calculated)/g/cm^3	1.921
Absorption coefficient/mm^{-1}	12.369
F(000)	1208
Crystal size/mm^3	0.2169 x 0.1295 x 0.0714
Theta range for data collection/°	4.476 to 74.320
Index ranges	-12<=h<=11, -11<=k<=21, -14<=l<=8
Reflections collected	7159
Independent reflections	4182 [R(int) = 0.0168]
Completeness to theta = 67.684°	98.3 %
Absorption correction	Semi-empirical from equivalents
Max. and min. transmission	1.00000 and 0.55430
Refinement method	Full-matrix least-squares on F^2
Data / restraints / parameters	4182 / 0 / 300
Goodness-of-fit on F^2	1.049
Final R indices [I>2sigma(I)]	R_1 = 0.0217, wR_2 = 0.0572
R indices (all data)	R_1 = 0.0240, wR_2 = 0.0593
Extinction coefficient	n/a
Largest diff. peak and hole/ e.Å^{-3}	0.916 and -1.223

*Table 9.5: Crystal data and structure refinement for [Ir(dFppz)(ppy)(acac)] (**10**)*

Empirical formula	$C_{25}H_{20}F_2IrN_3O_2$
Formula weight	624.64
Temperature/K	99.99(10)
Crystal system	orthorhombic
Space group	$P2_12_12_1$
a/Å	7.39189(8)
b/Å	23.8333(3)
c/Å	24.7471(3)
α/°	90
β/°	90
γ/°	90
Volume/Å^3	4359.78(8)
Z	8
ρ_{calc}g/cm^3	1.903
μ/mm^{-1}	12.254
F(000)	2416.0
Crystal size/mm^3	0.2411 × 0.0477 × 0.0362
Radiation	CuKα (λ = 1.54184)
2Θ range for data collection/°	7.418 to 147.384
Index ranges	$-9 \leq h \leq 8$, $-29 \leq k \leq 27$, $-20 \leq l \leq 30$
Reflections collected	14339
Independent reflections	8421 [R_{int} = 0.0473, R_{sigma} = 0.0492]
Data/restraints/parameters	8421/133/599
Goodness-of-fit on F^2	1.046
Final R indexes [I>=2σ (I)]	R_1 = 0.0538, wR_2 = 0.1326
Final R indexes [all data]	R_1 = 0.0559, wR_2 = 0.1340
Largest diff. peak/hole / e Å^{-3}	1.90/-1.82
Flack parameter	0.007(19)

9.2.2 2nd series

*Table 9.6: Crystal data and structure refinement for [Ir(dMeOppy)$_2$(acac)] (**11**).*

Empirical formula	$C_{31}H_{31}IrN_2O_6$
Formula weight	719.78
Temperature/K	100.00(10)
Crystal system	monoclinic
Space group	C2/c
a/Å	19.9591(5)
b/Å	10.0372(3)
c/Å	13.6981(3)
α/°	90
β/°	98.504(2)
γ/°	90
Volume/Å^3	2714.02(12)
Z	4
ρ_{calc}g/cm^3	1.762
μ/mm^{-1}	4.968
F(000)	1424.0
Crystal size/mm^3	0.2591 × 0.1087 × 0.0996
Radiation	MoKα (λ = 0.71073)
ϑ range for data collection/°	6.014 to 52.74
Index ranges	-24 ≤ h ≤ 19, -12 ≤ k ≤ 12, -17 ≤ l ≤ 15
Reflections collected	7728
Independent reflections	2780 [R_{int} = 0.0342, R_{sigma} = 0.0408]
Data/restraints/parameters	2780/0/185
Goodness-of-fit on F^2	1.056
Final R indexes [I>=2σ (I)]	R_1 = 0.0222, wR_2 = 0.0407
Final R indexes [all data]	R_1 = 0.0263, wR_2 = 0.0425
Largest diff. peak/hole / e Å^{-3}	1.38/-0.95

*Table 9.7: Crystal data and structure refinement for [Ir(dMeOMeppy)$_2$(acac)] (**12**).*

Empirical formula	$C_{33}H_{35}IrN_2O_6$
Formula weight	747.83
Temperature/K	100.00(10)
Crystal system	monoclinic
Space group	P21/c
a/Å	8.00385(19)
b/Å	33.6490(8)
c/Å	10.9787(3)
α/°	90
β/°	98.228(2)
γ/°	90
Volume/Å^3	2926.36(12)
Z	4
ρ_{calc}g/cm^3	1.697
μ/mm^{-1}	4.611
F(000)	1488.0
Crystal size/mm3	0.2759 × 0.0459 × 0.0229
Radiation	MoKα (λ = 0.71073)
2Θ range for data collection/°	4.842 to 52.74
Index ranges	$-9 \leq h \leq 10$, $-39 \leq k \leq 42$, $-11 \leq l \leq 13$
Reflections collected	16260
Independent reflections	5971 [R_{int} = 0.0340, R_{sigma} = 0.0471]
Data/restraints/parameters	5971/0/387
Goodness-of-fit on F^2	1.117
Final R indexes [I>=2σ (I)]	R_1 = 0.0293, wR_2 = 0.0470
Final R indexes [all data]	R_1 = 0.0412, wR_2 = 0.0487
Largest diff. peak/hole / e Å^{-3}	0.57/-1.36

*Table 9.8: Crystal data and structure refinement for [Ir(dMeOMeOppy)$_2$(acac)] (**13**).*

Empirical formula	$C_{34}H_{37}Cl_2IrN_2O_8$
Formula weight	864.75
Temperature/K	100.01(10)
Crystal system	monoclinic
Space group	P21/n
a/Å	14.5262(3)
b/Å	12.6964(3)
c/Å	18.1262(4)
α/°	90
β/°	94.5212(19)
γ/°	90
Volume/Å^3	3332.61(12)
Z	4
ρ_{calc}g/cm^3	1.724
μ/mm^{-1}	4.221
F(000)	1720.0
Crystal size/mm3	0.2969 × 0.1458 × 0.0785
Radiation	MoKα (λ = 0.71073)
2Θ range for data collection/°	4.508 to 51.358
Index ranges	-17 ≤ h ≤ 14, -15 ≤ k ≤ 14, -18 ≤ l ≤ 22
Reflections collected	13657
Independent reflections	6284 [R_{int} = 0.0256, R_{sigma} = 0.0362]
Data/restraints/parameters	6284/0/432
Goodness-of-fit on F^2	1.057
Final R indexes [I>=2σ (I)]	R_1 = 0.0234, wR_2 = 0.0525
Final R indexes [all data]	R_1 = 0.0274, wR_2 = 0.0548
Largest diff. peak/hole / e Å^{-3}	0.96/-1.28

*Table 9.9: Crystal data and structure refinement for [Ir(dMeOppy)(diFppy)(acac)] (**14**).*

Empirical formula	$C_{29}H_{25}F_2IrN_2O_4$
Formula weight	695.71
Temperature/K	99.98(12)
Crystal system	triclinic
Space group	P-1
a/Å	12.1849(6)
b/Å	14.0394(6)
c/Å	16.3672(9)
α/°	86.163(4)
β/°	71.486(4)
γ/°	72.439(4)
Volume/Å^3	2530.0(2)
Z	4
ρ_{calc}g/cm^3	1.827
μ/mm^{-1}	10.685
F(000)	1360.0
Crystal size/mm^3	0.1736 × 0.1286 × 0.0272
Radiation	CuKα (λ = 1.54184)
2Θ range for data collection/°	13.01 to 140.146
Index ranges	$-14 \leq h \leq 14$, $-17 \leq k \leq 15$, $-18 \leq l \leq 19$
Reflections collected	17965
Independent reflections	9547 [R_{int} = 0.0496, R_{sigma} = 0.0619]
Data/restraints/parameters	9547/0/693
Goodness-of-fit on F^2	1.099
Final R indexes [I>=2σ (I)]	R_1 = 0.0508, wR_2 = 0.1289
Final R indexes [all data]	R_1 = 0.0573, wR_2 = 0.1352
Largest diff. peak/hole / e Å^{-3}	2.15/-4.23

*Table 9.10: Crystal data and structure refinement for [Ir(dMeOppy)(diFppz)(acac)] (**15**).*

Empirical formula	$C_{27}H_{24}F_2IrN_3O_4$
Formula weight	684.69
Temperature/K	100.00(10)
Crystal system	triclinic
Space group	P-1
a/Å	9.4448(3)
b/Å	10.1096(4)
c/Å	13.2912(5)
α/°	99.958(3)
β/°	90.087(3)
γ/°	99.701(3)
Volume/Å^3	1231.46(8)
Z	2
ρ_{calc}g/cm^3	1.847
μ/mm^{-1}	5.476
F(000)	668.0
Crystal size/mm^3	0.3229 × 0.2029 × 0.1067
Radiation	MoKα (λ = 0.71073)
2Θ range for data collection/°	5.292 to 50.688
Index ranges	$-10 \leq h \leq 11$, $-12 \leq k \leq 12$, $-16 \leq l \leq 14$
Reflections collected	9281
Independent reflections	4500 [R_{int} = 0.0294, R_{sigma} = 0.0461]
Data/restraints/parameters	4500/12/338
Goodness-of-fit on F^2	1.062
Final R indexes [I>=2σ (I)]	R_1 = 0.0272, wR_2 = 0.0600
Final R indexes [all data]	R_1 = 0.0336, wR_2 = 0.0631
Largest diff. peak/hole / e Å^{-3}	1.94/-1.52

*Table 9.11: Crystal data and structure refinement for [Ir(dMeOMeppy)(diFppy)(acac)] (**16**).*

Empirical formula	$C_{30}H_{27}F_2IrN_2O_4$
Formula weight	709.73
Temperature/K	100.00(10)
Crystal system	orthorhombic
Space group	$Pna2_1$
a/Å	18.6457(3)
b/Å	8.29085(11)
c/Å	33.8945(4)
α/°	90
β/°	90
γ/°	90
Volume/Å^3	5239.70(12)
Z	8
ρ_{calc}g/cm^3	1.799
μ/mm^{-1}	5.151
F(000)	2784.0
Crystal size/mm^3	0.3316 × 0.0805 × 0.0406
Radiation	MoKα (λ = 0.71073)
2Θ range for data collection/°	4.808 to 52.742
Index ranges	$-23 \leq h \leq 20$, $-10 \leq k \leq 10$, $-41 \leq l \leq 42$
Reflections collected	29221
Independent reflections	10564 [R_{int} = 0.0289, R_{sigma} = 0.0352]
Data/restraints/parameters	10564/1/714
Goodness-of-fit on F^2	1.091
Final R indexes [I>=2σ (I)]	R_1 = 0.0225, wR_2 = 0.0432
Final R indexes [all data]	R_1 = 0.0249, wR_2 = 0.0443
Largest diff. peak/hole / e Å^{-3}	0.97/-0.56
Flack parameter	0.254(6)

*Table 9.12: Crystal data and structure refinement for [Ir(dMeOMeppy)(diFppz)(acac)] (**17**).*

Empirical formula	$C_{28}H_{26}F_2IrN_3O_4$
Formula weight	698.72
Temperature/K	100.00(10)
Crystal system	triclinic
Space group	P-1
a/Å	9.6790(2)
b/Å	10.0511(3)
c/Å	13.4790(4)
α/°	81.655(2)
β/°	88.575(2)
γ/°	77.765(2)
Volume/Å^3	1267.93(6)
Z	2
ρ_{calc}g/cm^3	1.830
μ/mm^{-1}	5.320
F(000)	684.0
Crystal size/mm^3	0.1804 × 0.1347 × 0.0665
Radiation	MoKα (λ = 0.71073)
2Θ range for data collection/°	4.19 to 50.7
Index ranges	$-11 \leq h \leq 11$, $-12 \leq k \leq 12$, $-16 \leq l \leq 16$
Reflections collected	18611
Independent reflections	4646 [R_{int} = 0.0368, R_{sigma} = 0.0341]
Data/restraints/parameters	4646/0/348
Goodness-of-fit on F^2	1.089
Final R indexes [I>=2σ (I)]	R_1 = 0.0198, wR_2 = 0.0403
Final R indexes [all data]	R_1 = 0.0240, wR_2 = 0.0421
Largest diff. peak/hole / e Å^{-3}	1.38/-0.71

*Table 9.13: Crystal data and structure refinement for [Ir(dMeOMeOppy)(diFppy)(acac)] (**18**).*

Empirical formula	$C_{30}H_{27}N_2O_5F_2Ir$
Formula weight	725.73
Temperature/K	100.01(10)
Crystal system	monoclinic
Space group	$P2_1/c$
a/Å	16.39901(19)
b/Å	8.68276(9)
c/Å	18.4194(2)
α/°	90
β/°	94.5675(10)
γ/°	90
Volume/Å^3	2614.38(5)
Z	4
ρ_{calc}g/cm^3	1.844
μ/mm^{-1}	5.166
F(000)	1424.0
Crystal size/mm^3	0.2671 × 0.0786 × 0.0554
Radiation	MoKα (λ = 0.71073)
2Θ range for data collection/°	5.834 to 52.744
Index ranges	$-20 \leq h \leq 20$, $-10 \leq k \leq 10$, $-23 \leq l \leq 23$
Reflections collected	52018
Independent reflections	5343 [R_{int} = 0.0320, R_{sigma} = 0.0166]
Data/restraints/parameters	5343/0/366
Goodness-of-fit on F^2	1.090
Final R indexes [I>=2σ (I)]	R_1 = 0.0170, wR_2 = 0.0368
Final R indexes [all data]	R_1 = 0.0205, wR_2 = 0.0384
Largest diff. peak/hole / e Å^{-3}	1.43/-0.42

*Table 9.14: Crystal data and structure refinement for [Ir(dMeOMeOppy)(diFppz)(acac)] (**19**).*

Empirical formula	$C_{28}H_{26}F_2IrN_3O_5$
Formula weight	714.72
Temperature/K	99.9(7)
Crystal system	triclinic
Space group	P-1
a/Å	9.62808(10)
b/Å	17.0206(2)
c/Å	17.0923(2)
α/°	107.1525(12)
β/°	96.5144(10)
γ/°	101.6147(10)
Volume/Å^3	2576.55(6)
Z	4
ρ_{calc}g/cm^3	1.842
μ/mm^{-1}	5.242
F(000)	1400.0
Crystal size/mm^3	0.2416 × 0.1891 × 0.1057
Radiation	MoKα (λ = 0.71073)
2Θ range for data collection/°	4.652 to 51.362
Index ranges	$-11 \leq h \leq 11$, $-20 \leq k \leq 20$, $-20 \leq l \leq 20$
Reflections collected	101892
Independent reflections	9779 [R_{int} = 0.0315, R_{sigma} = 0.0140]
Data/restraints/parameters	9779/0/713
Goodness-of-fit on F^2	1.059
Final R indexes [I>=2σ (I)]	R_1 = 0.0204, wR_2 = 0.0501
Final R indexes [all data]	R_1 = 0.0227, wR_2 = 0.0515
Largest diff. peak/hole / e Å^{-3}	3.04/-1.60

9.2.3 3rd series

Table 9.15: Crystal data and structure refinement for [Ir(mespim)$_2$(acac)] (20).

Empirical formula	$C_{41}H_{42.4}IrN_4O_{2.7}$
Formula weight	826.59
Temperature/K	99.98(10)
Crystal system	monoclinic
Space group	I2/a
a/Å	14.7734(3)
b/Å	27.6343(5)
c/Å	18.5641(4)
α/°	90
β/°	111.075(3)
γ/°	90
Volume/Å^3	7071.9(3)
Z	8
ρ_{calc}g/cm^3	1.553
μ/mm^{-1}	3.820
F(000)	3320.0
Crystal size/mm^3	0.3506 × 0.1365 × 0.1007
Radiation	MoKα (λ = 0.71073)
2Θ range for data collection/°	5.896 to 52.744
Index ranges	-18 ≤ h ≤ 14, -34 ≤ k ≤ 34, -23 ≤ l ≤ 23
Reflections collected	18652
Independent reflections	7227 [R_{int} = 0.0251, R_{sigma} = 0.0333]
Data/restraints/parameters	7227/0/458
Goodness-of-fit on F^2	1.055
Final R indexes [I>=2σ (I)]	R_1 = 0.0220, wR_2 = 0.0421
Final R indexes [all data]	R_1 = 0.0291, wR_2 = 0.0456
Largest diff. peak/hole / e Å^{-3}	0.83/-0.81

*Table 9.16: Crystal data and structure refinement for [Ir(mespim)(dFppy)(acac)] (**21**).*

Empirical formula	$C_{34}H_{28.5}F_2IrN_3O_2$
Formula weight	741.30
Temperature/K	100.0(3)
Crystal system	monoclinic
Space group	$P2_1/n$
a/Å	15.5700(18)
b/Å	18.6452(9)
c/Å	25.550(3)
α/°	90
β/°	128.108(19)
γ/°	90
Volume/Å^3	5836.3(16)
Z	8
ρ_{calc}g/cm^3	1.687
μ/mm^{-1}	9.266
F(000)	2916.0
Crystal size/mm^3	0.2098 × 0.133 × 0.024
Radiation	CuKα (λ = 1.54184)
2Θ range for data collection/°	5.676 to 140.148
Index ranges	$-13 \leq h \leq 18$, $-12 \leq k \leq 22$, $-31 \leq l \leq 30$
Reflections collected	22663
Independent reflections	11032 [R_{int} = 0.0524, R_{sigma} = 0.0526]
Data/restraints/parameters	11032/0/347
Goodness-of-fit on F^2	2.067
Final R indexes [I>=2σ (I)]	R_1 = 0.1693, wR_2 = 0.4282
Final R indexes [all data]	R_1 = 0.1945, wR_2 = 0.4777
Largest diff. peak/hole / e Å^{-3}	27.68/-9.03

Table 9.17: Crystal data and structure refinement for [Ir(CF_3ppz)$_2$(acac)] (23).

Empirical formula	$C_{26}H_{21}Cl_2F_6IrN_4O_2$
Formula weight	798.57
Temperature/K	100.00(10)
Crystal system	triclinic
Space group	P-1
a/Å	9.4497(3)
b/Å	10.9150(4)
c/Å	14.0977(5)
α/°	72.244(3)
β/°	80.576(3)
γ/°	84.238(3)
Volume/Å^3	1364.16(9)
Z	2
ρ_{calc}g/cm^3	1.944
μ/mm^{-1}	5.164
F(000)	772.0
Crystal size/mm^3	0.3886 × 0.2456 × 0.1177
Radiation	MoKα (λ = 0.71073)
2Θ range for data collection/°	4.978 to 50.696
Index ranges	$-11 \leq h \leq 11$, $-13 \leq k \leq 13$, $-14 \leq l \leq 16$
Reflections collected	11852
Independent reflections	4985 [R_{int} = 0.0375, R_{sigma} = 0.0487]
Data/restraints/parameters	4985/1/382
Goodness-of-fit on F^2	1.036
Final R indexes [I>=2σ (I)]	R_1 = 0.0241, wR_2 = 0.0498
Final R indexes [all data]	R_1 = 0.0269, wR_2 = 0.0516
Largest diff. peak/hole / e Å^{-3}	0.70/-1.02

9.2.4 Pic complexes

Table 9.18: Crystal data and structure refinement for [Ir(dFppy)(ppy)(pic)] (3a)

Empirical formula	$C_{28}H_{18}F_2IrN_3O_2$
Formula weight	658.65
Temperature/K	100.01(10)
Crystal system	orthorhombic
Space group	$Pna2_1$
a/Å	15.0856(2)
b/Å	16.3361(2)
c/Å	9.47782(13)
α/°	90
β/°	90
γ/°	90
Volume/Å^3	2335.71(6)
Z	4
ρ_{calc}g/cm^3	1.873
μ/mm^{-1}	5.764
F(000)	1272.0
Crystal size/mm^3	0.1932 × 0.1488 × 0.1233
Radiation	MoKα (λ = 0.71073)
2Θ range for data collection/°	4.968 to 54.958
Index ranges	$-19 \leq h \leq 18$, $-21 \leq k \leq 21$, $-11 \leq l \leq 12$
Reflections collected	24233
Independent reflections	5197 [R_{int} = 0.0312, R_{sigma} = 0.0267]
Data/restraints/parameters	5197/1/325
Goodness-of-fit on F^2	1.057
Final R indexes [I>=2σ (I)]	R_1 = 0.0178, wR_2 = 0.0348
Final R indexes [all data]	R_1 = 0.0214, wR_2 = 0.0364
Largest diff. peak/hole / e Å^{-3}	0.79/-0.93
Flack parameter	-0.021(4)

Table 9.19: Crystal data and structure refinement for [Ir(dFppy)(ppy)(pic)] (3b)

Empirical formula	$C_{29.5}H_{22}Cl_3F_2IrN_3O_{2.5}$
Formula weight	795.05
Temperature/K	100.01(10)
Crystal system	monoclinic
Space group	$P2_1/c$
a/Å	16.7317(5)
b/Å	12.3412(2)
c/Å	15.5940(4)
α/°	90
β/°	117.541(4)
γ/°	90
Volume/Å^3	2855.09(15)
Z	4
ρ_{calc}g/cm^3	1.850
μ/mm^{-1}	5.006
F(000)	1544.0
Crystal size/mm^3	0.2164 × 0.1215 × 0.0362
Radiation	MoKα (λ = 0.71073)
2Θ range for data collection/°	5.892 to 50.688
Index ranges	$-20 \leq h \leq 17$, $-13 \leq k \leq 14$, $-18 \leq l \leq 18$
Reflections collected	14404
Independent reflections	5204 [R_{int} = 0.0269, R_{sigma} = 0.0321]
Data/restraints/parameters	5204/0/415
Goodness-of-fit on F^2	1.025
Final R indexes [I>=2σ (I)]	R_1 = 0.0258, wR_2 = 0.0606
Final R indexes [all data]	R_1 = 0.0314, wR_2 = 0.0637
Largest diff. peak/hole / e Å^{-3}	2.29/-1.45

Table 9.20: Crystal data and structure refinement for [Ir(dFppy)(ppz)(pic)] (9a)

Empirical formula	$C_{26}H_{17}F_2IrN_4O_2$
Formula weight	647.63
Temperature/K	99.97(10)
Crystal system	monoclinic
Space group	$P2_1/n$
a/Å	9.2743(3)
b/Å	14.7104(4)
c/Å	16.5135(5)
α/°	90
β/°	93.301(3)
γ/°	90
Volume/Å^3	2249.18(11)
Z	4
ρ_{calc}g/cm^3	1.913
μ/mm^{-1}	11.923
F(000)	1248.0
Crystal size/mm^3	0.2106 × 0.0601 × 0.0459
Radiation	CuKα (λ = 1.54184)
2Θ range for data collection/°	8.056 to 136.498
Index ranges	$-8 \leq h \leq 11$, $-17 \leq k \leq 17$, $-19 \leq l \leq 19$
Reflections collected	12463
Independent reflections	4103 [R_{int} = 0.0353, R_{sigma} = 0.0347]
Data/restraints/parameters	4103/0/316
Goodness-of-fit on F^2	1.105
Final R indexes [I>=2σ (I)]	R_1 = 0.0314, wR_2 = 0.0803
Final R indexes [all data]	R_1 = 0.0361, wR_2 = 0.0840
Largest diff. peak/hole / e Å^{-3}	1.48/-1.91

Table 9.21: Crystal data and structure refinement for [Ir(dFppy)(ppz)(pic)] (9b)

Empirical formula	$C_{27.5}H_{20}Cl_3F_2IrN_4O_2$
Formula weight	775.02
Temperature/K	100.01(10)
Crystal system	monoclinic
Space group	$P2_1/c$
a/Å	16.3715(4)
b/Å	12.2266(2)
c/Å	15.6859(4)
α/°	90
β/°	118.521(3)
γ/°	90
Volume/Å^3	2758.76(13)
Z	4
ρ_{calc}g/cm^3	1.866
μ/mm^{-1}	12.455
F(000)	1500.0
Crystal size/mm^3	0.4159 × 0.1754 × 0.0943
Radiation	CuKα (λ = 1.54184)
2Θ range for data collection/°	6.144 to 144.228
Index ranges	$-20 \leq h \leq 14$, $-14 \leq k \leq 13$, $-19 \leq l \leq 19$
Reflections collected	16925
Independent reflections	5406 [R_{int} = 0.0310, R_{sigma} = 0.0253]
Data/restraints/parameters	5406/0/397
Goodness-of-fit on F^2	1.078
Final R indexes [I>=2σ (I)]	R_1 = 0.0350, wR_2 = 0.0841
Final R indexes [all data]	R_1 = 0.0356, wR_2 = 0.0845
Largest diff. peak/hole / e Å^{-3}	1.23/-1.55

9.3 UV-VIS AND EMISSION SPECTRA

9.4 1st series

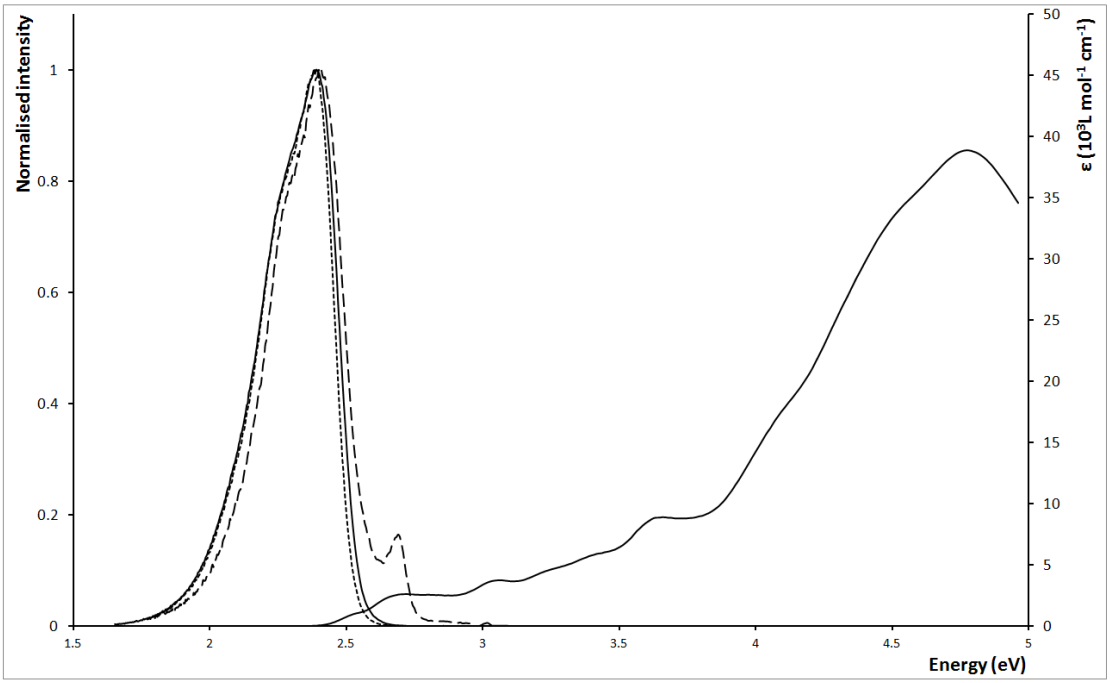

*Figure 9.2: Emission (left) and UV-visible (right) spectra of [Ir(ppy)$_2$(acac)] (**1**). DCM: solid line, CCl_4: dashed line, PMMA film: dotted line.*

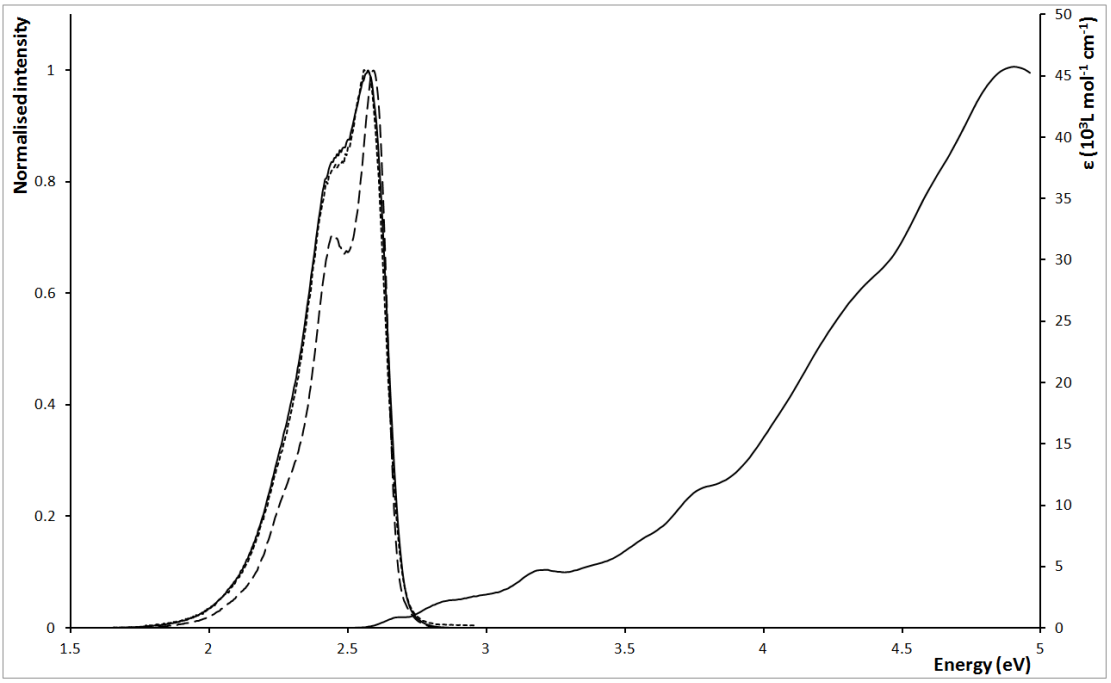

*Figure 9.3: Emission (left) and UV-visible (right) spectra of [Ir(dFppy)$_2$(acac)] (**2**). DCM: solid line, CCl_4: dashed line, PMMA film: dotted line.*

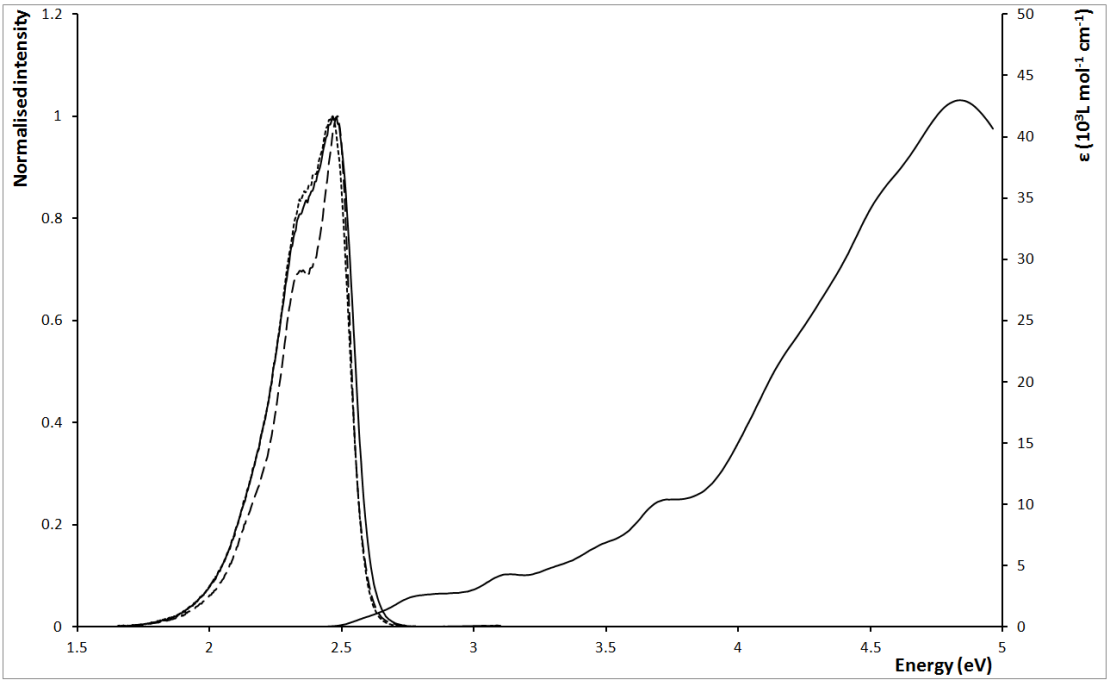

*Figure 9.4: Emission (left) and UV-visible (right) spectra of [Ir(dFppy)(ppy)(acac)] (**3**). DCM: solid line, CCl_4: dashed line, PMMA film: dotted line.*

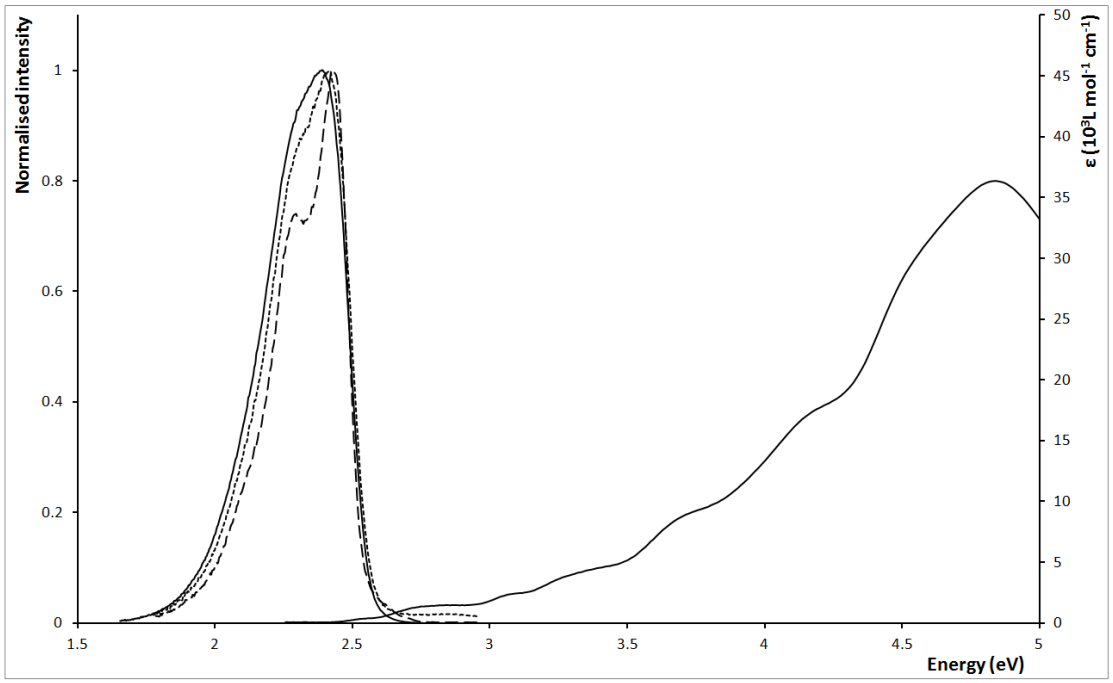

*Figure 9.5: Emission (left) and UV-visible (right) spectra of [Ir(ppy)(ppz)(acac)] (**7**). DCM: solid line, CCl_4: dashed line, PMMA film: dotted line.*

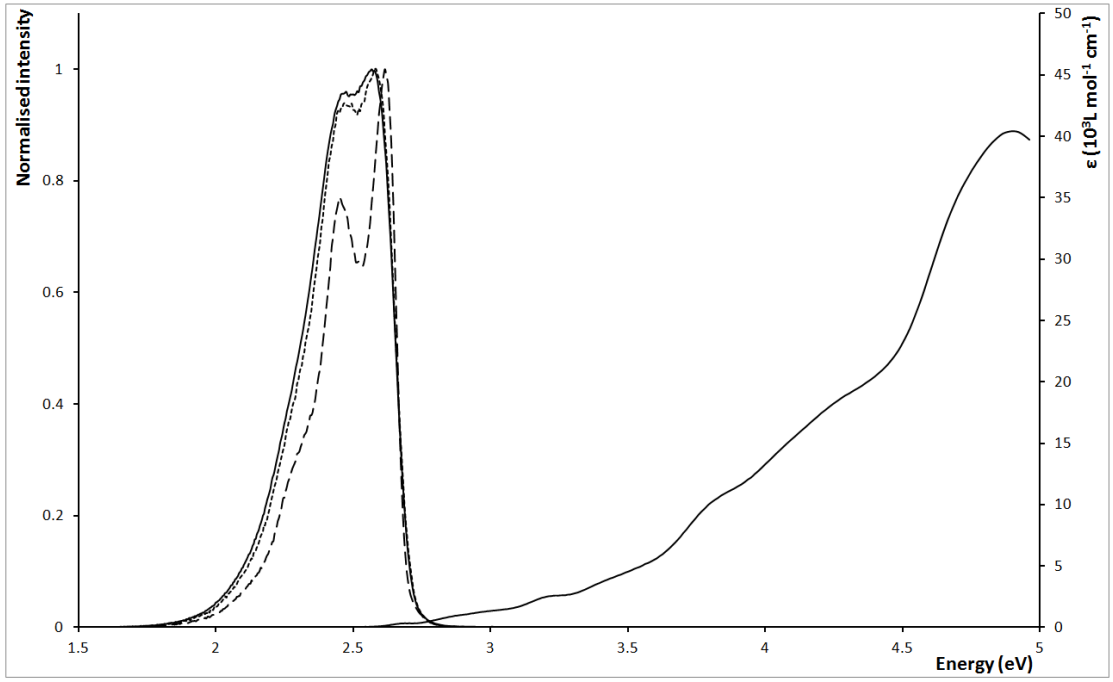

*Figure 9.6: Emission (left) and UV-visible (right) spectra of [Ir(dFppy)(dFppz)(acac)] (**8**). DCM: solid line, CCl_4: dashed line, PMMA film: dotted line.*

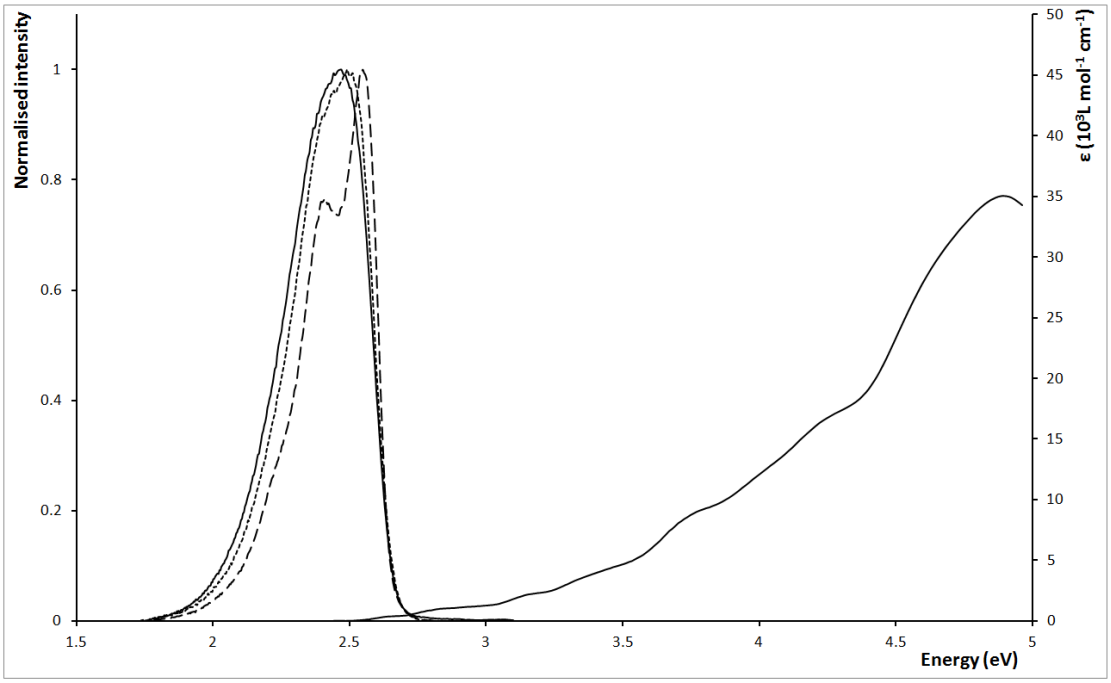

*Figure 9.7: Emission (left) and UV-visible (right) spectra of [Ir(dFppy)(ppz)(acac)] (**9**). DCM: solid line, CCl_4: dashed line, PMMA film: dotted line.*

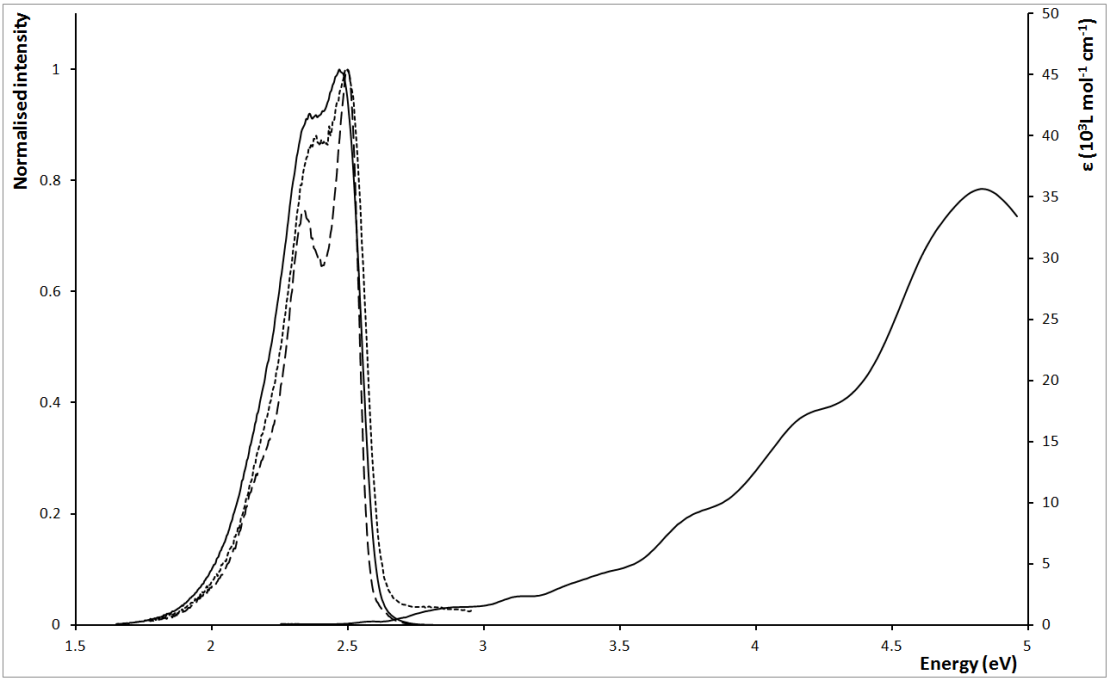

*Figure 9.8: Emission (left) and UV-visible (right) spectra of [Ir(dFppz)(ppy)(acac)] (**10**). DCM: solid line, CCl_4: dashed line, PMMA film: dotted line.*

9.4.1 2nd series

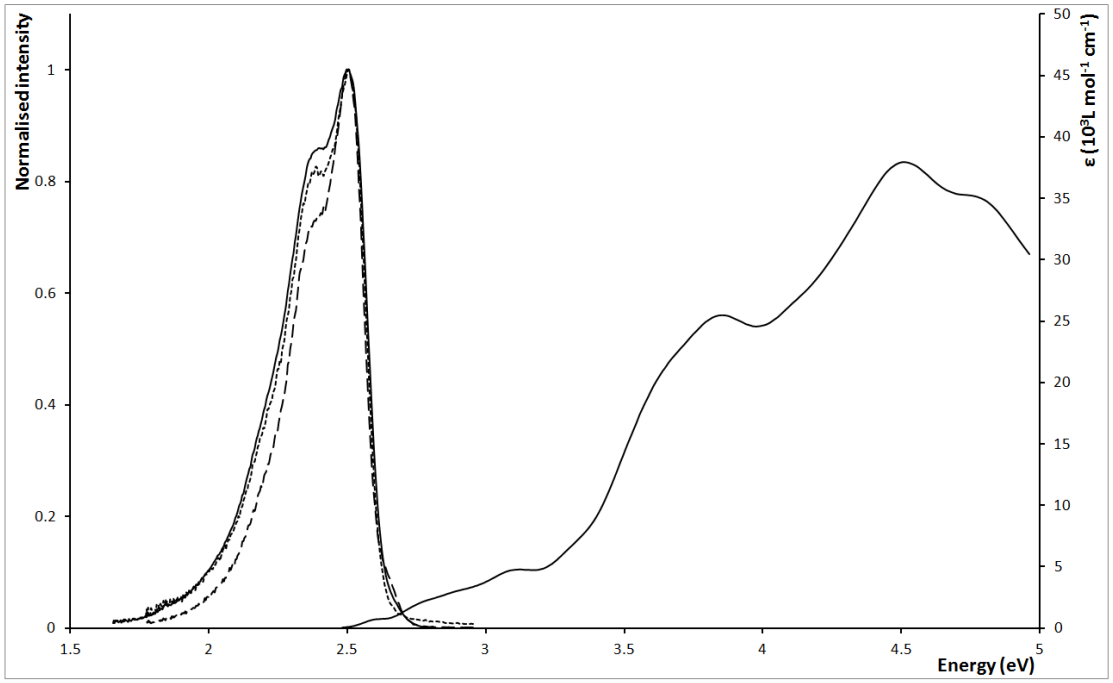

*Figure 9.9: Emission (left) and UV-visible (right) spectra of [Ir(dMeOppy)$_2$(acac)] (**11**). DCM: solid line, CCl_4: dashed line, PMMA film: dotted line.*

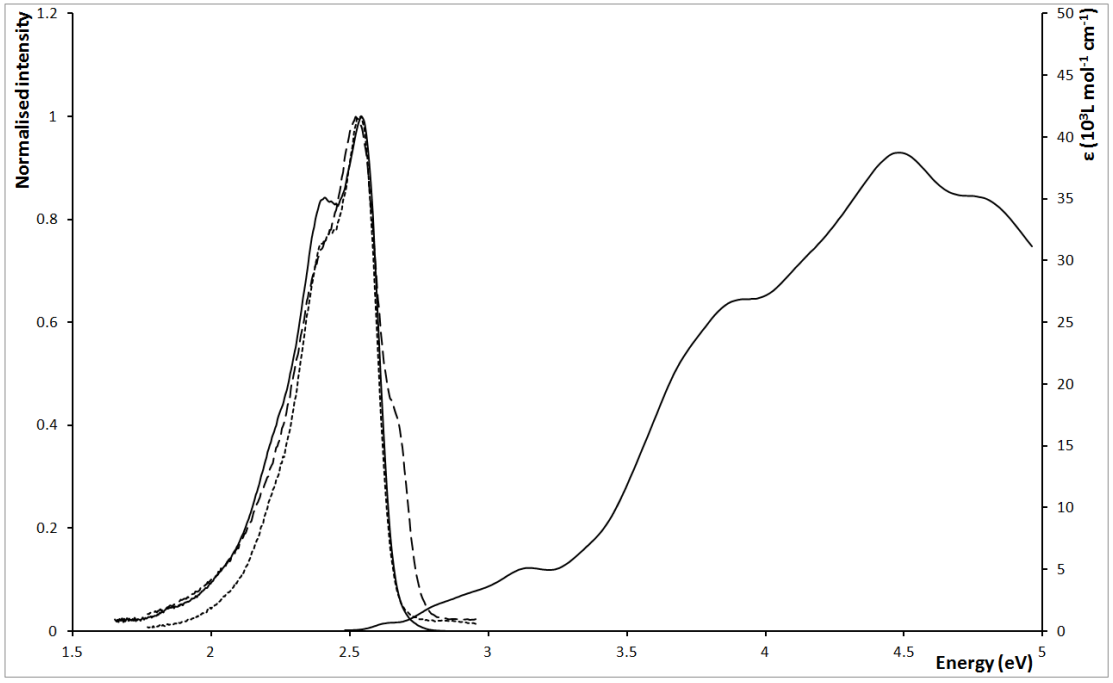

*Figure 9.10: Emission (left) and UV-visible (right) spectra of [Ir(dMeOMeppy)2(acac)] (**12**). DCM: solid line, CCl4: dashed line, PMMA film: dotted line.*

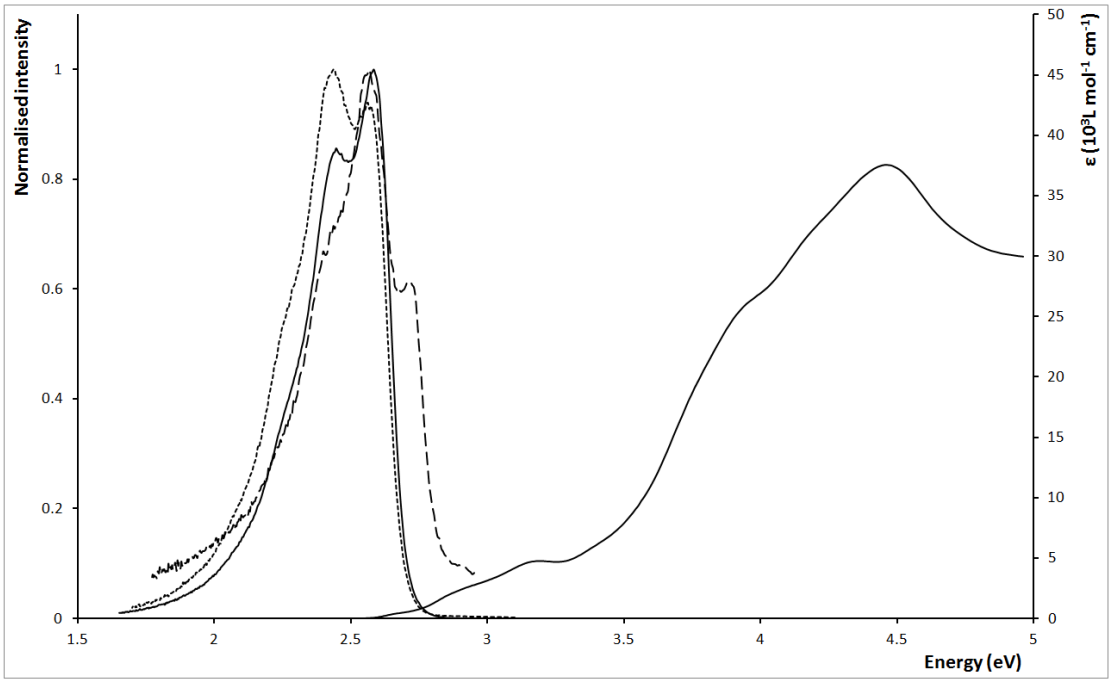

*Figure 9.11: Emission (left) and UV-visible (right) spectra of [Ir(dMeOMeOppy)$_2$(acac)] (**13**). DCM: solid line, CCl_4: dashed line, PMMA film: dotted line.NMR analyses*

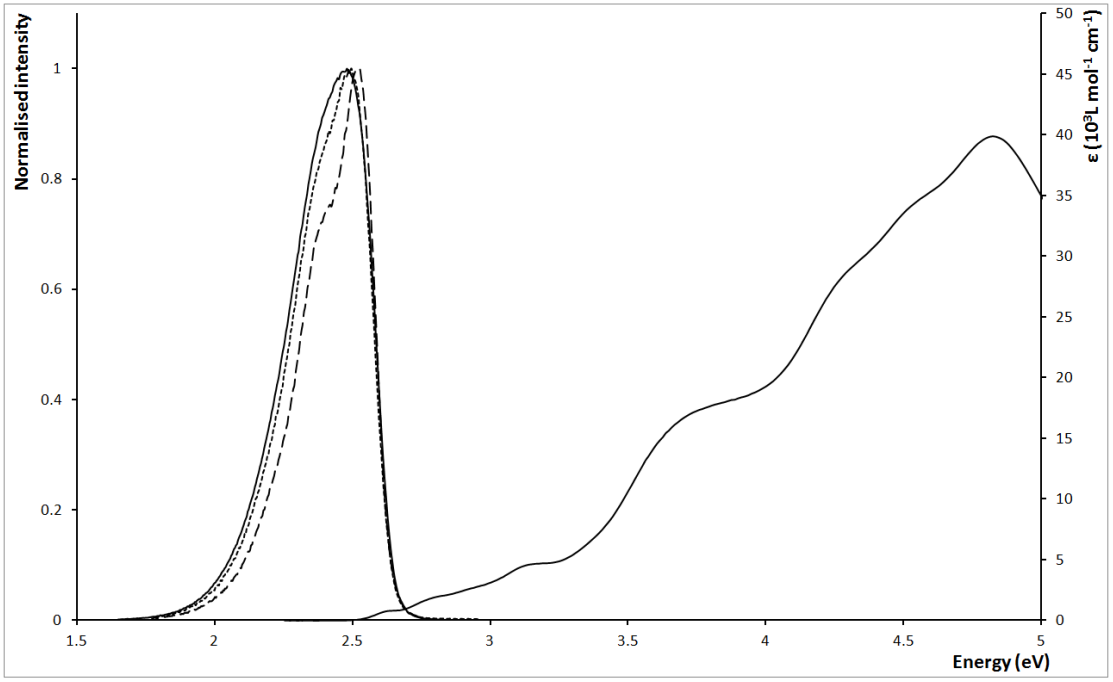

*Figure 9.12: Emission (left) and UV-visible (right) spectra of [Ir(dMeOppy)(dFppy)(acac)] (**14**). DCM: solid line, CCl_4: dashed line, PMMA film: dotted line.*

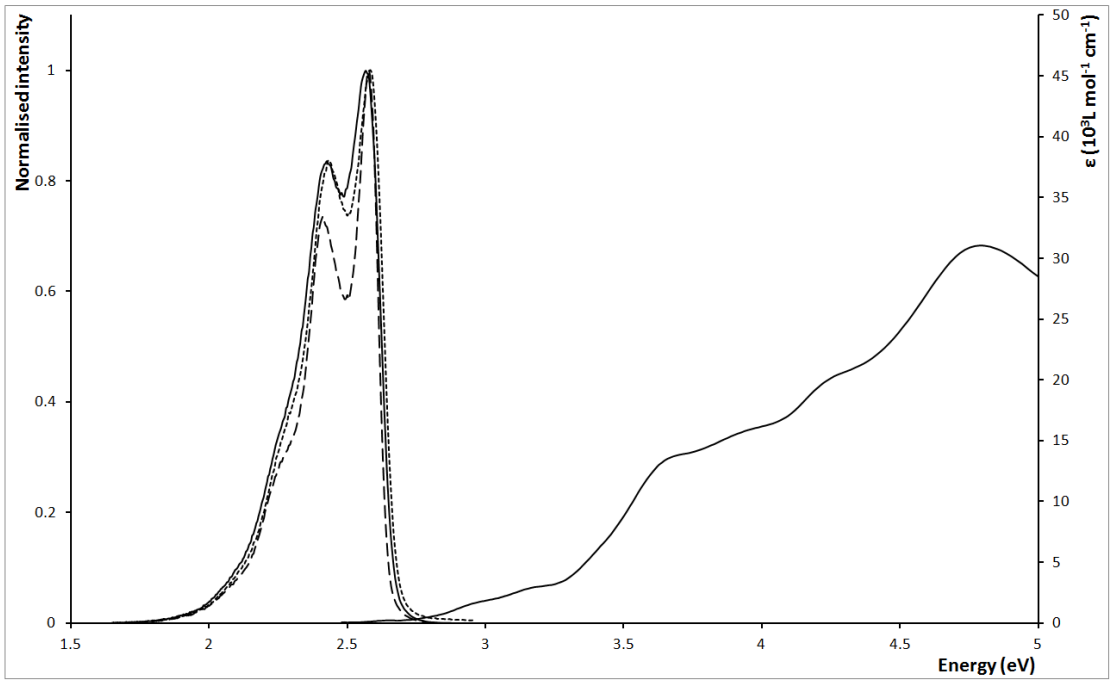

*Figure 9.13: Emission (left) and UV-visible (right) spectra of [Ir(dMeOppy)(dFppz)(acac)] (**15**). DCM: solid line, CCl_4: dashed line, PMMA film: dotted line.*

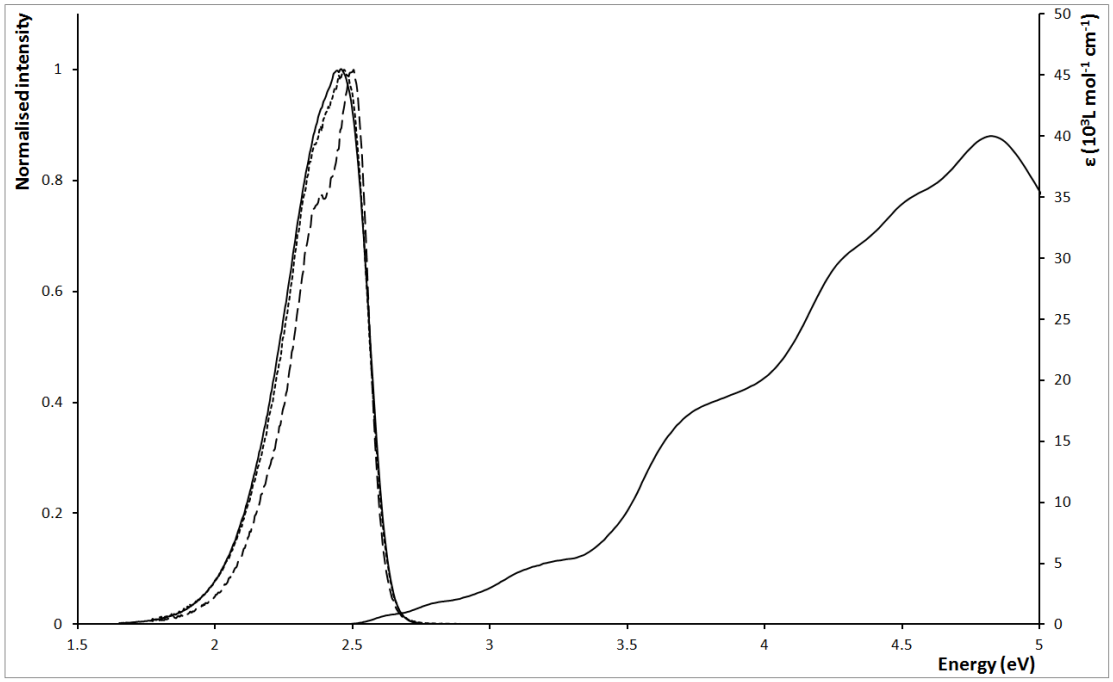

*Figure 9.14: Emission (left) and UV-visible (right) spectra of [Ir(dMeOMeppy)(dFppy)(acac)] (**16**). DCM: solid line, CCl_4: dashed line, PMMA film: dotted line.*

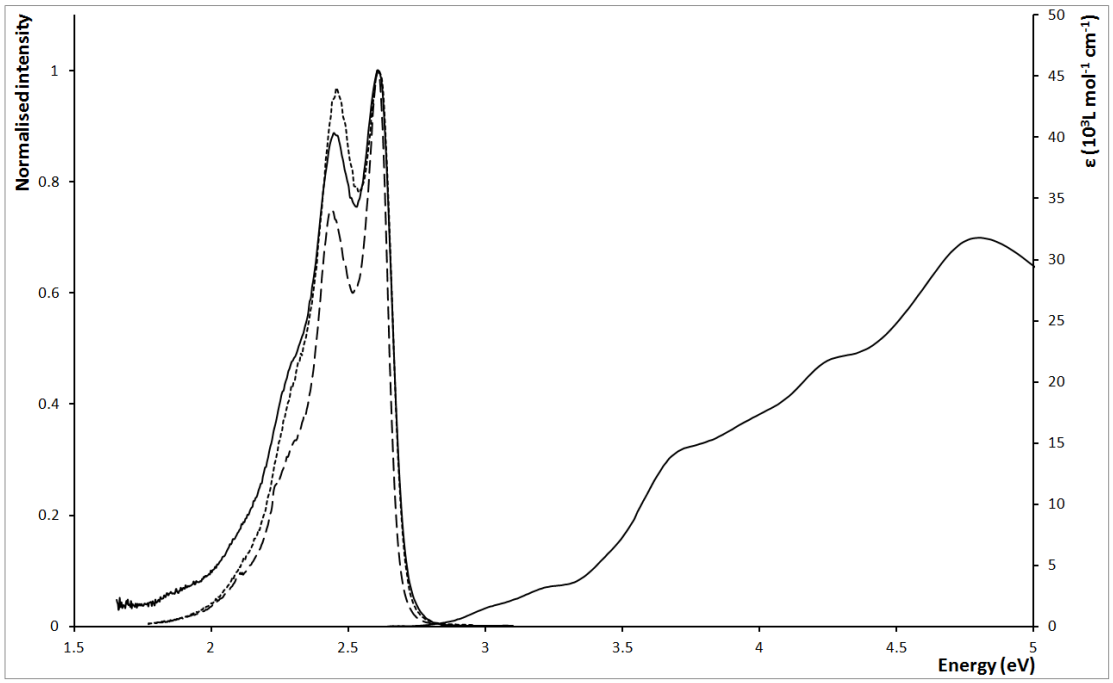

*Figure 9.15: Emission (left) and UV-visible (right) spectra of [Ir(dMeOMeppy)(dFppz)(acac)] (**17**). DCM: solid line, CCl_4: dashed line, PMMA film: dotted line.*

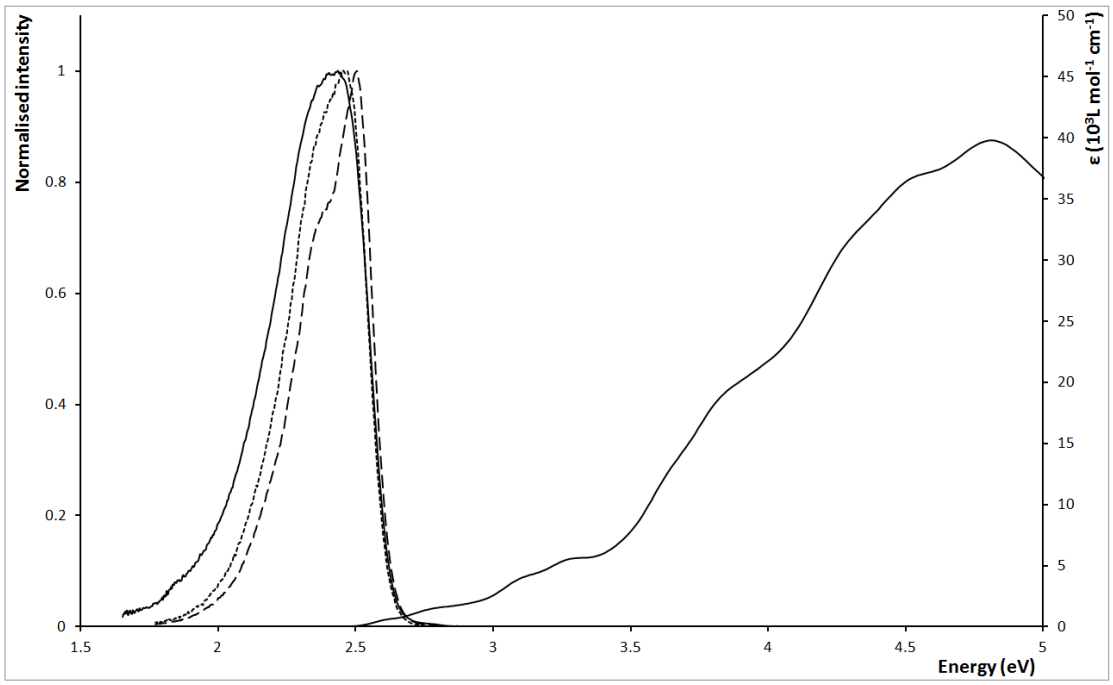

*Figure 9.16: Emission (left) and UV-visible (right) spectra of [Ir(dMeOMeOppy)(dFppy) (acac)] (**18**). DCM: solid line, CCl_4: dashed line, PMMA film: dotted line.*

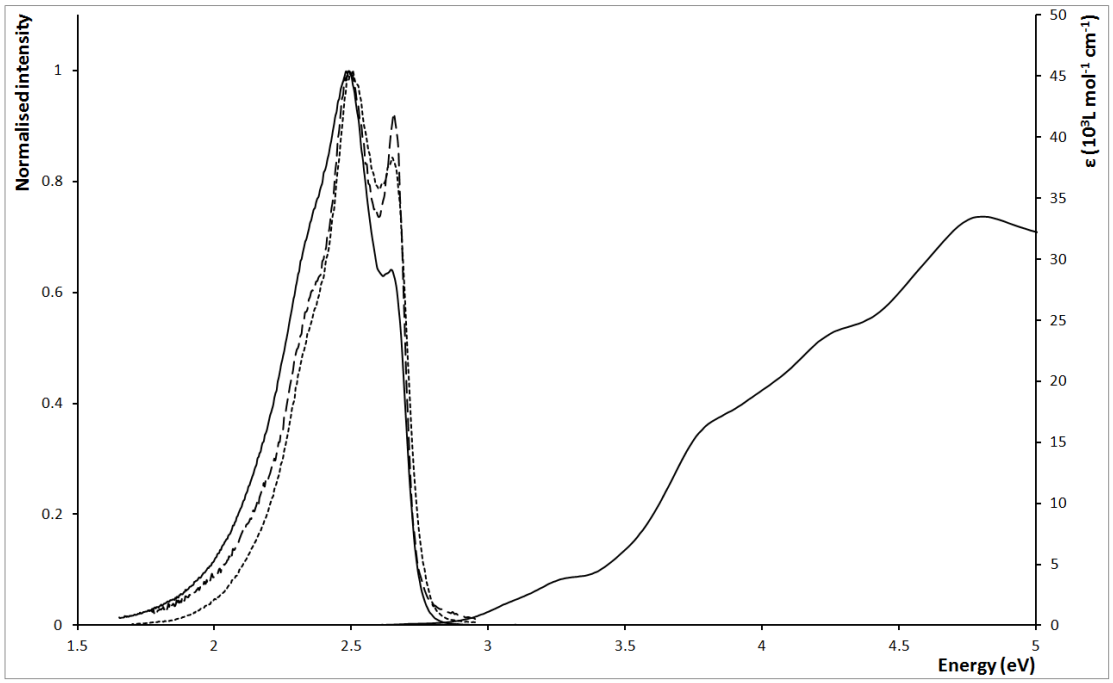

*Figure 9.17: Emission (left) and UV-visible (right) spectra of [Ir(dMeOMeOppy)(dFppz) (acac)] (**19**). DCM: solid line, CCl_4: dashed line, PMMA film: dotted line.*

9.4.2 3rd series

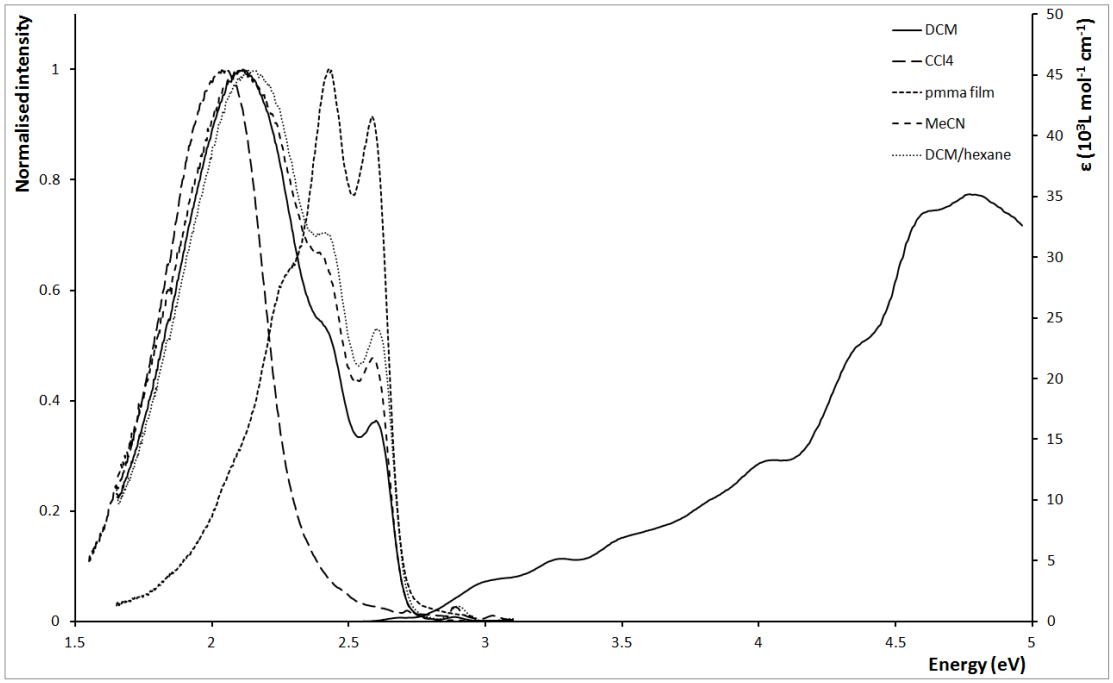

*Figure 9.18: Emission (left) and UV-visible (right) spectra of [Ir(mespim)$_2$(acac)] (**20**).*

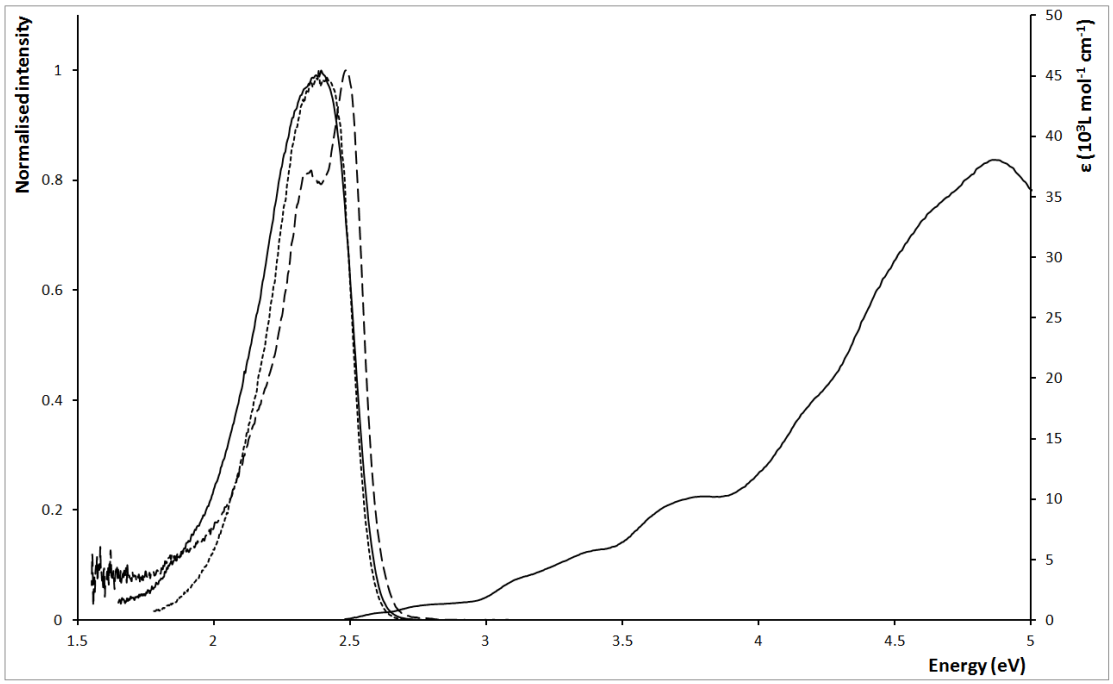

*Figure 9.19: Emission (left) and UV-visible (right) spectra of [Ir(mespim)(dFppy)(acac)] (**21**). DCM: solid line, CCl_4: dashed line, PMMA film: dotted line.*

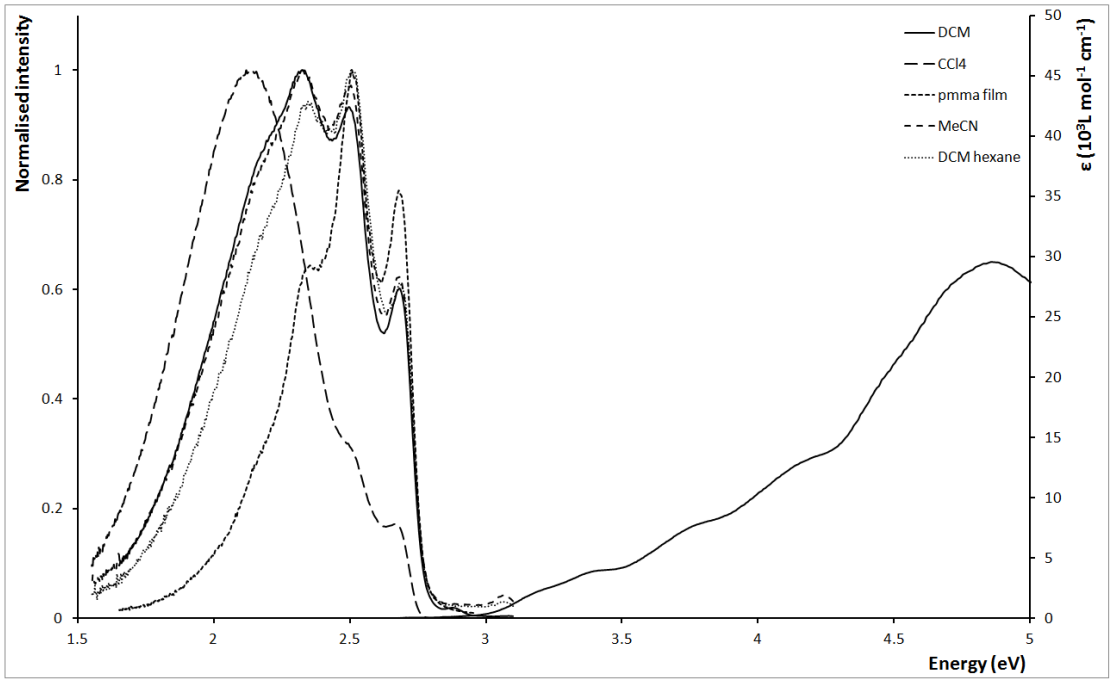

*Figure 9.20: Emission (left) and UV-visible (right) spectra of [Ir(mespim)(dFppz)(acac)] (**22**).*

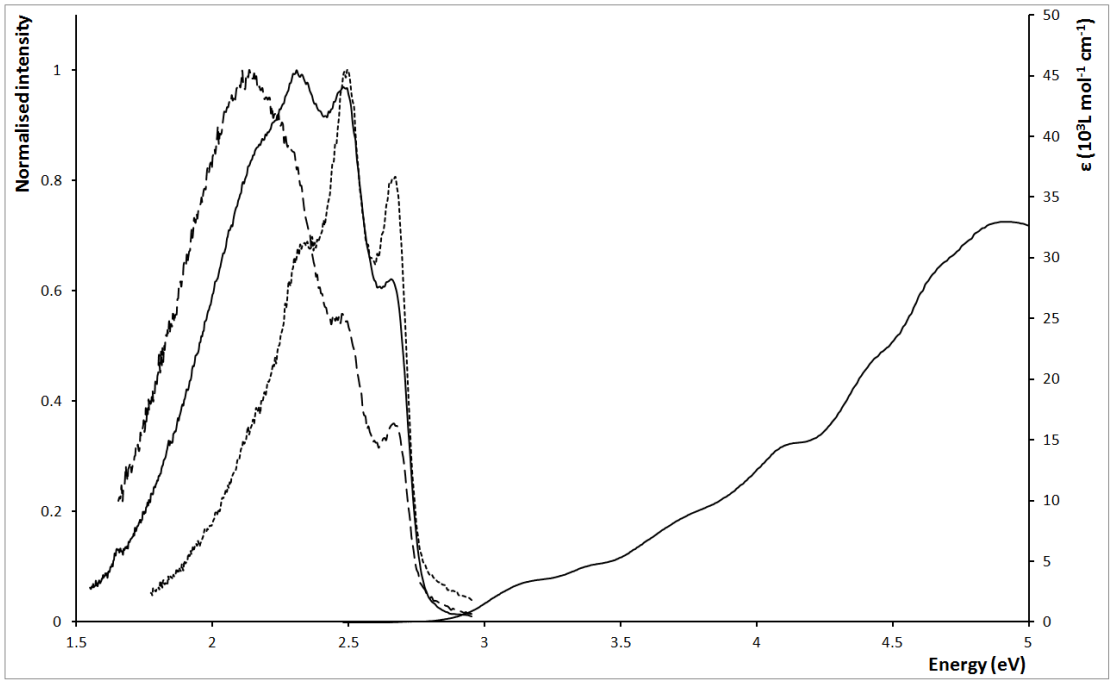

*Figure 9.21: Emission (left) and UV-visible (right) spectra of [Ir(mespim)(CF_3ppz)(acac)] (**24**). DCM: solid line, CCl_4: dashed line, PMMA film: dotted line.*

9.4.3 Pic complexes

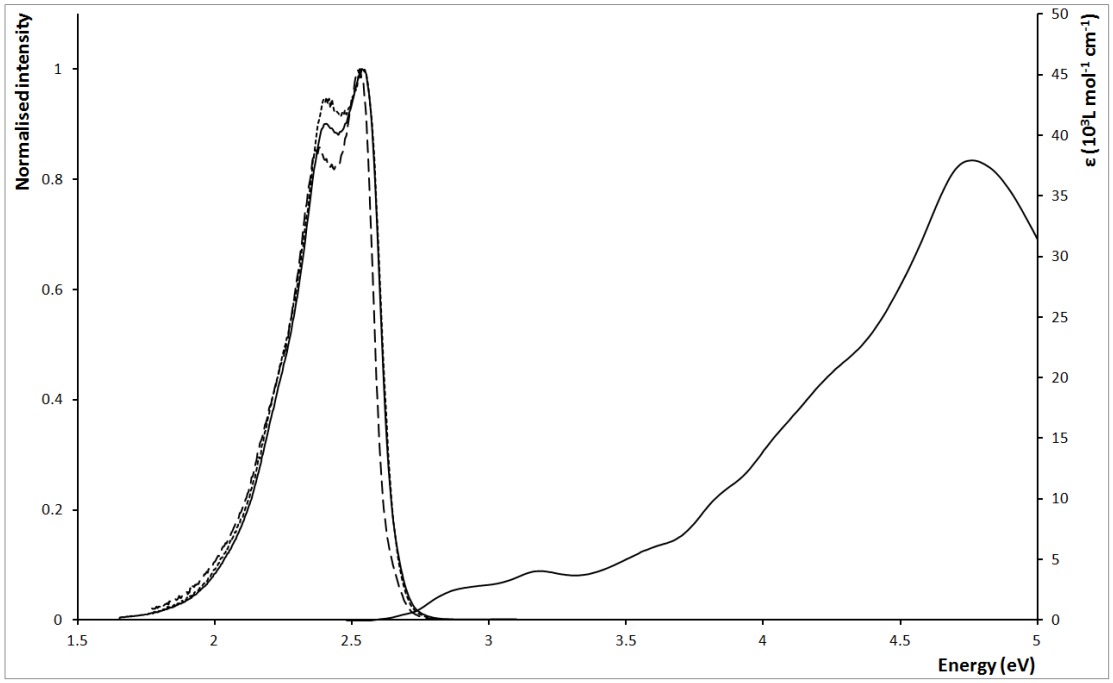

*Figure 9.22: Emission (left) and UV-visible (right) spectra of [Ir(dFppy)(ppy)(pic)] (**3a**). DCM: solid line, CCl_4: dashed line, PMMA film: dotted line.*

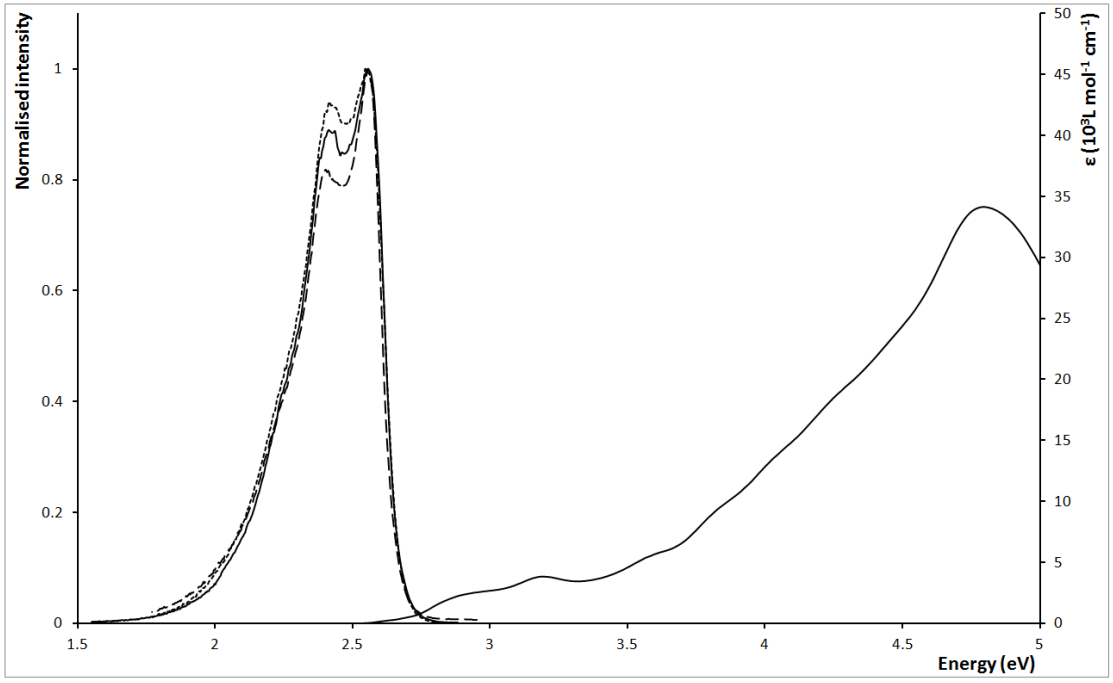

*Figure 9.23: Emission (left) and UV-visible (right) spectra of [Ir(dFppy)(ppy)(pic)] (**3b**). DCM: solid line, CCl_4: dashed line, PMMA film: dotted line.*

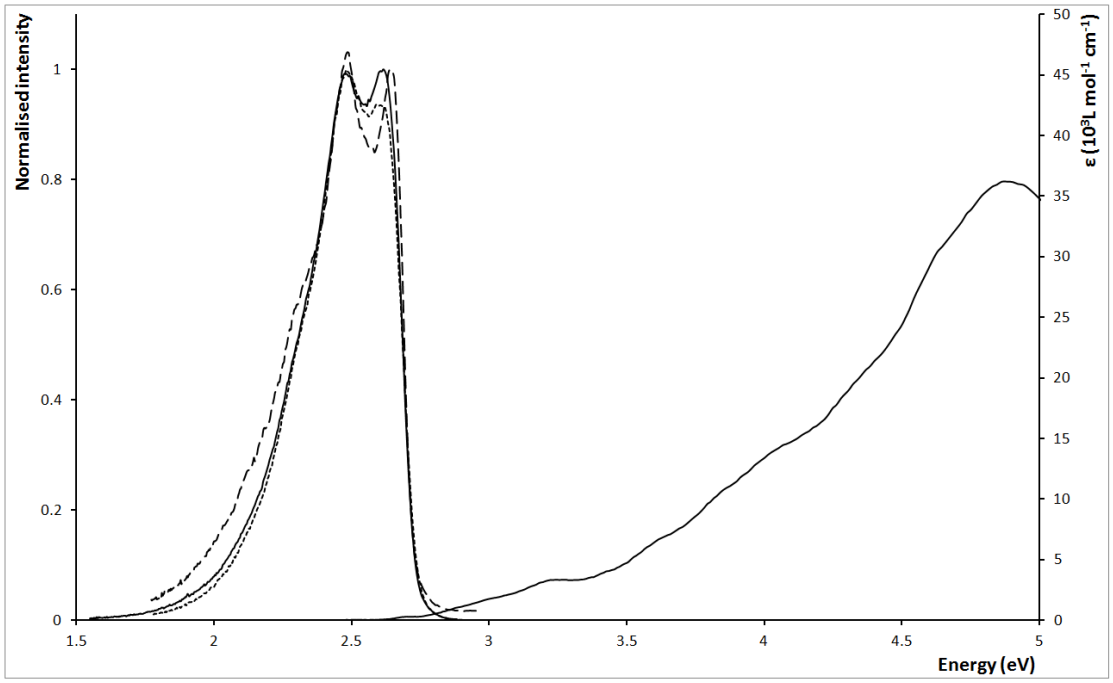

*Figure 9.24: Emission (left) and UV-visible (right) spectra of [Ir(dFppy)(ppz)(pic)] (**9a**). DCM: solid line, CCl_4: dashed line, PMMA film: dotted line.*

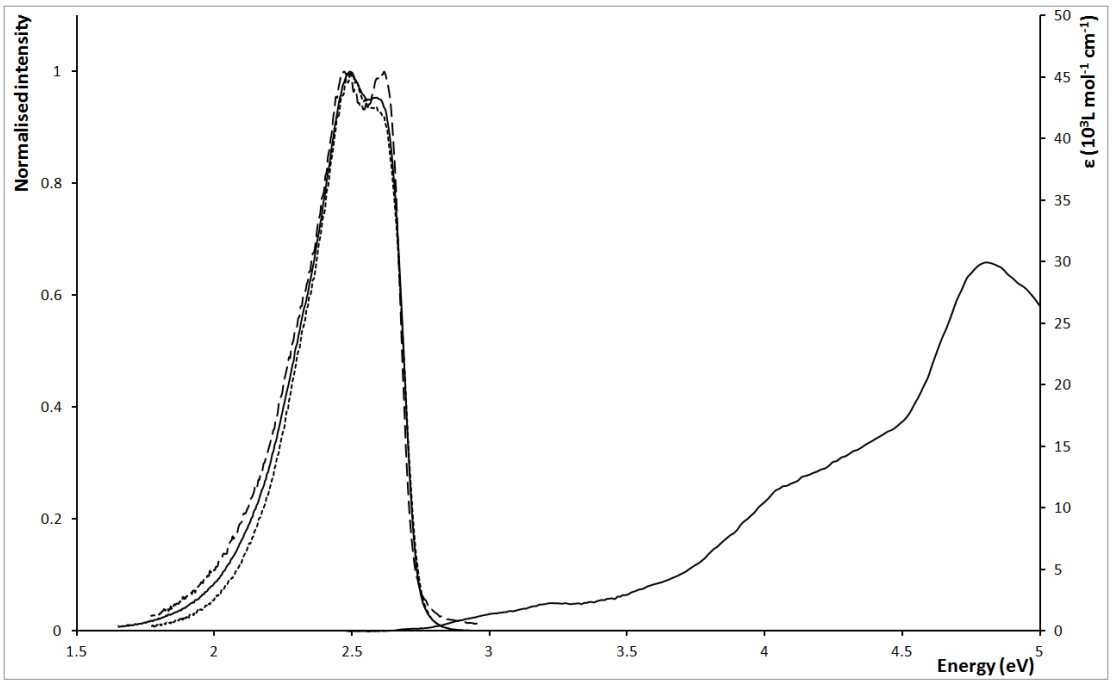

*Figure 9.25: Emission (left) and UV-visible (right) spectra of [Ir(dFppy)(ppz)(pic)] (**9b**). DCM: solid line, CCl_4: dashed line, PMMA film: dotted line.*

9.4.4 Emission spectra with Gaussian fittings

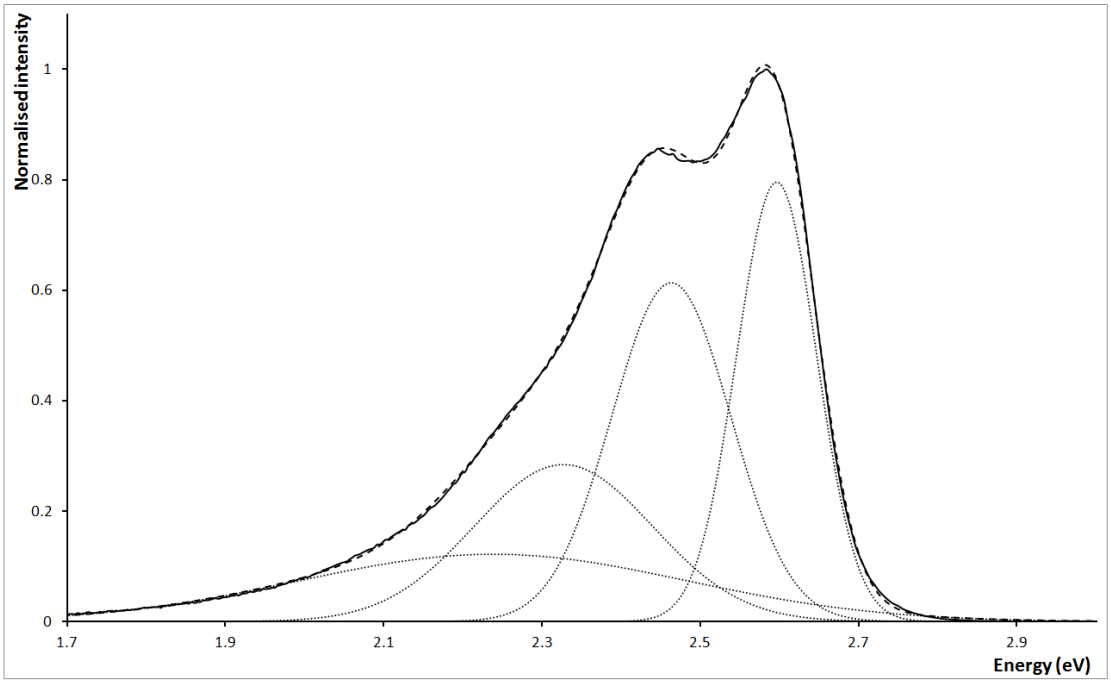

*Figure 9.26: Fit of the emission spectrum of [Ir(dMeOMeOppy)2(acac)] (**13**) with Gaussians. Solid line: normalised emission, dashed line sum of Gaussians, dotted line Gaussian curves.*

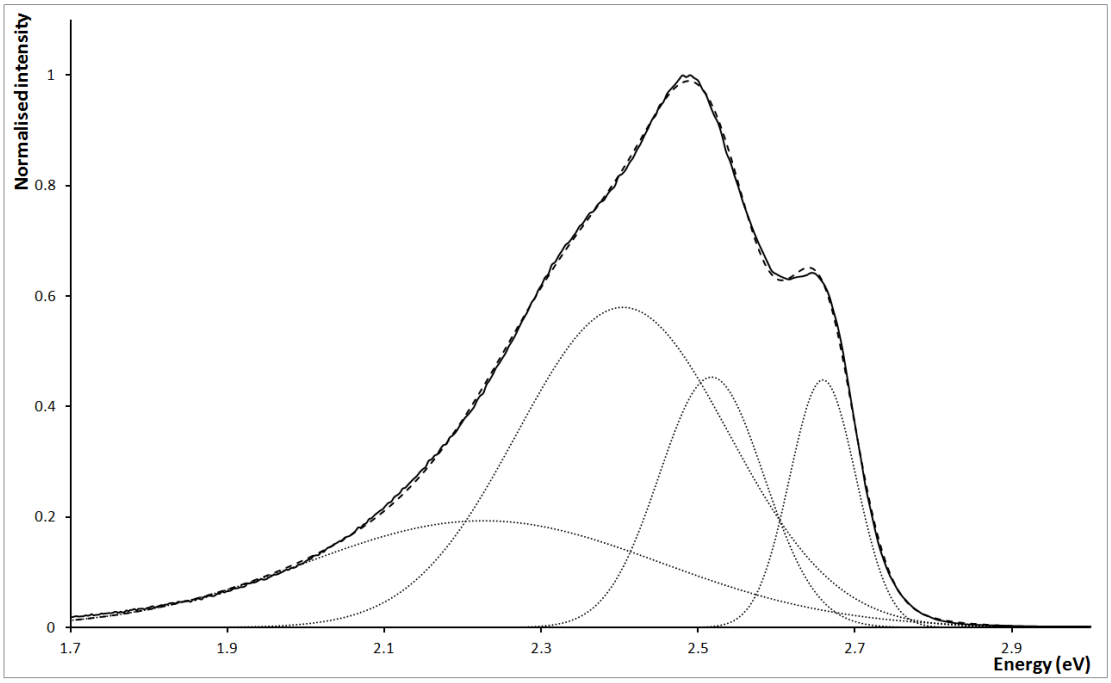

*Figure 9.27: Fit of the emission spectrum of [Ir(dMeOMeOppy)(dFppz)(acac)] (**19**) with Gaussians. Solid line: normalised emission, dashed line sum of Gaussians, dotted line Gaussian curves.*

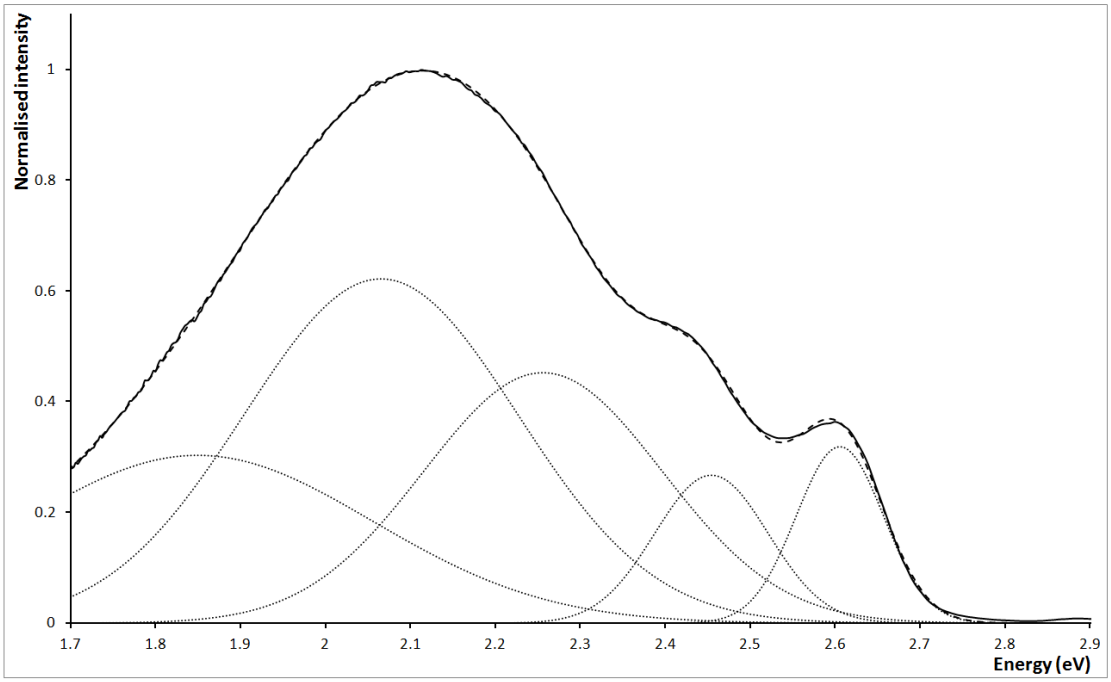

*Figure 9.28: Fit of the emission spectrum of [Ir(mespim)$_2$(acac)] (**20**) with Gaussians. Solid line: normalised emission, dashed line sum of Gaussians, dotted line Gaussian curves.*

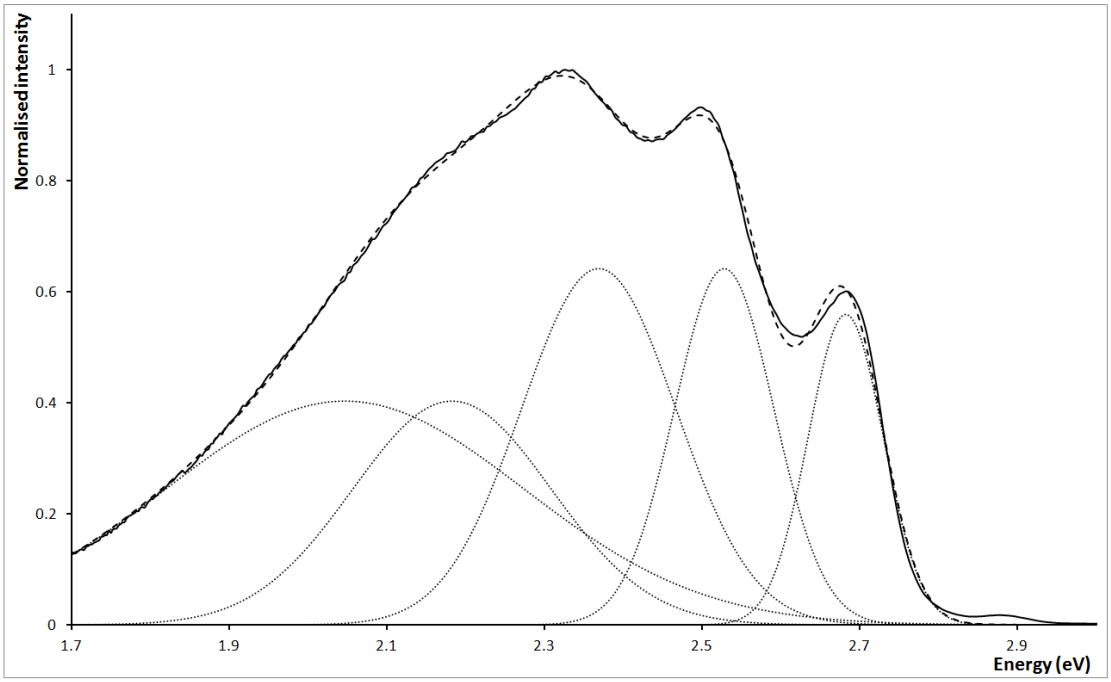

*Figure 9.29: Fit of the emission spectrum of [Ir(mespim)(dFppz)(acac)] (**22**) with Gaussians. Solid line: normalised emission, dashed line sum of Gaussians, dotted line Gaussian curves.*

9.5 NMR ANALYSES

All NMR spectra were measured in $CDCl_3$ unless stated otherwise.

9.5.1 [Ir(ppy)$_2$(acac)] (1)

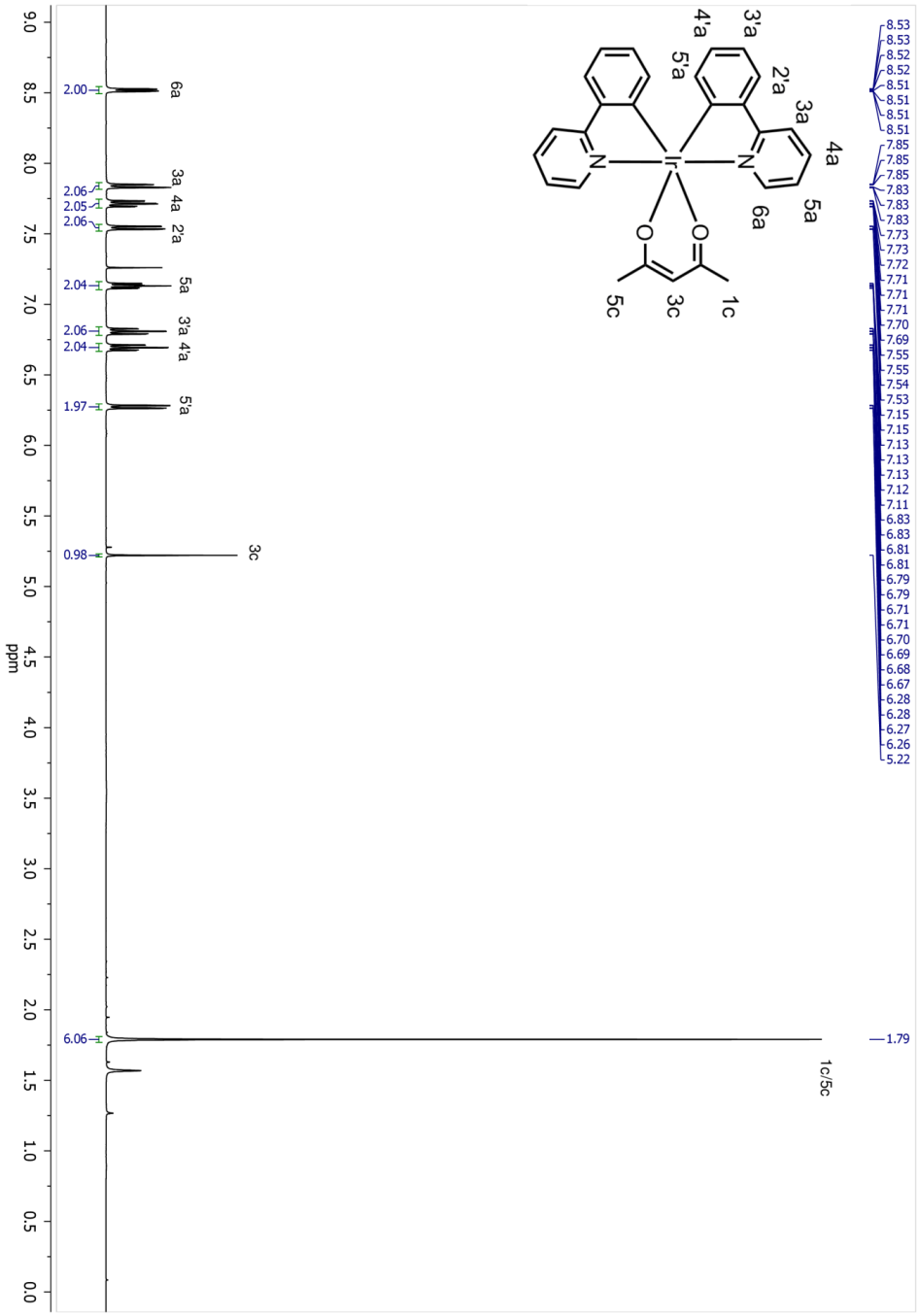

*Figure 9.30: ^{1}H-NMR spectrum of [Ir(ppy)$_2$(acac)] (**1**).*

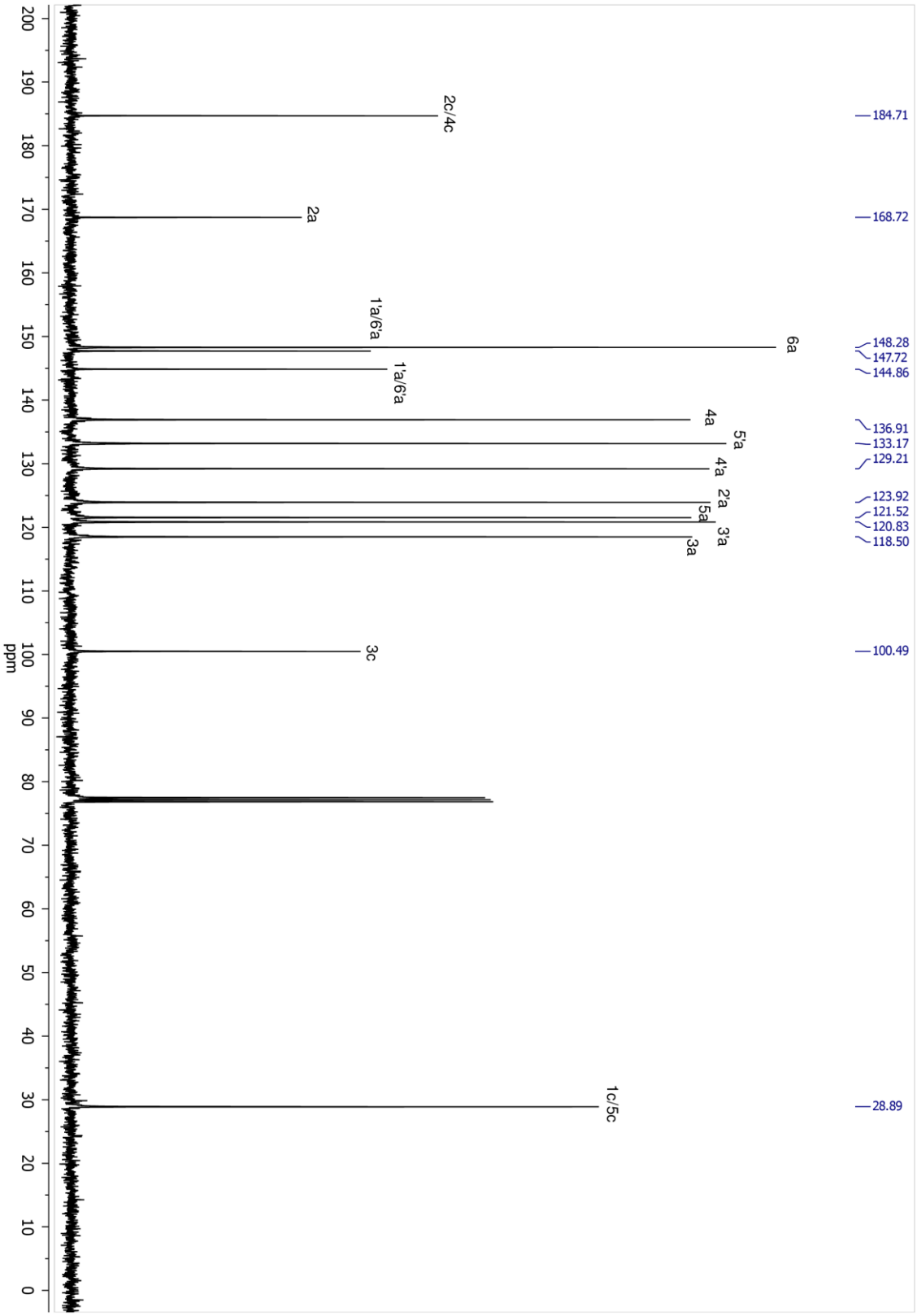

*Figure 9.31: ^{13}C-NMR spectrum of [Ir(ppy)$_2$(acac)] (**1**).*

9.6 [Ir(dFppy)$_2$(acac)] (2)

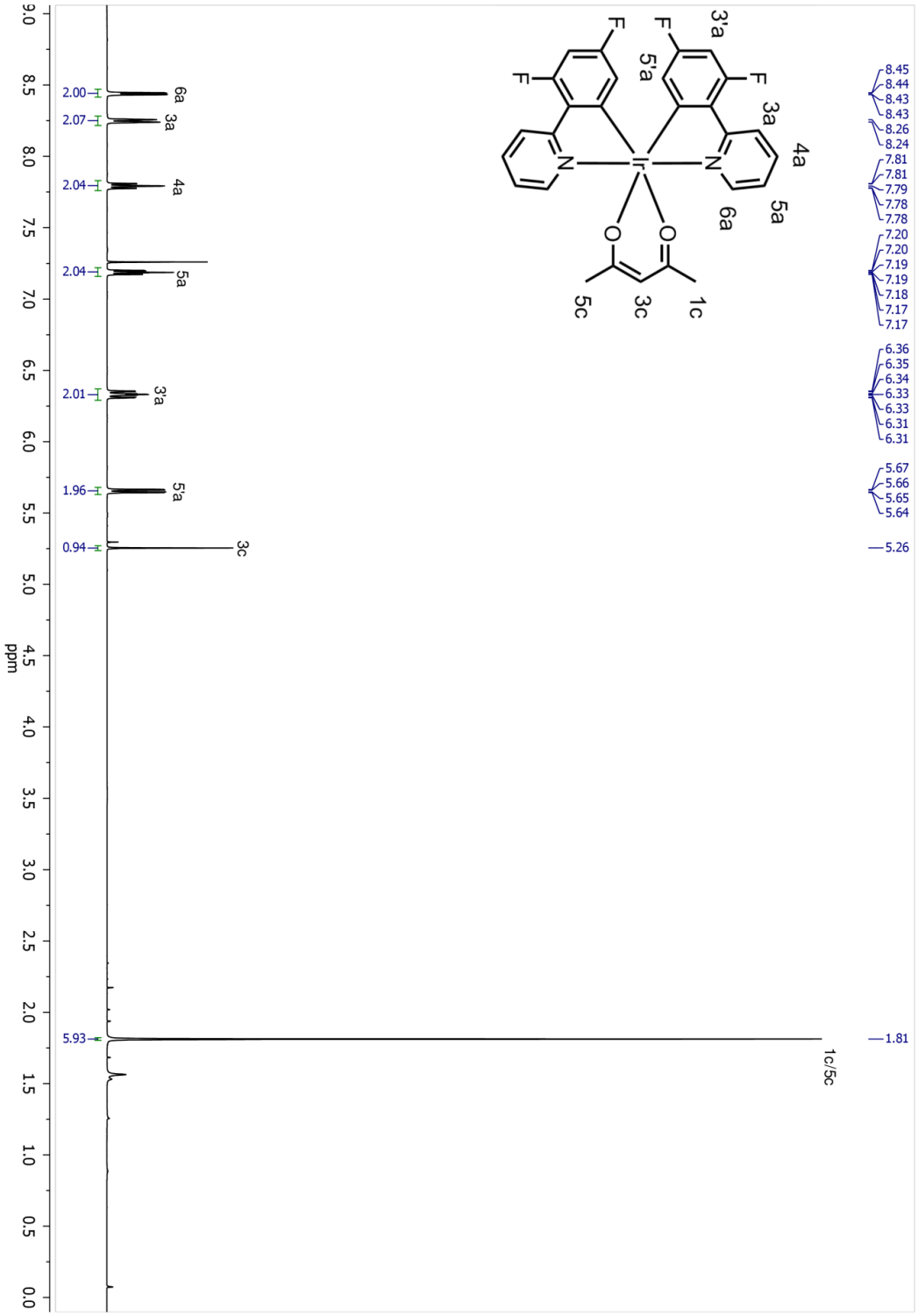

*Figure 9.32: ^{1}H-NMR spectrum of [Ir(dFppy)$_2$(acac)] (**2**).*

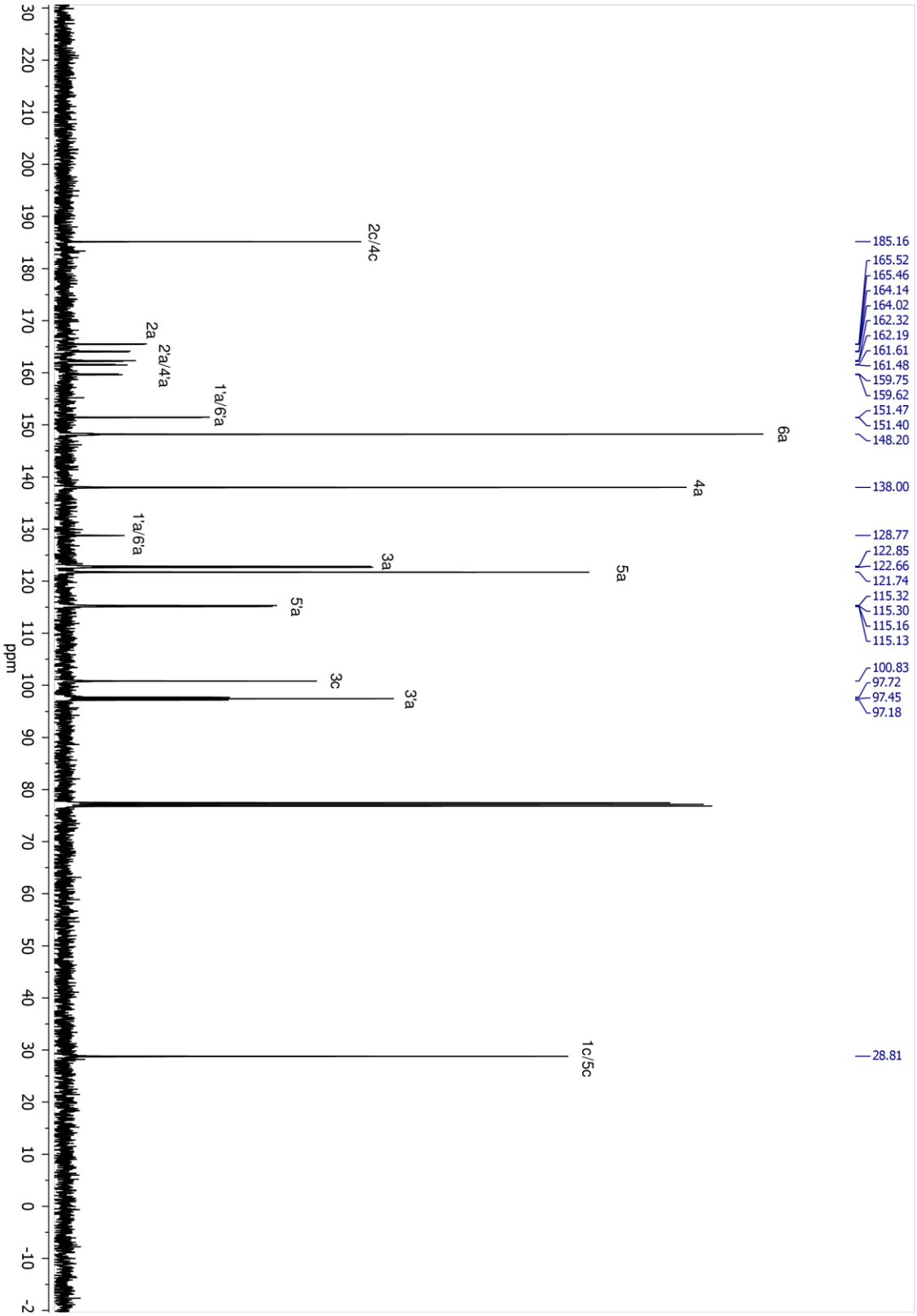

*Figure 9.33: 13C-NMR spectrum of [Ir(dFppy)$_2$(acac)] (**2**).*

9.6.1 [Ir(dFppy)(ppy)(acac)] (3)

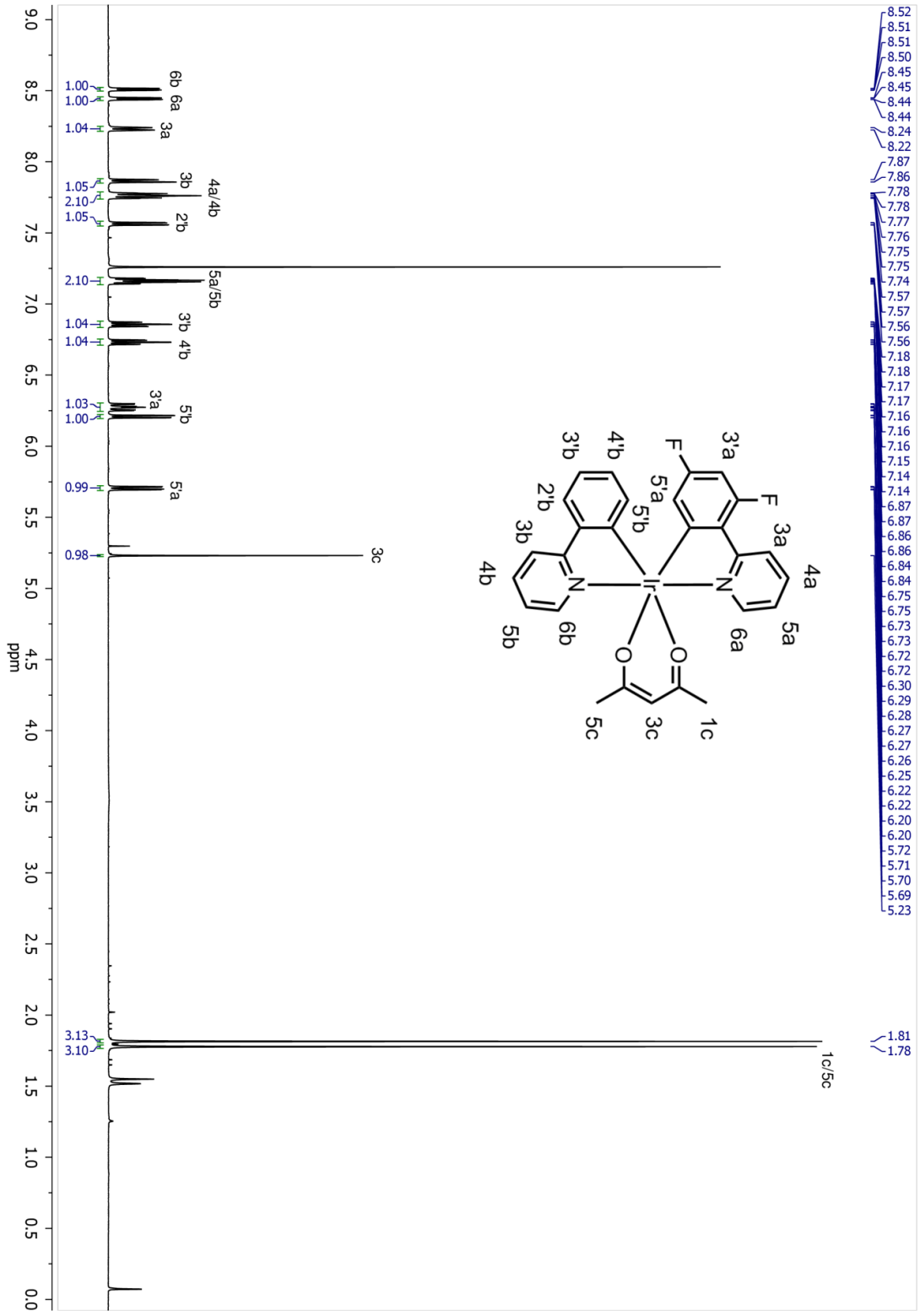

*Figure 9.34: ^{1}H-NMR spectrum of [Ir(dFppy)(ppy)(acac)] (**3**).*

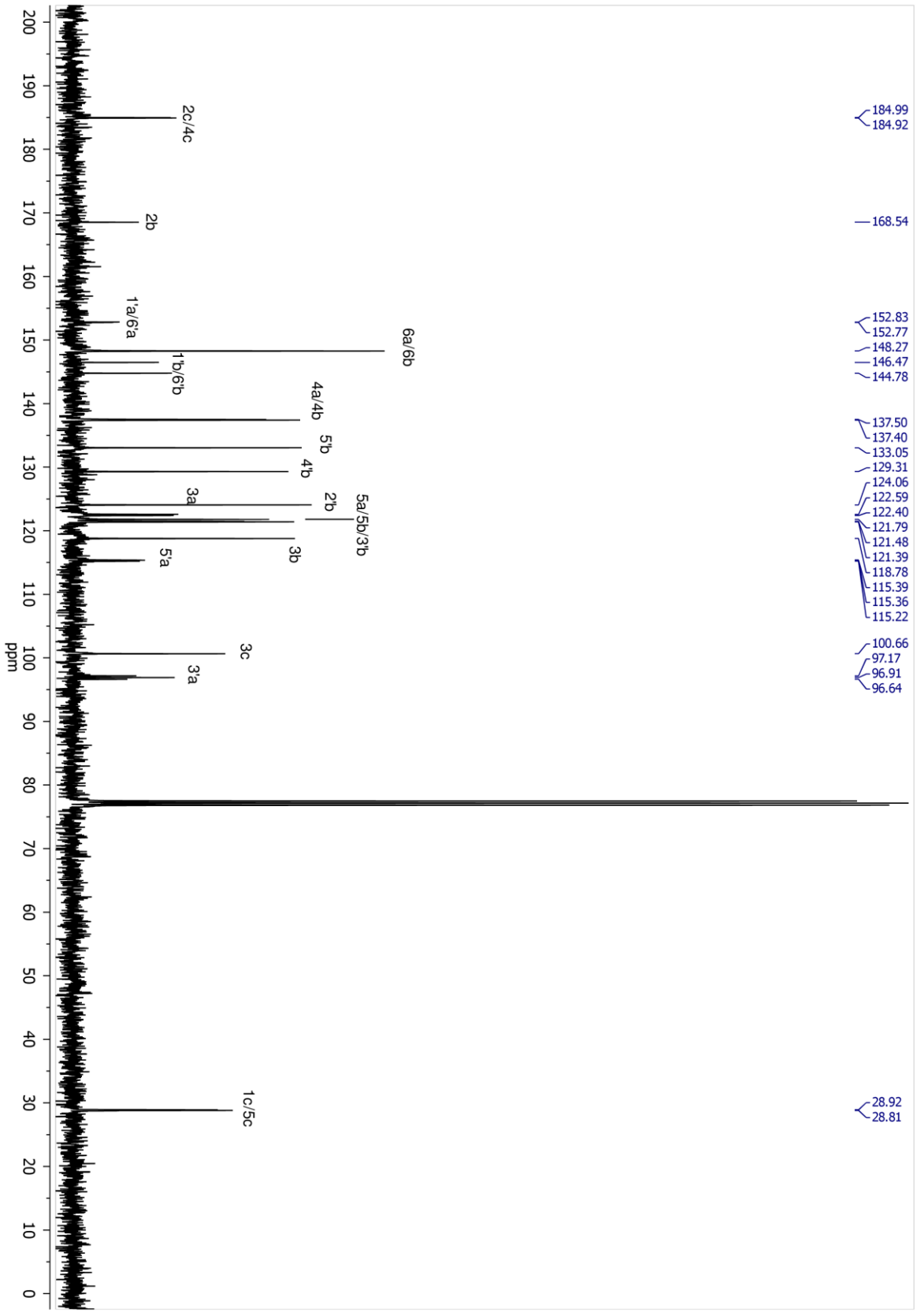

*Figure 9.35: ^{13}C-NMR spectrum of [Ir(dFppy)(ppy)(acac)] (**3**).*

9.6.2 [Ir(ppz)$_2$(acac)] (4)

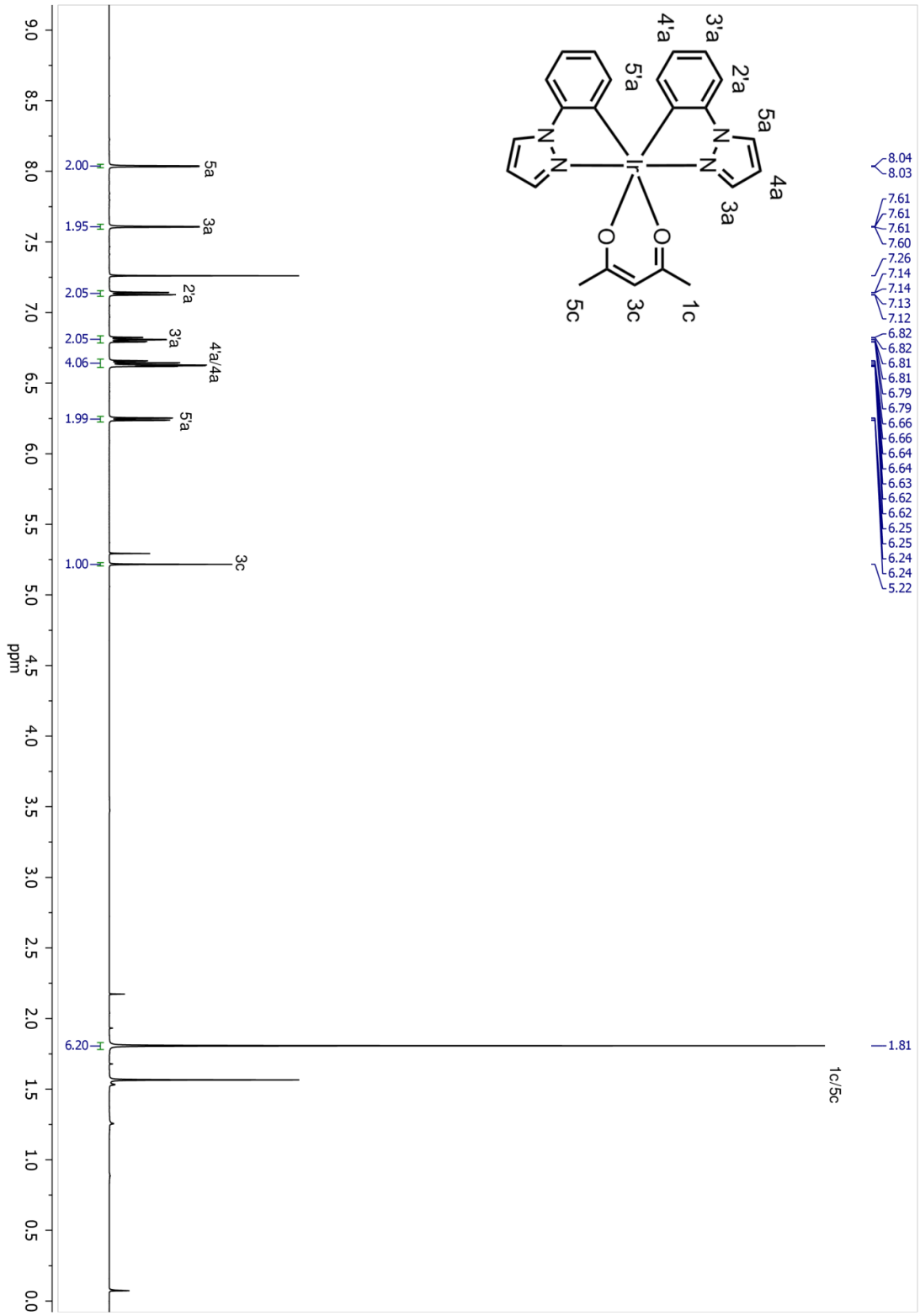

*Figure 9.36: ^{1}H-NMR spectrum of [Ir(ppz)$_2$(acac)] (**4**).*

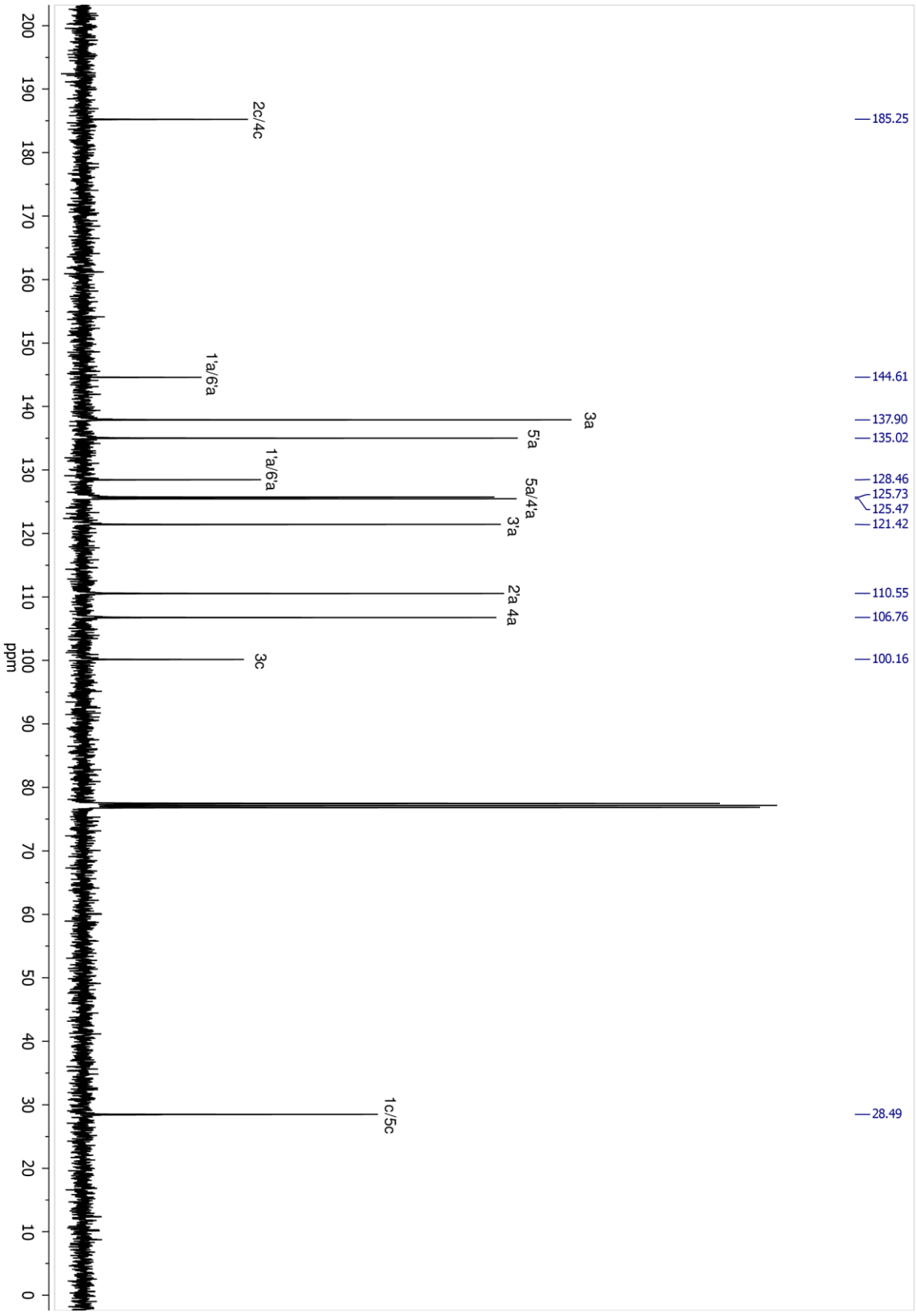

*Figure 9.37: ^{13}C-NMR spectrum of [Ir(ppz)$_2$(acac)] (**4**).*

9.6.3 [Ir(dFppz)$_2$(acac)] (5)

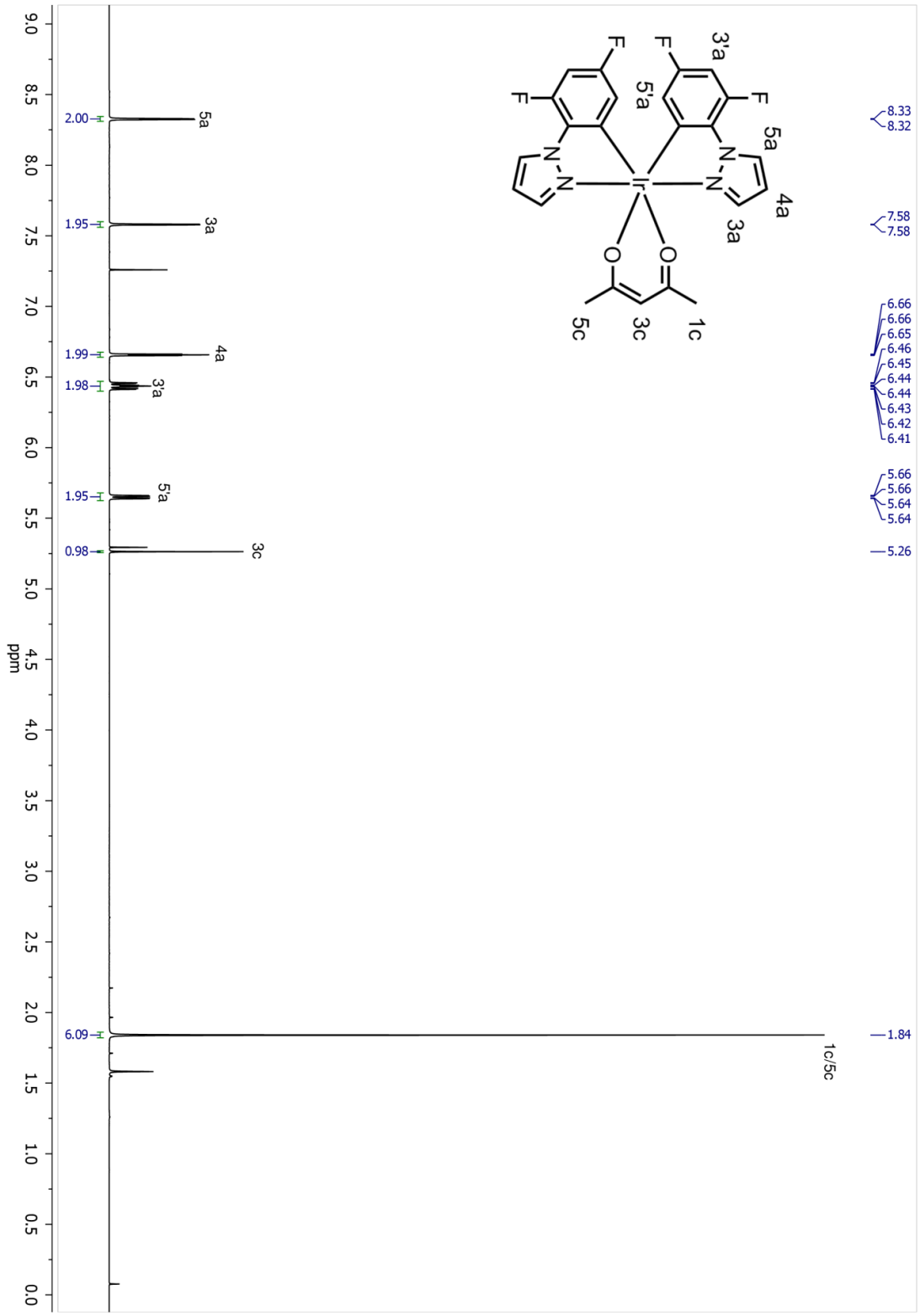

*Figure 9.38: ^{1}H-NMR spectrum of [Ir(dFppz)$_2$(acac)] (**5**).*

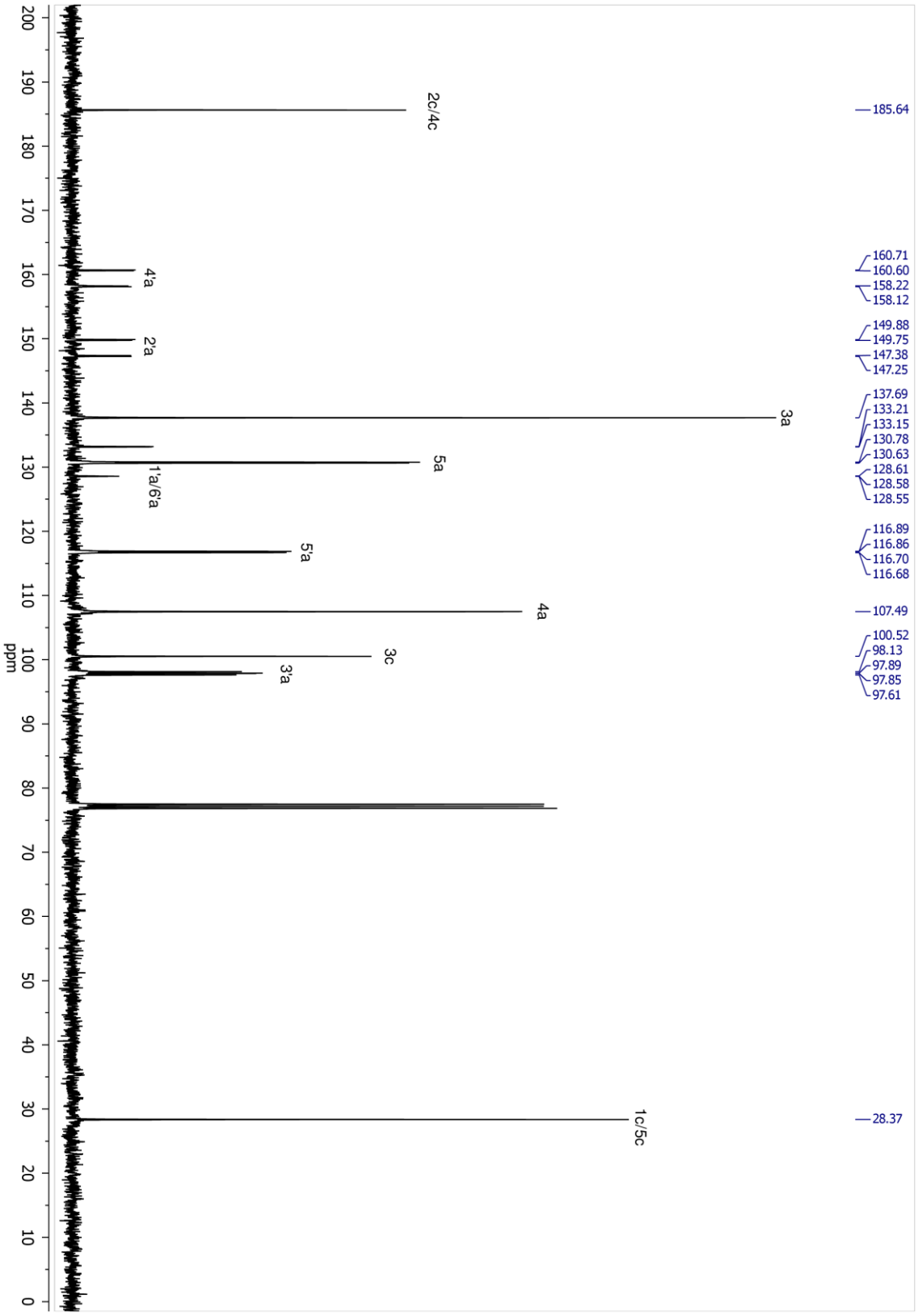

*Figure 9.39: ^{13}C-NMR spectrum of [Ir(dFppz)$_2$(acac)] (**5**).*

9.6.4 [Ir(dFppz)(ppz)(acac)] (6)

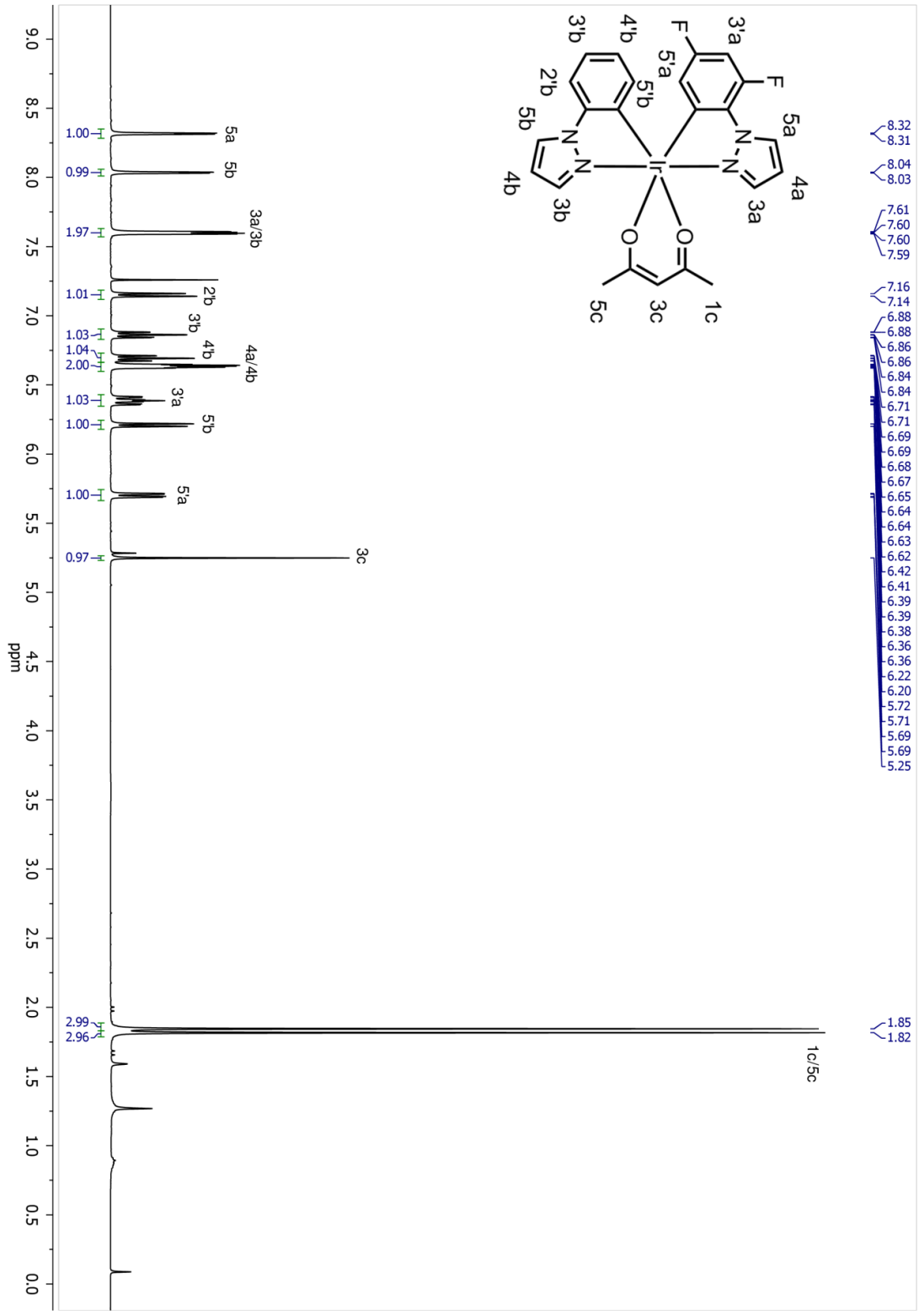

*Figure 9.40: [1]H-NMR spectrum of [Ir(dFppz)(ppz)(acac)] (**6**).*

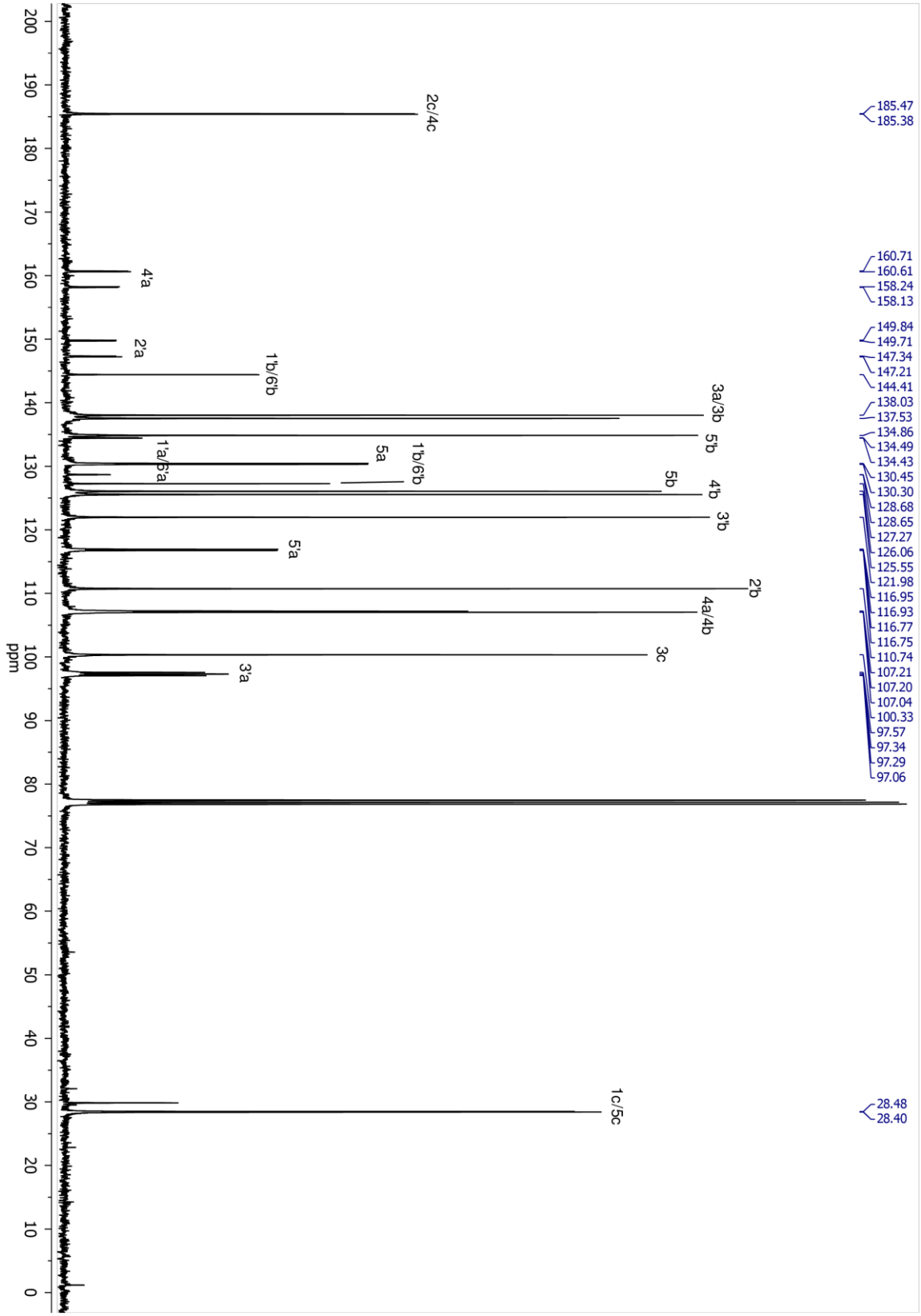

Figure 9.41: [13]C-NMR spectrum of [Ir(dFppz)(ppz)(acac)] (6).

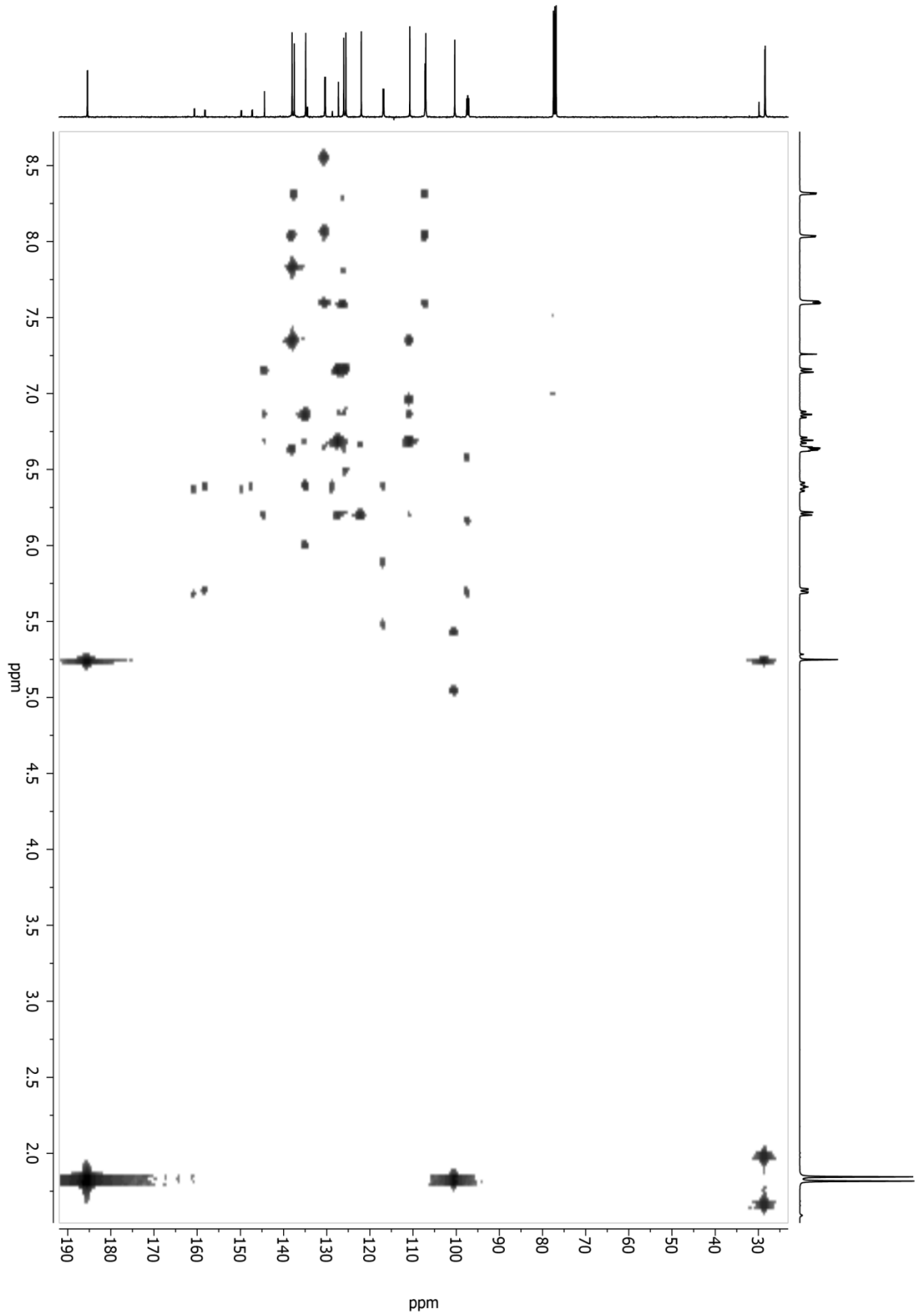

*Figure 9.42: HMBC spectrum of [Ir(dFppz)(ppz)(acac)] (**6**).*

9.6.5 [Ir(ppy)(ppz)(acac)] (7)

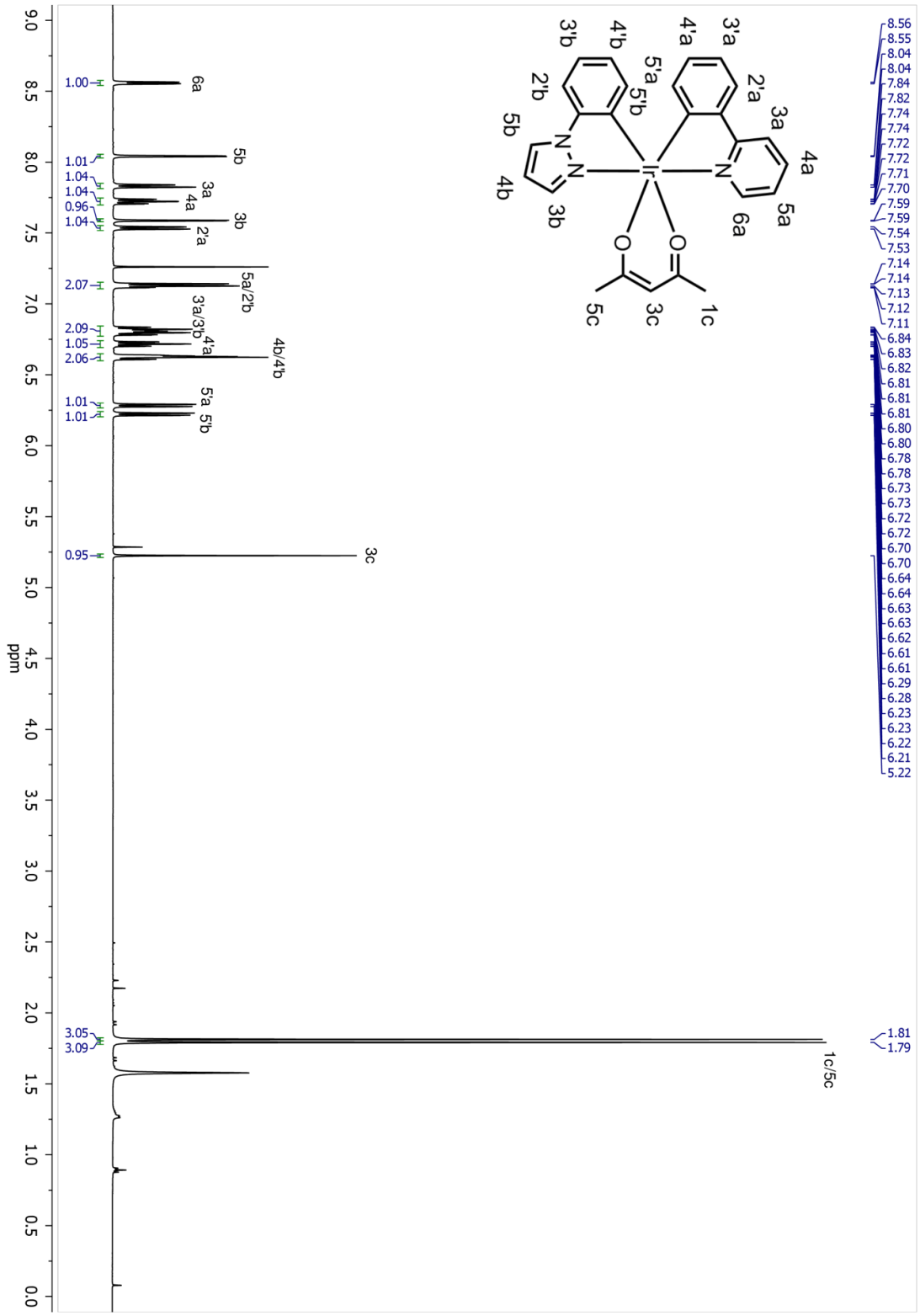

Figure 9.43: [1]H-NMR spectrum of [Ir(ppy)(ppz)(acac)] (7).

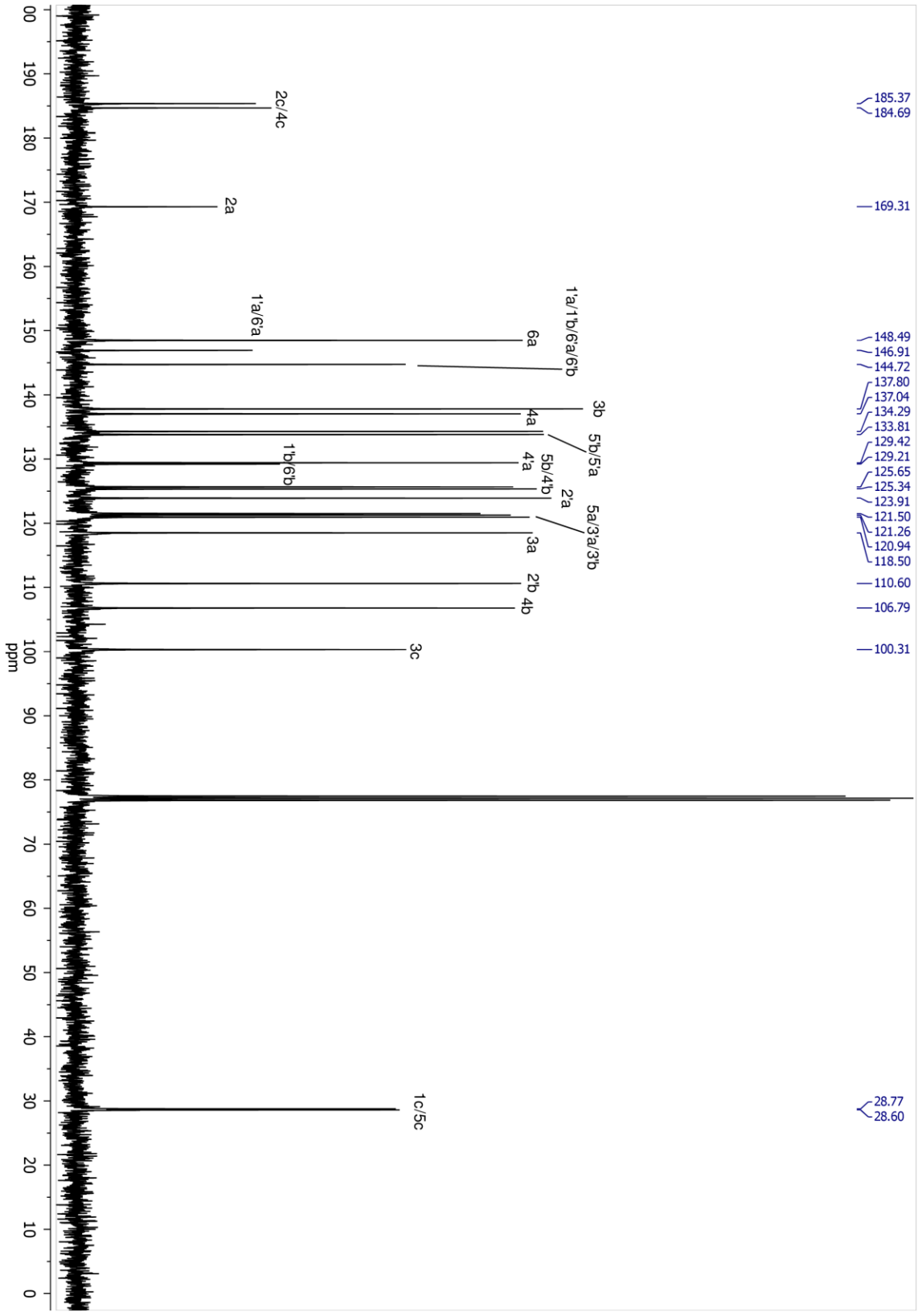

*Figure 9.44: ^{13}C-NMR spectrum of [Ir(ppy)(ppz)(acac)] (**7**).*

9.6.6 [Ir(dFppy)(dFppz)(acac)] (8)

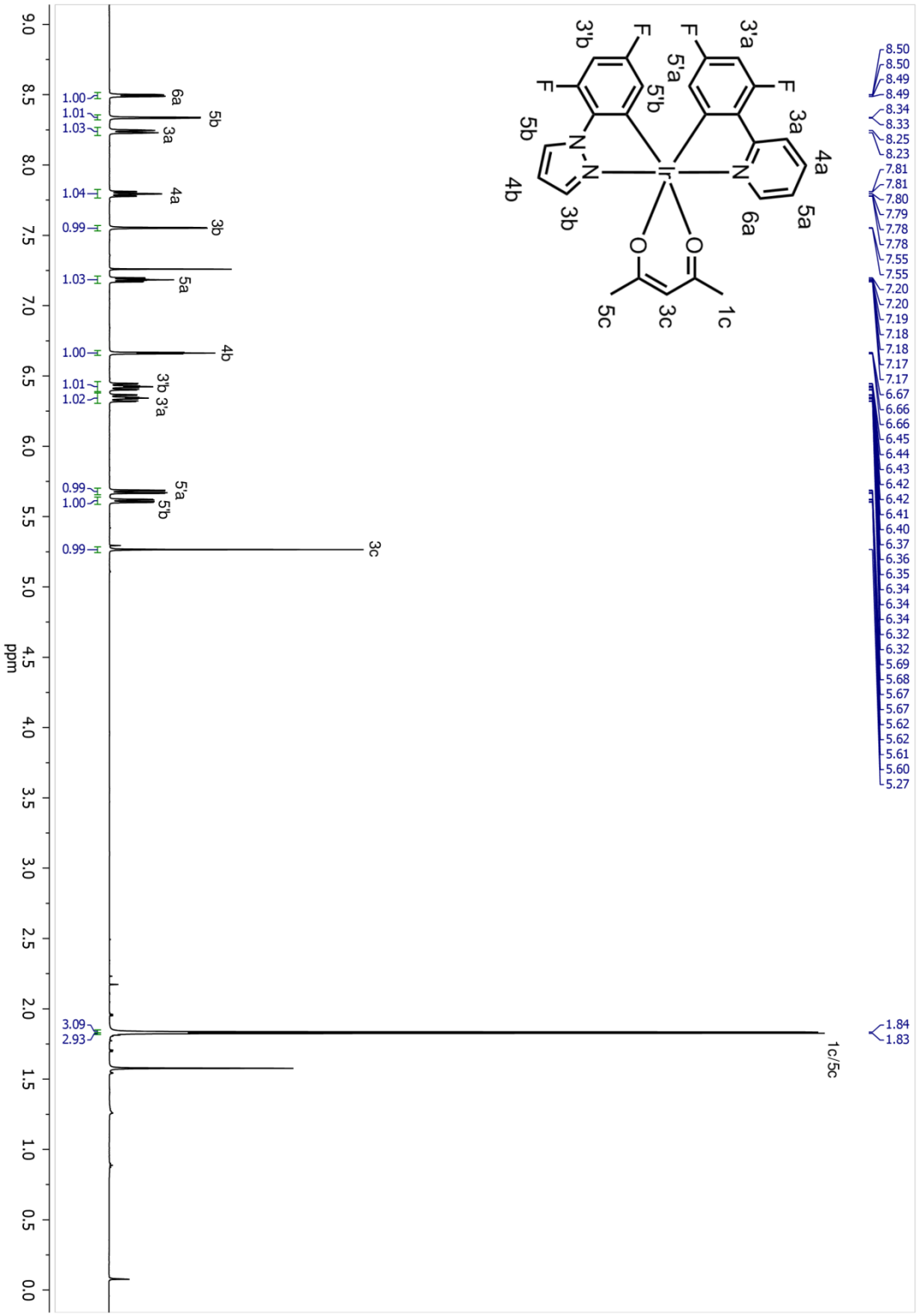

*Figure 9.45: ^{1}H-NMR spectrum of [Ir(dFppy)(dFppz)(acac)] (**8**).*

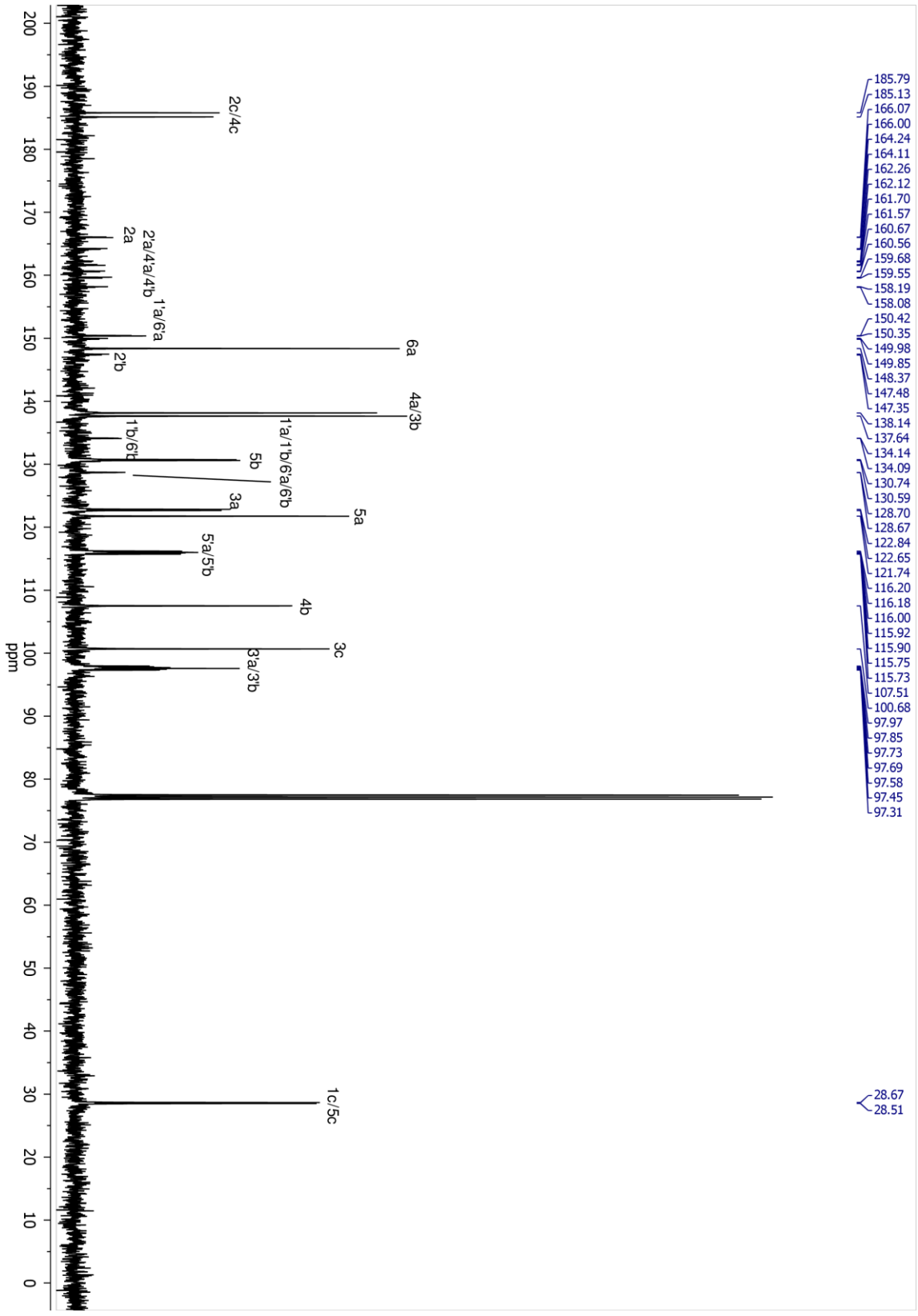

*Figure 9.46: ^{13}C-NMR spectrum of [Ir(dFppy)(dFppz)(acac)] (**8**).*

9.6.7 [Ir(dFppy)(ppz)(acac)] (9)

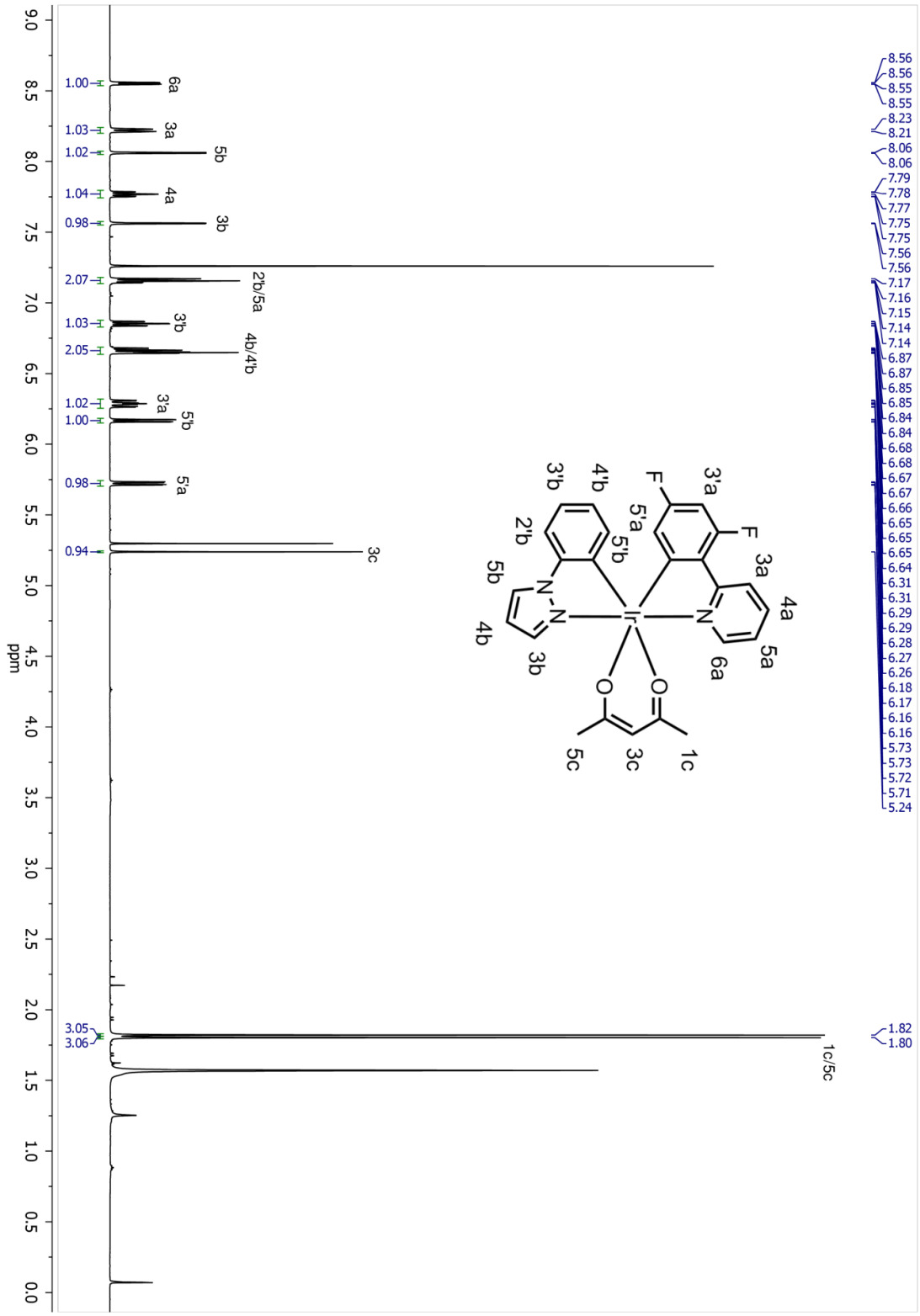

*Figure 9.47: [1]H-NMR spectrum of [Ir(dFppy)(ppz)(acac)] (**9**).*

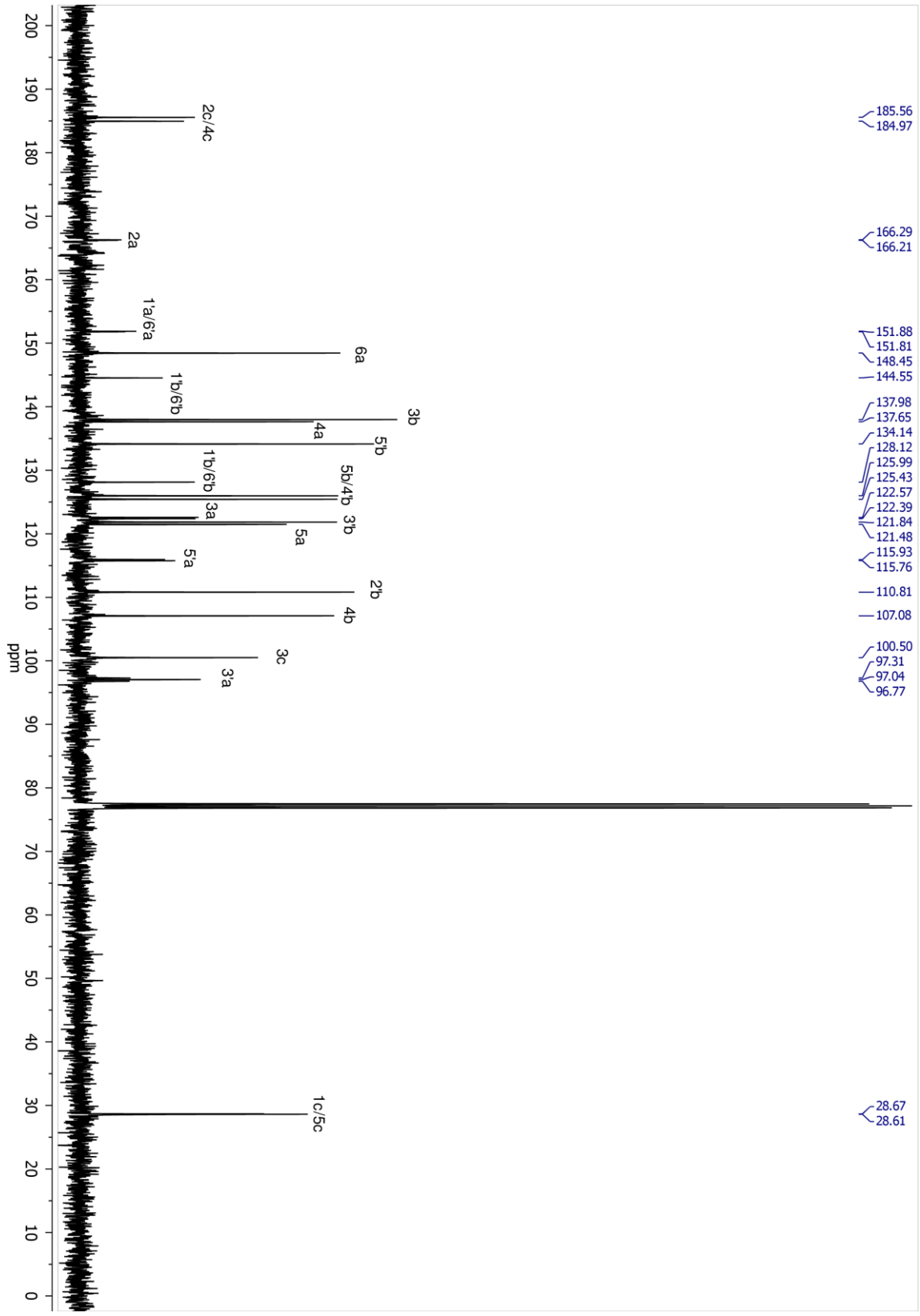

*Figure 9.48: [13]C-NMR spectrum of [Ir(dFppy)(ppz)(acac)] (**9**).*

9.6.8 [Ir(dFppz)(ppy)(acac)] (10)

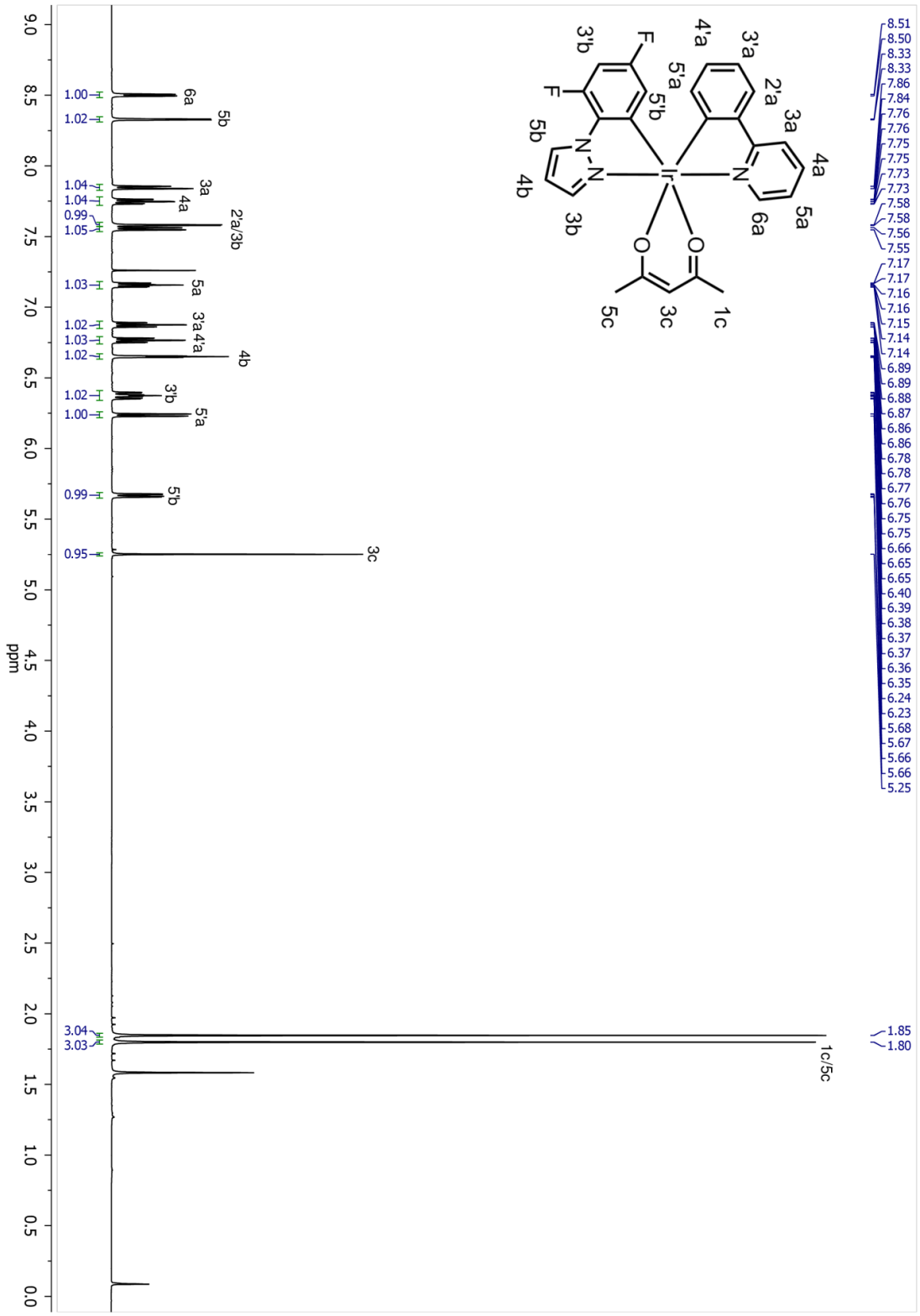

*Figure 9.49: [1]H-NMR spectrum of [Ir(dFppz)(ppy)(acac)] (**10**).*

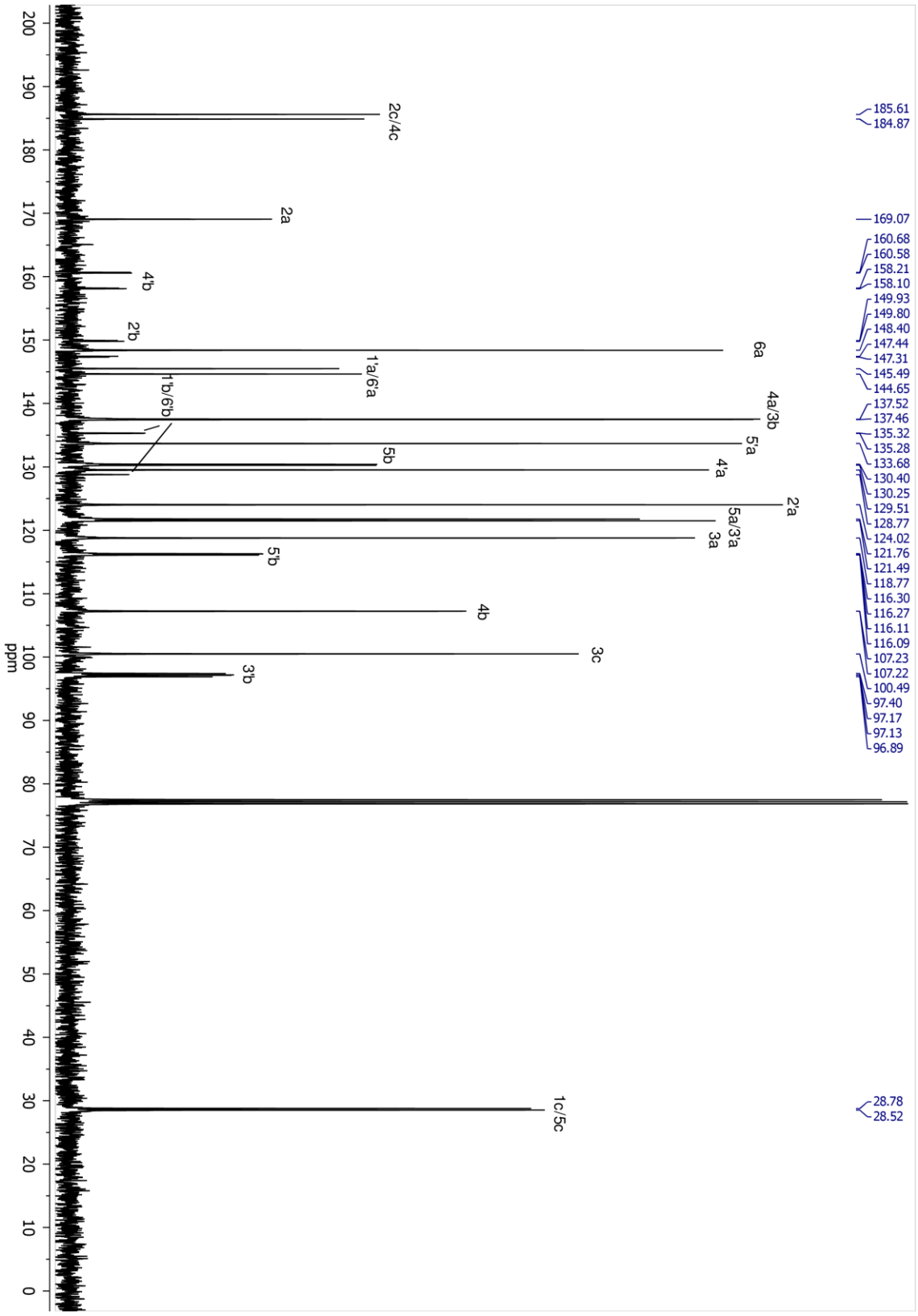

*Figure 9.50: [13]C-NMR spectrum of [Ir(dFppz)(ppy)(acac)] (**10**).*

9.6.9 [Ir(dMeOppy)$_2$(acac)] (11)

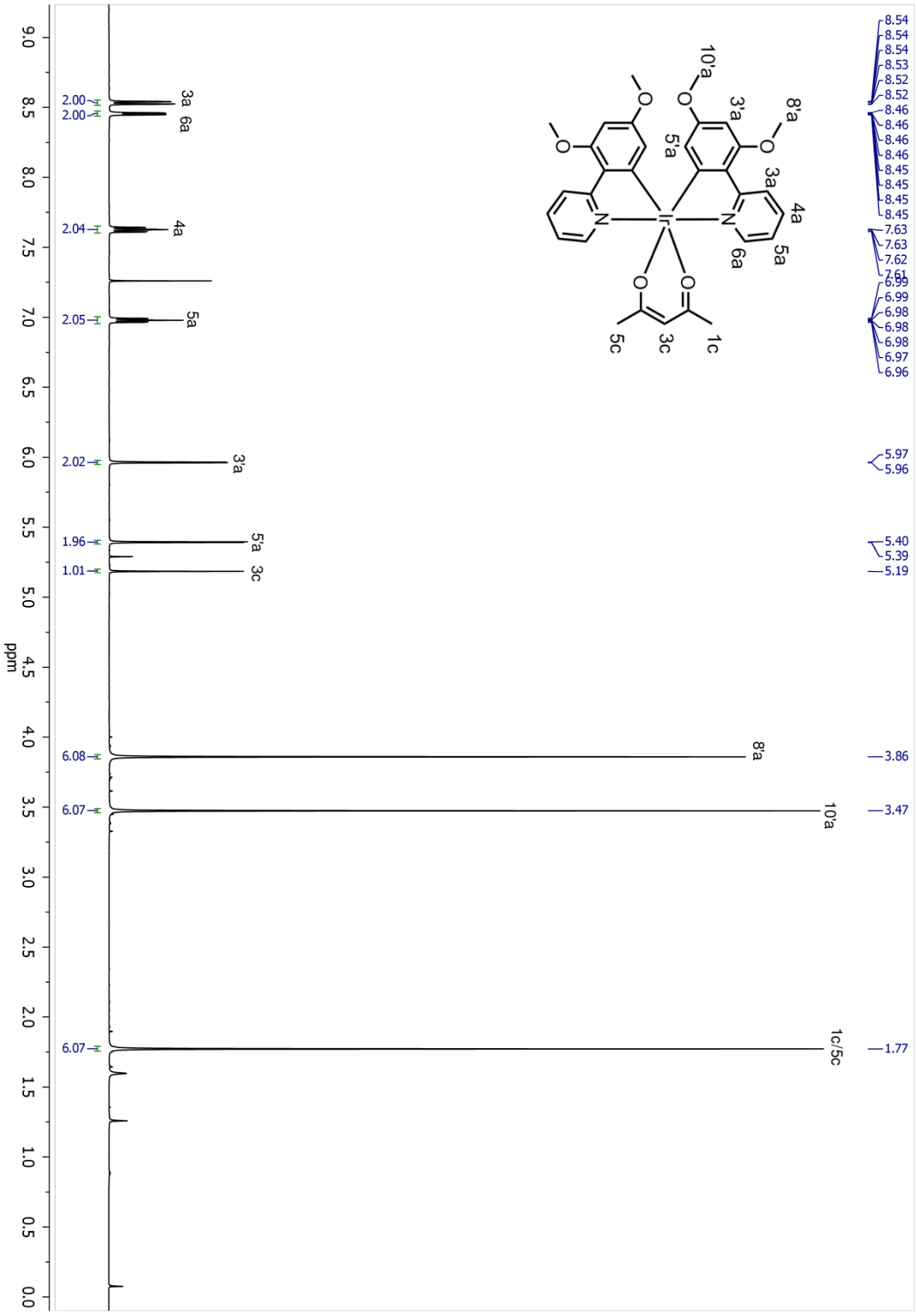

*Figure 9.51: ^{1}H-NMR spectrum of [Ir(dMeOppy)$_2$(acac)] (**11**).*

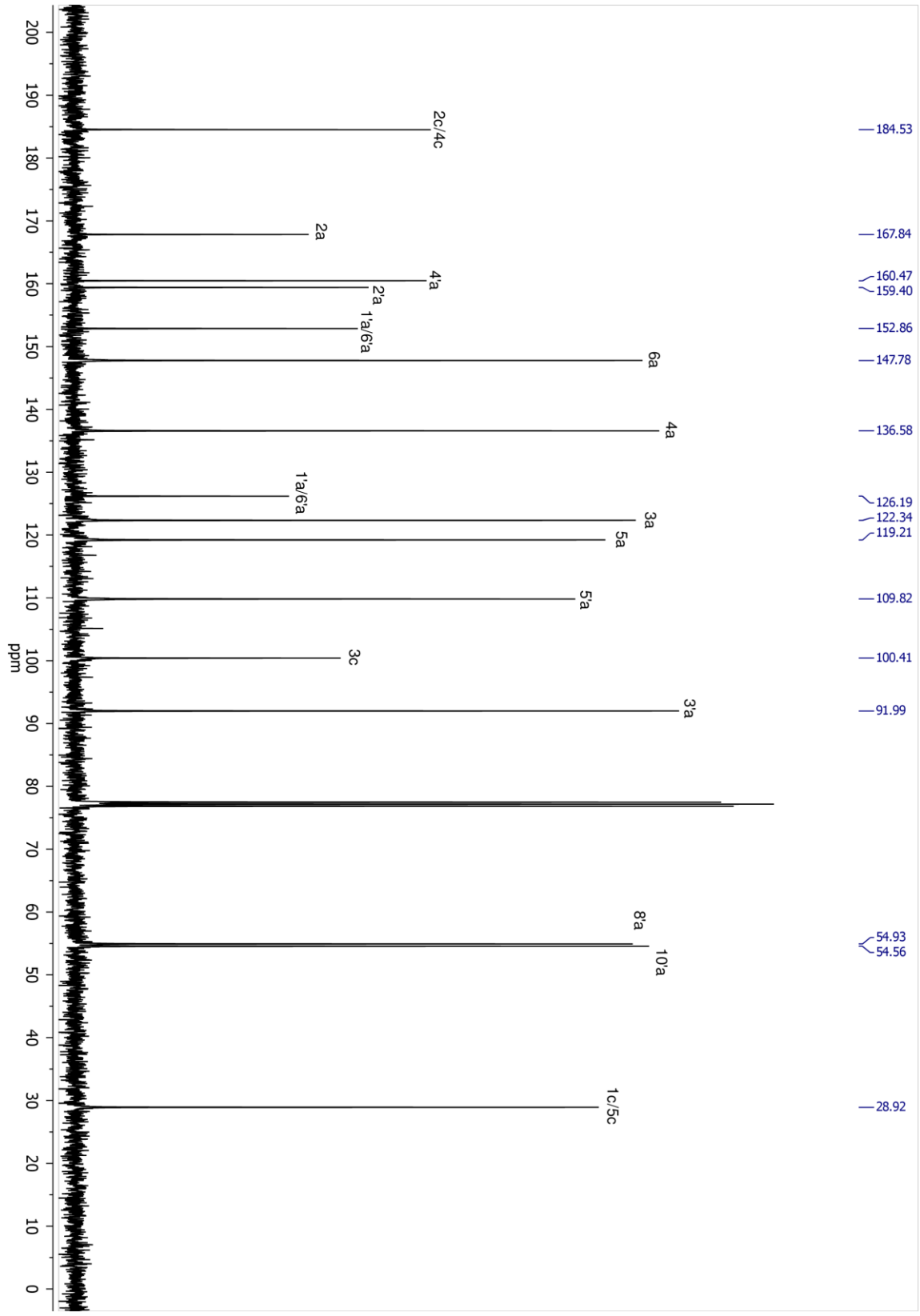

*Figure 9.52: ^{13}C-NMR spectrum of [Ir(dMeOppy)$_2$(acac)] (**11**).*

9.6.10 [Ir(dMeOMeppy)$_2$(acac)] (12)

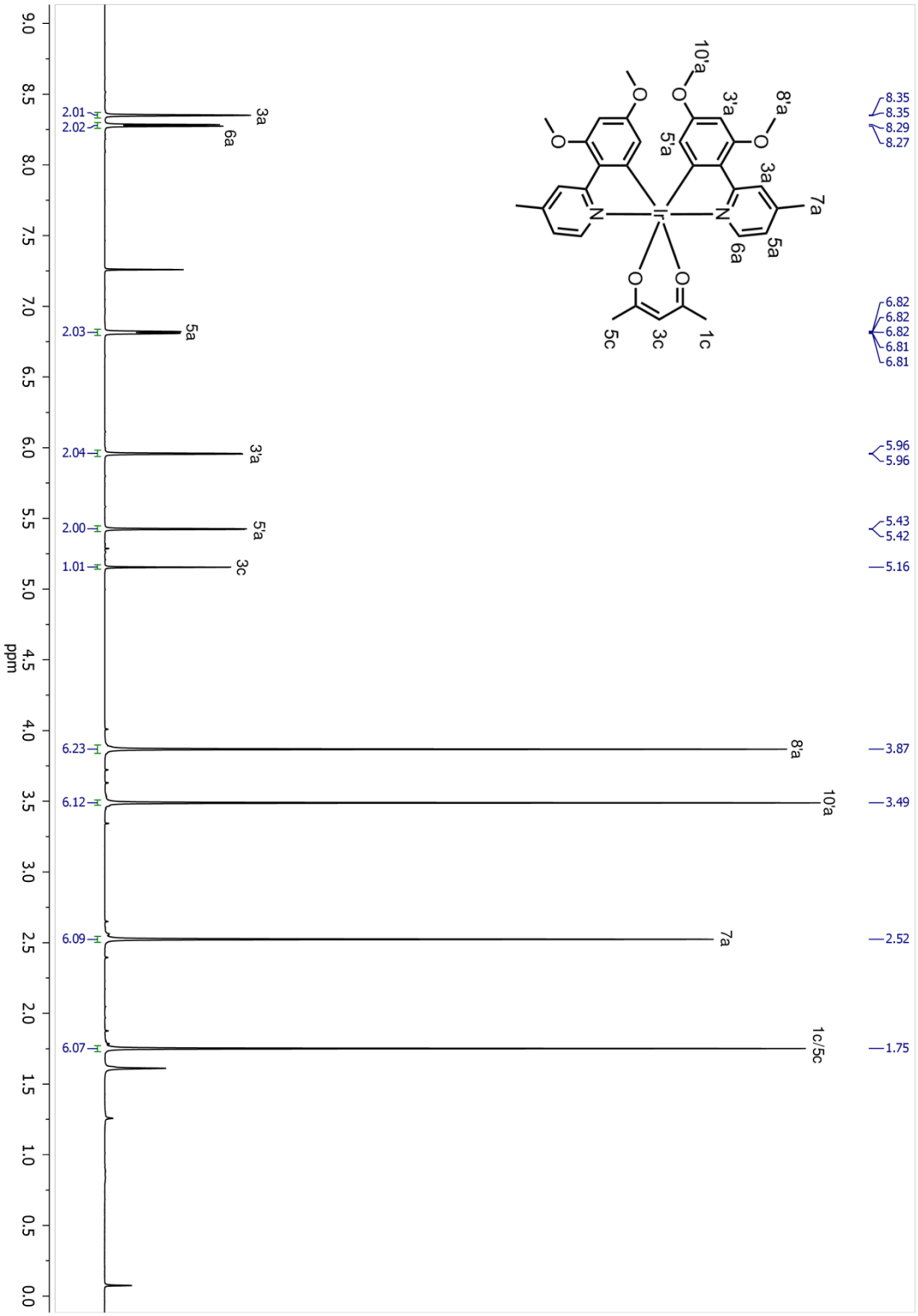

*Figure 9.53: ^{1}H-NMR spectrum of [Ir(dMeOMeppy)$_2$(acac)] (**12**).*

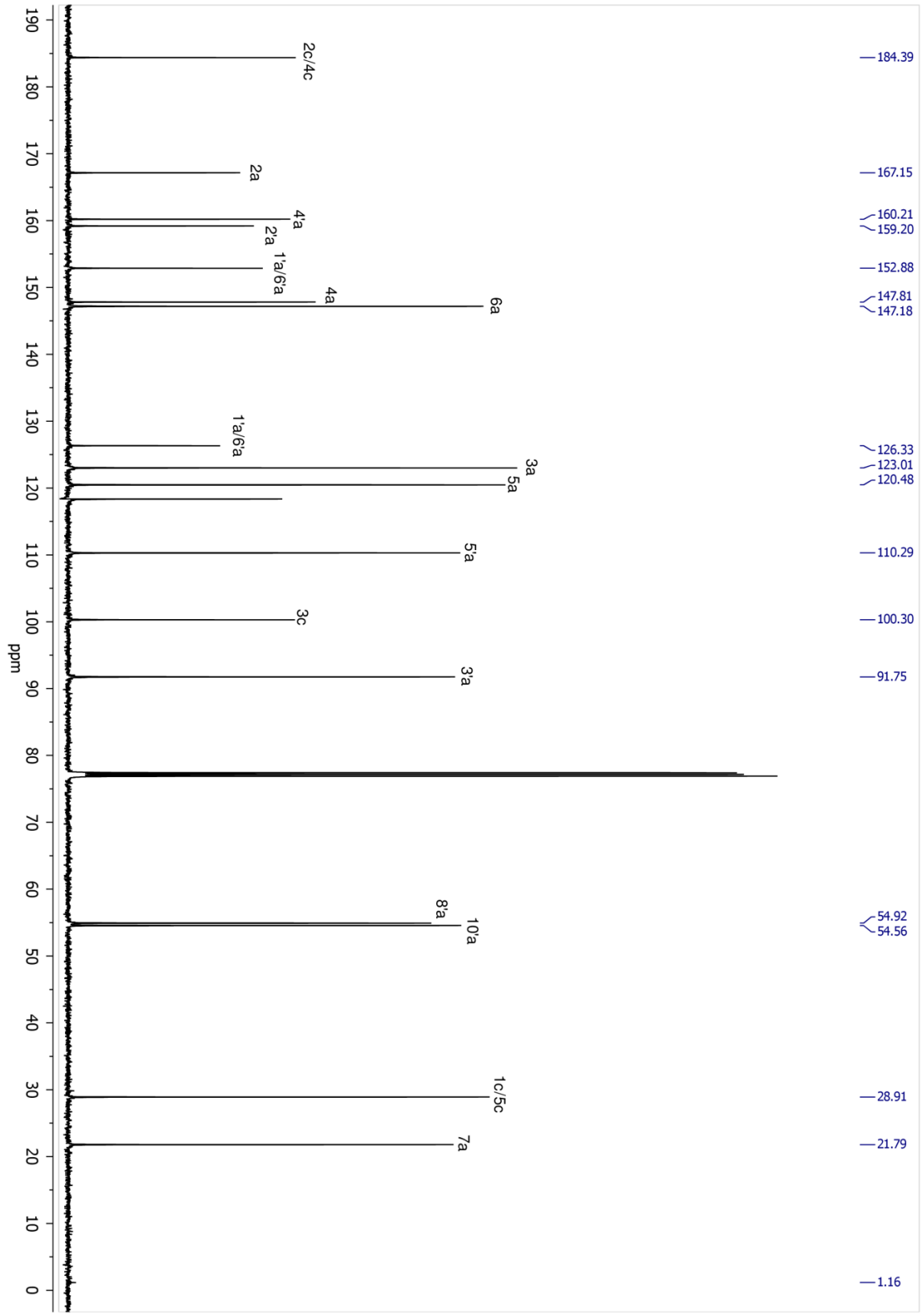

*Figure 9.54: ^{13}C-NMR spectrum of [Ir(dMeOMeppy)$_2$(acac)] (**12**).*

9.6.11 [Ir(dMeOMeOppy)$_2$(acac)] (13)

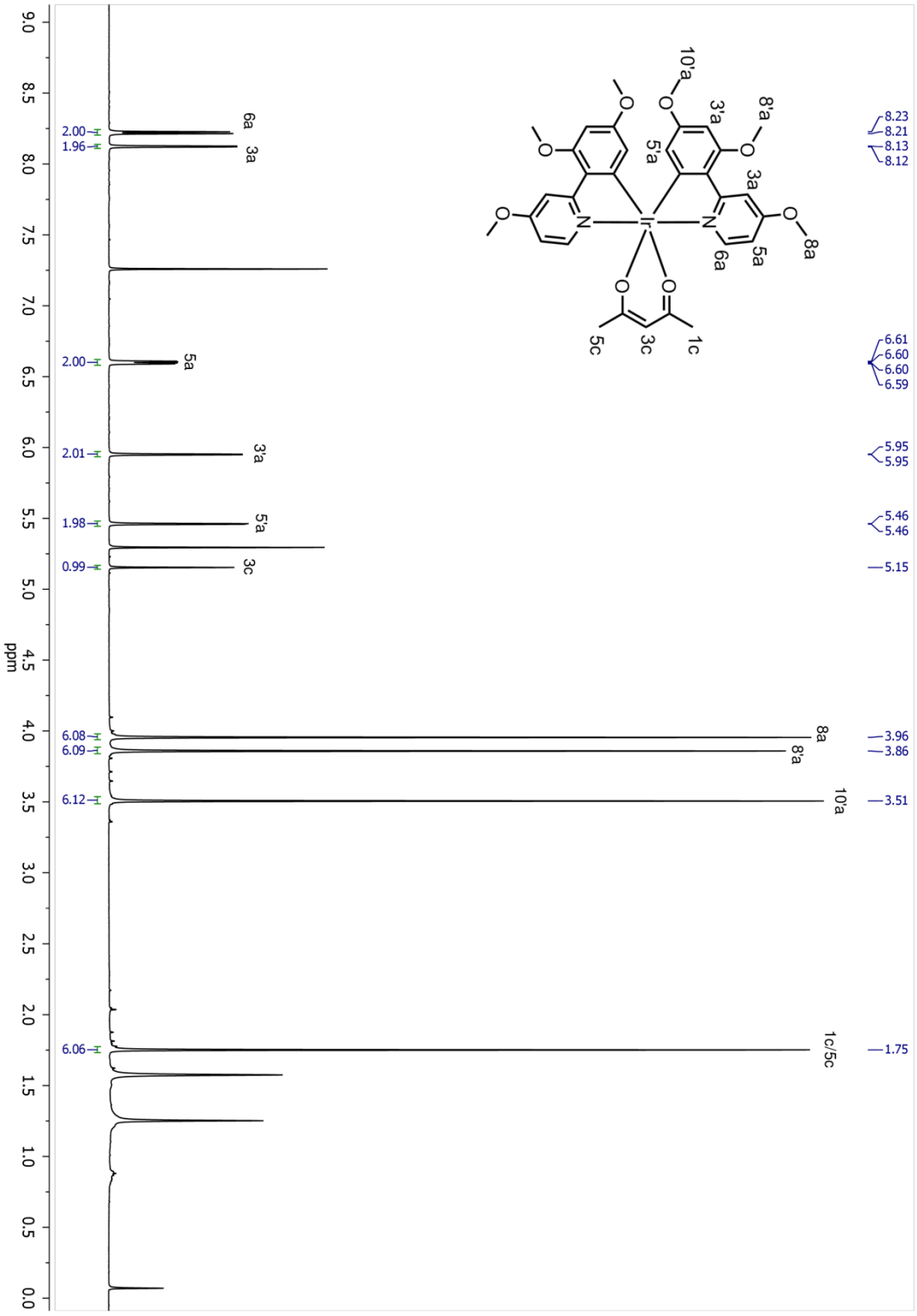

*Figure 9.55: ^{1}H-NMR spectrum of [Ir(dMeOMeOppy)$_2$(acac)] (**13**).*

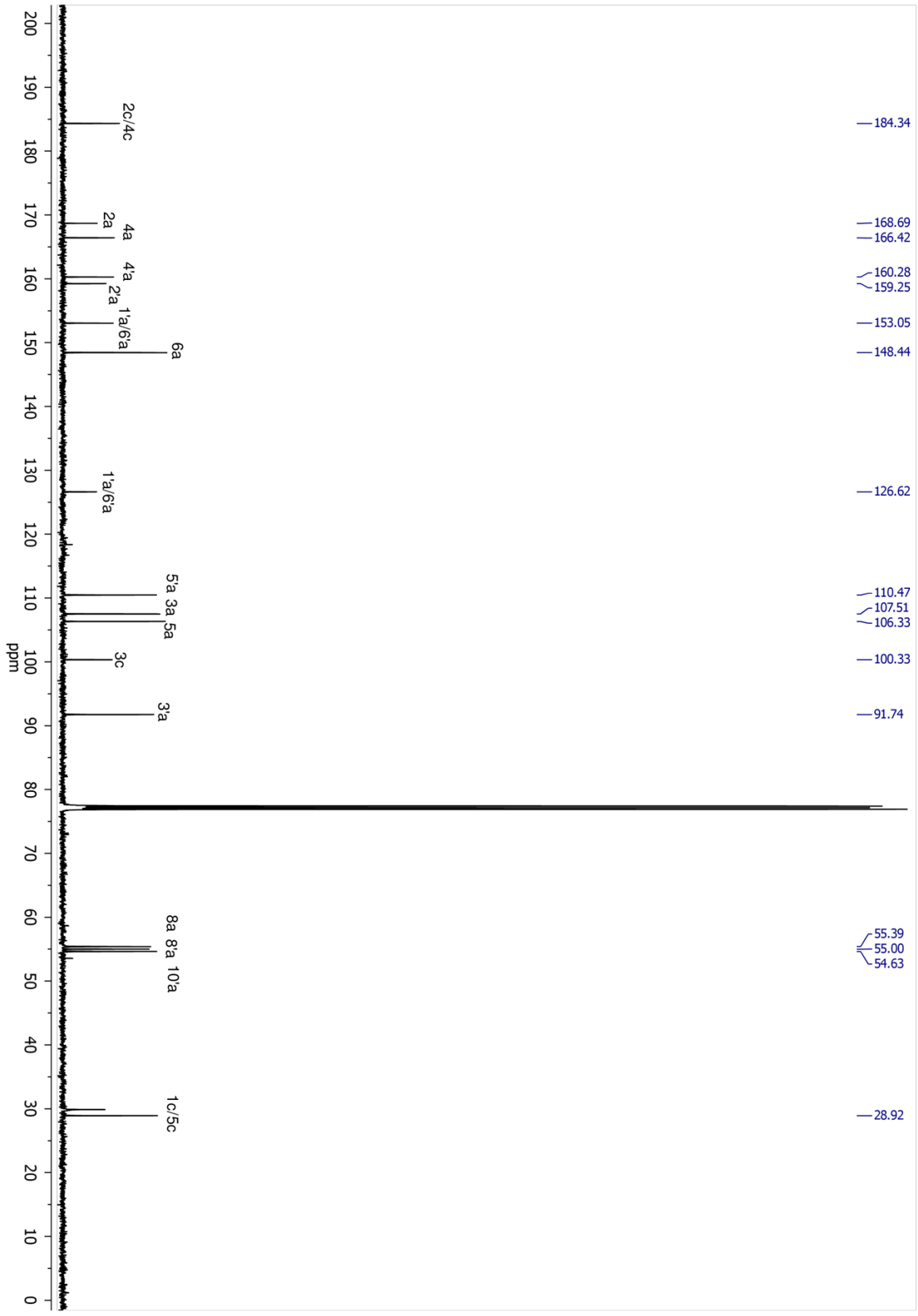

*Figure 9.56: ^{13}C-NMR spectrum of [Ir(dMeOMeOppy)$_2$(acac)] (**13**).*

9.7 [Ir(dMeOppy)(dFppy)(acac)] (14)

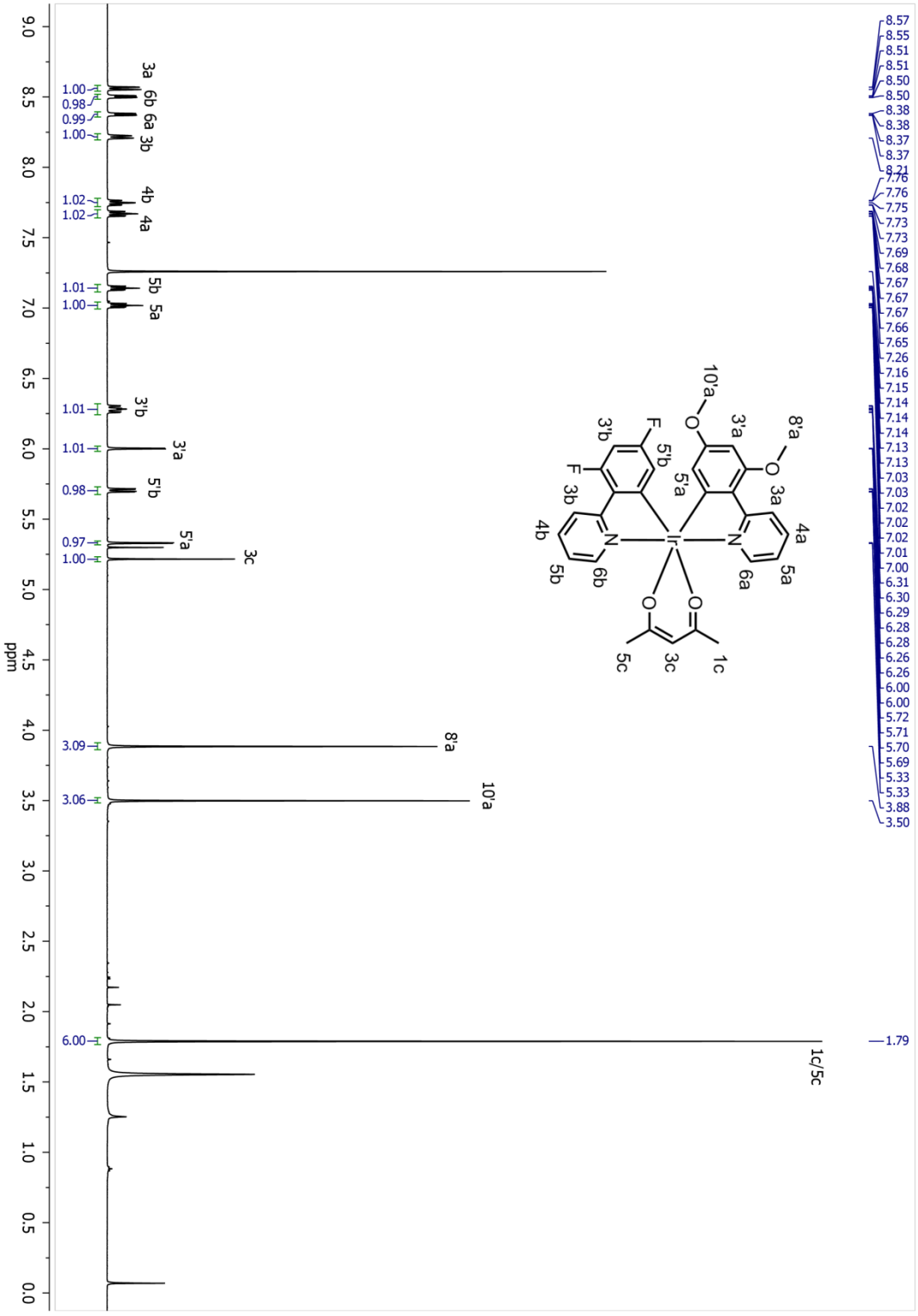

*Figure 9.57: [1]H-NMR spectrum of [Ir(dMeOppy)(dFppy)(acac)] (**14**).*

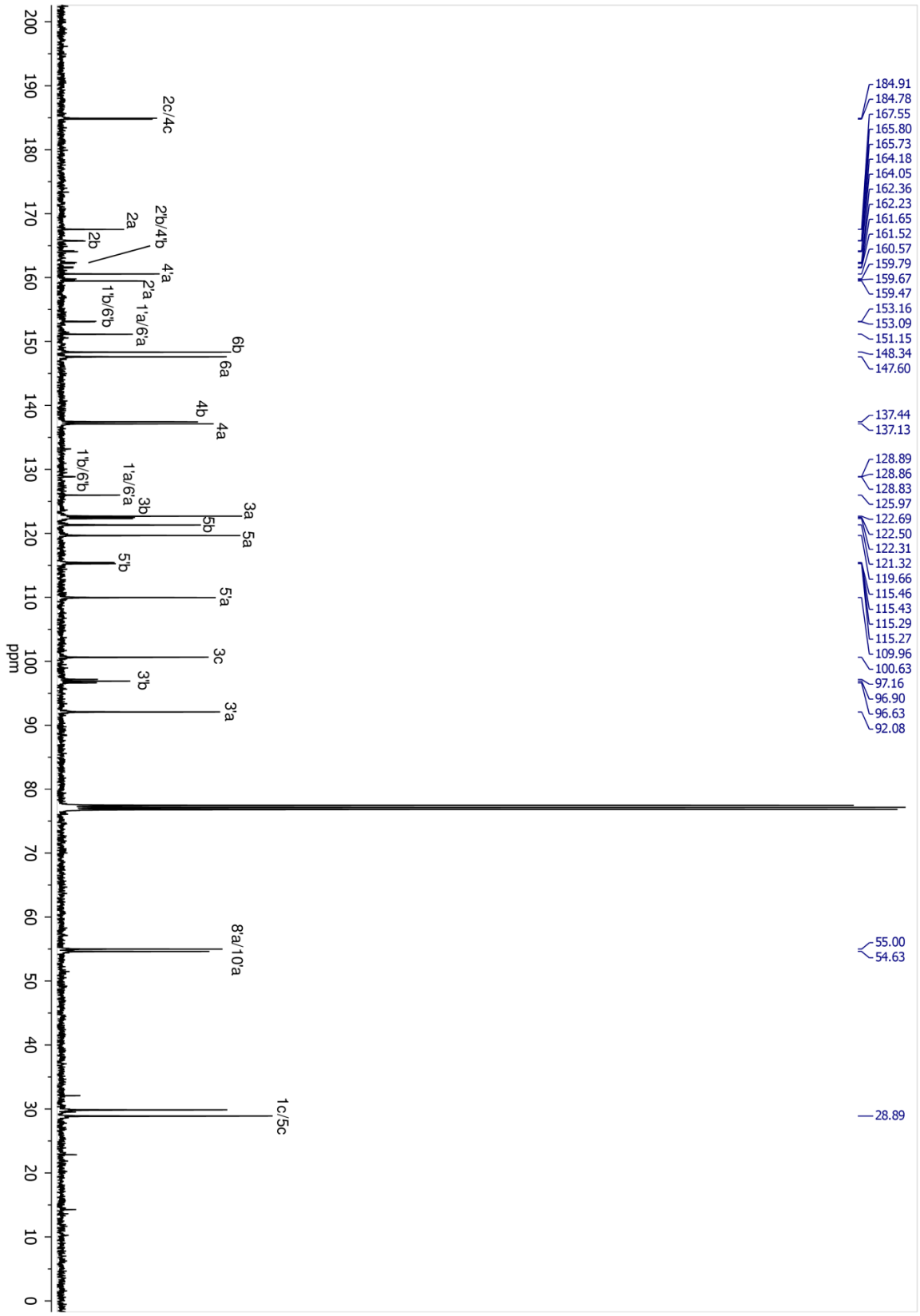

*Figure 9.58: ^{13}C-NMR spectrum of [Ir(dMeOppy)(dFppy)(acac)] (**14**).*

9.7.1 [Ir(dMeOppy)(dFppz)(acac)] (15)

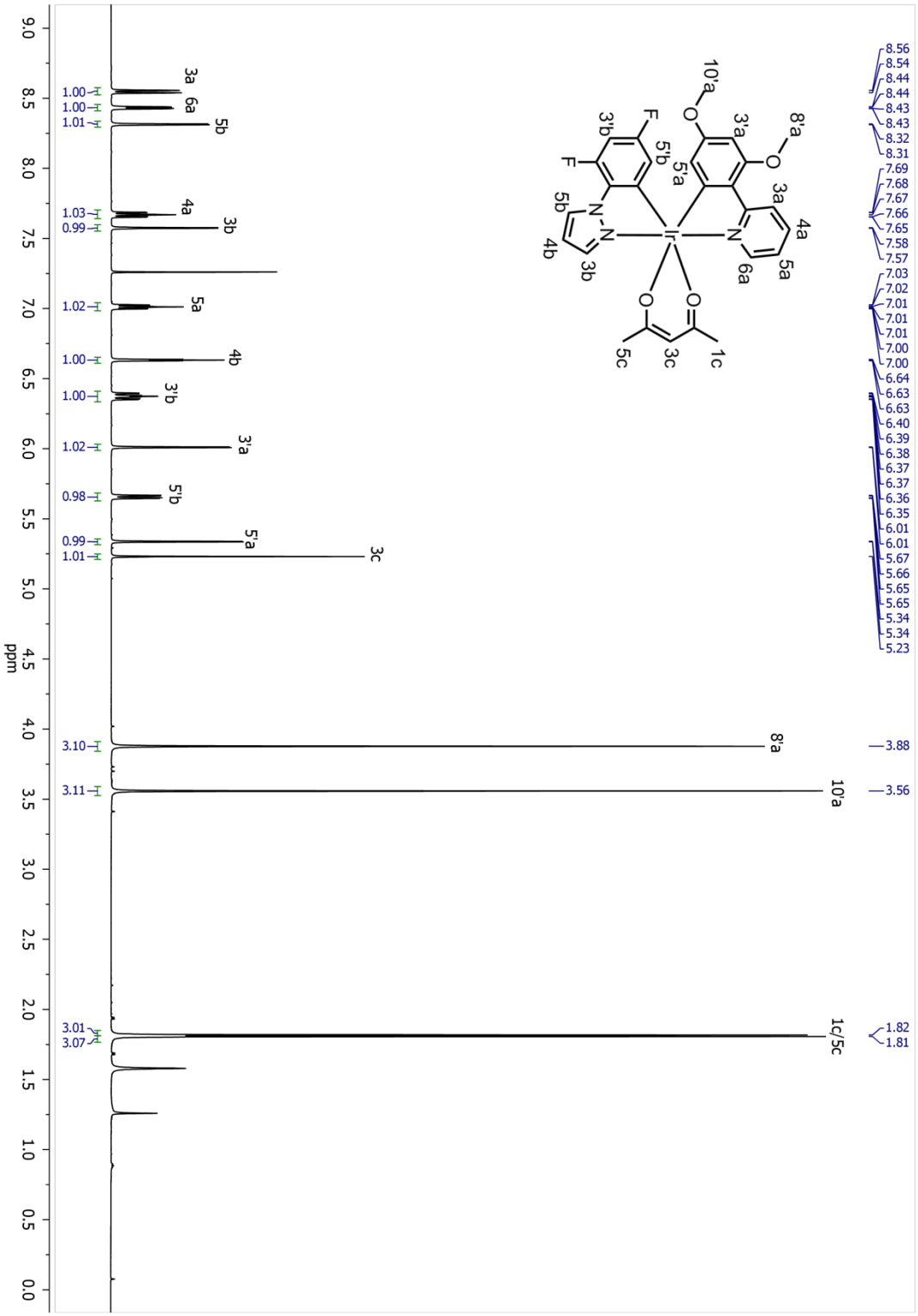

*Figure 9.59: ^{1}H-NMR spectrum of [Ir(dMeOppy)(dFppz)(acac)] (**15**).*

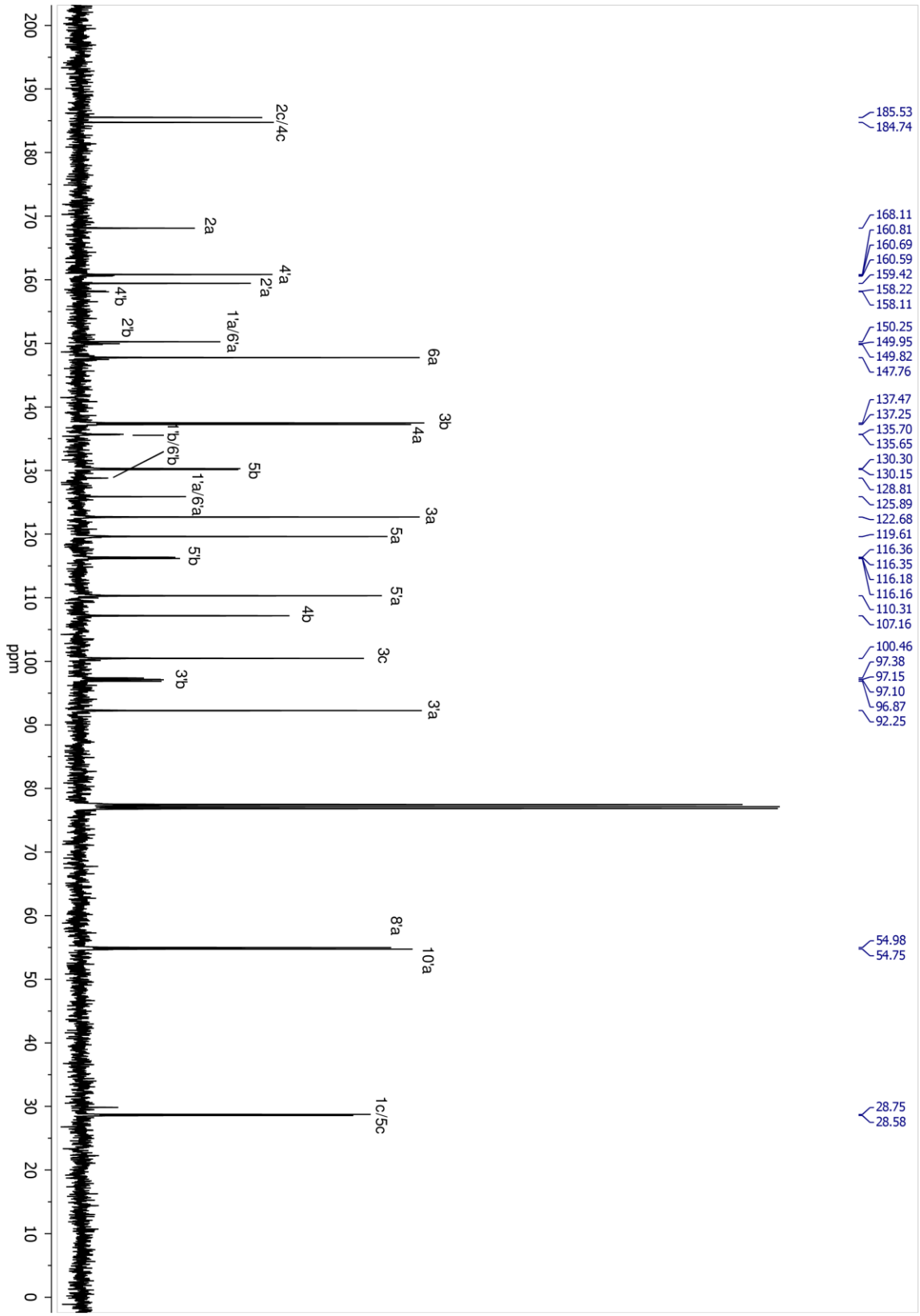

*Figure 9.60: [13]C-NMR spectrum of [Ir(dMeOppy)(dFppz)(acac)] (**15**).*

9.7.2 [Ir(dMeOMeppy)(dFppy)(acac)] (16)

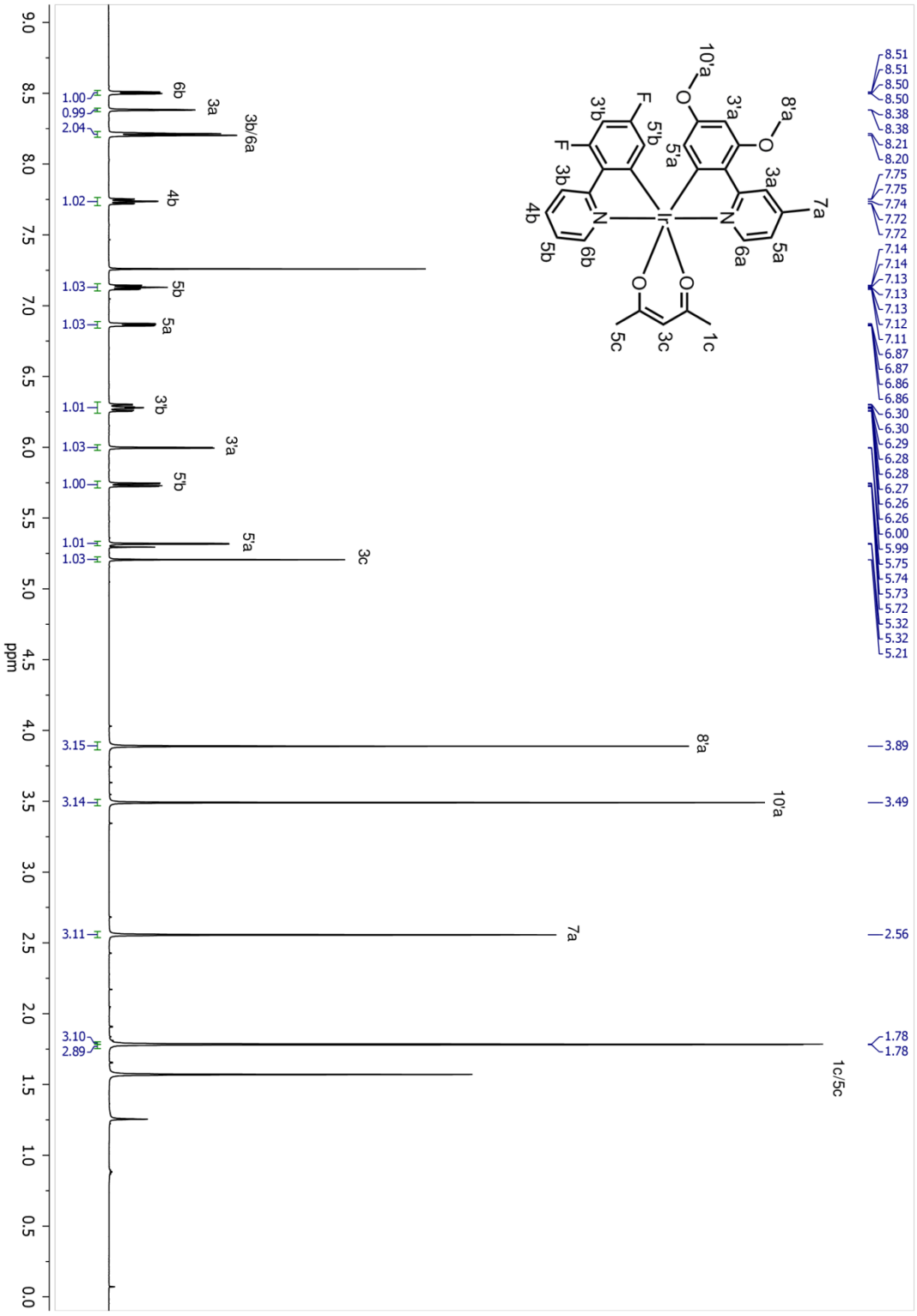

*Figure 9.61: ^{1}H-NMR spectrum of [Ir(dMeOMeppy)(dFppy)(acac)] (**16**).*

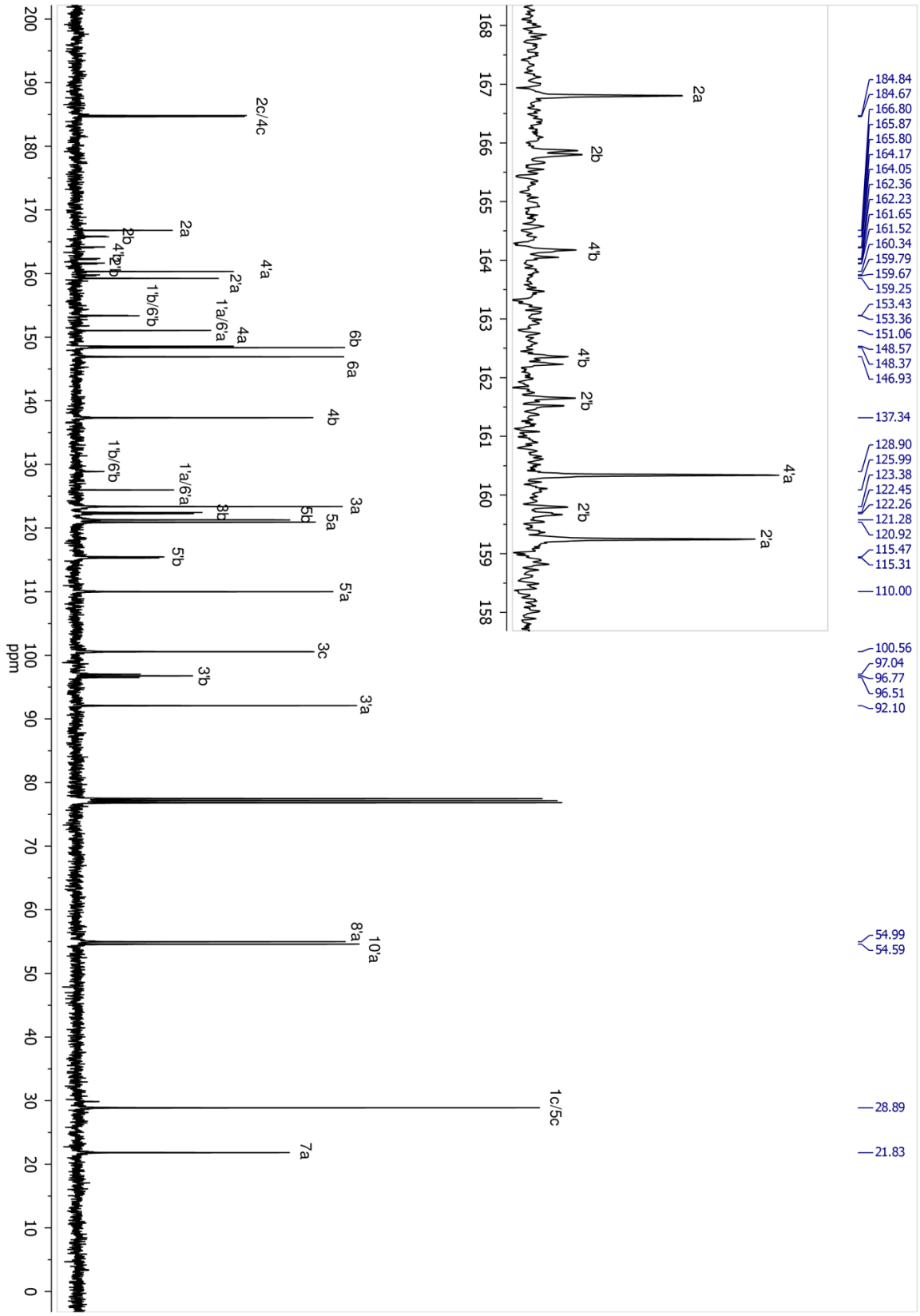

*Figure 9.62: ^{13}C-NMR spectrum of [Ir(dMeOMeppy)(dFppy)(acac)] (**16**).*

9.7.3 [Ir(dMeOMeppy)(dFppz)(acac)] (17)

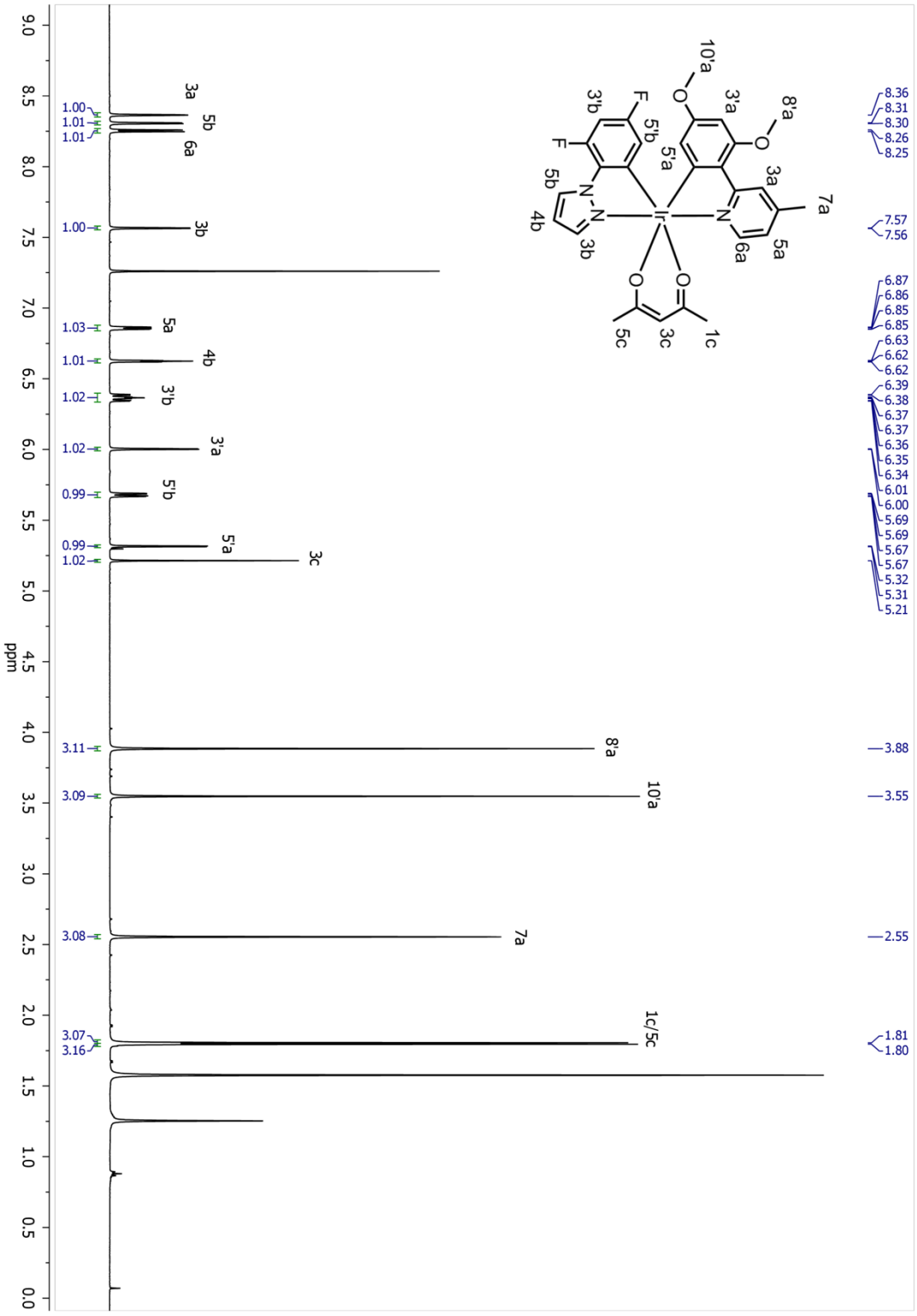

*Figure 9.63: ^{1}H-NMR spectrum of [Ir(dMeOMeppy)(dFppz)(acac)] (**17**).*

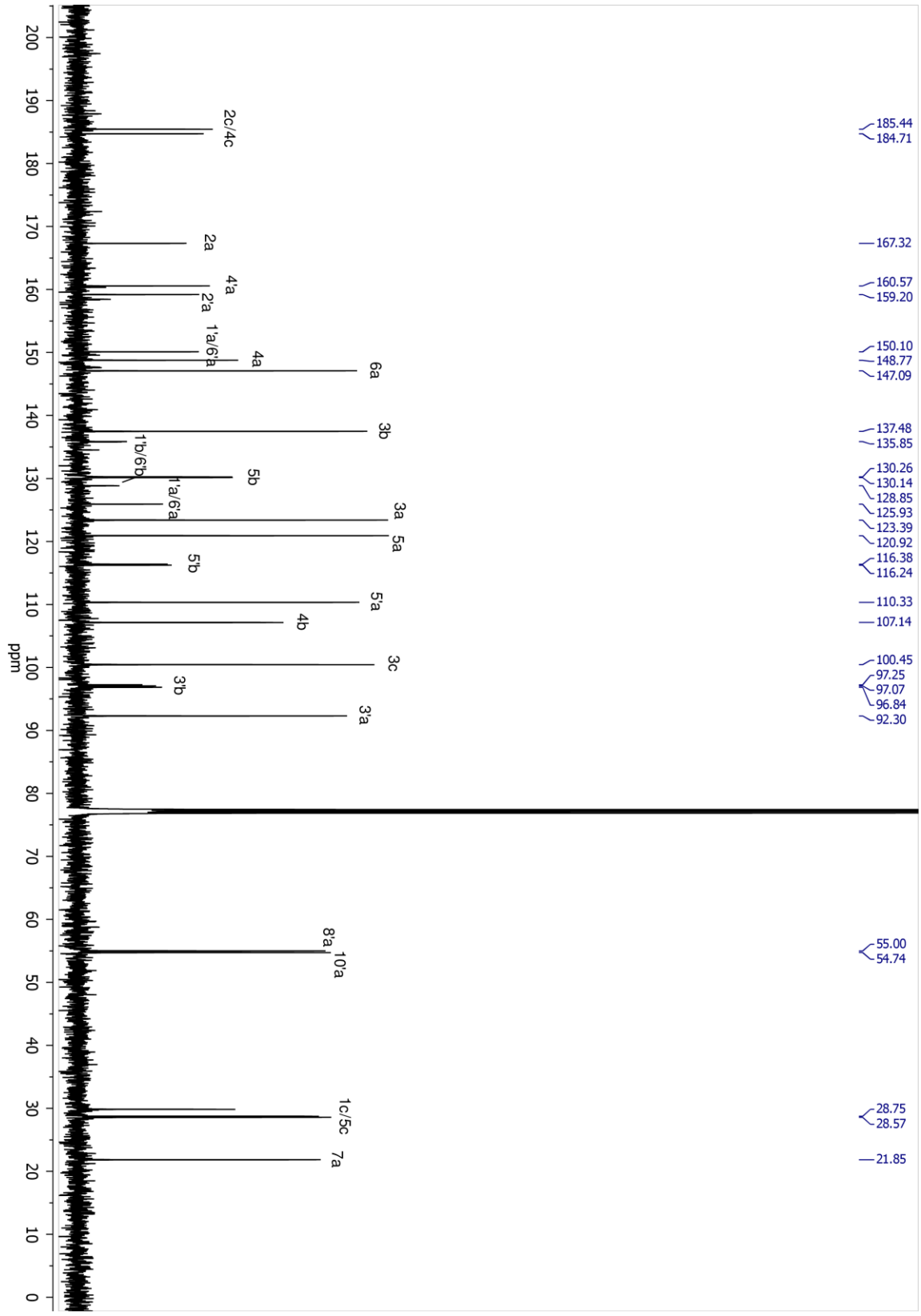

*Figure 9.64: [13]C-NMR spectrum of [Ir(dMeOMeppy)(dFppz)(acac)] (**17**).*

9.7.4 [Ir(dMeOMeOppy)(dFppy)(acac)] (18)

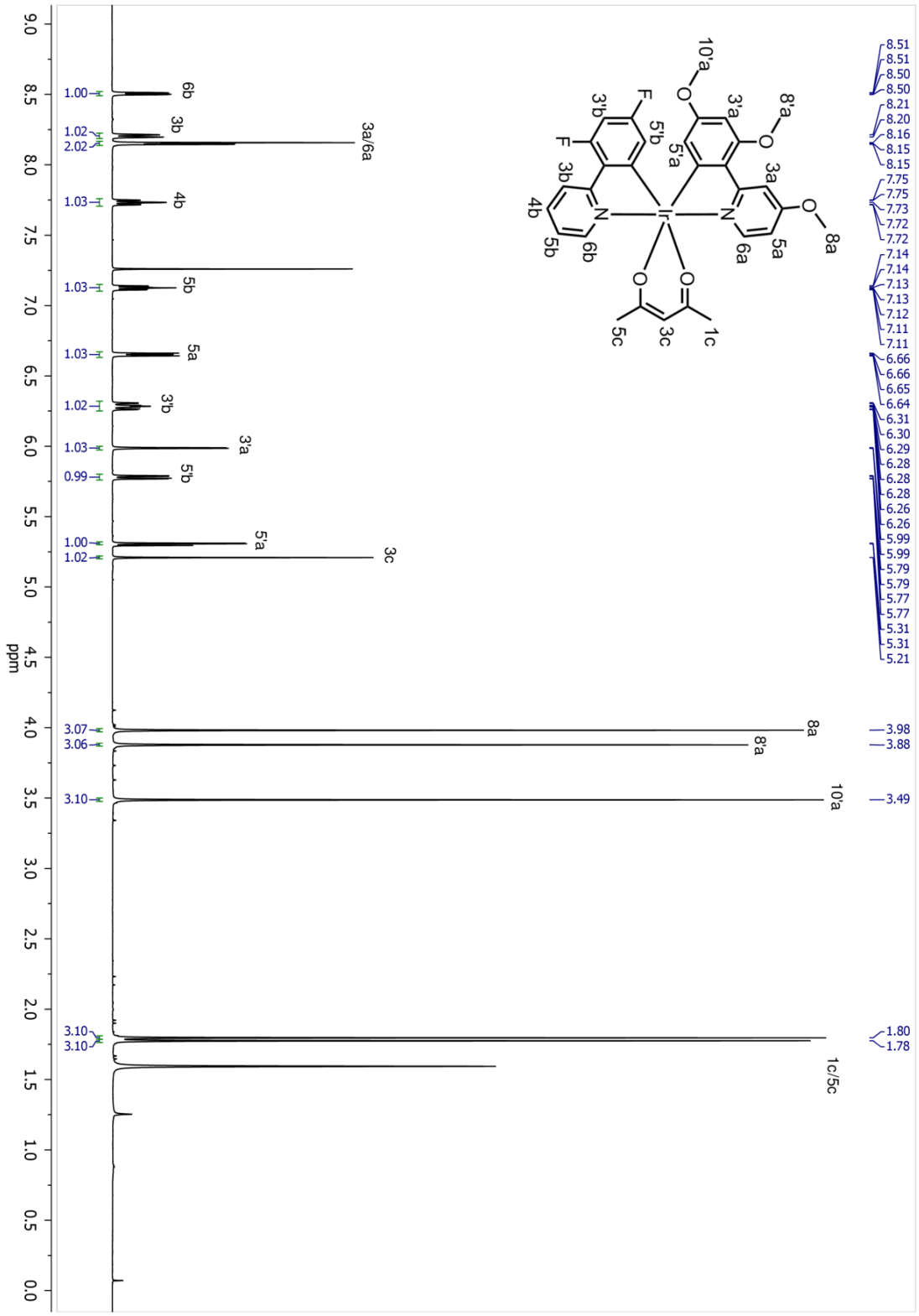

*Figure 9.65: [1]H-NMR spectrum of [Ir(dMeOMeOppy)(dFppy)(acac)] (**18**).*

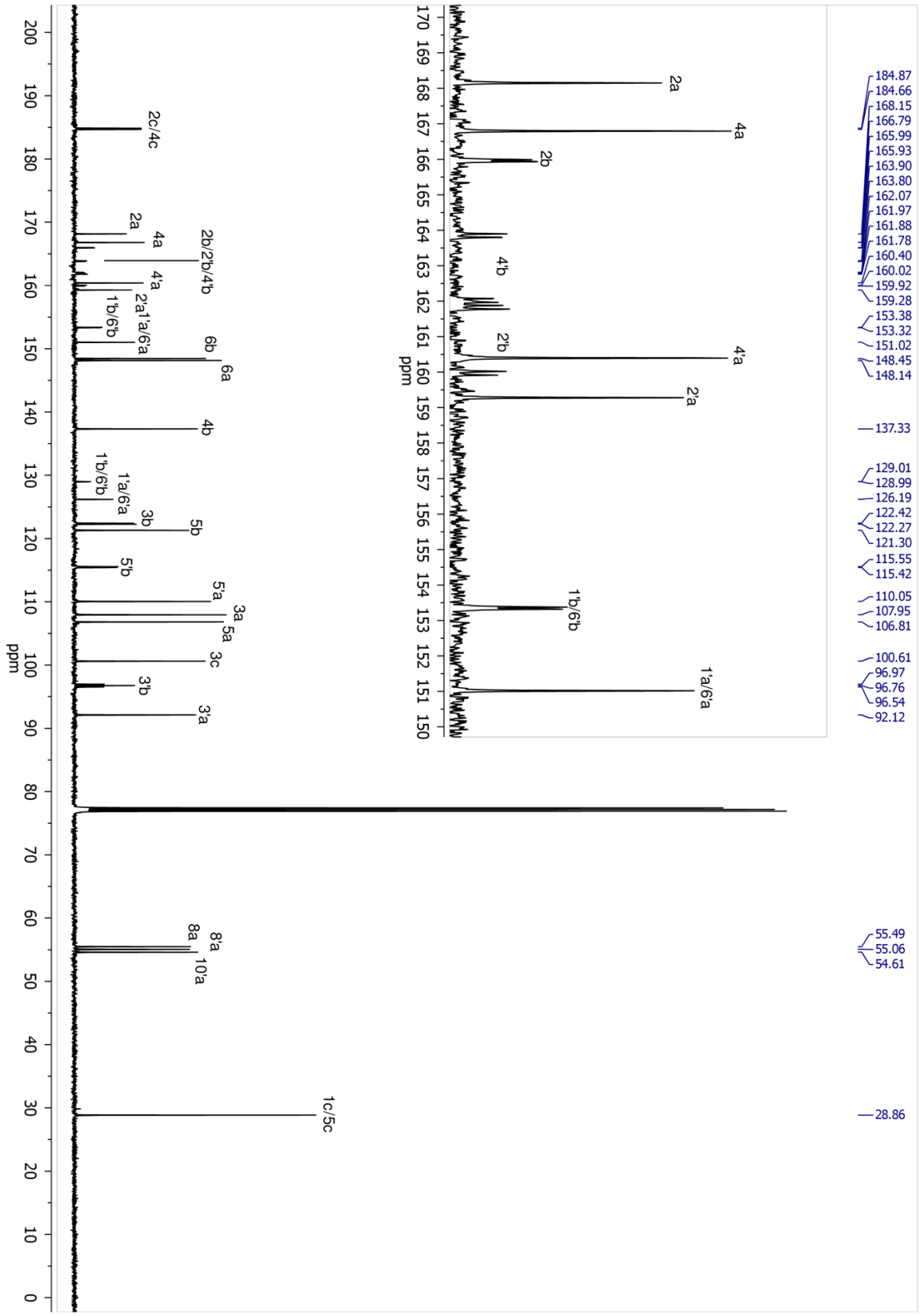

*Figure 9.66: [13]C-NMR spectrum of [Ir(dMeOMeOppy)(dFppy)(acac)] (**18**).*

9.7.5 [Ir(dMeOMeOppy)(dFppz)(acac)] (19)

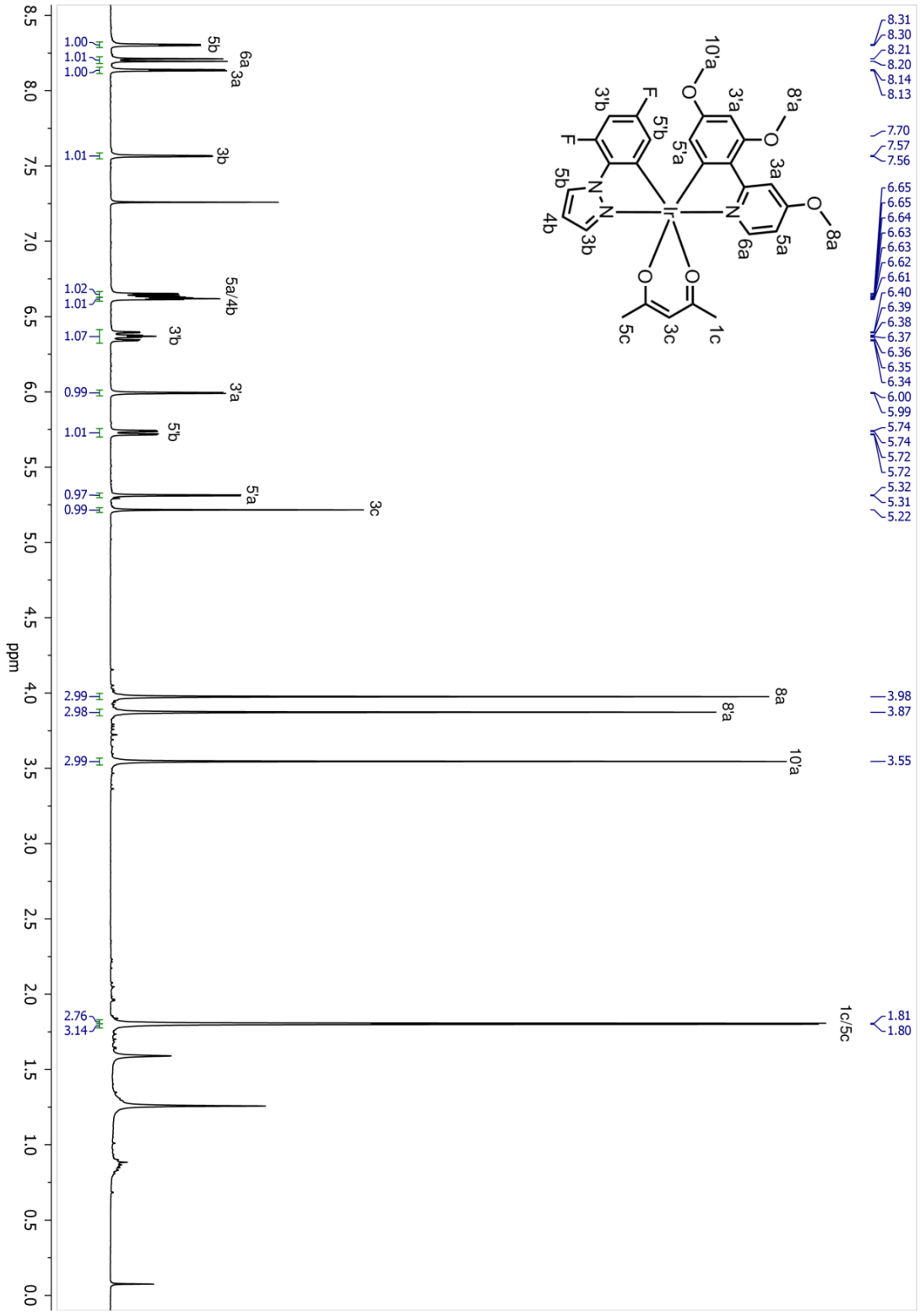

*Figure 9.67: ^{1}H-NMR spectrum of [Ir(dMeOMeOppy)(dFppz)(acac)] (**19**).*

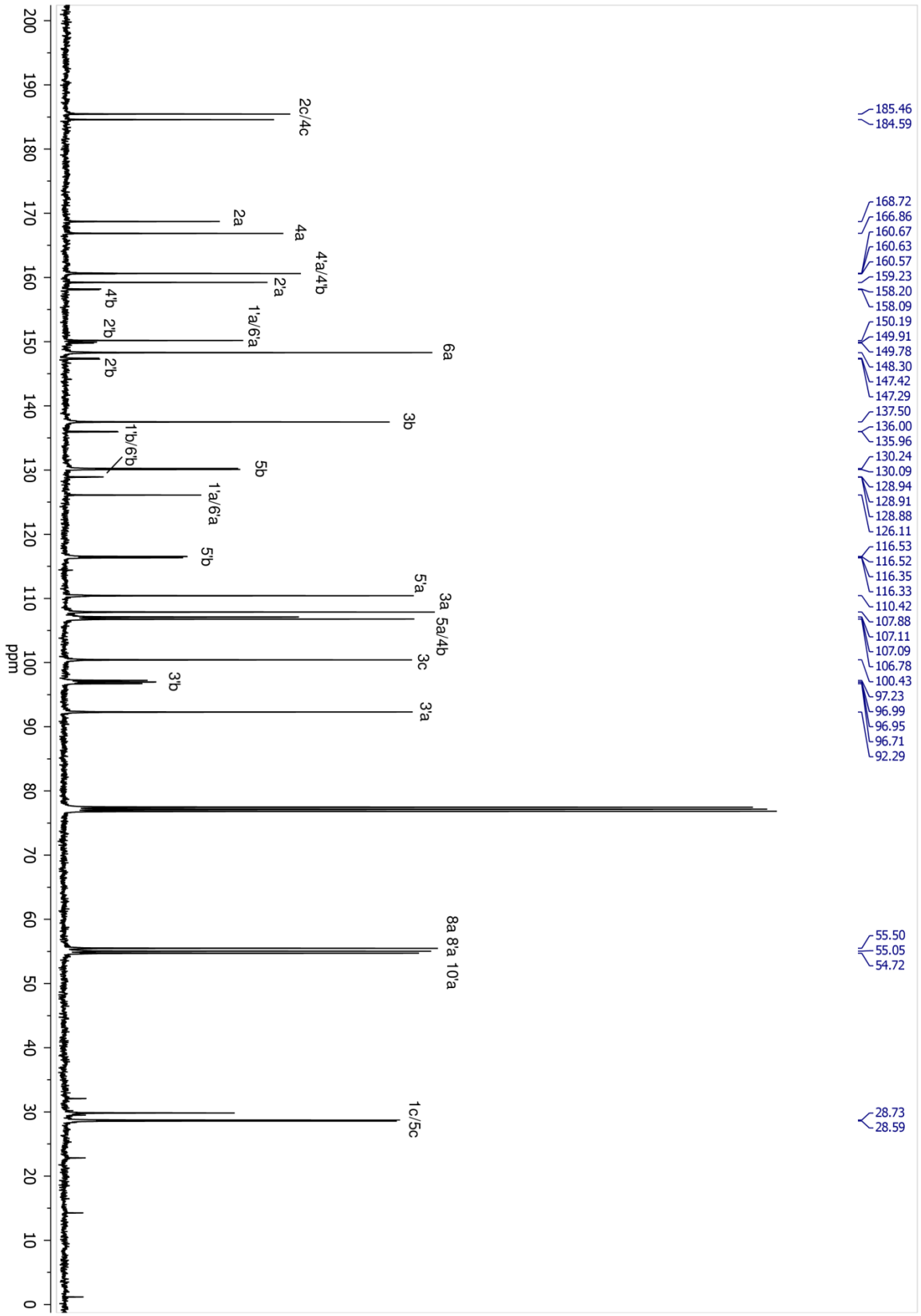

*Figure 9.68: ^{13}C-NMR spectrum of [Ir(dMeOMeOppy)(dFppz)(acac)] (**19**).*

9.7.6 [Ir(mespim)$_2$(acac)] (20)

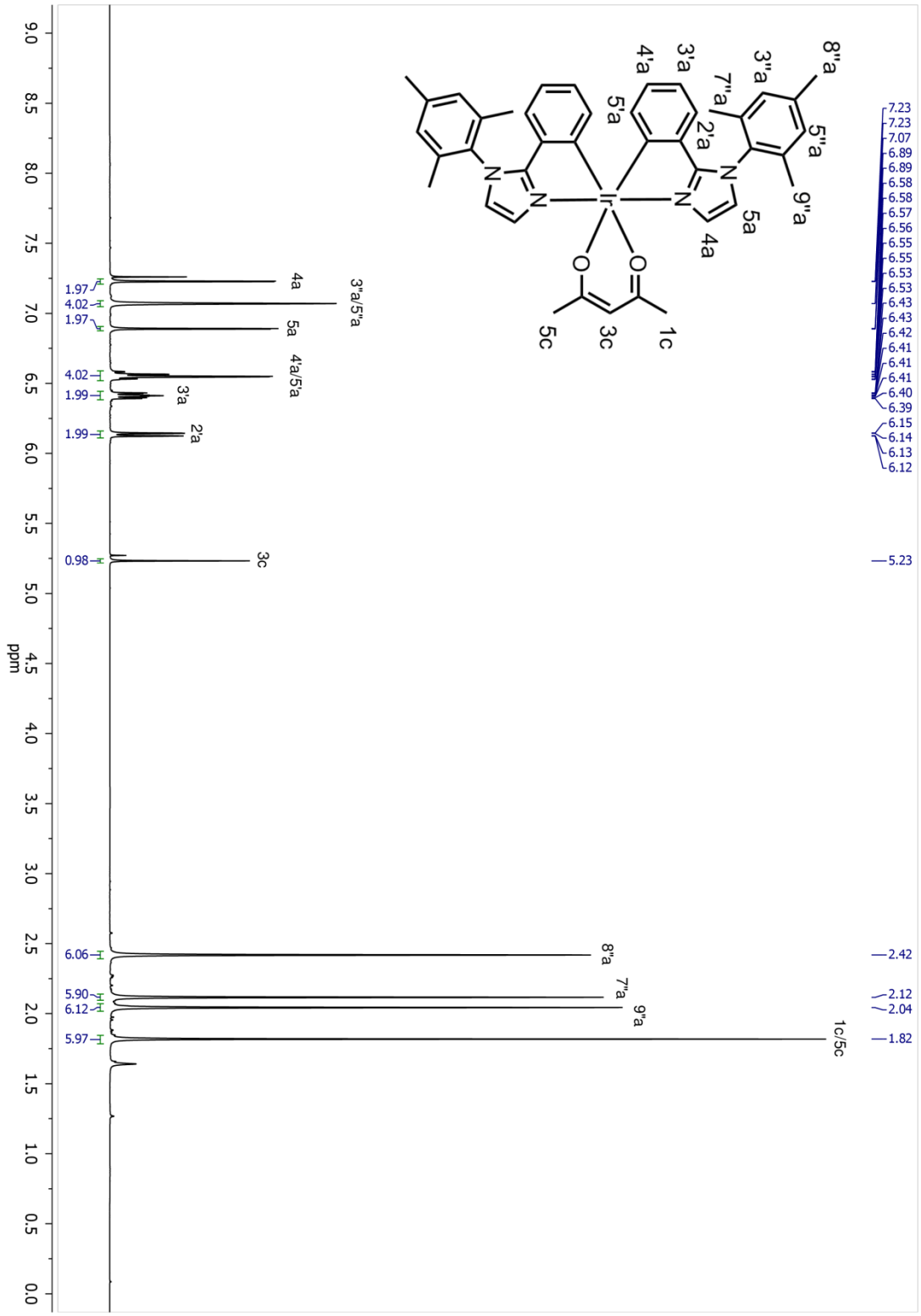

*Figure 9.69: ^{1}H-NMR spectrum of [Ir(mespim)$_2$(acac)] (**20**).*

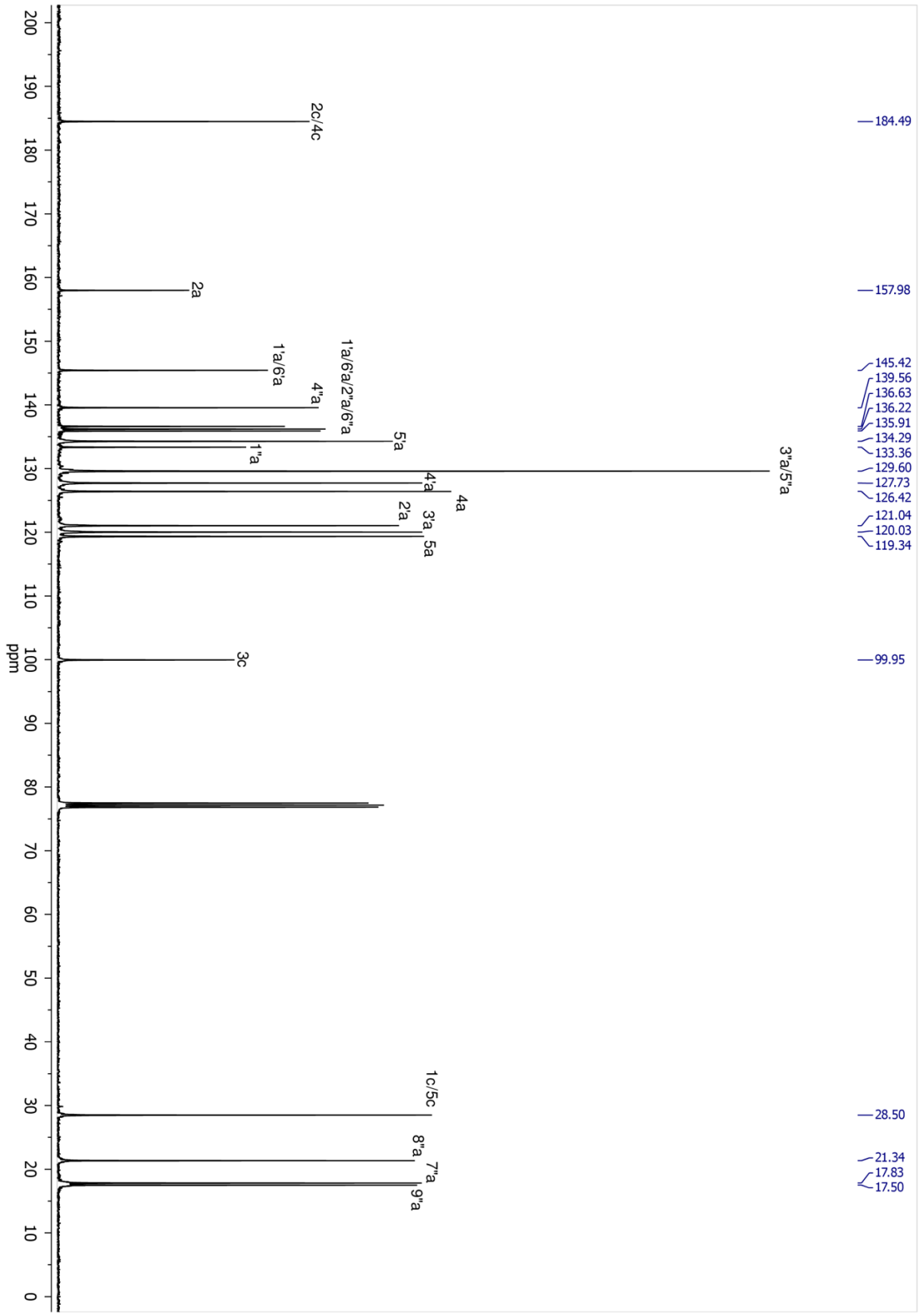

*Figure 9.70: ^{13}C-NMR spectrum of [Ir(mespim)$_2$(acac)] (**20**).*

9.7.7 [Ir(mespim)(dFppy)(acac)] (21)

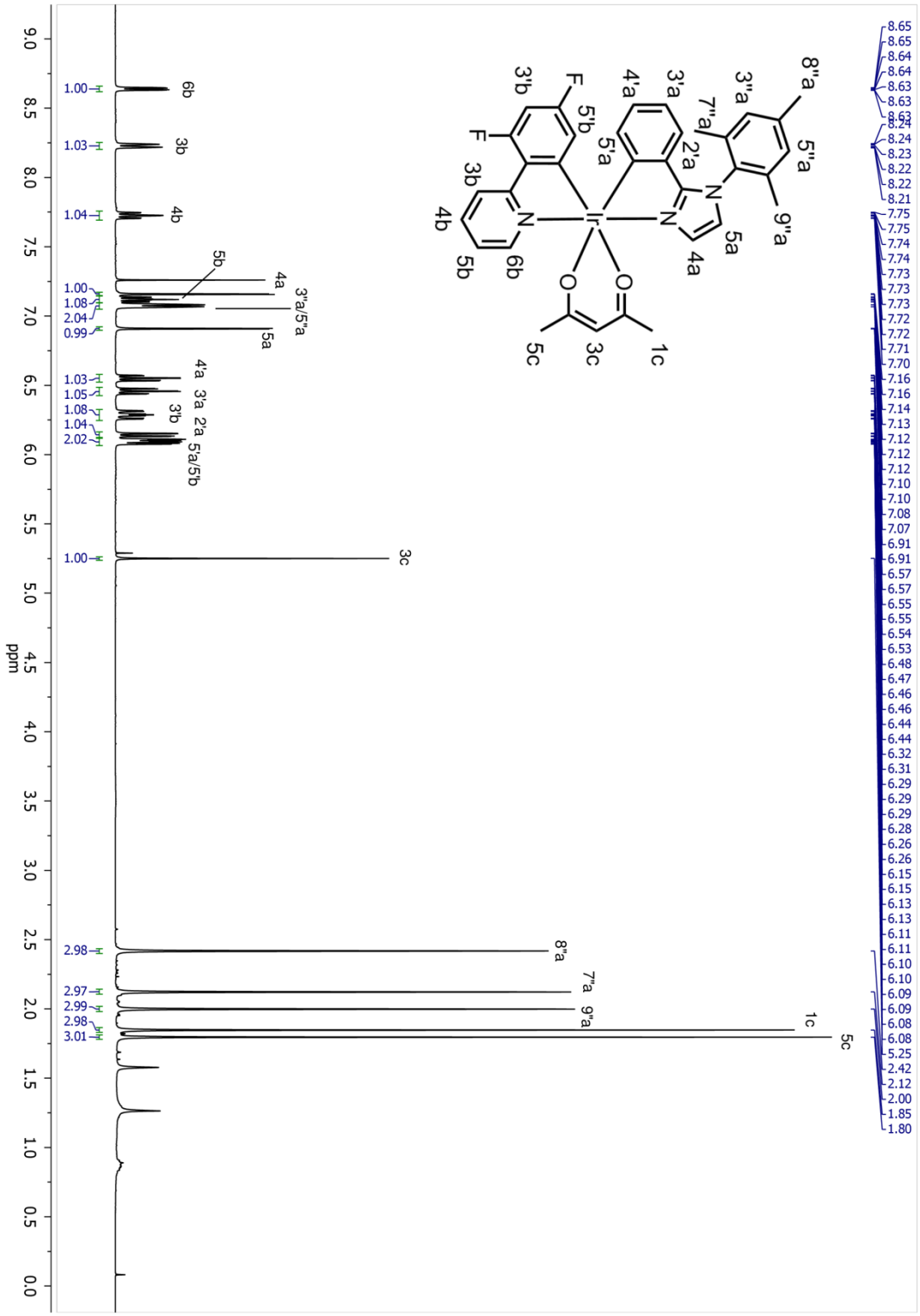

*Figure 9.71: ^{1}H-NMR spectrum of [Ir(mespim)(dFppy)(acac)] (**21**).*

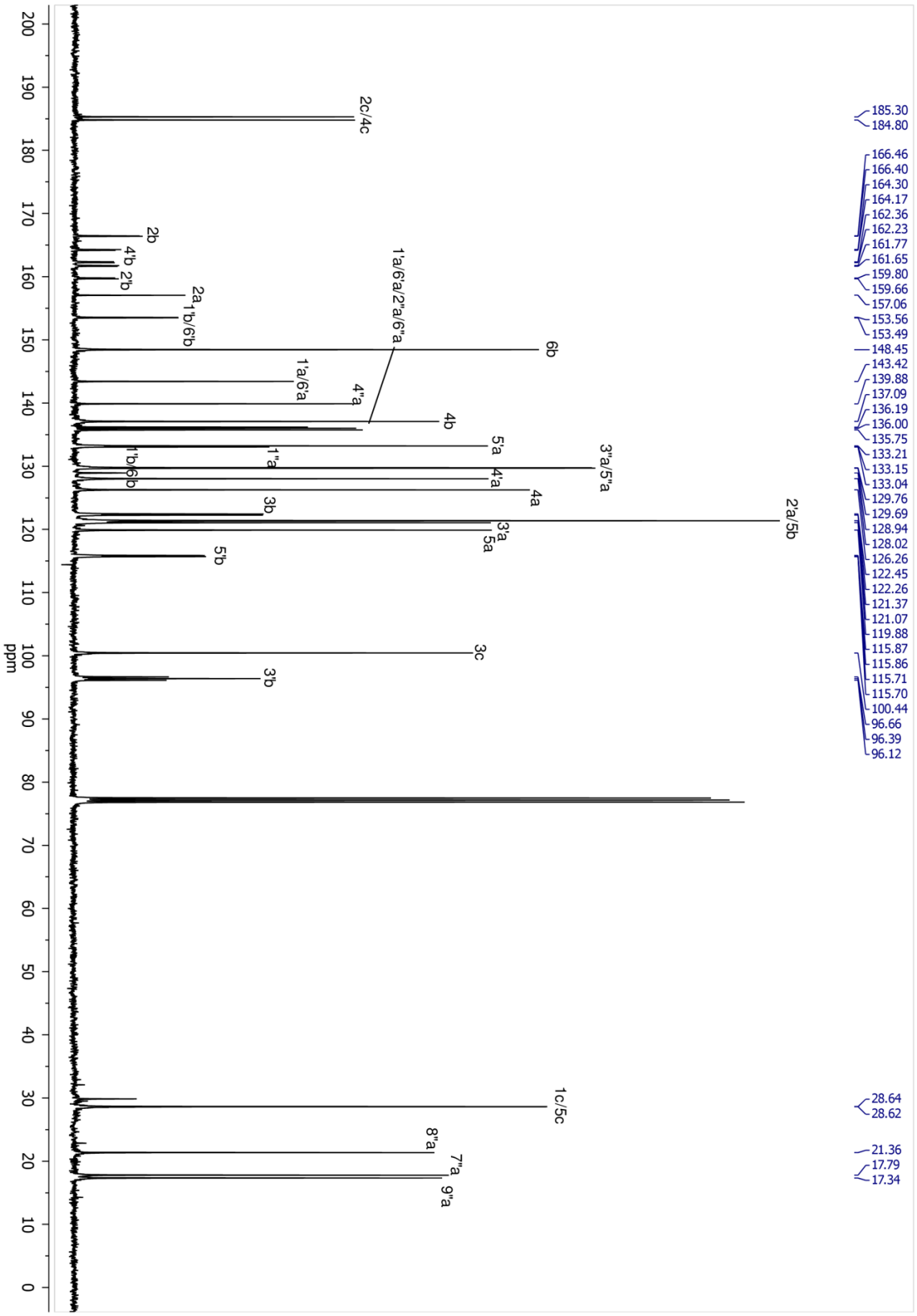

*Figure 9.72: ^{13}C-NMR spectrum of [Ir(mespim)(dFppy)(acac)] (**21**).*

9.7.8 [Ir(mespim)(dFppz)(acac)] (22)

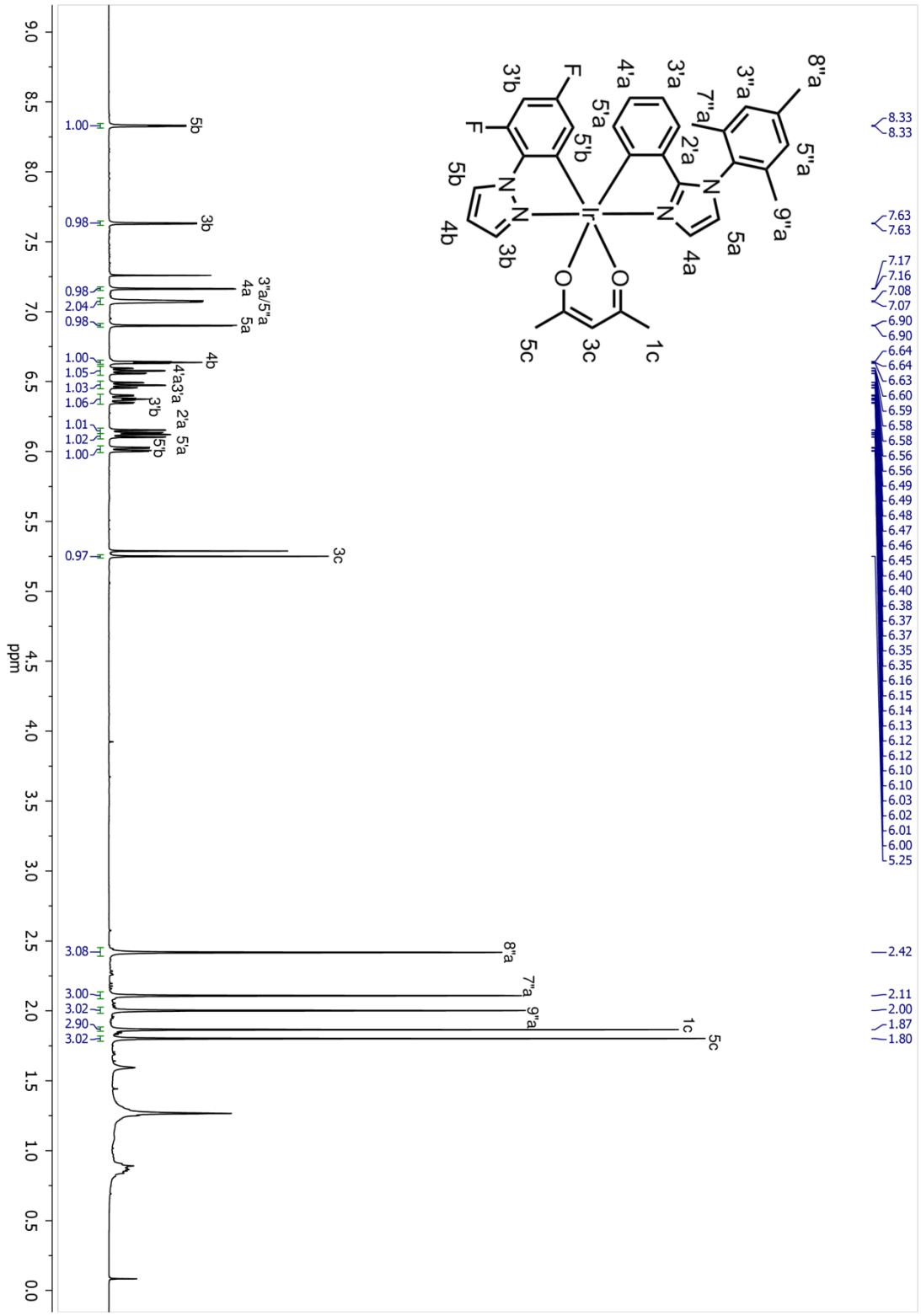

*Figure 9.73: [1]H-NMR spectrum of [Ir(mespim)(dFppz)(acac)] (**22**).*

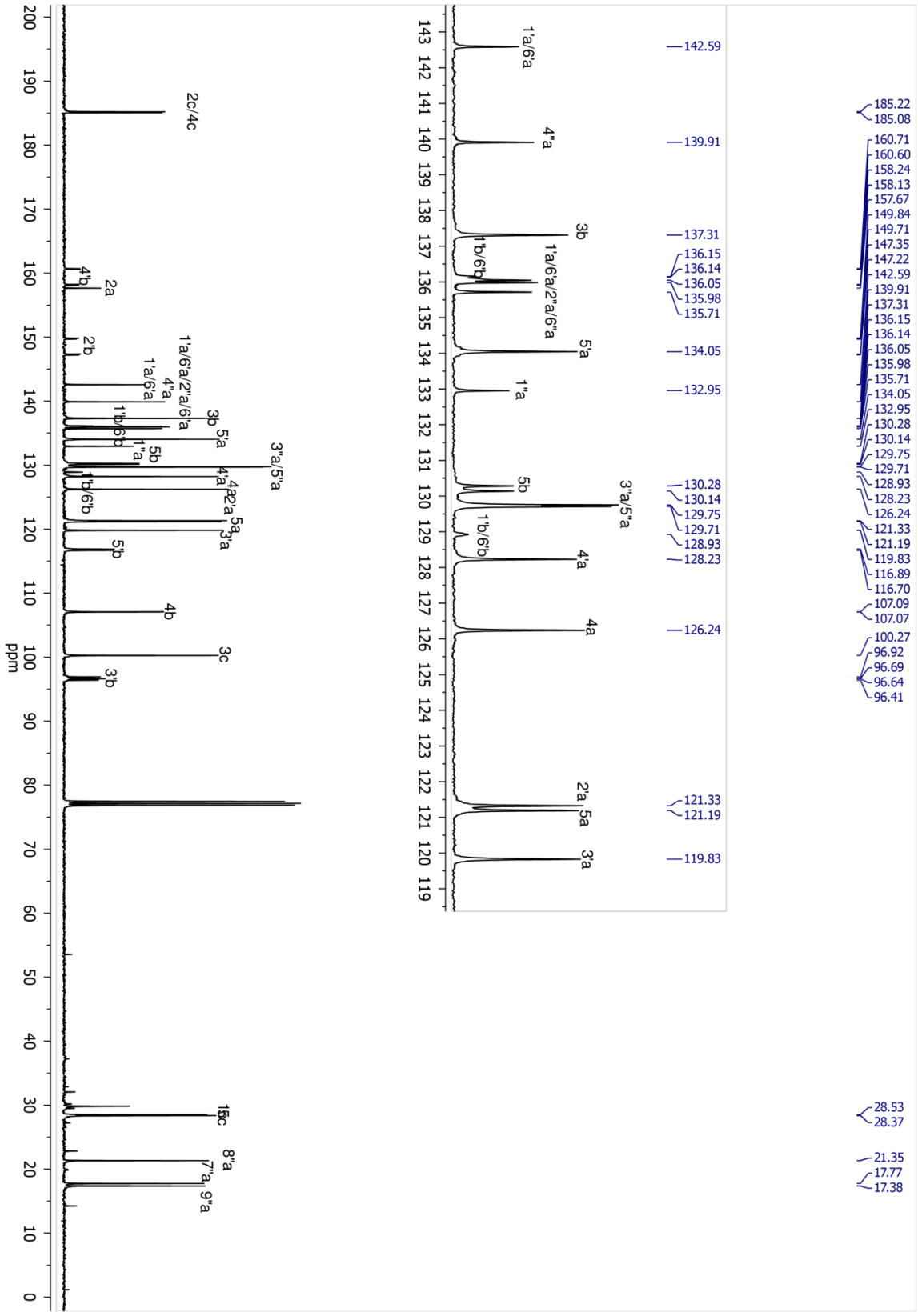

*Figure 9.74: ^{13}C-NMR spectrum of [Ir(mespim)(dFppz)(acac)] (**22**).*

9.7.9 [Ir(CF$_3$ppz)$_2$(acac)] (23)

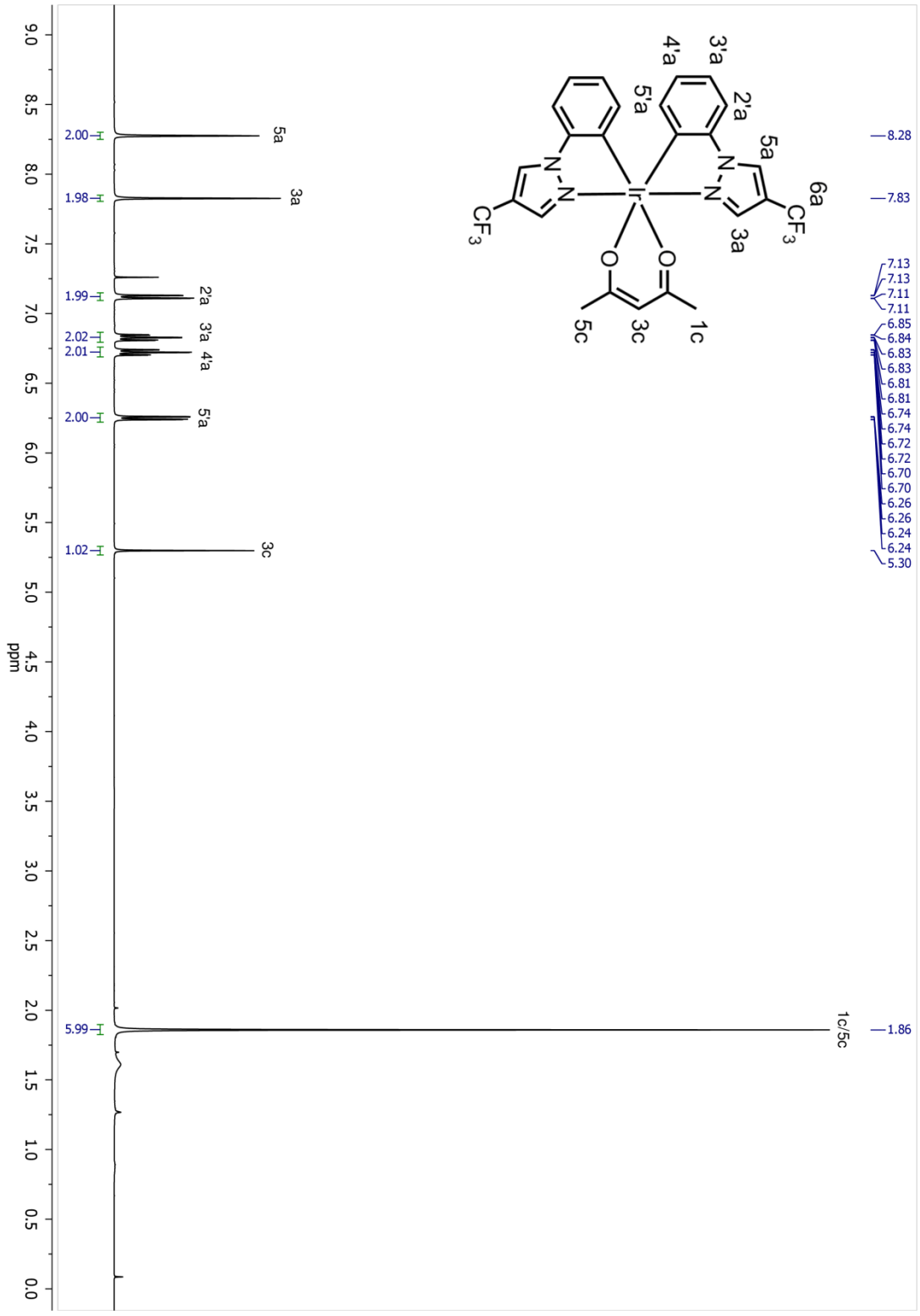

*Figure 9.75: ^{1}H-NMR spectrum of [Ir(CF$_3$ppz)$_2$(acac)] (**23**).*

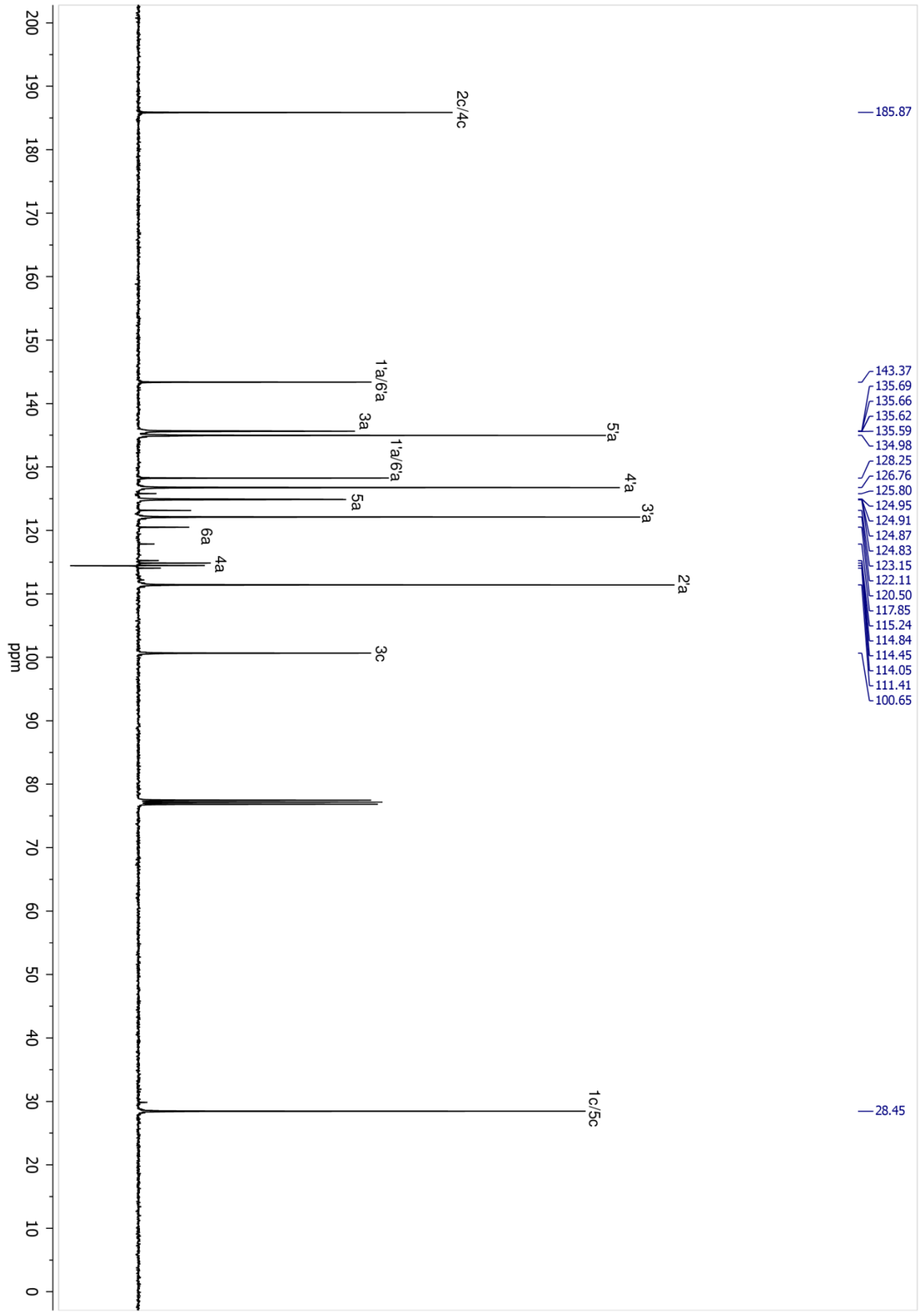

*Figure 9.76: ^{13}C-NMR spectrum of [Ir(CF$_3$ppz)$_2$(acac)] (**23**).*

9.7.10 [Ir(mespim)(CF$_3$ppz)(acac)] (24)

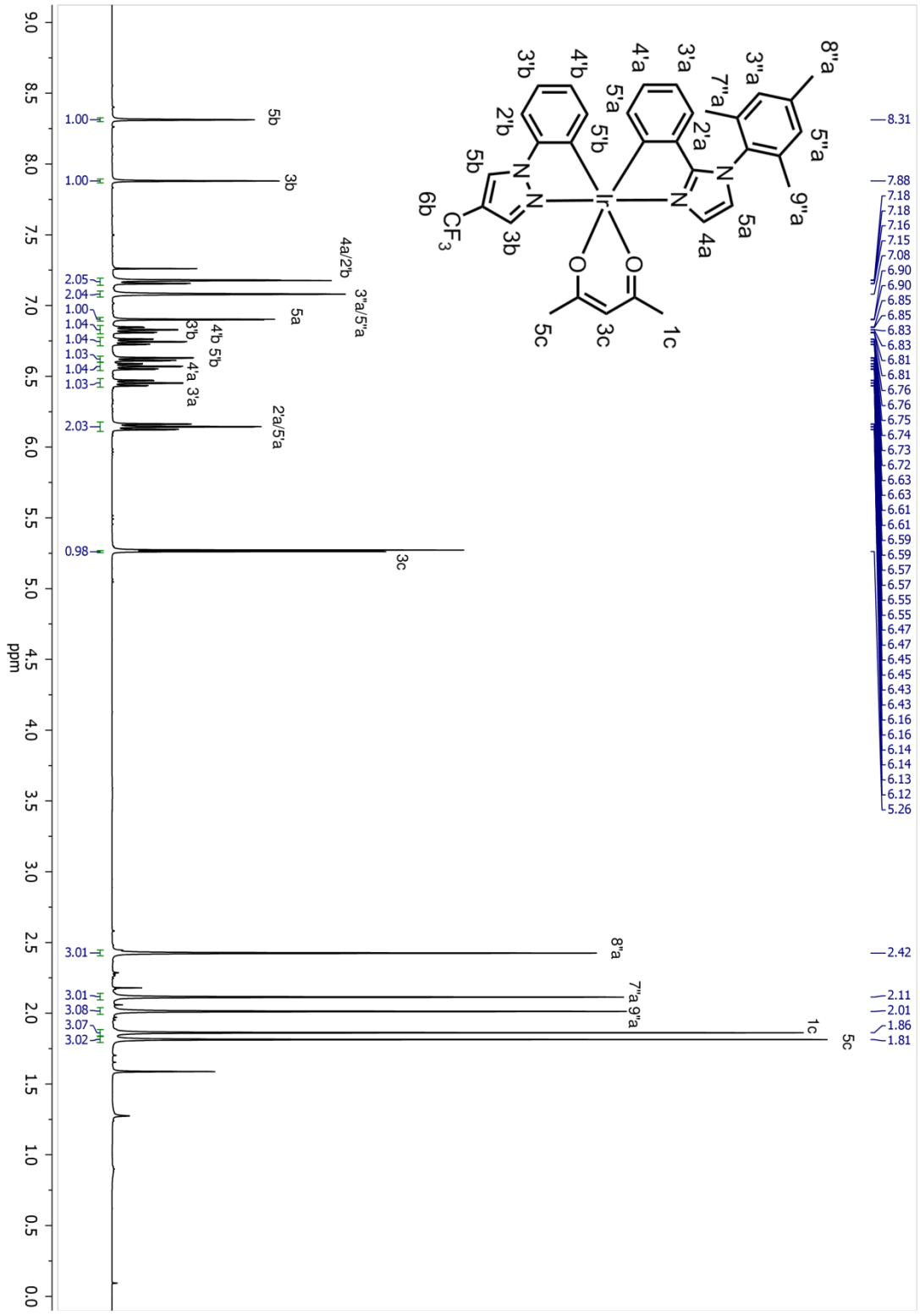

*Figure 9.77: ^{1}H-NMR spectrum of [Ir(mespim)(CF$_3$ppz)(acac)] (**24**).*

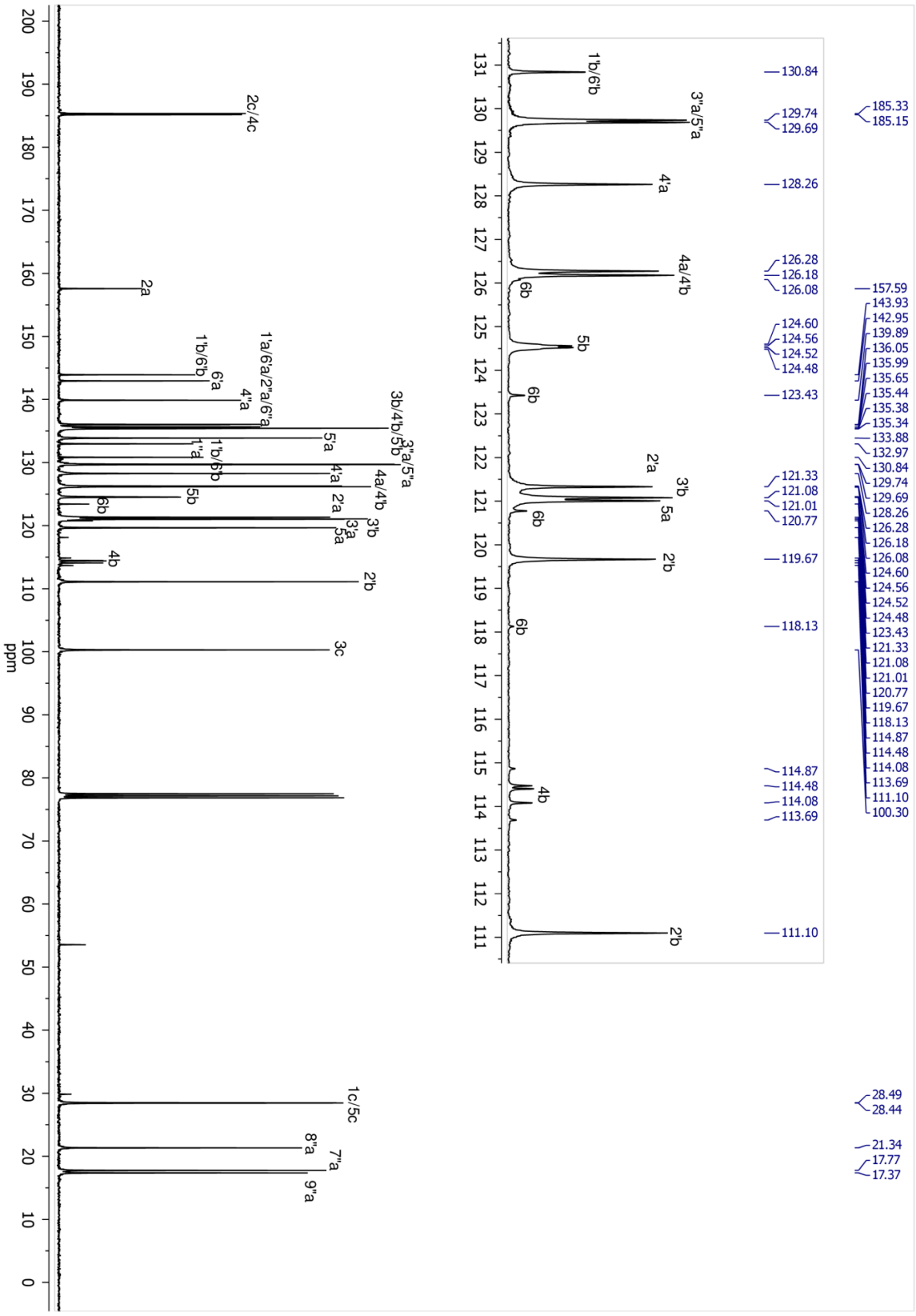

*Figure 9.78: ^{13}C-NMR spectrum of [Ir(mespim)(CF$_3$ppz)(acac)] (**24**).*

9.7.11 [Ir(dFppy)(ppy)(pic)] (3a)

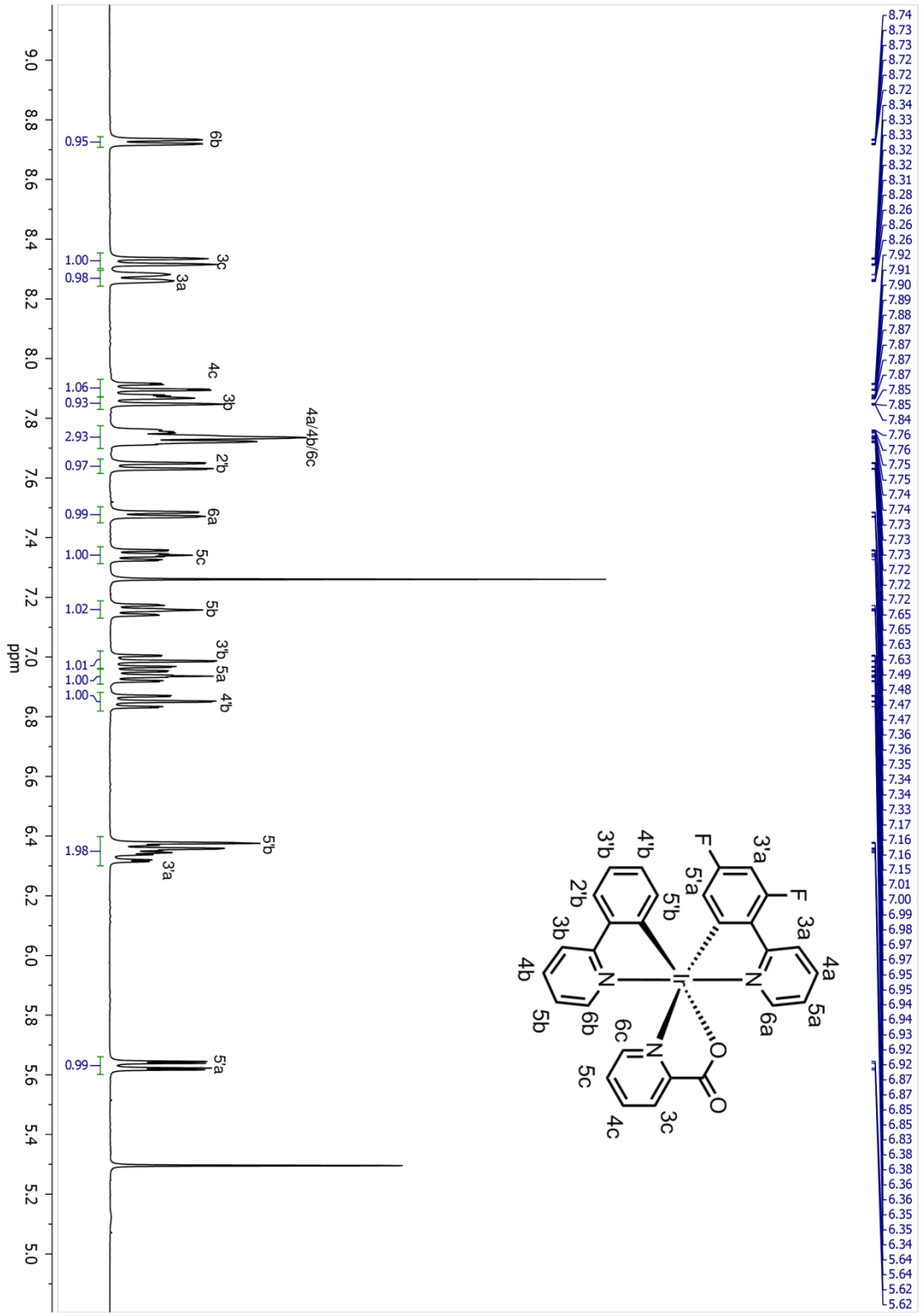

*Figure 9.79: [1]H-NMR spectrum of [Ir(dFppy)(ppy)(pic)] (**3a**).*

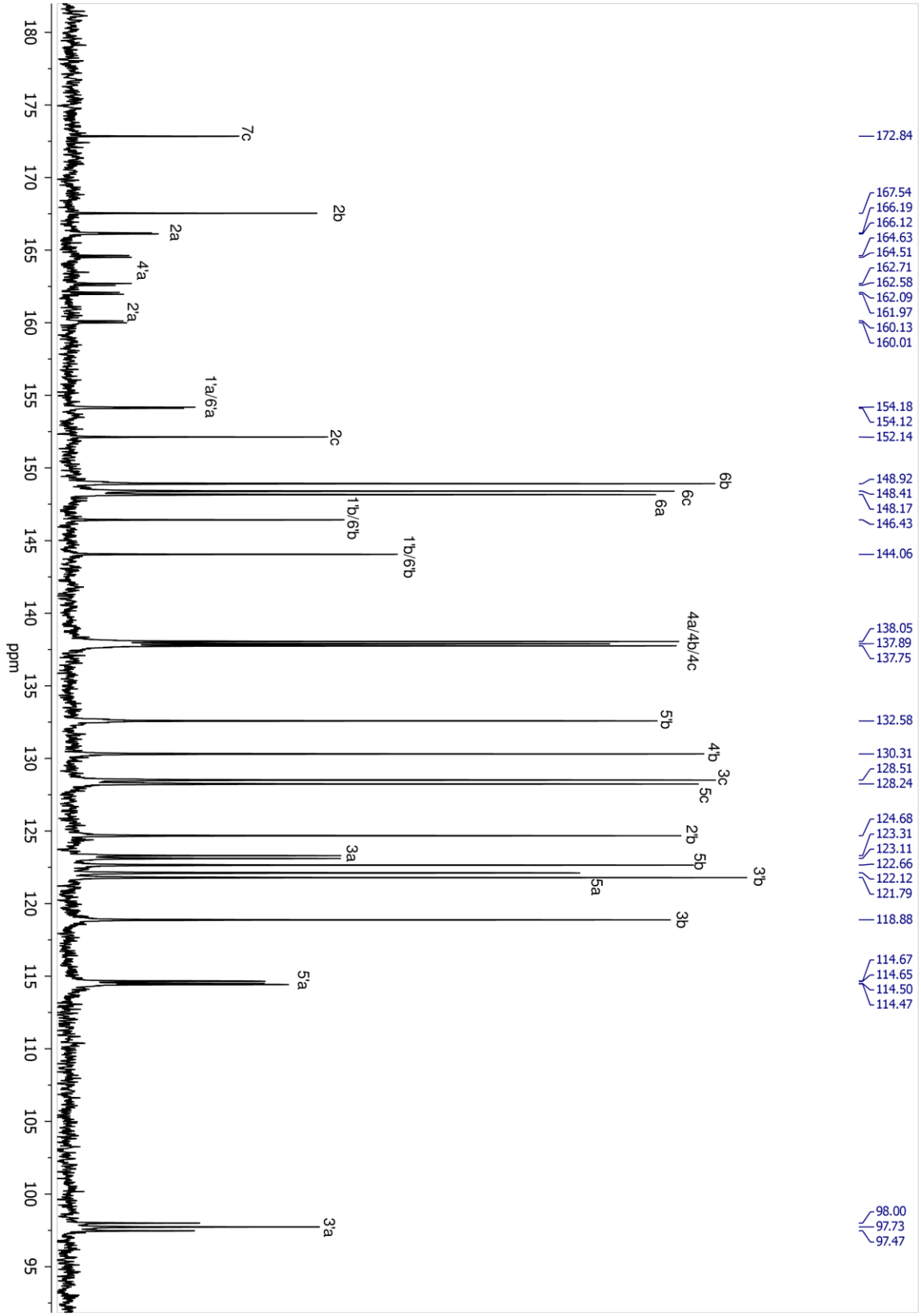

*Figure 9.80: ^{13}C-NMR spectrum of [Ir(dFppy)(ppy)(pic)] (**3a**).*

9.7.12 [Ir(dFppy)(ppy)(pic)] (3b)

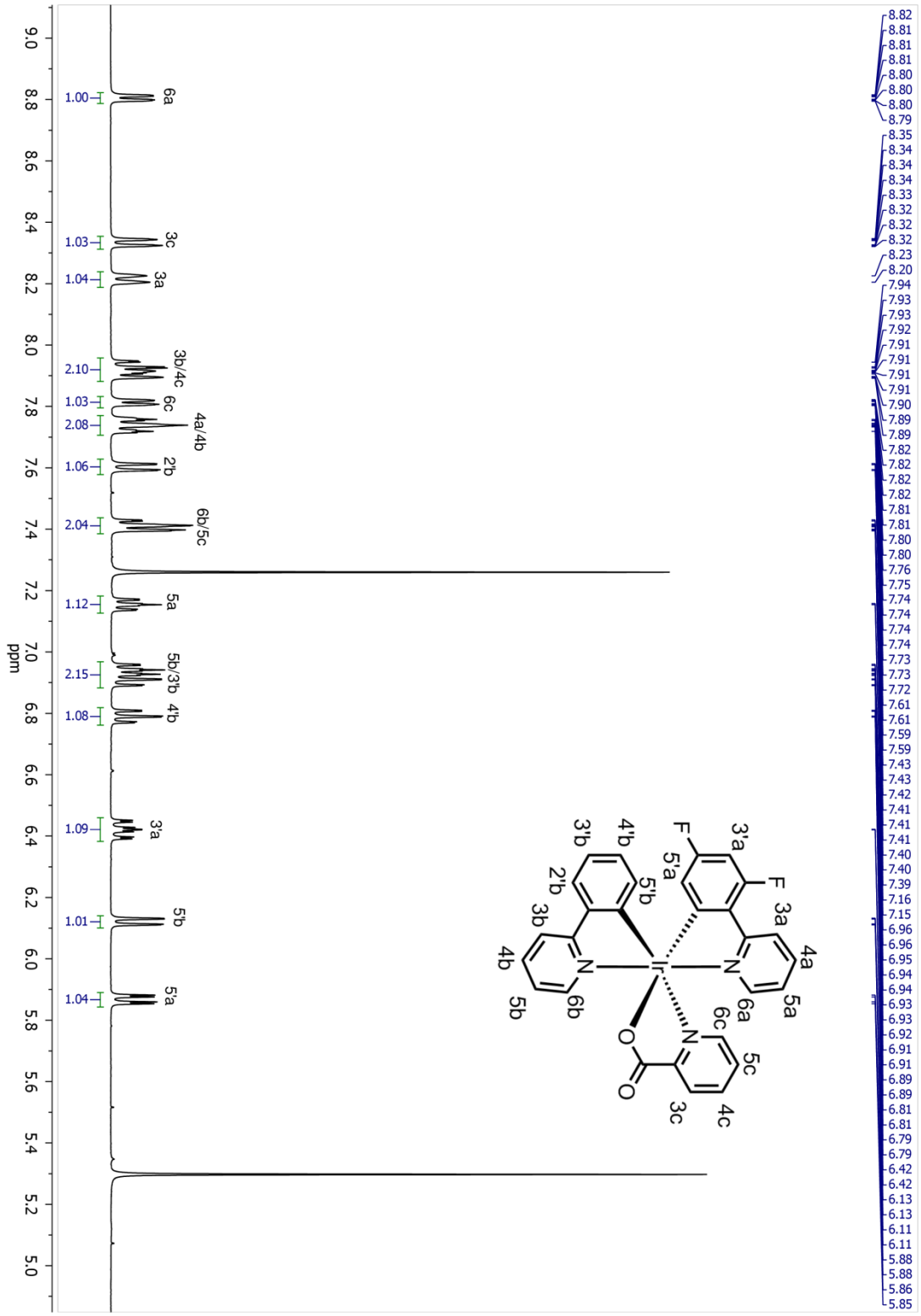

*Figure 9.81: ^{1}H-NMR spectrum of [Ir(dFppy)(ppy)(pic)] (**3b**).*

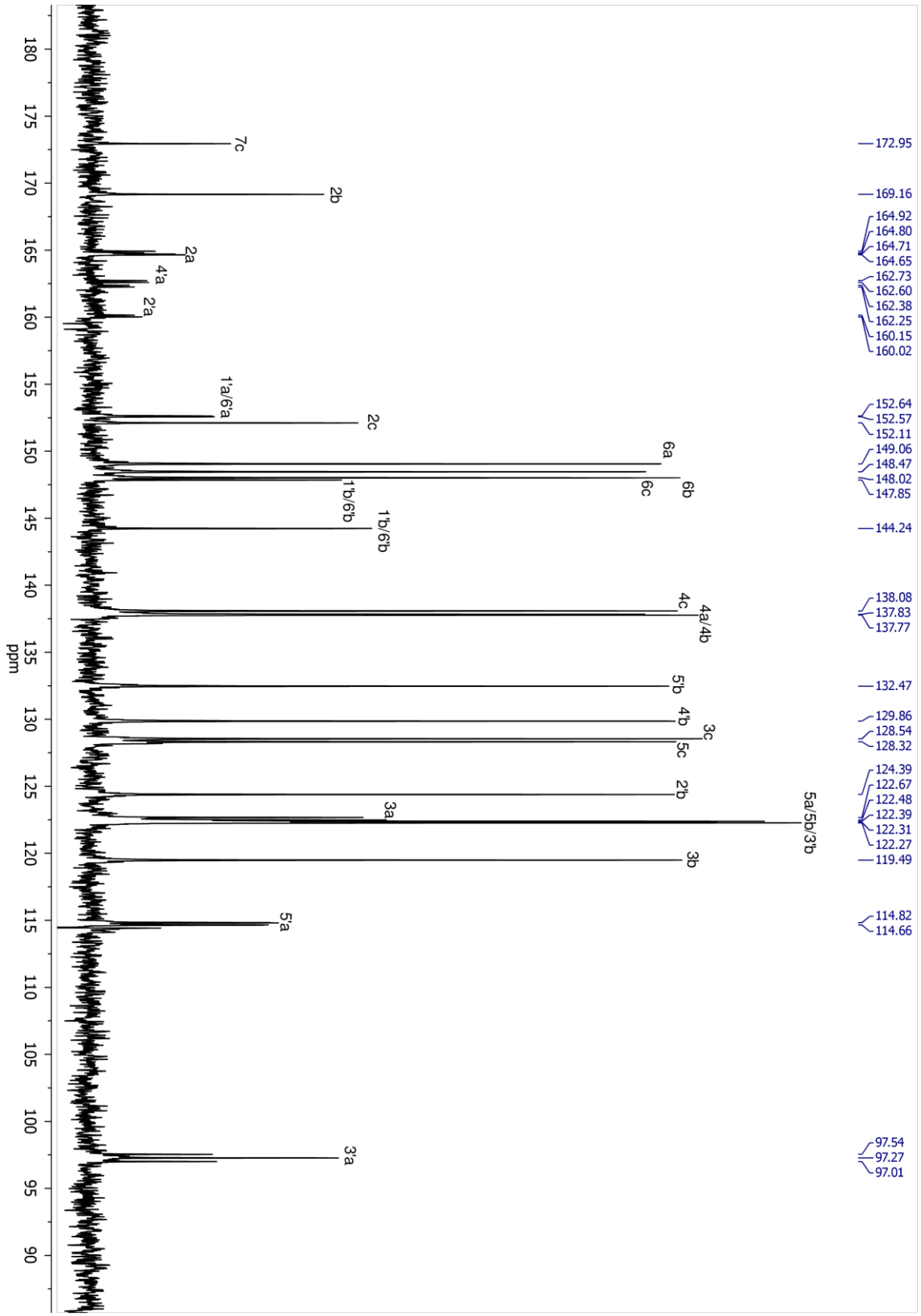

*Figure 9.82: [13]C-NMR spectrum of [Ir(dFppy)(ppy)(pic)] (**3b**).*

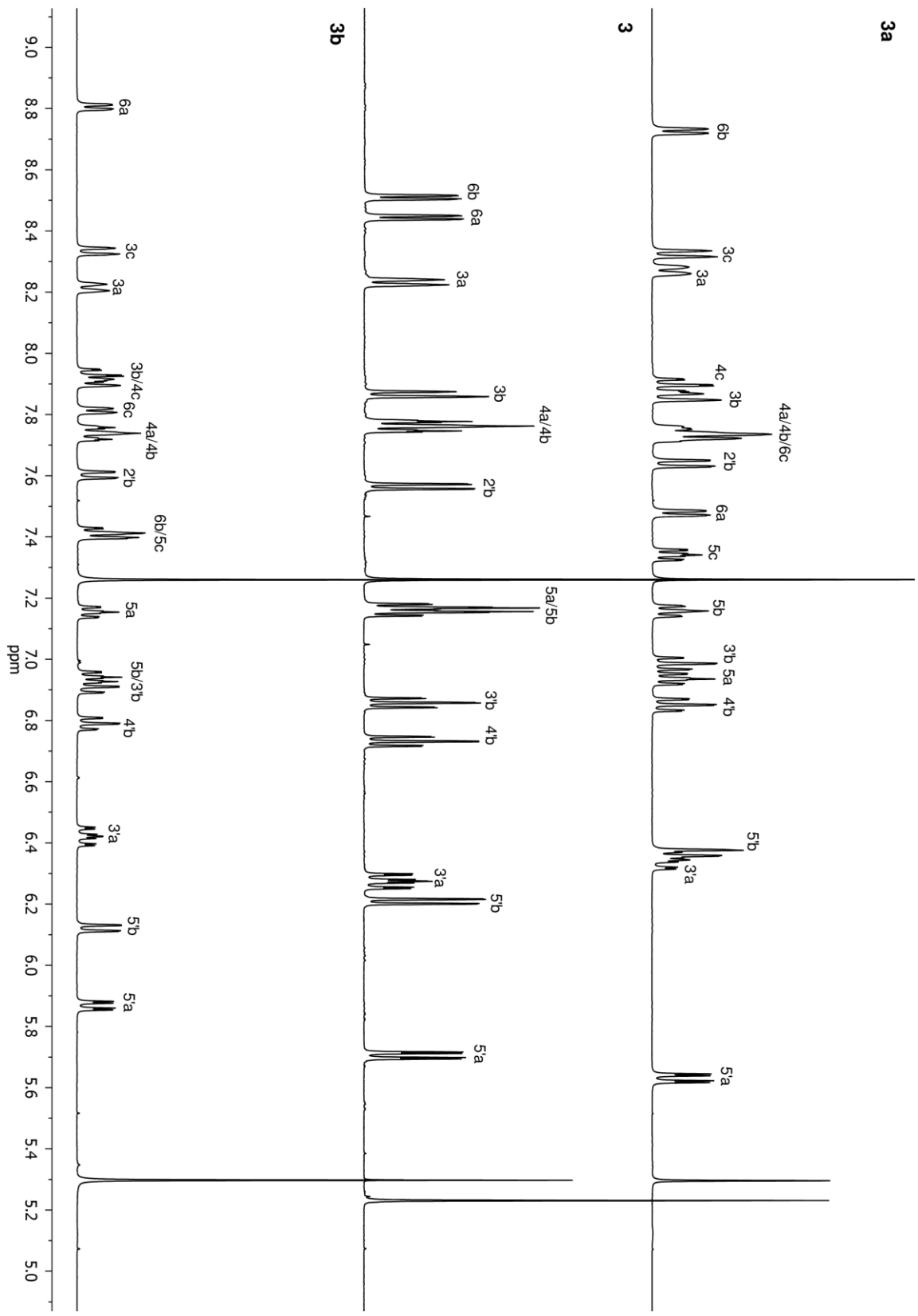

*Figure 9.83: Comparison of the ^{1}H-NMR spectra of **3a**, **3** and **3b**.*

9.7.13 [Ir(dFppy)(ppz)(pic)] (9a)

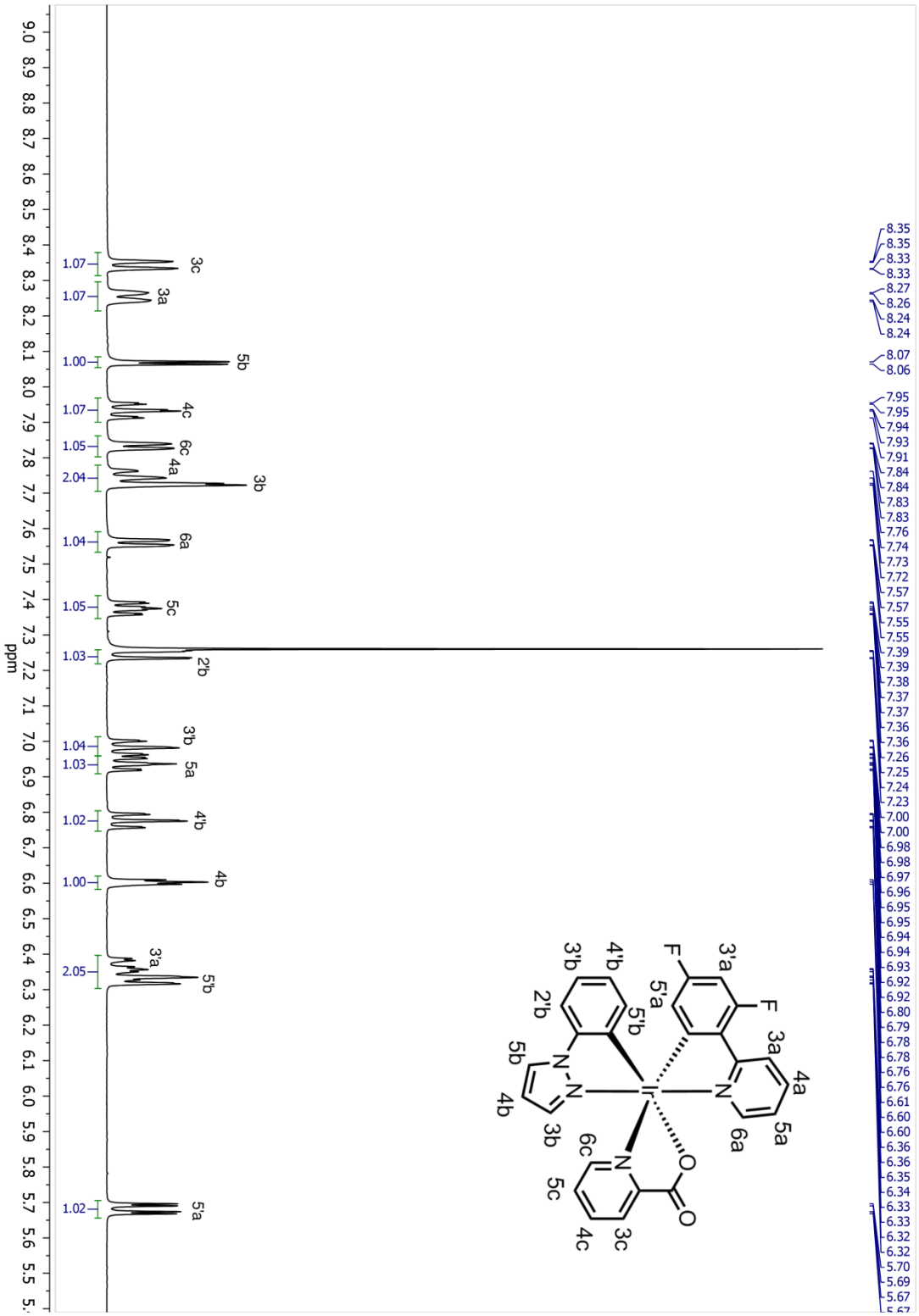

*Figure 9.84: [1]H-NMR spectrum of [Ir(dFppy)(ppz)(pic)] (**9a**).*

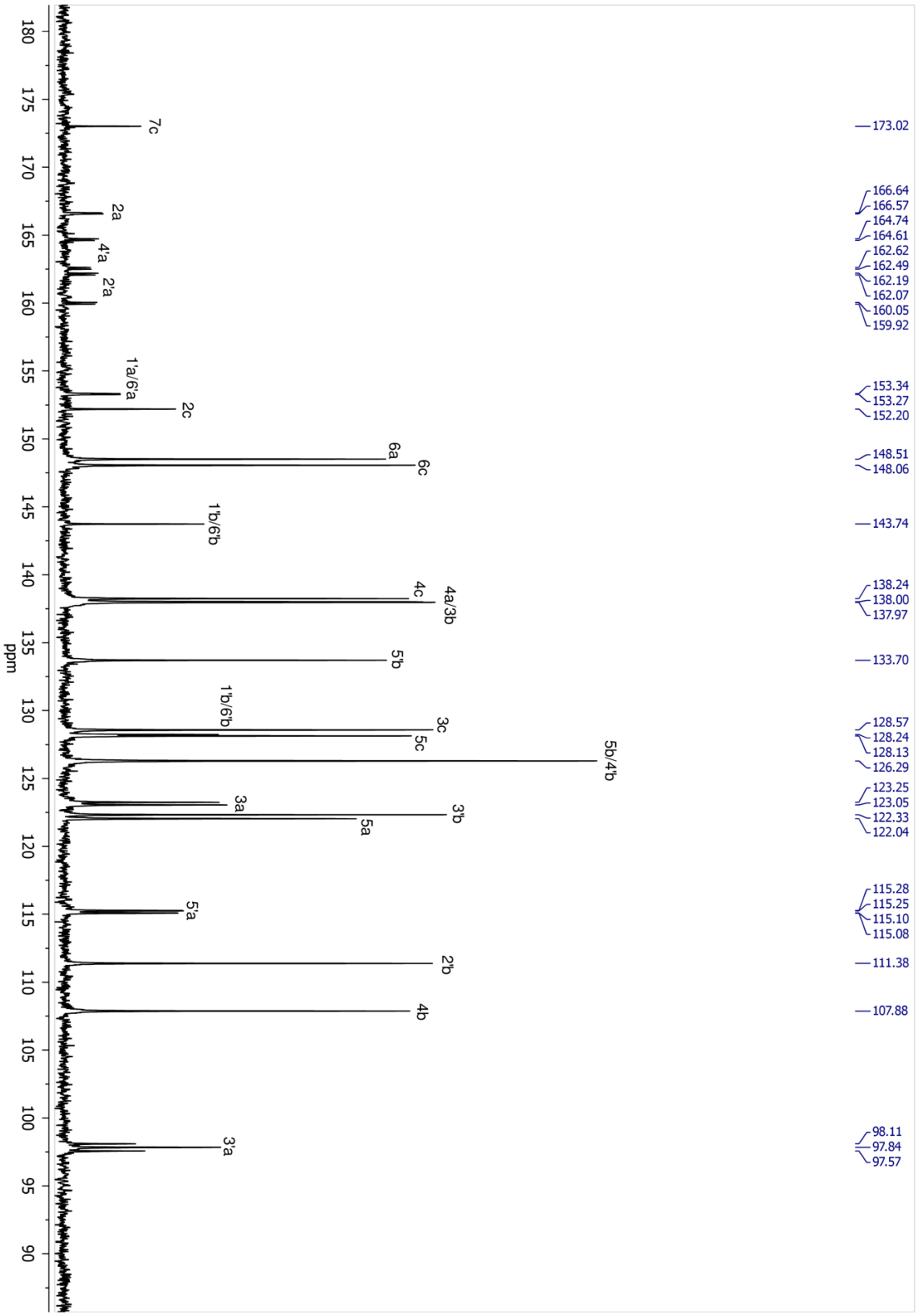

*Figure 9.85: [13]C-NMR spectrum of [Ir(dFppy)(ppz)(pic)] (**9a**).*

9.7.14 [Ir(dFppy)(ppz)(pic)] (9b)

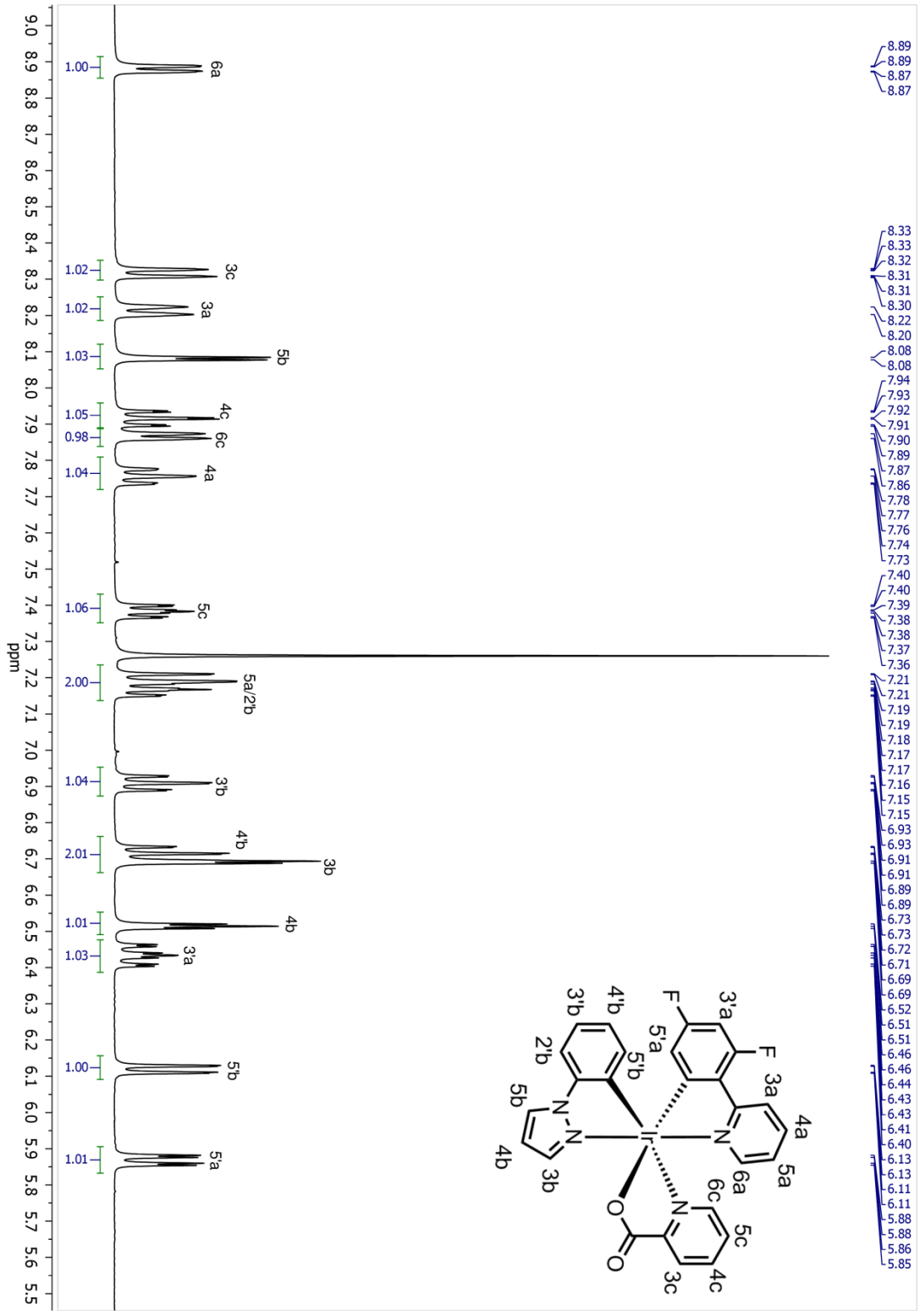

*Figure 9.86: [1]H-NMR spectrum of [Ir(dFppy)(ppz)(pic)] (**9b**).*

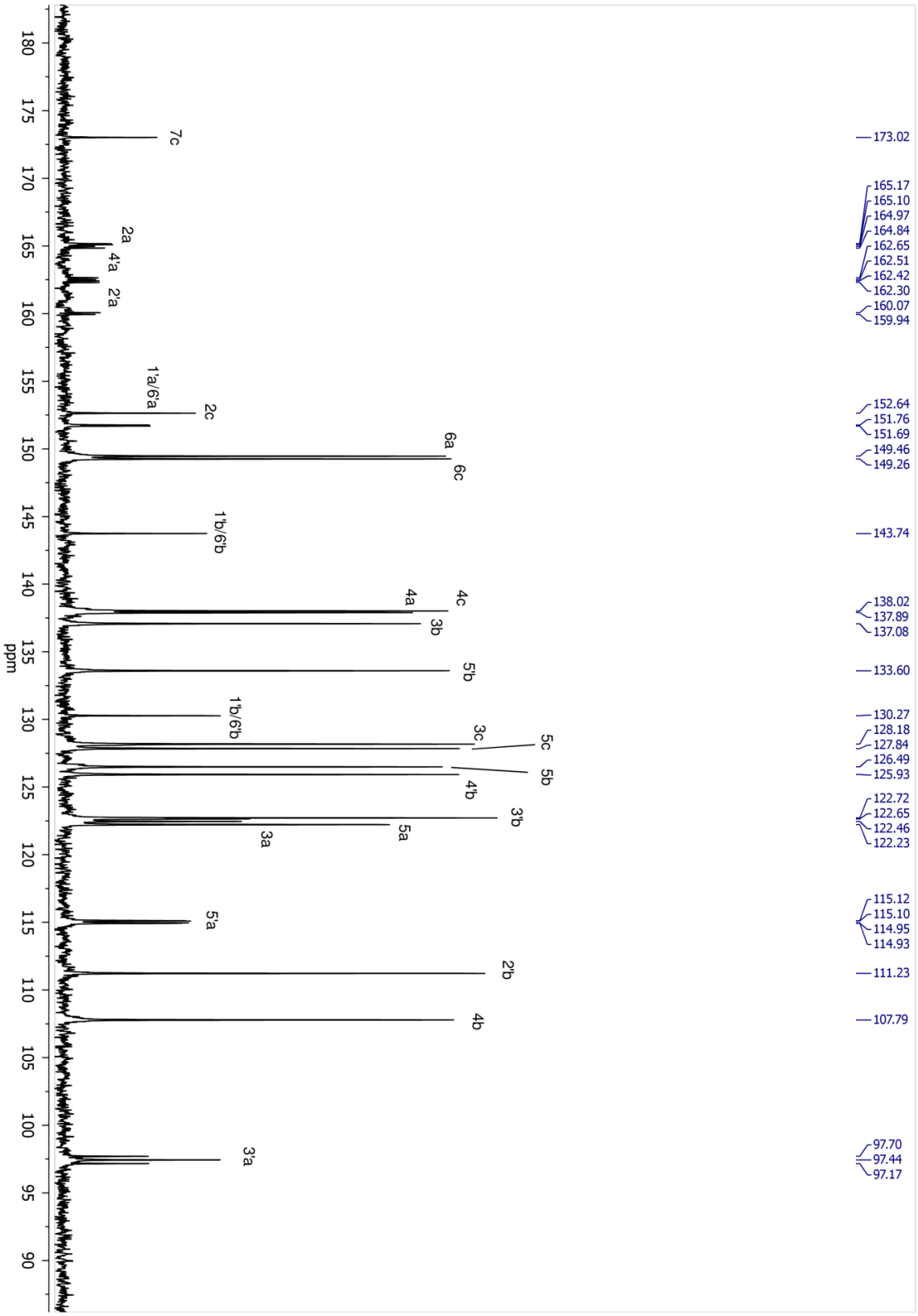

*Figure 9.87: ^{13}C-NMR spectrum of [Ir(dFppy)(ppz)(pic)] (**9b**).*

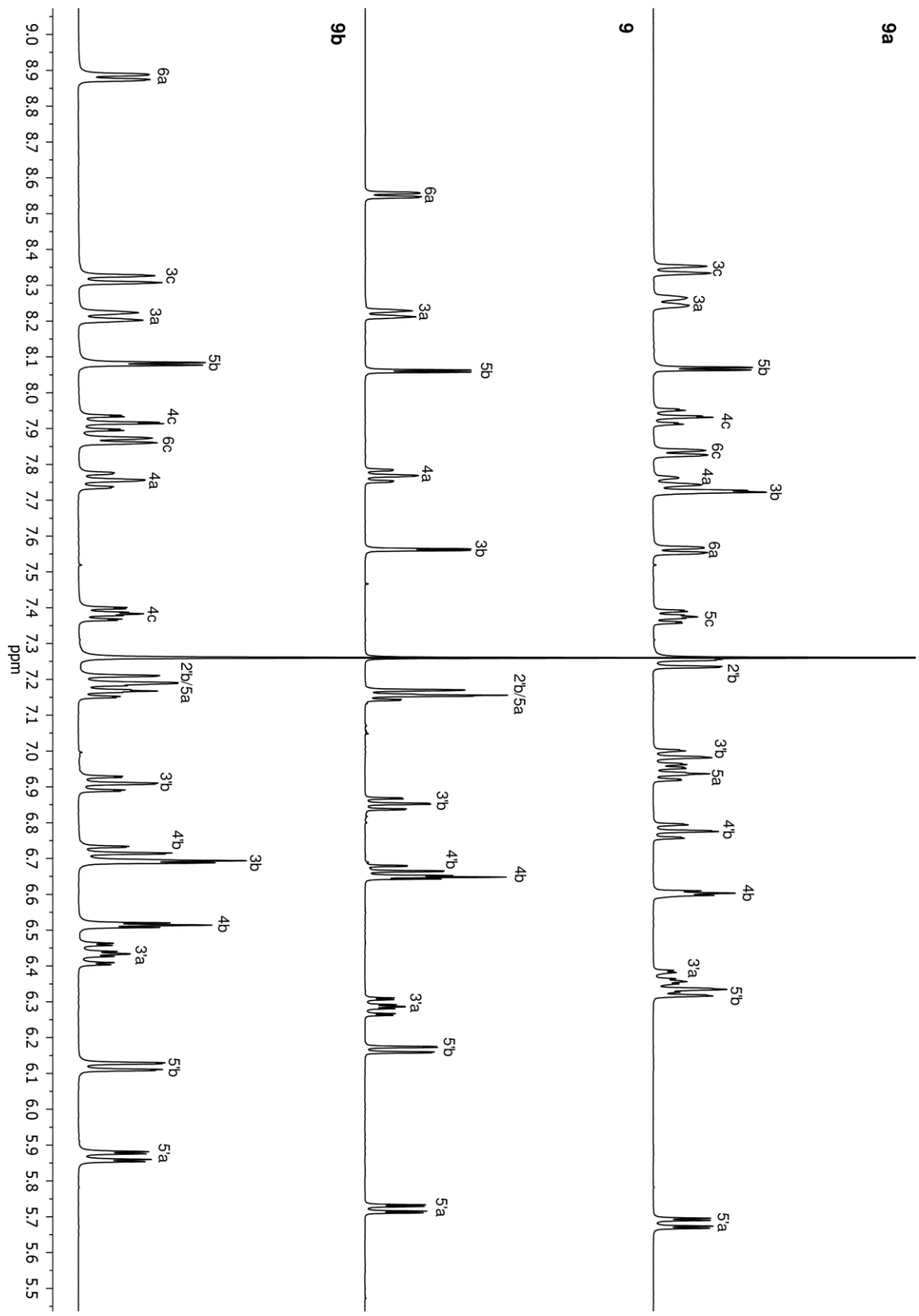

*Figure 9.88: Comparison of the ^{13}C-NMR spectra of **9a**, **9** and **9b**.*